

UNIVERSITY OF SOUTHAMPTON
FACULTY OF ENGINEERING, SCIENCE AND MATHEMATICS
SCHOOL OF CIVIL ENGINEERING AND THE ENVIRONMENT

**RELATIVE SOIL/WALL STIFFNESS EFFECTS ON
RETAINING WALLS PROPPED AT THE CREST**

BY

MARIA DIAKOUMI

THESIS FOR THE DEGREE OF DOCTOR OF PHILOSOPHY

MAY 2007

ACKNOWLEDGEMENTS

I would like to express my sincere gratitude to my supervisor Professor William Powrie for his valuable and continuous support, advice, guidance, patience and encouragement throughout the analysis and write-up of this thesis.

I would like to thank Dr Mike Byfield for his advice on Mathematica programme.

I'm grateful to my close friend Dr Asimina Maniopoulou for the advice, useful discussions and moreover the moral support and understanding during the last years.

Thanks to Dr David Richards and Dr Jo Clark for providing the data for the retaining wall at Ashford.

I would also like to thank Dr Antonis Zervos who encouraged me to start the project.

Many thanks to the Geotechnical Group of the School of Civil Engineering and the Environment for the financial support; I wouldn't have been able to undertake this project without it.

Special thanks to Clive Farquhar for the help with the printing and more importantly for the support and encouragement during the write-up of the thesis.

Finally, I should thank my family and all my friends who have made this experience really enjoyable.

UNIVERSITY OF SOUTHAMPTON
FACULTY OF ENGINEERING, SCIENCE AND MATHEMATICS
SCHOOL OF CIVIL ENGINEERING AND THE ENVIRONMENT
PHD THESIS
RELATIVE SOIL/WALL STIFFNESS EFFECTS ON RETAINING WALLS
PROPPED AT THE CREST

ABSTRACT

This thesis is focused on developing a practical design method, with reference to Eurocode 7 (EC7,1995), for retaining walls propped at the crest, which satisfies safety against collapse and serviceability requirements and incorporates both the real nature of soil behaviour and the wall flexibility.

For stiff walls, the rotation of the wall at the prop and the normalized prop loads, bending moments and deformations have been calculated for a range of values of retained height ratios, initial earth pressure coefficients and soil stiffness. The relative soil/wall flexibility has been quantified by means of a critical flexibility ratio that distinguishes a stiff from a flexible system.

The method is applied to flexible walls by idealising the wall flexibility into a simple mechanism and introducing new kinematically admissible fields to associate the mobilized shear strain with the mobilized shear strength in each soil zone by a hyperbolic relationship. The results are compared to those derived from Eurocode 7 (EC7, 1995) and are presented in curves to illustrate any differences. The advantage of this solution is that both the wall flexibility and the soil stiffness are considered in a simple calculation and it can be applied in a reasonably general manner.

The validity of this method has been assessed by comparison to results presented in previous research and to published data obtained from monitored case histories. The method can provide reasonably accurate results and is an improvement to linear elastic soil models or empirical techniques and thus can be a useful design tool.

NOTATION

A	Parameter in the calculation of the bending moments and deformations of a retaining wall
A	Parameter used in the transformed hyperbolic stress-strain relationship
A_1	Parameter used in the transformed hyperbolic stress-strain relationship
A_o	Parameter related to the soil plasticity
B	Parameter used in the transformed hyperbolic stress-strain relationship
B	Parameter in the calculation of the bending moments and deformations of a retaining wall
B_1	Parameter used in the transformed hyperbolic stress-strain relationship
C	Parameter in the calculation of the bending moments and deformations of a retaining wall
D	Parameter in the calculation of the bending moments and deformations of a retaining wall
E	Young's modulus. Subscripts may be used as follows: i (initial tangent); sec (secant); tan (tangent); u (undrained)
E^*	Rate of increase of Young's modulus with depth
E'	Drained Young's modulus
EI	Bending stiffness
F	Prop load
F	Factor of safety. A subscript may be used to describe how the factor of safety is applied.
F_s	Factor of safety applied to soil strength
$F/\gamma_s H^2$	Normalised prop load
F_{EC7}	Prop load according to Eurocode 7
F_{fes}	Prop load according to the free earth support method
F'_{EC7}	Normalised prop load according to Eurocode 7 equal to F_{EC7}/H^2
F'_{exp}	Experimental normalised maximum prop load according to Rowe (1955)
F'_{fes}	Normalised prop load according to the free earth support method equal to F_{fes}/H^2 (Rowe, 1952)
F'_{th}	Theoretical normalised prop load according to Rowe (1955)

G	Shear modulus. Subscripts may be used as follows: o (initial tangent); sec (secant); tan (tangent).
G^*	Rate of increase of shear modulus with depth
H	Overall length of a retaining wall
J_1, J_2	Constants of integration in the calculation of the deformations of a retaining wall
K	Parameter in the calculation of the bending moments and deformations of a retaining wall
K_a	Active earth pressure coefficient
K_{aR}	Coulomb active earth pressure coefficient
K_i	Pre-excavation earth pressure coefficient
K_o	In situ earth pressure coefficient
K_p	Passive earth pressure coefficient
K_{pR}	Coulomb passive earth pressure coefficient
L	Parameter in the calculation of the critical flexibility ratio
M	Bending moment. Subscripts may be used as follows: i (value at i_{th} point along the retaining wall); max (maximum value); $max,EC7$ (maximum value according to Eurocode, <i>EC7,1995</i>); max,fes (maximum value according to the free earth support method)
M'	Normalised maximum bending moment equal to $M_{max}/(\gamma_s H^3)$
M'_{fes}	Normalised maximum bending moment according to the free earth support method equal to $M_{max,fes}/H^3$ (Rowe,1952)
M'_{EC7}	Normalised maximum bending moment according to Eurocode 7 equal to $M_{max,EC7}/H^3$
M'_{exp}	Experimental normalised maximum bending moment according to Rowe (1955)
M'_{th} (1955)	Theoretical normalised maximum bending moment according to Rowe (1955)
OCR	Overconsolidation ratio
R	Rowe's (1952, 1955) flexibility number
R_{crit}	Critical flexibility ratio
R_f	Parameter used in the hyperbolic stress-strain relationship (Duncan and Cheng, 1970)

a	Parameter used in the hyperbolic stress-strain relationship (Duncan and Cheng, 1970)
b	Parameter used in the hyperbolic stress-strain relationship (Duncan and Cheng, 1970)
c_u	Undrained shear strength
d	Embedment depth of a retaining wall
f	Subscript used to denote final conditions
h	Retained height of a retaining wall
f	Subscript used to denote horizontal
i	Subscript used to denote points along the retaining wall
ki	Rotational spring stiffness
m	Retained height ratio ($=h/H$)
m_r	Rowe's (1952, 1955) soil parameter
max	Subscript used to denote maximum value of a parameter
n	Number of springs
n_o	Parameter related to the soil plasticity
p'	Mean effective stress
p_b	Passive pressure
p_r'	Reference pressure of 1 kPa
p_o'	Initial mean effective stress; average principal effective stress at the tip of current yield locus
q	Surface surcharge
q	Deviator stress
s	Average total stress: defines centre of Mohr circle of stress on σ -axis
s'	Average effective stress: defines centre of Mohr circle of stress on σ' -axis
t	Radius of Mohr circle of stress
u	Pore water pressures
ult	Subscript used to denote the ultimate value of a parameter
v	Subscript used to denote vertical
vol	Subscript used to denote volumetric
w	Load
z	Depth coordinate
z_i	Depth of i_{th} poin

β	Denotes the ratio: depth to anchor level / overall height
γ	Shear strain
γ_s	Soil unit weight
δ	Angle of soil/wall friction
δ_{act}	Angle of soil/wall friction behind the wall
δ_i	Displacement at i_{th} point along the retaining wall
δ_{pass}	Angle of soil/wall friction in front of the wall
$\delta\gamma$	Change in the shear strain
$\delta\varepsilon$	Change in the direct strain
$\delta\theta_i$	Change in the rotation at i_{th} point along the retaining wall
$\delta\tau$	Change in the shear stress
ε	Direct strain. Subscripts are used: h (horizontal); v (vertical);
ε_a	Axial strain
ε_{vol}	Volumetric strain
$\varepsilon_1, \varepsilon_3$	Major and minor principal strains
θ	Rotation
ν	Poisson's ratio
ρ	Critical flexibility according to Rowe (1952, 1955)
ρ_c	Critical flexibility according to Rowe (1952, 1955)
σ, σ'	Total and effective stress. Subscripts are used as follows: h (horizontal); v (vertical); o (initial)
σ_1, σ_3	Major and minor total stress
σ_1', σ_3'	Major and minor effective stress
σ'_{haR}	Effective horizontal active stresses for a wall in limit equilibrium according to Rowe (1952, 1955)
σ'_{hpR}	Effective horizontal passive stresses for a wall in limit equilibrium according to Rowe (1952, 1955)
τ	Shear stress. Subscripts are used as follows: f (final); o (initial); ult (ultimate); un (undrained)
φ'	Soil strength
φ_{crit}'	Critical soil strength
φ_{design}'	Design soil strength
φ_{mob}'	Mobilised soil strength
φ_{peak}'	Peak soil strength

ψ_i, ω_i

Relative rotations of i_{th} point along the retaining wall

CONTENTS

Acknowledgements.....	i
Abstract.....	ii
Notation.....	iii
1. General introduction.....	1
1.1 Introduction	1
1.2 Objectives of the research.....	3
2. Analysis and design of retaining walls.....	5
2.1 Introduction.....	5
2.2 Analysis of retaining walls.....	5
2.2.1 Limit equilibrium methods for embedded retaining walls.....	5
2.2.2 Fixed earth support conditions for unpropped embedded walls.....	5
2.2.3 Free earth support conditions for embedded walls propped at the crest.....	8
2.2.4 Fixed earth support conditions for walls propped at the crest.....	9
2.2.5 Earth pressure coefficients and the contribution of soil-wall friction	10
2.2.6 Estimation of the displacements.....	11
2.3 Codes of practice for retaining walls.....	15
2.3.1 Modern codes of practice for embedded retaining walls in the ultimate limit state.....	16
2.3.2 Modern codes of practice for embedded retaining walls at the serviceability limit state.....	18
2.3.3 Limitations of current design practice.....	19
2.4 The mobilised strength method.....	20
2.4.1 Theoretical background of the method.....	20
2.4.2 Evaluation and accuracy of results.....	24
2.4.3 Design procedure based on the mobilised strength method.....	25
2.5 Summary.....	27
3. Analysis and design of stiff retaining walls propped at the crest.....	28
3.1 Introduction.....	28
3.2 The relative soil / wall stiffness.....	28
3.2.1 Flexibility number.....	37
3.2.2 Critical flexibility ratio.....	39
3.3 Stress distributions.....	39
3.3.1 Behind the retaining wall.....	39
3.3.2 In front of the retaining wall.....	44
3.4 Wall rotation.....	49
3.5 Prop loads.....	52
3.6 Bending moments.....	54
3.7 Deformations.....	54
3.8 Critical flexibility ratio.....	56
3.9 Summary.....	59
4. Analysis and design of flexible retaining walls propped at the crest.....	60
4.1 Introduction.....	60
4.2 Soil behaviour.....	60

4.2.1 Soil stress-strain behaviour.....	61
4.2.2 Theoretical modelling of soil behaviour.....	73
4.2.3 Hyperbolic stress-strain relationship.....	76
4.2.4 Comparison with other soil models.....	79
4.3 Application of the mobilized strength method to flexible retaining walls.....	87
4.3.1 Assumptions.....	87
4.3.2 Wall rotations.....	88
4.3.3 Mobilised strength.....	94
4.4 Wall flexural rigidity analysis.....	97
4.4.1 Flexural rigidity analysis for a retaining wall propped at the crest...	110
4.5 ULS calculations for a retaining wall propped at the crest in conditions of zero pore water pressures.....	114
4.6 SLS calculations for a flexible retaining wall propped at the crest in drained conditions.....	116
4.7 Summary.....	135
5. Analysis and design of flexible retaining walls propped at the crest in conditions of pore water pressures corresponding to linear seepage.....	136
5.1 Introduction.....	136
5.2 ULS calculations: Original water table at ground level.....	136
5.3 SLS calculations: Original water table at ground level.....	138
5.4 ULS calculations: Original water table at half the retained height level.	152
5.5 SLS calculations: Original water table at half the retained height level.	154
5.6 Reduction curves for stiff clays and sands.....	167
5.7 Summary.....	170
6. Comparison between the MSD method and other methods of analysis..	171
6.1 Introduction.....	171
6.2 Comparison between the MSD method and Rowe's analysis.....	172
6.2.1 Transformed axes.....	172
6.2.2 Experimental curves.....	179
6.2.3 Theoretical curves.....	184
6.3 Comparison of the MSD method between stiff and flexible walls.....	186
6.3.1 Example 1.....	188
6.3.2 Example 2.....	190
6.4 Summary.....	192
7. Validation of the MSD method for flexible walls with case histories.....	193
7.1 Introduction.....	193
7.2 Case History 1: Propped contiguous bored pile wall at Walthamstow...	194
7.3 Case History 2: Propped diaphragm wall at the A406/A10 junction.....	199
7.4 Case History 3: Propped secant pile wall at Hackney to M11 link.....	204
7.5 Case History 4: A contiguous bored pile wall on the Channel Tunnel Rail Link at Ashford.....	209
7.6 Case History 5: A secant pile embedded retaining wall at Bell Common Tunnel in Essex.....	215

7.6.1 Case History 5: Finite element analysis for a propped retaining wall at Bell Common Tunnel in Essex.....	220
7.7 Summary.....	222
8. Conclusions and further work.....	224
8.1 Conclusions.....	224
8.2 Further work.....	226
References.....	227
Appendices.....	234

1. GENERAL INTRODUCTION

1.1 INTRODUCTION

The construction of excavations and retaining walls is now a common solution to the congestion in urban areas and its inevitable consequences of limited building space, high land cost, overloaded transport and scarce parking space. Advances in construction methods and the improved accuracy of monitoring systems encourage its application to many large scale engineering projects in a variety of soils. However, the design procedure is often complicated, since soil-structure interaction may have an important effect on the behaviour of retaining walls and the control of deformations required to minimise disturbance to the adjacent properties at a minimum construction cost.

Retaining walls should maintain stability and prevent excessive deformations and bending moments. Avoidance of collapse or other form of structural failure of the wall is ensured by limit state design, known as the Ultimate Limit State (ULS). However, a wall should not only be remote from collapse, but must also meet specific service performance requirements. Excessive deformations and associated ground movements, excessive stresses in walls and props or unwanted leakage of ground water through or beneath the wall can all be considered as another limit state known as the Serviceability Limit State (SLS), that a wall should also be designed to avoid. Depending on the properties of the soil and the retaining wall, the avoidance of collapse may predominate in some design cases, while serviceability can be more critical in others.

Codes of practice recommend limit equilibrium calculations with the soil strength being reduced by a factor of safety F_s , to ensure that the wall is remote from the Ultimate Limit State (ULS). Guidelines to avoid the Serviceability Limit State are fewer and less clear than for the ultimate state, since deformations are often assumed to be a secondary problem and are predicted by calculations based on elasticity theory. However, in reality soil is not a linear isotropic elastic material and its stiffness depends on both stress and strain; hence in some cases past experience and recorded behaviour of retaining walls is

used as guidance in design, but this empirical knowledge can only be applied to similar and comparable cases.

Numerical methods such as finite element analysis are increasingly used to develop analytical models that represent non-linear soil behaviour. Their accuracy depends on the selected soil model and although in recent years substantial progress has been made, there remain significant drawbacks which restrict their application. The use of more sophisticated soil models and soil parameters derived from high quality laboratory test data does not always contribute to the correct prediction of strains and deformations. Moreover, the assumptions are such that the evaluation of the results may be difficult, and although they may be applicable to specific sites, they are often inappropriate for other design cases. The use of a detailed model could cause complications and be unacceptably time consuming in design analysis. The great numbers of parameters required for the development of the soil model, the calibration of the values and their sensitivity restrict significantly the practicality of these methods. Taking into account the expertise and the cost involved when adopting such rigorous soil models, the designer should decide whether their use is justified.

Therefore, the development of a simple and practical design method that can reliably determine the factor of safety against Ultimate Limit failure in the ground and the likely in service deformations for walls propped at the crest would be a useful tool in the design of retaining walls. The geostructural mechanism proposed by Bolton and Powrie (1988) relates the wall deformations to the proportion of the actually mobilised soil strength in a limit equilibrium analysis for stiff cantilever or propped at the crest retaining walls. The mobilised soil strength can then be used to estimate the factor of safety on soil strength. The advantages of this approach are its simplicity, the small number of the required input parameters and its potential to provide a general design solution.

Previous research (Rowe, 1952) has shown that wall flexibility could cause a reduction in bending moments compared with stiffer walls. Considering also the non-linear behaviour of soil, with soil stiffness being dependent on the stress and strain level, there is a need for a new approach that takes into account both of these effects in the design of retaining walls. An expression that quantifies the overall flexibility of the soil and the retaining wall needs to be established and the term “stiff” or “flexible” system might be

more appropriate than referring merely to the wall flexibility in the analysis of retaining walls. A critical flexibility value that distinguishes a flexible system from a stiff one should be defined and its sensitivity to other parameters should be checked.

For stiff systems the geostitutional mechanism procedure (Bolton and Powrie, 1988) could then be used to explore the effect of the soil stress-strain response on wall rotations, deformations, bending moment and prop loads. Application of a modified form of the geostitutional mechanism to flexible systems might be possible, and its potential should be investigated for walls with different embedment depths and flexibilities and for soils with different earth pressure coefficients and stiffness parameters in drained and undrained conditions.

1.2 OBJECTIVES OF THE RESEARCH

This dissertation is aimed at developing a simple and reliable design procedure, with reference to the codes of practice, that can be used as an alternative to either empirical or potentially expensive and complicated numerical solutions. The method will be able to determine the factor of safety against a limit state failure in the ground and provide an estimate of the in service deformations for retaining walls propped at the crest. The post-installation stress state and the stress-strain response, together with the relative soil-wall flexibility and other soil-structure interaction effects, that lead to a variation in soil strain and hence mobilised soil strength with depth, will be taken into account.

More specifically the objectives of this research are:

- To review, evaluate and compare previous research, current design procedures and their limitations (Chapter 2).
- To quantify the relative soil / wall flexibility and define a critical flexibility value that distinguishes a stiff from a flexible system for walls with different

embedment depths and flexibilities and for soils with different earth pressure coefficients and stiffness parameters (Chapter 3).

- To develop a geostitruktural mechanism for flexible systems and explore the effect of the wall flexibility and soil stress-strain response on their design parameters. To compare the results to those derived from the modern codes of practice (Chapter 4).
- To incorporate the pore water pressures with the water table at different levels (Chapter 5).
- To compare the results obtained from the geostitruktural mechanism to experimental and theoretical results presented by Rowe (1952, 1955). To illustrate any similarities or differences in the application of the geostitruktural mechanism to stiff and flexible systems (Chapter 6).
- To assess the validity of the methods by comparison with data from monitored case studies (Chapter 7).

The volume and complexity of the calculations involved in the establishment of the methods described above were facilitated by Mathematica, a computer programme that combines symbolic manipulation, numerical mathematics and graphics. A detailed description of the calculations carried out in Mathematica is provided in the Appendices.

2. ANALYSIS AND DESIGN OF RETAINING WALLS

2.1 INTRODUCTION

In this chapter the different methods used in current engineering practice and the codes of practice for the calculation of collapse conditions and the estimation of the in service deformations in the design of retaining walls are presented and discussed. The methods are evaluated and the restrictions associated with their application to design are indicated. The need for a simple design solution that incorporates the real nature of soil behaviour is underlined. Finally, the mobilised strength method introduced by Bolton and Powrie (1988) is described and discussed.

2.2 ANALYSIS OF RETAINING WALLS

2.2.1 Limit equilibrium methods for embedded retaining walls

To assess the stability of an embedded retaining wall, limit equilibrium methods or lower bound solutions are often used. Limit equilibrium methods are based on the calculation of the maximum height of excavation or the minimum depth of embedment for which static equilibrium may be maintained; this is the limit equilibrium situation. In the lower bound approach proposed by Rankine (1857), the earth pressure distributions in certain zones of soil are described by the active and passive limit values (K_a and K_p).

2.2.2 Fixed earth support conditions for unpropped embedded walls

Unpropped embedded walls are frequently used for temporary and permanent support of excavations up to 4-5 m high. Formed of steel sheet piles or constructed *in situ* using reinforced concrete, they consist of a vertical structural element embedded into the ground

below the retained material. The force required to retain the material behind the wall is obtained from the upper part of the wall due to its stiffness and the embedment of the lower part. In front of the embedded portion of the wall passive earth pressures are developed to resist the pressures of the retained soil behind the wall.

Assuming that a structural failure of the wall does not occur, unpropped embedded walls will tend to fail by rotation about a pivot point near the toe at some depth z_p below formation level. On the verge of collapse the stress distribution on the wall can be obtained by assuming frictionless discontinuities running vertically and horizontally through the pivot point and the toe. The limiting lateral effective stress distribution for an unpropped wall is shown in Figure 2.1. In zones where the wall is moving away from the soil the lateral effective stresses are at the active limit

$$\sigma'_h = K_a \sigma'_v, \quad K_a = (1 - \sin\phi') / (1 + \sin\phi') \quad (2.1)$$

where σ'_h and σ'_v are the horizontal and vertical effective stresses, K_a is the active earth pressure coefficient and ϕ' is the soil angle of shearing resistance. In zones where the wall is moving into the soil the lateral effective stresses are at the passive limit

$$\sigma'_h = K_p \sigma'_v, \quad K_p = (1 + \sin\phi') / (1 - \sin\phi') \quad (2.2)$$

where K_p is the passive earth pressure coefficient. A centre of rotation near the toe is required for moment equilibrium, so below this point the wall is assumed to deflect towards the retained soil. This causes a switch in soil pressures, with the passive pressures now induced in the soil behind the wall and the active pressures induced in the soil in front.

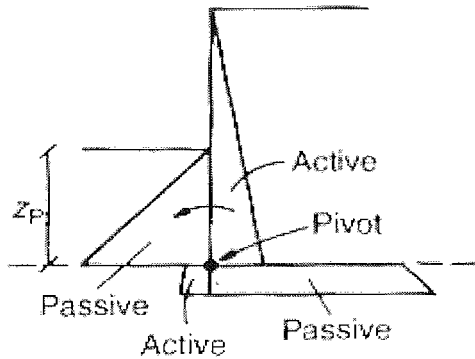


Figure 2.1: Idealised effective stress distribution for an unpropped embedded retaining wall (Powrie, 1997).

In this approach, which is known as the fixed earth support method, there are two unknowns that must be calculated using the conditions of horizontal and moment equilibrium. These are the depth of embedment required for limiting equilibrium and the depth z_p to the pivot point. For ease of calculation, the lateral stresses below the level of the pivot point may be replaced by a point force Q (Figure 2.2).

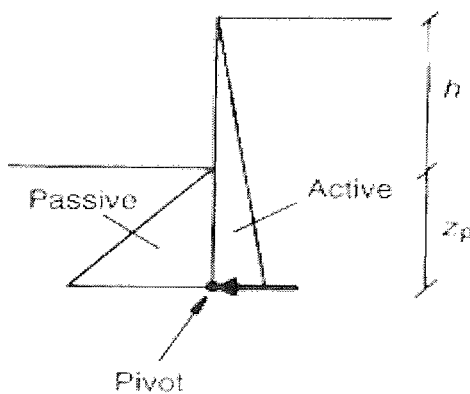


Figure 2.2: Approximate stress analysis for unpropped walls (Powrie, 1997).

In this case the two unknowns are the force Q and the depth z_p , which can be calculated by taking moments about the pivot. The required depth of embedment is then conventionally taken as $d = 1.2 z_p$. It is necessary to check that this additional depth of embedment is actually sufficient to mobilise the force Q below the pivot point. For most real walls, the stress analysis described above with the values of K_a and K_p obtained from

Equations (2.1) and (2.2) will result in an over-conservative estimation because the effects of soil-wall friction are neglected.

2.2.3 Free earth support conditions for embedded walls propped at the crest

For deep excavations, unpropped embedded walls are inadequate and installation of props or anchors at one or more levels is required. Assuming that a structural failure of the wall or the props does not occur, an embedded wall will tend to fail by rotation about the position of the prop. In this method, which is known as the free earth support method, the effect of any possible fixity below the excavation level is not considered and hence the toe of the wall is assumed to be free to move laterally.

The effective stress distribution at failure shown in Figure 2.3 may be determined by assuming stress discontinuities running vertically on both sides of the wall and horizontally through the toe. The two unknowns in this case are the depth of embedment and the prop load. The depth of embedment d can be calculated by taking moments about the prop and then the prop load F is calculated from the horizontal force equilibrium.

The free earth support method will lead to overconservative results, because the effects of soil-wall friction and also the lateral stress reduction behind the wall due to soil arching when the prop is rigid are both neglected.

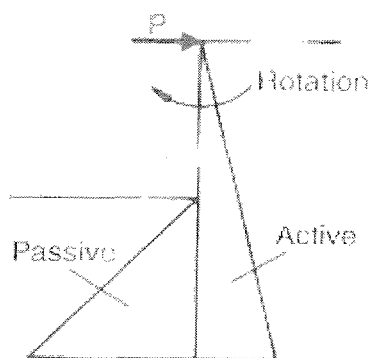


Figure 2.3: Idealised stress distribution for an embedded wall propped at the crest (Powrie,1997).

2.2.4 Fixed earth support conditions for walls propped at the crest

A fixed earth support calculation may be considered appropriate for an embedded wall propped at the crest, if the wall is sufficiently flexible. The idealised and simplified effective stress distributions are shown in Figure 2.4. In this approach it is assumed that there is a point of fixity near the toe, which results in a reversal in the sign of the bending moments due to the wall flexibility. However, the system shown in Figure 2.4 is statically indeterminate since a collapse mechanism is not defined, unless some further assumption is made. Williams and Waite (1993) suggest that the point of contraflexure at which the bending moment is zero, occurs at the level where the net pressure acting on the wall is zero, in order to calculate the prop force and the depth of embedment. Alternatively, such a system would be statically determinate for a propped wall where the prop yields at a constant load and the prop yield load is known (Powrie, 1997).

Although this approach may be appropriate for flexible walls, since it takes into account in a way the effects of the wall bending, it is not generally recommended for stiff walls in clay soils (Padfield and Mair, 1984).

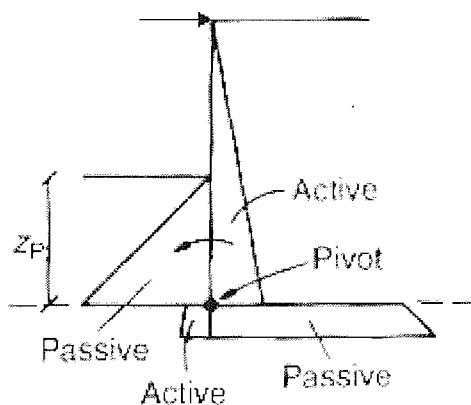


Figure 2.4: Effective stress distribution based on the *fixed earth support* method for embedded walls propped at the crest (Powrie, 1997).

2.2.5 Earth pressure coefficients and the contribution of soil-wall friction

The shear stresses generated at the soil/wall interface can contribute to wall stability; thus it is common, particularly in an effective stress analysis, to use modified values of earth pressure coefficients. The soil/wall friction and hence the modified values of earth pressure coefficients depend on the direction and degree of the relative movement between the wall and the soil. It is generally assumed that the soil exerts a downward shear force on the wall in the active zone and an upward shear force in the passive zone. This decreases the active earth pressure coefficient K_a and increases the passive earth pressure coefficient K_p , in order to take account of the soil/wall friction.

However, there is considerable uncertainty in defining the direction of soil/wall friction below the point of rotation for unpropped walls. Krey's (1932) experiments on a small-scale model of a cantilever wall embedded in sand indicated that the value of K_p was larger above the centre of rotation of the wall than below it, consistent with the direction of soil/wall friction being downwards below this point. Bica and Clayton's (1998) laboratory-based experiments, which modelled the embedded length of cantilever walls on sand, confirmed Krey's opinion on the downwards direction of soil/wall friction below the centre of rotation on the retained side.

Regarding the magnitude of wall friction, Rowe (1963) suggested that the maximum soil/wall friction angle that can possibly be developed, δ_{max} , has two components, $\delta_{max} = \varphi_w + r$, where φ_w is the true friction angle between the soil grains and the material of the wall and r is the wall roughness angle. For practical purposes this might imply $\delta_{max} \approx \varphi'_{crit}$. Most design methods adopt values of soil/wall friction δ which are somewhat less than the soil strength φ' . More details regarding the recommendations of some popular codes of practice will be given later in this chapter.

2.2.6 Estimation of the displacements

The soil displacements associated with excavations comprise of vertical and horizontal movements. Vertical heave within the excavation occurs in response to the vertical load relief in front of the retaining wall, while wall movements behind the wall result from the removal of lateral support. Horizontal movements are usually more critical than vertical behind the wall because they can cause more damage to adjacent buildings and services (Gaba *et al*, 2003).

Although soil is a non-linear material and its stiffness depends on its stress history, stress state and stress/strain path, calculations of soil and wall deformations are often based on elasticity theory and a constant soil stiffness modulus is assumed. The advantage of this is that a number of standard solutions and methods of analysis for elastic materials can then be used (e.g. Terzaghi, 1943; Boussinesq, 1885; Newmark, 1942; Fadum, 1948).

However, the complexity of the theoretical analyses has led to the use of empirical methods based on observational data for the estimation of the pattern and magnitude of deformations in current design practice. Peck (1969) presented a chart that separates the settlements induced by excavations in clay soils into three zones depending on some of the properties of the clay and the excavation. Peck's chart as shown in Figure 2.5 generally overestimates settlements as it is based on data from retaining systems that are outdated (Diakoumi and Lavdas, 2003); hence his results may be used for the estimation of the upper deformation limits. Clough and O'Rourke (1990) proposed envelopes of short term ground settlements behind different types of retaining walls, based on observational data from a number of excavations in sands, stiff to hard clays and soft to medium clays. These empirical settlement profiles are presented in Figure 2.6, where the distance from the wall is expressed as a ratio of the maximum excavation depth H_e and the distribution of settlements δ_v is shown as a proportion of the maximum settlement behind the wall $\delta_{v_{mx}}$. According to Gaba *et al* (2003), they provide a conservative estimate of the distribution of settlements.

Hsieh and Ou (1998), based on observational data from ten deep excavations in Taipei (Ou *et al*, 1993), presented two possible settlement profiles as shown in Figure 2.7. In the

spandrel settlement profile the maximum settlement is observed just behind the retaining wall, whereas in the concave profile the maximum settlement is measured at a distance from the wall. Regarding the horizontal movements, Long (2001) presented graphs of measured normalised maximum wall deflections against the support system stiffness $\rho_s = EI / \gamma_w h^4$, where EI is the rigidity of the wall, γ_w is the bulk unit weight of water and h is the average vertical distance between the props, for a great number of case histories of walls embedded in a stiff stratum but retaining varying amounts of soft ground. According to Long (2001), wall deflections may increase substantially for walls embedded in a stiff stratum that retain a significant thick stratum of soft soil, have soft soil at formation level and are designed with a large factor of safety (greater than 3). More data from monitored retaining walls in various soil conditions with different construction techniques and support systems have been published and are often used in current design practice.

Advances in computer software have encouraged the use of numerical modelling that takes into consideration the interaction between the soil and the wall. Some popular types of software used in the simplest form of soil-structure analysis are WALLAP and FREW, in which the wall is modelled as a beam and the soil as a series of horizontal springs (subgrade reaction method) or as an elastic continuum (pseudo-finite element method). These forms of analysis have the potential to model the full soil-structure interaction and construction sequence, to take account of pre-excavation stress state and to calculate the wall deflections, bending moments and prop loads in a relatively straightforward way. However, the ground movements around the wall can not be calculated, the input parameters should be calibrated against field measurements and are likely to provide only a rough estimation of the soil behaviour; hence, their results should be regarded as an approximate solution (Gaba *et al*, 2003).

More advanced software packages such as CRISP, FLAC, PLAXIS and ABAQUS use finite element or finite difference methods. They can incorporate complex soil models with the soil stiffness varying with strain and anisotropy, model support details, wall and excavation geometry and calculate wall and ground movements, bending moments and prop loads taking into account any possible soil consolidation effects. Despite their potential, numerical modelling has significant drawbacks that will be discussed later in this chapter.

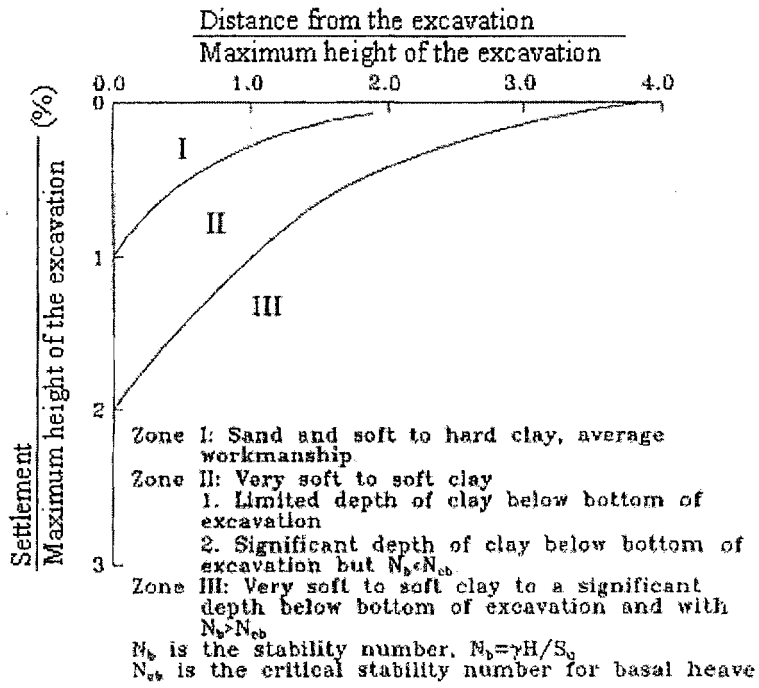


Figure 2.5: Estimation of settlements for excavations in clay soils by Peck (1969).

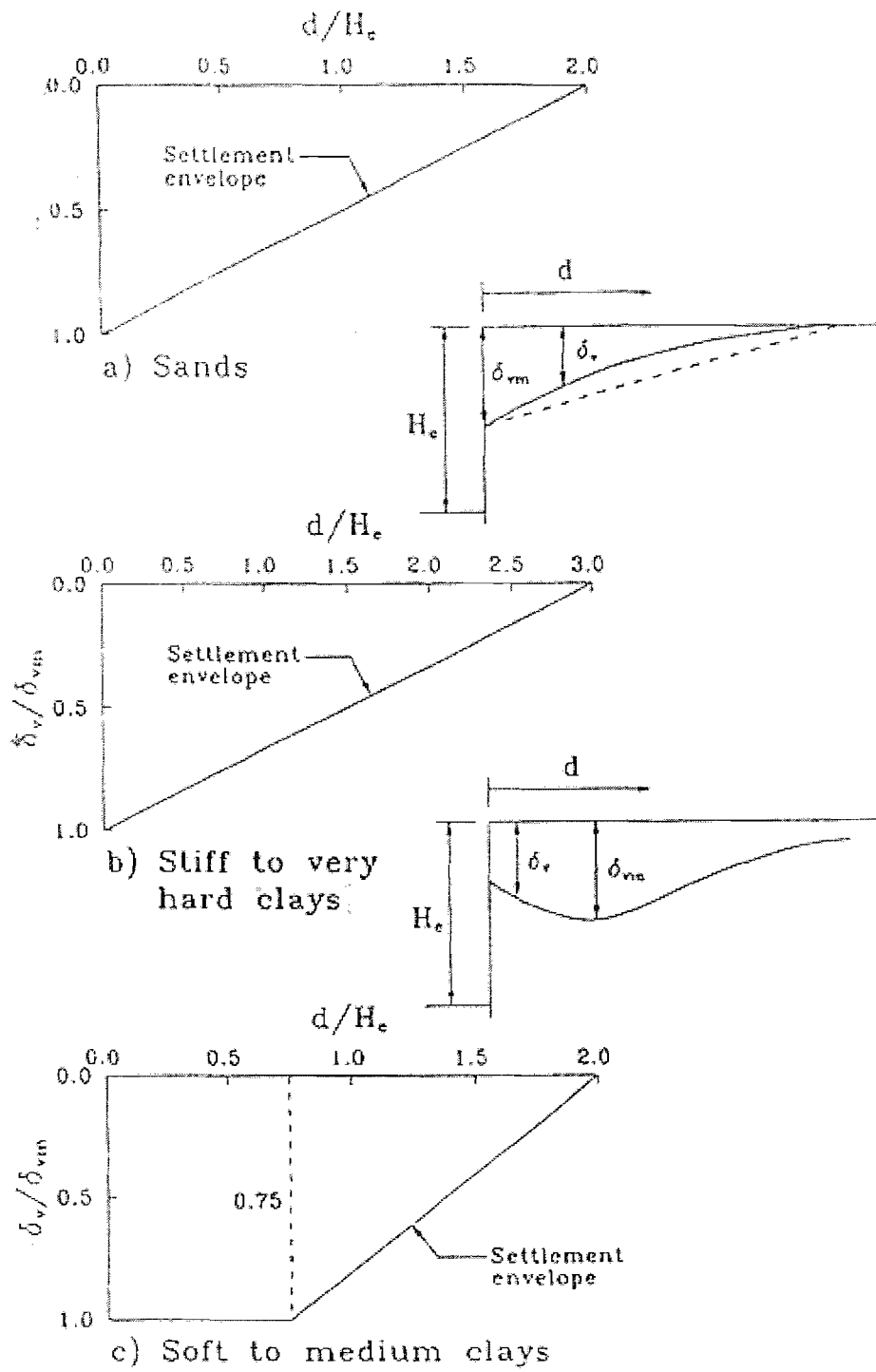


Figure 2.6: Estimation of settlement envelopes by Clough and O' Rourke (1990).

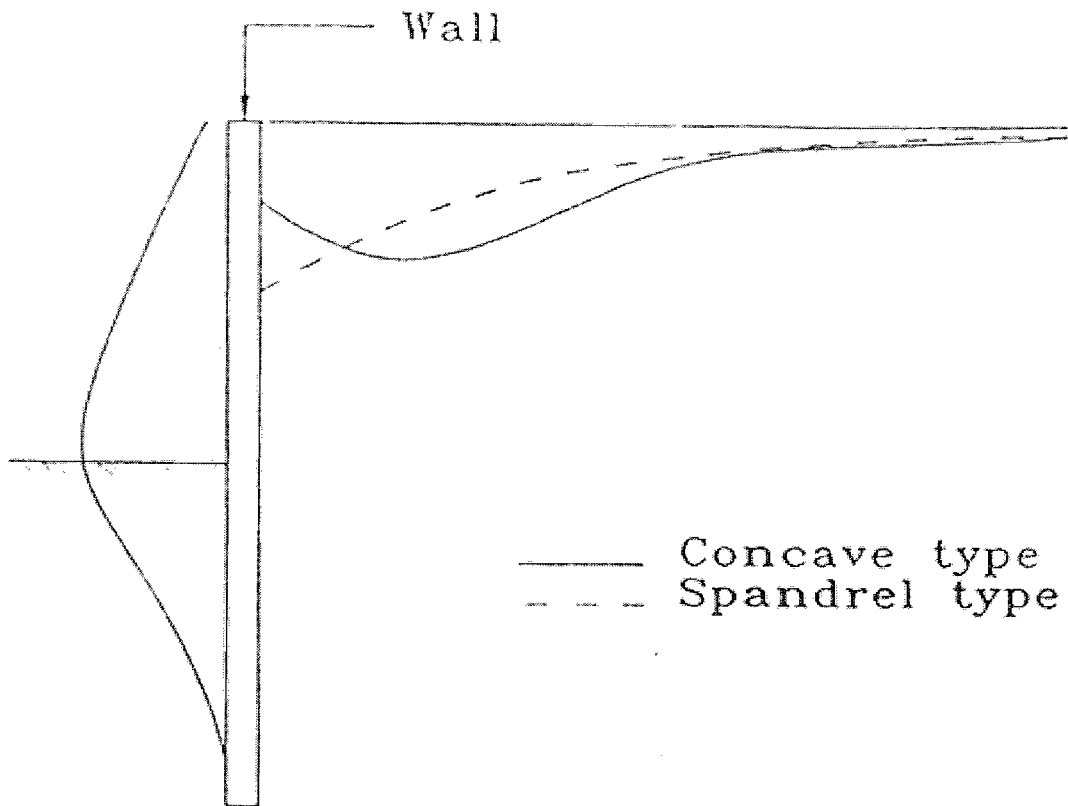


Figure 2.7: Estimation of the displacement profiles by Hsieh and Ou (1998).

2.3 CODES OF PRACTICE FOR RETAINING WALLS

The obvious practical and commercial significance and impact of codes of practice justifies the efforts of various committees over the years to develop a unified and internationally agreed method for the design of the retaining walls. Limit equilibrium methods use stress distributions behind and in front of the retaining wall to calculate the depth of embedment necessary just to prevent collapse of the wall. The stresses behind the wall are at their minimum possible values (the active limit), while the stresses in front of the wall are at their maximum possible values (the passive limit). The stress state of the soil everywhere is in equilibrium without violating the failure condition $\tau / \sigma' = \tan\phi'$. For the actual design condition, it is necessary to increase the depth of embedment beyond that required merely to prevent collapse in order to allow for uncertainties and avoid excessive deformations. The collapse limit state is known as the ultimate limit state (ULS), whereas acceptable performance of the wall in terms of displacement, damage and appearance is related to another limit state known as the serviceability limit state (SLS).

The soil loads on an embedded retaining wall at failure in the ground are not as easily identified as they are in a conventional structural analysis. Historically, a factor of safety F has been applied to one of the parameters in a collapse calculation to distance the wall both from an ultimate and serviceability failure. The confusion in the definition and selection of a factor of safety is illustrated by the diversity of the methods that have been adopted in the past. Such examples are:

- The application of a factor of safety F_d to the embedment depth derived from a limit equilibrium calculation using unfactored soil strengths.
- The reduction of the passive earth pressure coefficients by a factor F_p .
- The reduction of the moment of the net resisting pressure by a factor F_{np} .

Comparative figures provided by Burland *et al* (1981) and extensive calculations carried out by Gaba *et al* (2003, Appendix A7) demonstrate the inconsistency and sometimes lack of safety associated with some of these methods.

2.3.1 Modern codes of practice for embedded retaining walls in the ultimate limit state

The design method adopted by the modern codes of practice such as BS8002 (BSI, 2001), Eurocode 7 (1995) and CIRIA report C580 (Gaba *et al*, 2003) against ultimate limit states requires a limit equilibrium or other stability calculation with the application of a factor of safety F_s (or strength mobilisation factor M) to the actual soil strengths, which are reduced in order to distance the retaining walls from collapse.

The uncertainties in possible future loading conditions are taken into account by increasing the retained height by 10% of the retained height for embedded cantilever walls, normally up to a maximum of 0.5m, representing an unplanned excavation in front of the wall and by assuming an additional uniform surcharge of 10 kPa acting on the retained soil surface. However, the value of the strength mobilisation factor M adopted by each code is different. The different values of factors of safety in each code are presented below. A more detailed description of the procedure which should be followed can be found in each of the modern codes of practice.

A. EUROCODE 7

Eurocode 7 (1995) recommends that the design strength φ'_{design} used in the ULS calculation should be equal to $\tan^{-1}\{(tan \varphi') / 1.25\}$, where φ' is a moderately conservative estimate of the effective angle of friction relevant to the ultimate limit state. The term moderately conservative actually means that only 5% of the sample values will be more unfavourable. The suggested maximum design values of the soil / wall friction angle δ_{design} are $0.67 \varphi'_{crit}$ for smooth concrete and φ'_{crit} for rough concrete, so that the selection of $\delta_{design} = \varphi'_{crit}$ might be allowed in the ultimate limit state calculation. The recommended design value of the undrained shear strength $t_{u,design}$ in a total stress calculation is equal to the value of the actual soil strength t_u divided by a factor $M = 1.4$.

B. CIRIA Report C580

CIRIA Report C580 (Gaba *et al*, 2003) is in agreement with Eurocode 7 on the values of the design strength φ'_{design} and the maximum values of the soil / wall friction angle δ_{design} used in the ultimate limit state calculation. However, the recommended design value of the undrained shear strength $t_{u,design}$ in a total stress calculation is reduced to $t_u / 1.5$, i.e. an increased factor of safety $M=1.5$ is used. The maximum value of wall adhesion allowed in the design is $0.5 \times t_{u,design}$, which is equivalent to $t_u / 3$. Furthermore, the use of numerical soil-structure analysis is suggested instead of simple limit equilibrium calculations, particularly for complex structures that are statically indeterminate, where the potential mechanism of collapse is not obvious or where the construction sequence must be considered.

C. BS8002

BS8002 (BSI, 2001) recommends that the design strength φ'_{design} should be the lesser of $\tan^{-1}\{(tan \varphi'_{peak}) / 1.2\}$ and φ'_{crit} . The suggested maximum value of the soil / wall friction angle δ_{design} is $\tan^{-1}(0.75 \times tan \varphi'_{design})$. For a total stress ultimate limit calculation the value of the undrained shear strength used in the design $t_{u,design}$ should be $t_u / 1.5$, which is in agreement with CIRIA Report. BS8002 allows a wall adhesion in the design of $0.75 \times t_{u,design}$, which is equivalent to a maximum value of $0.5 \times t_u$.

2.3.2 Modern codes of practice for embedded retaining walls at the serviceability limit state

The ultimate limit state calculations, factored as described above, should ensure that the wall is remote from collapse. However, excessive deformation and associated ground movements, excessive stresses in walls or props or unwanted leakage of groundwater through or beneath the wall can be considered as another limit state, known as the serviceability limit state (SLS) and a wall should be designed to avoid it. In reality, the soil strengths mobilised may be different on each side, different at different depths and dependent on the wall-flexibility and soil-structure interaction effects which will result in a variation in soil strain with depth. Therefore, an analysis aimed at determining the exact stress state in the soil adjacent to the wall can be very complicated.

Eurocode 7, CIRIA Report C580 and BS8002 distinguish the ultimate limit state from the serviceability limit state. CIRIA Report C580 (Gaba *et al.*, 2003) recommend that some form of numerical analysis that takes account of soil-structure interaction effects should be carried out. This analysis should be based on the actual wall geometry and the actual soil strength parameters. If the limit equilibrium approach is adopted for walls with a prop near the crest, Gaba *et al* (2003) point out that the wall bending moments are overestimated, and the prop loads are underestimated in comparison with a soil-structure interaction analysis. They suggest that the SLS bending moment diagram should be “sketched in” between the maximum of the limit equilibrium distribution using the full strength of the soil and the actual toe of the wall. The bending moment distribution in true limiting equilibrium is calculated with the wall having the embedment needed just to prevent collapse with unfactored soil strengths, an increased excavation depth and additional external loads as required by the code. This approach is presented in Figure 2.8. More details can be found in Gaba *et al* (2003).

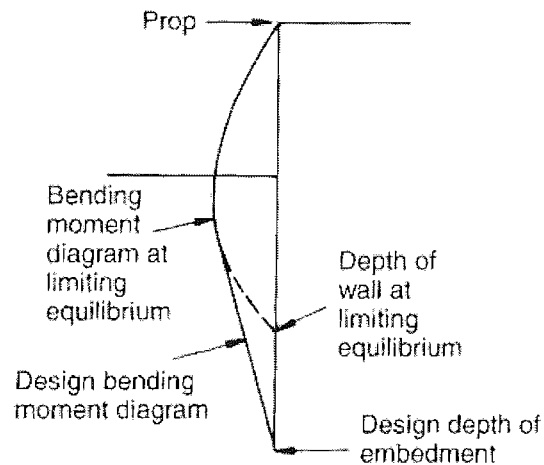


Figure 2.8: Design bending moments as estimated in CIRIA Report C580.

2.3.3 Limitations of current design practice

The use of observational data from monitored case studies cannot cover every contingency in design, since the range of encountered soil conditions, construction sequences and support systems is wide. The amount of data related to recently developed and advanced construction methods is significantly restricted. In addition, the reliability of data from case histories depends on the technology, accuracy and calibration of the monitoring systems that were used, and results may depend to some extent on the quality of the workmanship. Hence, conservative values of parameters are often chosen for design, despite the increased cost that this entails.

The methods used in soil-structure interaction analysis such as subgrade reaction or pseudo-finite element are relatively straightforward, but can only provide approximate solutions. More complex analyses using finite element and finite difference methods might seem an alternative for design, but depend hugely on the accuracy of the chosen soil model. Their results should be calibrated against reliable field measurements. However, such data has to be comparable and available so that the numerical solutions can be verified. The most important disadvantage is the number of the required input parameters, their calibration and the volume of the results may frustrate any comparison and evaluation. The possible sensitivity of the solutions to a small change in a particular

parameter is another potential drawback that cannot be neglected. The expertise in the use of advanced software programmes and the significant numerical modelling experience required from the user, and the cost and time involved in using complex models cannot be justified in every case.

Gaba *et al* (2003) recommend that the complexity of the structure and the construction process, the required information, the input data available and economy should be taken into consideration in selecting the appropriate method of analysis. Some simple calculations are suggested to serve as a check on more complex methods and the importance of a simple calculation with appropriate soil data in preference to a complex analysis with inappropriate data is emphasised.

2.4 THE MOBILISED STRENGTH DESIGN (MSD) METHOD

2.4.1 Theoretical background of the method

From the above, a simple method that relates the mobilised soil strength to the displacements in a rational and consistent way will be of significant practical value to the design of retaining walls. Bolton and Powrie (1988) proposed a geostructural mechanism for stiff walls in clays in order to relate the rigid body rotation of the wall to the maximum shear strain in the adjacent soil and hence to the ground movements. The shear strain in the adjacent soil can be related to the mobilised strength required for equilibrium, and then the soil and wall deformations under working conditions can be estimated from the equilibrium calculation. This approach has been introduced for stiff walls, for which the effective stress distributions on either side can be assumed to be approximately linear with depth and the ground movements due to wall bending can be neglected. Powrie (1985) has suggested that the construction of a diaphragm wall in clay would reduce the initial earth pressure coefficient, K_o , towards unity prior to excavation. Therefore, this approach as presented by Bolton and Powrie (1988) is based on the assumption that $K_o=1$.

Figure 2.9 shows a kinematically admissible soil displacement field compatible with the outward rotation of an anchored retaining wall, as proposed by Milligan (1983). The soil is shearing at a constant angle of dilatancy ψ and significant deformations occur within a zone bounded by a line at 45° from the base of the wall to the ground surface.

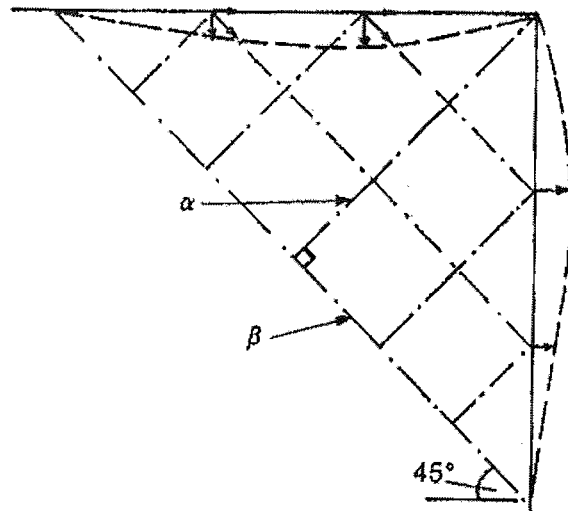


Figure 2.9: Kinematically admissible displacement field for an anchored retaining wall (Milligan 1983).

Bolton and Powrie (1988) subdivided the active and passive zones behind and in front of a wall into triangles, in which the verticals and horizontals are assumed as frictionless displacement discontinuities and the hypotenuses as zero extension lines. In a simplified approach the angle of dilation was taken to be equal to zero. Although this is realistic in undrained conditions, in drained conditions over consolidated clay will dilate until it ruptures. This will cause shear softening until sufficient soil has reached a critical state and no further dilation will take place. Therefore, the assumption of zero dilation is justified by the fact that dilation is significant only in determining the size of the shear zone rather than the magnitude of strain within it.

The idealised displacement mechanism for a stiff unproped wall rotating about its toe is shown in Figure 2.10a. It has been assumed that significant soil movement during excavation will occur mainly in the zones defined approximately by lines drawn at 45° , extending upward from the toe and that the line OA is a zero extension line. This is consistent with a shearing triangle AOV , beyond which the soil is effectively rigid. Within

this triangle the shear strain increment $\delta\gamma$ according to Mohr circle (Fig. 2.10b) is uniform and equal to twice the strain increment $\delta\epsilon$. The triangle AOV is extending horizontally by $h \delta\theta$ and compressing vertically by $h \delta\theta$, where $\delta\theta$ is the wall rotation and the compression is taken positive. Assuming zero rate of dilation:

$$\delta\epsilon_v + \delta\epsilon_h = 0 \tag{2.4.1}$$

$$\delta v = \delta u \tag{2.4.2}$$

From the Mohr circle:

$$\delta\gamma = (\delta\epsilon_v - \delta\epsilon_h) = \delta v / h - (-\delta u / h) = \delta\theta - (-\delta\theta) = 2 \delta\theta \tag{2.4.3}$$

It is obvious that a reversed rotation would lead to reversed strains.

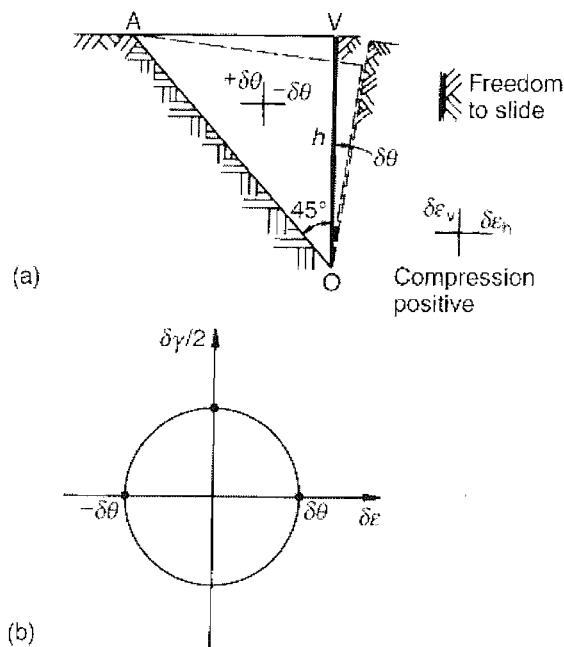


Figure 2.10: Admissible strains for a wall rotating about its toe (Bolton and Powrie, 1988).

The same mechanism can be used for a stiff unpropped wall rotating about a point O near the toe as shown in Figure 2.11.

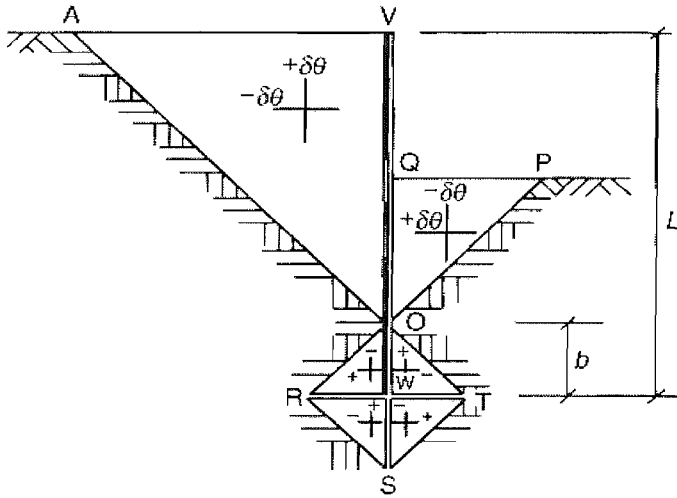


Figure 2.11: Admissible strains for an unpropped wall rotating about a point O near its toe (Bolton and Powrie, 1988).

In this case six, instead of two, deforming triangles are formed, but the shear strain increment $\delta\gamma$ in each of them remains uniform and equal to twice the incremental wall rotation $\delta\theta$.

Figure 2.12 shows a similar strain field for a stiff propped wall rotating about its crest V . In this case, the magnitudes of strain within the triangles in front of the wall differ, however the consideration of the larger of the two strains would be safer; that is the shear strain on the excavated side of the wall, which is $(1 + h / d)$ times that on the retained side, where h is the retained height and d is the depth of embedment.

The mobilised soil strength, expressed by the mobilised angle of friction ϕ'_{mob} , assumed to be the same on both sides of an unpropped wall and uniform with depth, can be related to the shear strain via undrained triaxial tests on a representative soil sample rather than empirical data. Undrained plane strain data were used instead of drained ones because they were associated with lower soil stiffness and hence with more onerous conditions. The linear stress distributions can be used for a wall of any geometry, so as to calculate the mobilised soil strength ϕ'_{mob} required for equilibrium and the corresponding shear strain can be derived from the graph of mobilised soil strength ϕ'_{mob} against shear strain γ for the specific soil. From the geomechanical mechanism described above, the magnitude of the wall rotation and soil movements can be determined. Bolton and Powrie (1988)

carried out centrifuge tests modelling both the short term and long term behaviour of cantilever and propped at the crest walls retaining clay with different retained heights and embedment depths. The pattern of the deformations obtained from the tests was comparatively close to those estimated using kinematically admissible strain fields.

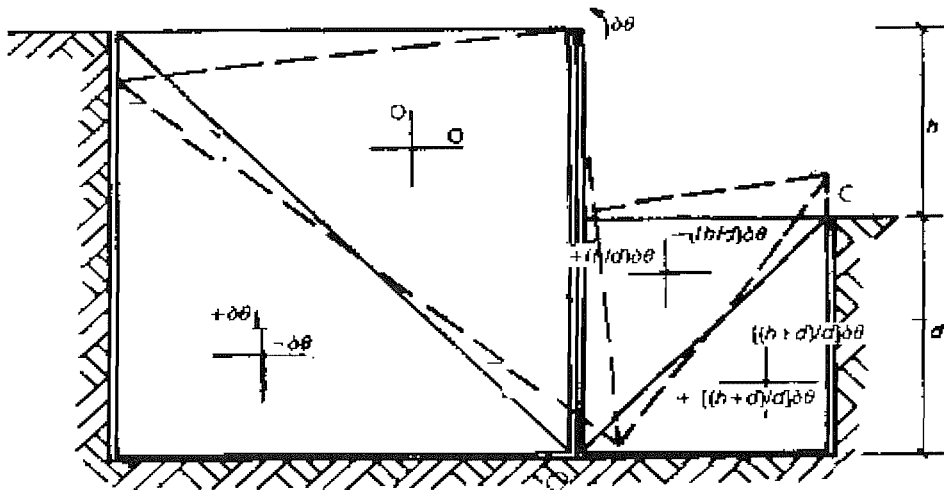


Figure 2.12: Admissible strains for a wall rotating about its crest (Bolton and Powrie, 1988).

2.4.2 Evaluation and accuracy of results

The short-term and long-term crest deflections of an unpropped wall with a retained height of 10 m and an embedment depth of 20 m retaining clay were measured during centrifuge tests and compared with the displacements calculated using the mobilised strength method (Bolton and Powrie, 1988). The comparison attests that the measured deflections were very close to the ones that were calculated with a soil / wall interface friction angle equal to the mobilised angle of shearing resistance, $\delta = \varphi'_{mob}$. If the soil / wall friction was ignored ($\delta = 0$), the deflections were overpredicted.

In the case of a wall propped at the crest with a retained height of 10 m and an embedment depth of 15 m, the prop forces measured in the centrifuge tests were close to the calculated ones. The values of prop force derived from a short-term calculation were

in slightly better agreement than those obtained from a long-term calculation. The measured maximum bending moments were again close to the calculated values, with the long-term calculations being more accurate than the short-term ones. In the calculations the shear strain on the excavated side was taken as $(1 + h / d)$ times that on the retained side, in accordance with the geostrophical mechanism presented in Figure 2.12.

The centrifuge tests retaining clay demonstrated the potential of the mobilised strength approach to provide satisfactorily accurate design solutions for stiff walls in clay. The advantages of the method are that it provides a simple and reliable solution avoiding the uncertainty involved in the selection of an appropriate factor of safety or the complexity of a detailed soil-structure analysis. In addition, the incorporation of consistent strain fields allows the ready adoption of real data obtained from appropriate stress paths. One of the assumptions used in this approach is that the mobilised soil strength ϕ'_{mob} is the same on both sides of the wall. However, this is not always the case, since the pre-excavation soil stresses and the method of construction can result in a change in the initial stress paths behind the wall and therefore in a different response of the soil behind the wall in comparison with the soil in front of the wall. Moreover, the analysis was carried out in undrained conditions and the pre-excavation earth pressure coefficient K_o was assumed to be close to unity. Therefore, further analyses is required to assess the influence of pore water pressures, the effects of values of K_o different from one, and a possible difference in the soil strength mobilisation in front and behind the wall.

2.4.3 Design procedure based on the mobilised strength method

Osman (2004) illustrated two possible design procedures for rigid retaining walls using the mobilised strength method. These are presented in Figure 2.13. Following the first procedure an engineer should first decide the limits imposed on the deformations based on the sensitivity of the adjacent properties. The maximum allowed wall rotation can be determined and related to the mobilised shear strain through an idealised displacement mechanism. The average mobilised shear strength can then be deduced from a stress-strain curve obtained from laboratory soil tests on representative soil samples. Finally, a

limit equilibrium calculation assuming linear stress distributions behind and in front of the wall is carried out for the specified mobilised strength and hence the essential retained height ratio H/D is calculated.

An alternative design procedure could commence with the selection of the preferred retained height ratio H/D , followed by a limit equilibrium calculation which involves the stress distributions for the specific wall dimensions and leads to the estimation of the mobilised shear strength. The shear strain is found from the stress-strain curve and the wall rotation is calculated through admissible strain fields. The maximum deflections can then be obtained and compared to serviceability limits. If they exceed the serviceability limit, selection of a new retained height ratio is required and the procedure should be repeated from the beginning.

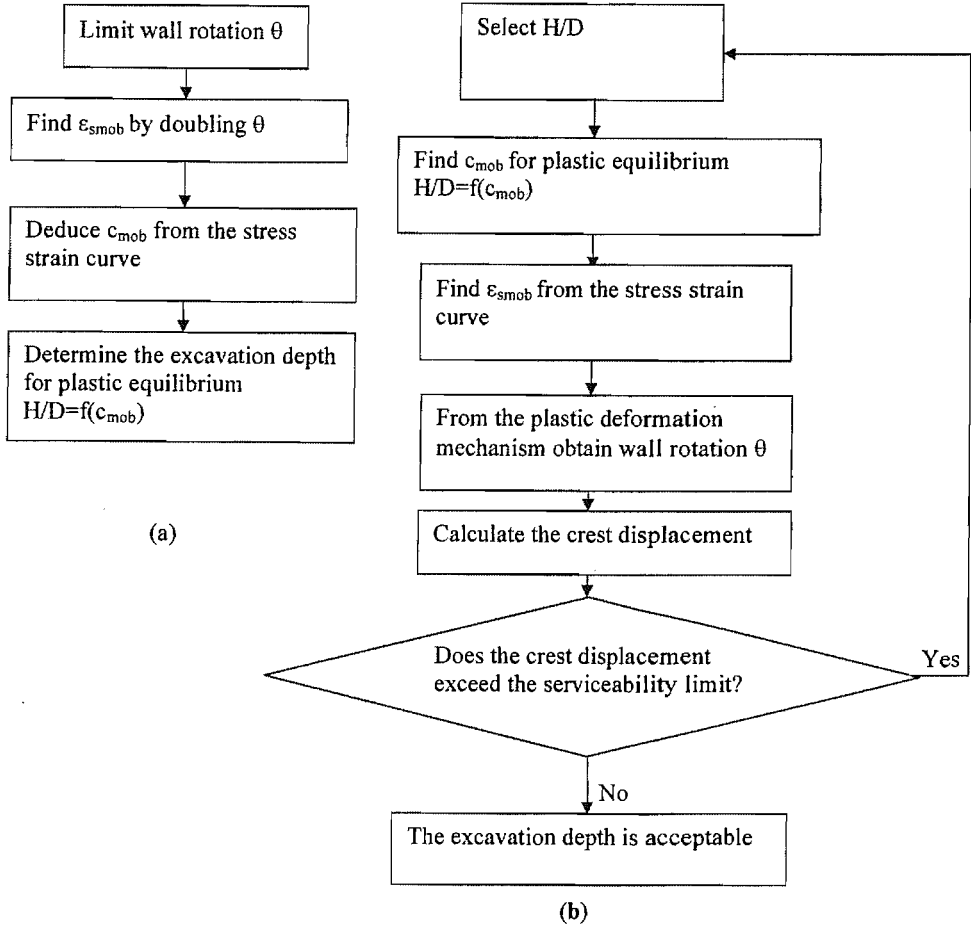


Figure 2.13: Possible design procedures for rigid retaining walls using the mobilised strength method (Osman, 2004).

2.5 SUMMARY

The limitations in the current design methods and codes of practice attest the need for a simple method for the calculation of the serviceability bending moments and displacements that incorporates the real nature of the soil behaviour in a consistent manner. The theoretical background and the accuracy of the mobilised strength method are presented. The main advantage of this method is the straight forward way of relating the mobilised soil strength to the wall and soil displacements under working conditions. Finally, two example procedures of incorporating the mobilised strength method in the design are displayed.

3. ANALYSIS AND DESIGN OF STIFF RETAINING WALLS PROPPED AT THE CREST

3.1 INTRODUCTION

The relative soil / wall stiffness may have a considerable effect on the performance of a retaining wall. According to Potts and Day (1990) flexible walls attract smaller bending moments than stiff walls in the same conditions due to the redistribution of the soil stresses acting on the wall. Although there might be an economic benefit from the design of a flexible wall, the wall and ground displacements may be greater than for a stiffer wall. Moreover, the soil strains depend on the level of the soil stiffness. Research that has been carried out previously regarding the relative soil / wall stiffness is reviewed, evaluated and discussed.

In this chapter, wall rotations are related to the retained to overall height ratios, the soil stiffness and the initial earth pressure coefficients with regard to the mobilized strength for retaining walls propped at the crest. A general design framework is presented which distinguishes flexible from stiff systems for walls propped at the crest with different retained to overall height ratios, retaining different soils with varying stiffnesses and different initial earth pressure coefficients.

3.2 THE RELATIVE SOIL / WALL STIFFNESS

Most of the simple methods commonly used in retaining wall analysis or design neglect the effects of the relative soil / wall stiffness. However, stiffness may have a considerable influence on the deformations and bending moments of a retaining wall under working conditions, especially for walls propped near the crest. Rowe (1952) defined the stiffness of a wall by means of a flexibility, $\rho = H^4 / EI$, where H is the overall height of the wall, E the Young's modulus of the wall and I the second moment of inertia per unit length.

To quantify the effects of the wall flexibility, he carried out a series of model tests on anchored sheet pile walls retaining dry sand varying the flexibility ρ . He repeated his tests for various surcharge, anchor levels, anchor yield and dredge levels, so as to generalise his results.

In the case of unyielding tie-back anchors, he found that the horizontal stress distribution behind the retaining wall was non-linear (Figure 3.1). This was explained by a reduction in the lateral stress approximately at the mid-section of the wall as a consequence of the increase in the lateral stress at the unyielding section near the anchor. However, an outward movement at the anchor point of less than $H / 1000$ was sufficient to generate fully active conditions and a linear distribution of lateral stress behind the wall (Rowe,1952). In reality, the distributions of the active pressures behind the wall can be considered linear, since movements at the anchor point more than $H / 1000$ will probably occur, if the supports are not pre-stressed. The assumption of full active pressures behind the wall seems reasonable, since Rowe used sand which was placed loosely in order to keep the pre-excavation lateral earth pressure coefficients low.

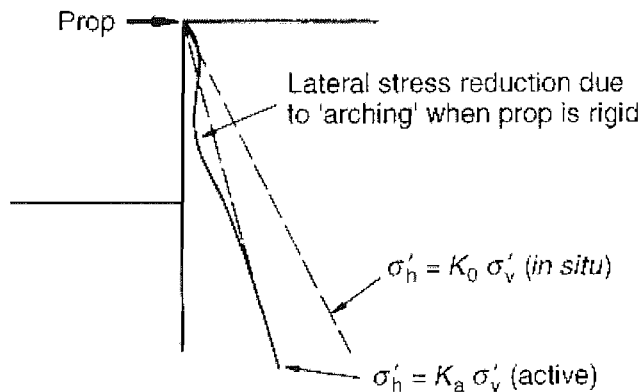


Figure 3.1: Reduction of lateral stress behind the wall when the prop is rigid (Powrie 1997).

Rowe's results demonstrate significantly reduced values of anchor loads and maximum bending moments compared with those calculated using the free earth support method with full active and factored passive pressures. He found that the pattern of the reduction was independent of the surcharge, anchor level and dredge level and depended on the wall flexibility expressed in the term of ρ and the density of the soil. He presented his

results in figures with the anchor loads and bending moments divided by the values calculated with the factored free earth support method and plotted against the logarithm of the wall flexibility ρ for loose and dense sands (Figure 3.2). In Figure 3.2 the wall flexibility ρ is calculated in $\text{ft}^5 / \text{lb} \times \text{in}^2$ units.

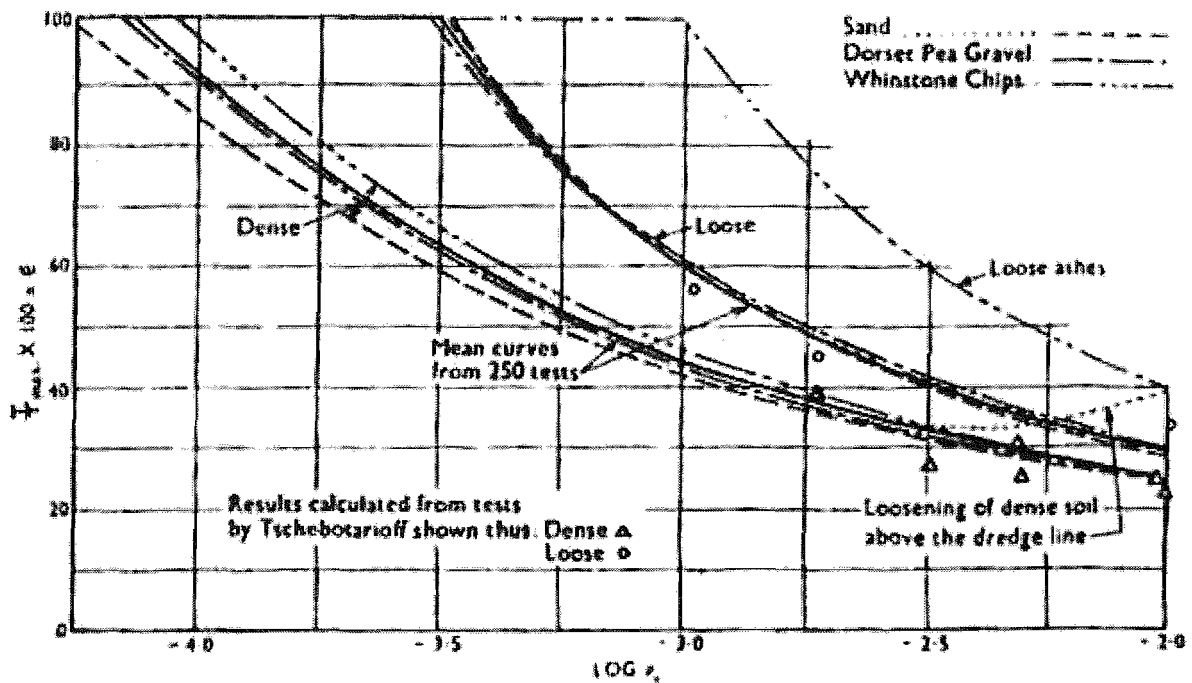


Figure 3.2: Moment reduction as a function of wall flexibility for dense and loose sands (Rowe, 1952).

According to Rowe, a retaining wall can be characterised as stiff when the deflection at the excavation level is less than the deflection at the toe, so that the stress distribution in front of the wall is approximately linear. The bending moments measured in his tests for stiff walls were very close to those calculated using the free earth support method, based on a fully active triangular stress distribution behind the wall and on a passive triangular distribution with passive pressures reduced by a factor F_p , in front of the wall.

If the deflection at excavation level is significantly greater than at the toe, the wall may be characterised as flexible and the stress distribution in front of the wall will be non-linear. This is because the centroid of the stress distribution in front of a flexible retaining wall is raised as shown in Figure 3.3. Therefore, Rowe defined the critical wall flexibility ρ_c as the value at which the deflection at the excavation level is equal to the deflection at the toe and the bending moment starts to fall below the factored free earth

values. He related ρ_c to the coefficient of volume compressibility of the soil and he also investigated its dependence on the retained height ratio h / H (where h is the retained height) and the depth of the anchor.

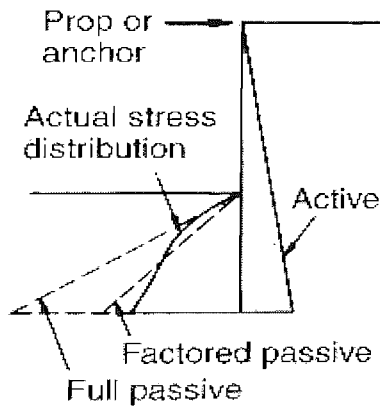


Figure 3.3: Stress distribution on both sides of a flexible wall (Powrie, 1997).

In a later analysis of anchored sheet pile walls by Rowe (1955), it was assumed that the lateral effective stresses behind the wall had reached the active limit and the lateral effective stress p_b in front of the wall at depth x below the excavation level was given by the expression

$$p_b = m_r x y / d \quad (3.1)$$

where d is the embedment depth of the wall, y is the deflection and m_r is a soil stiffness parameter. Rowe presented his results in a single reduction curve, which shows the bending moment as a percentage of the free earth support value plotted against the logarithm of $m_r \rho$. The parameter $m_r \rho$ is known as the flexibility number and is given the symbol R . Powrie (1997) multiplied Rowe's values by 144 and redrew Rowe's curve with $m_r \rho$ converted in consistent units (Figure 3.4). According to Rowe, the theoretical critical flexibility number $m_r \rho$ in consistent units (SI) is generally approaching 1000 for dense sand and is in agreement with his experimental data. However, in the case of stiffer walls in loose sand, the critical flexibility number derived from the experiments was approximately 2500 in consistent units (SI) and thus considerably higher than the theoretical value.

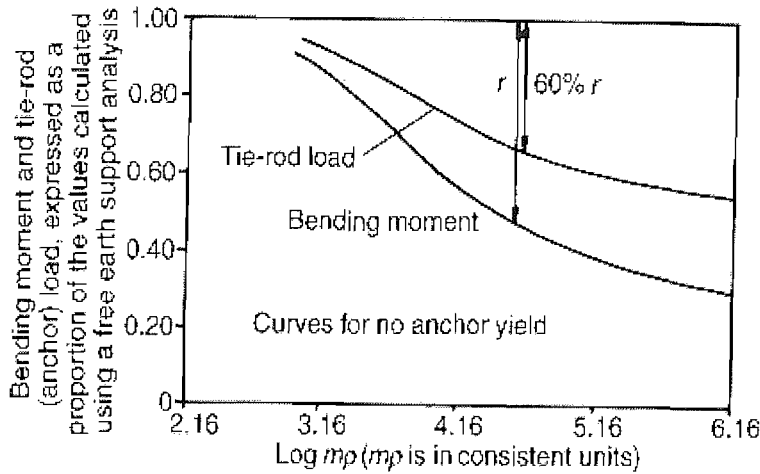


Figure 3.4: Moment reduction curve as a function of soil/wall flexibility (Powrie, 1997).

The wall deflection can be analysed in a component due to a rigid body rotation and a component due to wall bending (Figure 3.5).

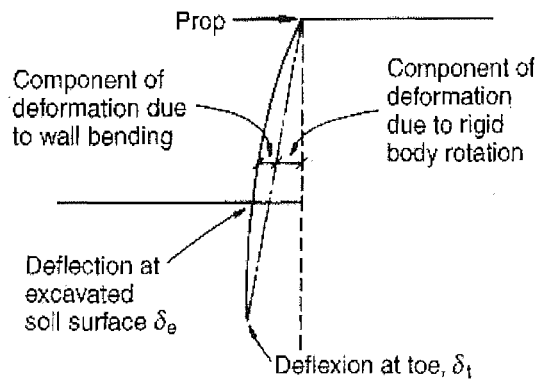


Figure 3.5: Components of wall displacements (Powrie, 1997).

Rowe's results are of importance because he quantified the effects of the bending component of wall deformation and therefore the effects of the bending stiffness of the wall. The figures he produced were simple and the influence of the retained height ratio a , the depth to the anchor level divided by the overall height β and the surcharge coefficient q was taken into account (Table 3.1), so his results can be used for a range of cases.

There are many parameters that should be taken into account when the relative soil / wall stiffness is investigated. In Table 3.1 the values of some parameters that Rowe used in

his experiments are listed. The values of some parameters are not given, because it is not clear which values he adopted. This makes comparison with other work difficult. Moreover, the ranges of the values he considered are small, so that the application of his method can not be considered safe for all the cases. The doubts about the wall and soil characteristics he chose will be amplified below.

Rowe modelled an excavated wall, so the validity of his results is uncertain for backfilled walls. The retained to overall height ratio, h / H , investigated is in the range of 0.6~0.8. However, this may not be suitable for walls where the groundwater level in the retained soil is high, because smaller values of h / H would be required. The curves he presented were for the case of a slightly yielding anchor, so they are not reliable for pre-stressed anchors, which would be expected to result in slightly higher bending moments and anchor loads. Moreover, the units Rowe used for the calculation of the wall flexibility ρ , are $\text{ft}^5 / \text{lb} \times \text{in}^2$, so its application is not easy and calculations are required to convert it to consistent units.

Rowe's tests were carried out in dry sand, so the effect of the pore water pressures, which can be very significant for wall stability, were not considered. In addition, the definition of m_r in expression (3.1) as a soil stiffness parameter is unusual. If y / d is taken as indicative of the magnitude of the linear strain, then $m_r x$ would be the Young's modulus of the soil and m_r a measure of the rate of increase of Young's modulus with depth, E^* . The operational values of E and hence of E^* will decrease with increasing shear strain, but this variation is not easily defined in Rowe's analysis. Powrie (1997) argued that the use of G^* , which is the rate of increase of the shear modulus G with depth, may be more appropriate. This will be discussed later. Moreover, the pre-excavation lateral earth pressure coefficients in Rowe's tests were low. Although this is reasonable for sandy soils, in the case of overconsolidated clays with high pre-excavation lateral earth pressure coefficients, the applicability of his reduction curves is open to question.

Rowe compared the anchor loads and the bending moments measured in his experiments to the values calculated in the free earth support method with the passive pressures reduced by a factor of safety, F_p . This procedure was suggested in the former UK code of practice CP2 but, as already mentioned, modern codes of practice require the application

of a factor of safety to the soil strength directly. Therefore, Rowe's figures cannot easily be used directly in current design.

Another analysis of the effect of the bending stiffness on wall movements, bending moments and prop loads was carried out by Potts and Fourie (1985). In this analysis, the pre-excavation earth pressure coefficient K_i , which is the ratio σ'_h / σ'_v after wall installation and immediately prior to excavation of the soil in front of the wall, was given values of $K_i = 2.0$ and 0.5 . It is important to mention that K_i is different from the in situ earth pressure coefficient K_o , due to the lateral stress relief that occurs during wall installation. The behaviour of four walls with different stiffnesses, varying from a rigid to a soft wall, was investigated.

Potts and Fourie's results indicate that for the two more flexible walls, the calculated bending moments were lower than those derived from limit equilibrium calculations, using a factor of safety, F_r , defined by Burland, Potts and Walsh (1981), for both $K_i = 0.5$ and $K_i = 2.0$. In this case, their results are in agreement with Rowe's analysis. However, for the two stiffer walls the bending moments were lower at $K_i = 0.5$, but greatly exceeded the limit equilibrium values at $K_i = 2.0$. For this last case it was found that the earth pressures behind the wall were far from linearly distributed. A similar conclusion was made for the prop loads, so that a divergence from Rowe's analysis is obvious. The wall and soil characteristics that Potts and Fourie (1985) adopted¹ are presented in Table 3.1. Their results refer to a single value of the retained height ratio h / H , a specific depth of anchor ($\beta=0$) and a specific type of soil. Therefore, their results may not be valid for other cases.

Potts and Fourie did not take into account the difference between the pre-excavation earth pressure coefficients after wall installation K_i and the in situ earth pressure coefficient K_o , although wall installation will tend to reduce the lateral stresses below their initial values in the soil close to the wall. In Potts and Fourie's analysis the wall with $E^* \rho = 420$, where $E^* = 6000 \text{ kN} / \text{m}^3$ is the rate of increase of soil Young's modulus with depth, was characterised as stiff although the deflection at the excavation level exceeded the deflection at the toe. This is not consistent with Rowe's flexibility criterion,

¹ In Potts and Fourie (1985) analysis the bending stiffnesses of the walls are given in (kN / m^2) . However, this is believed to be a typographical error, since the bending stiffness should be in $(\text{kN} \text{m}^2 / \text{m})$ units.

which infers that in this case the critical flexibility number $E^* \rho$ is less than 420. In the calculation of bending moments in limit equilibrium, Potts and Fourie (1985) used a factor of safety, F_r , defined by Burland, Potts and Walsh (1981), which is different from the factor of safety, F_p , that Rowe used and the factor of safety, F_s , used in modern codes of practice.

The review of the two methods of characterising the relative soil / wall stiffness indicates that a direct comparison between them may give misleading results. An attempt to list the parameters involved in the problem in consistent units for ease of comparison is presented in Table 3.1.

It is obvious from results of previous research as presented above that a change in the relative soil / wall stiffness can alter significantly the bending moments and prop loads; thus its effects on the design of retaining walls should not be neglected. However, the values of the parameters in previous research were not varied over wide ranges of values, which is necessary if a general understanding is to be obtained. The influence of the pore water pressures should also be considered. Finally, to quantify the relative soil / wall stiffness and study its effects on a design calculation, a more consistent and clearer definition of soil stiffness is required.

	Rowe	Potts& Fourie
Type of wall	Excavated	<ul style="list-style-type: none"> • Excavated • Backfilled
Anchor / prop yield	No	No
Prop stiffness	No data	No data
h / H (m)	• 0.6 • 0.7 • 0.8	0.765
β (ratio: depth to anchor level / overall height)	• 0 • 0.1 • 0.2 • 0.3	0
q (surcharge pressure / γH)	• 0 • 0.1 • 0.2	No data
$Log\rho$ (wall flexibility, $\rho=H^4/EI$ in m^3/KN)	-1.29 ~ 0.96	<ul style="list-style-type: none"> • -4.16 • -1.16 • 0.31 • 0.84
ϕ' (degrees)	30° ~ 50°	25°
δ_{active}	2/3 ϕ'	0
$\delta_{passive}$	ϕ'	ϕ'
Void ratio	0.53 ~ 1.76	No data
E (kN/m²)	No data	6000 z
μ (Poisson's ratio)	No data	0.2
γ (soil unit weight in kN/m²)	No data	20
ν (angle of dilation in degrees)	No data	ϕ'
c' (soil's cohesion)	No data	0
K_i (after wall installation)	Low	• 0.5 • 1.0 • 1.5 • 2.0
K_a	No data	0.33
K_p	K_p / F_p ($F_p=1.5$)	3.9
Pore water pressures	0	0
Method of prediction	Free earth support with application of F_n to the passive	Free earth support with application of F_r
Method of analysis	Experiments	Finite element analysis

Table 3.1

K_i denotes the earth pressure coefficient before excavation and after installation of the wall

K_a denotes the active earth pressure coefficient

K_p denotes the passive earth pressure coefficient h/H denotes the retained height ratio

β denotes the ratio: depth to anchor level / overall height

δ_{act} denotes the angle of soil/wall friction behind the wall

δ_{pass} denotes the angle of soil/wall friction in front of the wall

3.2.1 Flexibility number

Rowe defined a flexibility number $R = m \rho = m H^4 / EI$, where m is a rather ambiguous parameter used to express the soil stiffness. He also defined the critical wall flexibility ρ_c as the value at which the deflection at the excavation level is equal to the deflection at the toe. In this definition the influence of the soil stiffness on the wall deformations is not considered. Li (1990) introduced a different definition of a flexibility number quantifying the relative importance of wall deflections due to rigid body rotation and bending. This approach is presented below.

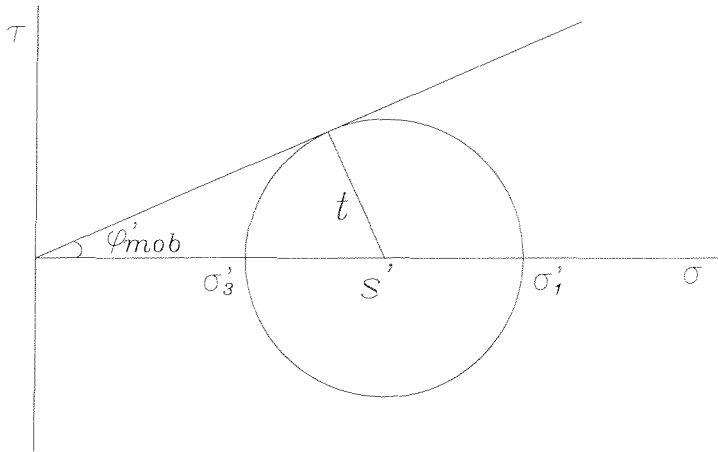


Figure 3.6: Mohr circle of stress.

From the geometry of the Mohr circle of stresses shown in Figure 3.6 the mobilised soil strength is defined by the relationship

$$\varphi'_{mob} = \sin^{-1} [t / s'] \quad (3.2)$$

where t is the maximum shear stress and is equal to the radius of the Mohr circle

$$t = 0.5 [\sigma'_1 - \sigma'_3] \quad (3.3)$$

and s' is the average effective stress which is located at the centre of the Mohr circle

$$s' = 0.5 [\sigma'_1 + \sigma'_3] \quad (3.4)$$

In Equations (3.3) and (3.4) σ'_1 and σ'_3 are the major and minor effective stresses respectively. The maximum shear stress can be expressed as

$$t = G \gamma \quad (3.5)$$

where G is the secant shear modulus of the soil and γ is the shear strain.

Therefore, from Equations (3.2) and (3.5):

$$\phi'_{mob} = \sin^{-1} [G \gamma / s'] \quad (3.6)$$

The use of a single $\phi'_{mob}-\gamma$ curve on one side of the wall is equivalent to the assumption of an increasing shear modulus with average effective stress s' and hence with depth. If G^* is the rate of increase of the shear modulus G with depth, Li (1990) used the geostructural mechanism for an initial earth pressure coefficient $K_o = 1$ to show that the rigid body rotation is governed by γ_s / G^* , where γ_s is the unit weight of the soil and that in undrained conditions the bending deformation is dependent on $\gamma_s H^4 / EI$, where H is the overall height and EI the bending stiffness of the wall. Figure 3.5 shows that the deflection of a retaining wall is due partly to a rotation as a rigid body and partly due to the effects of bending. Therefore, Li (1990) defined a flexibility number quantifying the relative importance of wall deflections due to rigid body rotation and bending

$$[\gamma_s / G^*] \div [\gamma_s H^4 / EI] = G^* H^4 / EI \quad (3.7)$$

This definition of a flexibility number seems similar to Rowe's definition $m_r H^4 / EI$. However, the use of the rate of increase of the shear modulus G^* instead of m_r is considered a more direct and clear description of the soil stiffness.

3.2.2 Critical flexibility ratio

The flexibility number as identified by Li (1990) and Rowe's definition of the critical flexibility of the wall can be combined to distinguish a stiff from a flexible system. To take into account both the wall flexibility and the soil stiffness, the term flexible or stiff system is used instead of one referring merely either to the wall or to the soil. The critical flexibility ratio is defined as the specific value of $G^* H^4 / E I$ at which the deflection at the excavation level of a retaining wall is equal to the deflection at the toe and is denoted by R_{crit} . If a system has values of $G^* H^4 / E I$ greater than R_{crit} , it is characterised as a flexible system, whereas if the values of $G^* H^4 / E I$ are less than R_{crit} , the system is regarded as stiff.

The calculations for the critical flexibility ratio that are presented later in this chapter are aimed at providing a general solution for soils with different initial earth pressure coefficients, in drained or undrained conditions and for walls propped at the crest with different retained height ratios h / H . Moreover, the variation of the values of R_{crit} with other parameters is investigated. However, since the geostructural mechanism is used to quantify R_{crit} , its application is restricted to stiff walls. An attempt to apply the geostructural mechanism to flexible walls also, will be discussed in Chapter 4.

3.3 STRESS DISTRIBUTIONS

3.3.1 Behind the retaining wall

The total stresses behind the retaining wall before excavation are assumed to be linear and proportional to the depth, with a pre-excavation horizontal total stress coefficient:

$$K_o = \sigma_{ho} / \sigma_{vo} \quad (3.8)$$

Then, at a depth z below ground level

$$\sigma_{vo} = \gamma_s z \quad (3.9)$$

where σ_{vo} the vertical total stresses and γ_s is the bulk unit weight of the soil and

$$\sigma_{ho} = K_o \gamma_s z \quad (3.10)$$

where σ_{ho} the horizontal total stresses.

The initial shear stress is

$$\tau_o = 1/2 (\sigma_1 - \sigma_3) \quad (3.11)$$

where σ_1, σ_3 are the major and minor principal stresses respectively. If we assume that $\sigma_{vo} = \sigma_1$ and $\sigma_{ho} = \sigma_3$ (i.e., $K_o < 1$), then :

when $K_o < 1$,

$$\tau_o = 1/2 (\sigma_{vo} - \sigma_{ho}) = 1/2 (\gamma_s z - K_o \gamma_s z) = 1/2 (1 - K_o) \gamma_s z > 0 \quad (3.12)$$

when $K_o > 1$,

$$\tau_o = 1/2 (1 - K_o) \gamma_s z < 0 \quad (3.13)$$

when $K_o = 1$,

$$\tau_o = 1/2 (1 - K_o) \gamma_s z = 0 \quad (3.14)$$

After a small rotation of the retaining wall $\delta\theta$ into the excavation, the vertical total stresses will remain the same whereas the horizontal stresses will be reduced below their initial pre-excavation values:

$$\sigma_v = \gamma_s z$$

$$\sigma_h < \sigma_{ho} \quad (3.15)$$

The shear stress τ_f at this stage, assuming that $\sigma_v = \sigma_1$ and $\sigma_h = \sigma_3$ (i.e., $K_o < 1$), is:

$$\tau_f = 1/2 (\sigma_1 - \sigma_3) = 1/2 (\sigma_v - \sigma_h) = 1/2 (\gamma_s z - \sigma_h) \quad (3.16)$$

In Equation (3.16) $\tau_f > 0$ since the horizontal stresses will approach their active values. Hence the incremental shear stress is

$$\begin{aligned} \delta\tau &= \tau_f - \tau_o = 1/2 (\sigma_v - \sigma_h) - 1/2 (\sigma_{vo} - \sigma_{ho}) = \\ & 1/2 (\gamma_s z - \sigma_h) - 1/2 \gamma_s z (1 - K_o) = 1/2 (K_o \gamma_s z - \sigma_h) \end{aligned} \quad (3.17)$$

which gives:

$$\sigma_h = K_o \gamma_s z - 2 \delta\tau \quad (3.18)$$

According to the geotechnical mechanism (Bolton & Powrie 1988), the rigid body rotation of a stiff wall propped at the crest can be related to the maximum shear strain in the soil behind the retaining wall via the relationship

$$\delta\gamma = 2 \delta\theta \quad (3.19)$$

where $\delta\theta$ is the rotation of the wall towards the excavation taken to be positive and $\delta\gamma$ is the shear strain in the soil. The incremental shear strain can then be related to the incremental shear stress required for equilibrium assuming that the concepts of elasticity theory still hold. Hence,

$$\delta\tau = G \delta\gamma \quad (3.20)$$

where G is the soil shear modulus. Since the soil shear modulus is not a constant but depends on the shear strain and the stress state, the rate of increase of G with depth is usually used:

$$G = G^* z \rightarrow G^* = G/z \quad (3.21)$$

So from Equations (3.19), (3.20) and (3.21):

$$\delta\tau = 2 G^* z \delta\theta \quad (3.22)$$

In Equation (3.22) $\delta\tau$ and $\delta\theta$ represent absolute values. Assuming that the final shear stress τ_f is greater than the initial shear stress τ_o and substituting Equation (3.22) in equation (3.18):

$$\sigma_h = K_o \gamma_s z - 4 G^* z \delta\theta \quad (3.23)$$

The above Equation relates the total horizontal stresses behind the wall after a small wall rotation to the initial in situ earth pressure coefficient K_o , the wall rotation $\delta\theta$ and the soil stiffness, which is expressed as the rate of increase of the soil shear modulus with depth G^* . If $\tau_o > \tau_f$:

$$\delta\tau = \tau_o - \tau_f = 1/2 (\sigma_{vo} - \sigma_{ho}) - 1/2 (\sigma_v - \sigma_h) = 1/2 (\sigma_h - K_o \gamma_s z) \quad (3.24)$$

From equations (3.22) and (3.24):

$$\sigma_h = K_o \gamma_s z + 4 G^* z \delta\theta \quad (3.25)$$

Equation (3.25) indicates that as the rotation of the wall towards the excavation increases, the horizontal stresses behind the wall increase as well. However, the wall rotation will cause a relief in the horizontal stresses behind the wall, which will decrease towards their active values; hence, the assumption $\tau_o > \tau_f$ cannot be correct. The distribution of the total horizontal stresses behind the wall is therefore derived from Equation (3.23). The Mohr circles of total stresses when $K_o < 1$, $K_o > 1$ and $K_o = 1$ are presented in Figures 3.7, 3.8 and 3.9 respectively.

- A. If $K_o < 1$, then $\sigma_{vo} > \sigma_{ho} \rightarrow \tau_o > 0$ and $\tau_f > 0$. Assuming $\sigma_v = \sigma_{vo} > \sigma_{ho} > \sigma_h$:
 $\tau_f - \tau_o > 0$

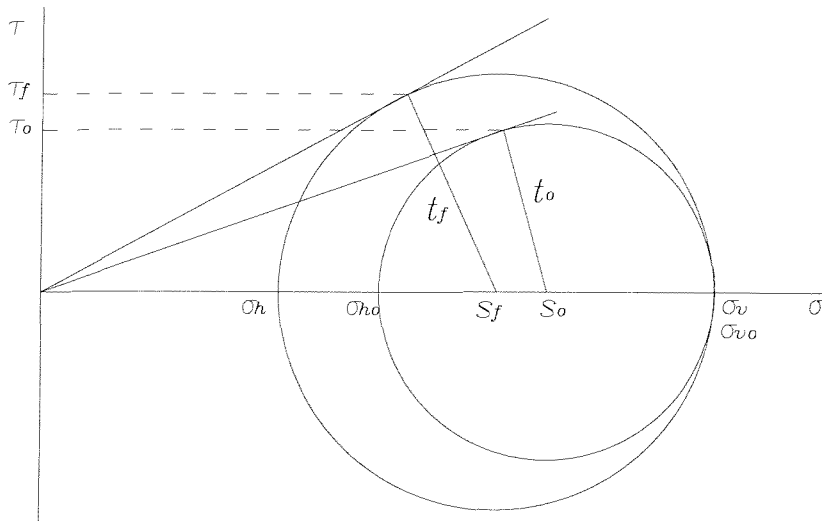


Figure 3.7: Mohr circle of total stresses behind a retaining wall before and after excavation ($K_o < 1$).

- B. If $K_o > 1$, then $\sigma_{vo} < \sigma_{ho} \rightarrow \tau_o < 0$ and $\tau_f > 0$. Therefore $\tau_f - \tau_o > 0$ since $\sigma_{ho} > \sigma_v$
 $= \sigma_{vo} > \sigma_h$.

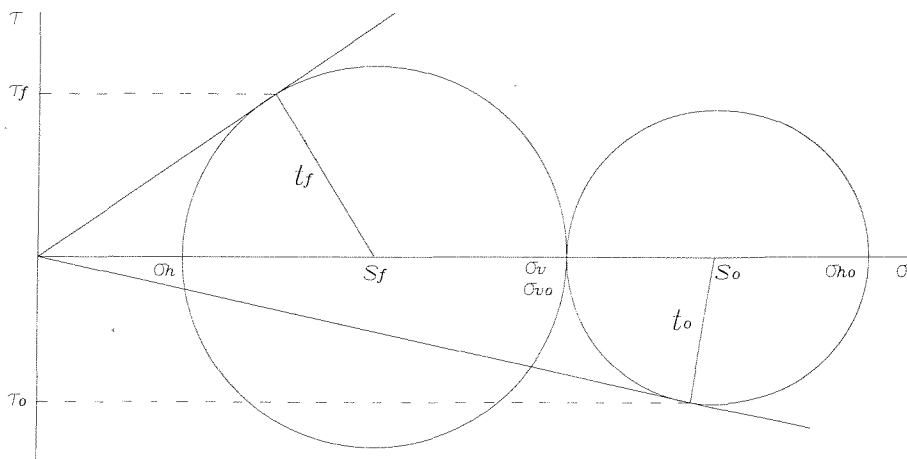


Figure 3.8: Mohr circle of total stresses behind a retaining wall before and after excavation ($K_o > 1$).

C. If $K_o = 1$, then $\tau_o = 0$, $\tau_f > 0$. Therefore: $\tau_f - \tau_o > 0$.

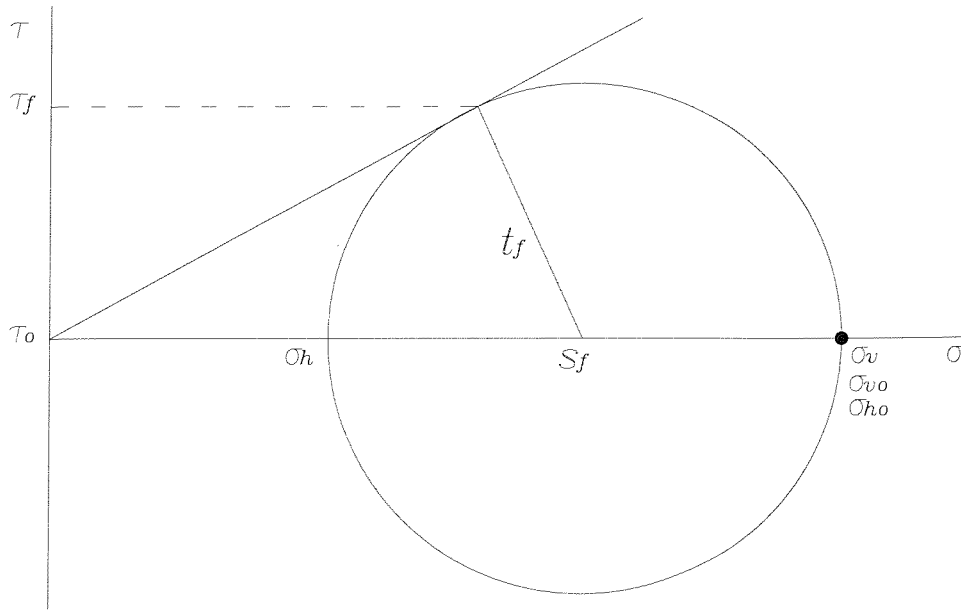


Figure 3.9: Mohr circle of total stresses behind a retaining wall before and after excavation ($K_o = 1$).

3.3.2 In front of the retaining wall

The total stresses at a depth z below the ground level before excavation are again assumed to be linear and proportional to the depth

$$\sigma_{vo} = \gamma_s z \quad (3.26)$$

$$\sigma_{ho} = K_o \gamma_s z \quad (3.27)$$

where σ_{vo} , σ_{ho} are the vertical and horizontal stresses in front of the wall respectively. If we assume that $\sigma_{vo} = \sigma_1$, $\sigma_{ho} = \sigma_3$, then the initial shear stress is:

when $K_o < 1$,

$$\tau_o = 1/2 (\sigma_{vo} - \sigma_{ho}) = 1/2 (\gamma_s z - K_o \gamma_s z) = 1/2 (1 - K_o) \gamma_s z > 0 \quad (3.28)$$

when $K_o > 1$,

$$\tau_o = 1/2 (1 - K_o) \gamma_s z < 0 \quad (3.29)$$

when $K_o = 1$,

$$\tau_o = 1/2 (1 - K_o) \gamma_s z = 0 \quad (3.30)$$

After a rotation $\delta\theta$ of the retaining wall into the excavation, the total stresses and the shear stress are:

$$\sigma_v = \gamma_s (z - h) \quad (3.31)$$

$$\sigma_h > \sigma_{ho}$$

$$\tau_f = 1/2 (\sigma_1 - \sigma_3) = 1/2 (\sigma_v - \sigma_h) = 1/2 [\gamma_s (z - h) - \sigma_h] \quad (3.32)$$

In Equation (3.32) $\tau_f < 0$ since the horizontal stresses will approach their passive values. Following the same reasoning as before, the incremental shear stress is:

when $K_o < 1$,

$$\sigma_{vo} > \sigma_{ho} \rightarrow \tau_o > 0 \quad \text{and} \quad \sigma_v < \sigma_h \rightarrow \tau_f < 0 \rightarrow \tau_f - \tau_o < 0 \quad (3.33)$$

when $K_o > 1$,

$$\sigma_{vo} < \sigma_{ho} \rightarrow \tau_o < 0 \quad \text{and} \quad \sigma_v < \sigma_h \rightarrow \tau_f < 0$$

Therefore:

$$\sigma_v < \sigma_{vo} < \sigma_{ho} < \sigma_h \rightarrow \sigma_v - \sigma_h - \sigma_{vo} + \sigma_{ho} < 0 \rightarrow \tau_f - \tau_o < 0 \quad (3.34)$$

when $K_o = 1$,

$$\tau_o = 0 \quad \text{and} \quad \tau_f < 0 \rightarrow \tau_f - \tau_o < 0 \quad (3.35)$$

Therefore: $\delta\tau = \tau_o - \tau_f > 0 \rightarrow \delta\tau = 1/2 (\sigma_{vo} - \sigma_{ho}) - 1/2 (\sigma_v - \sigma_h) =$

$$= 1/2 [\gamma_s z (1 - K_o) - \gamma_s (z - h) + \sigma_h] = 1/2 (\sigma_h + \gamma_s h - K_o \gamma_s z) \quad (3.36)$$

From the geostructural mechanism the shear strain at the excavated side is $(1 + h / d)$ times that on the retained side of the wall, so:

$$\delta\gamma = 2 (1 + h / d) \delta\theta \quad (3.37)$$

where d is the wall embedment depth. Combining Equations (3.20), (3.21), (3.36) and (3.37):

$$\delta\tau = 2 G^* z (1 + h / d) \delta\theta \rightarrow$$

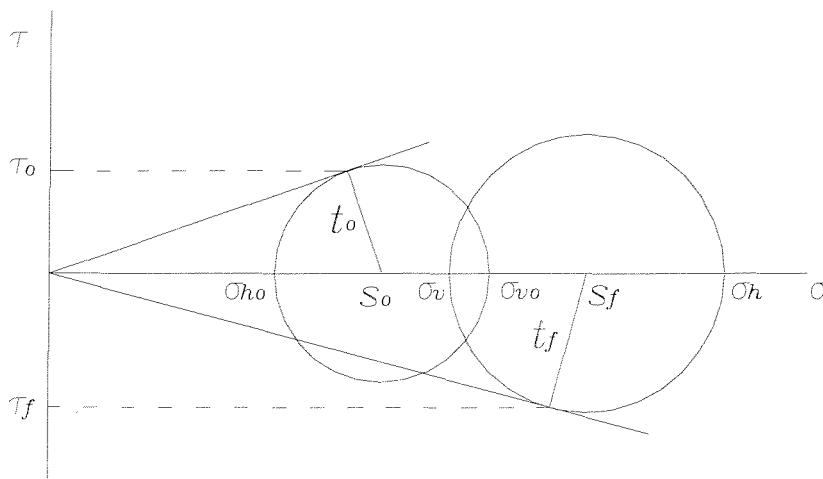
$$1/2 [\gamma_s z - K_o \gamma_s z - \gamma_s (z - h) + \sigma_h] = 2 G^* z (1 + h / d) \delta\theta \rightarrow$$

$$\sigma_h = K_o \gamma_s z - \gamma_s h + 4 G^* z (1 + h / d) \delta\theta \quad (3.38)$$

The Mohr circles of total stresses in front of the wall when $K_o < 1$, $K_o > 1$ and $K_o = 1$ are presented in Figures 3.10, 3.11 and 3.12 respectively. The horizontal stress distributions behind and in front of the retaining wall are plotted in Figure 3.13.

A. If $K_o < 1$, then $\tau_o > 0$, $\tau_f < 0$ and $\tau_o - \tau_f > 0$.

a. If $\sigma_{ho} < \sigma_v < \sigma_{vo} < \sigma_h$ the Mohr circle of total stresses may be drawn as:



(a)

b. If $\sigma_v < \sigma_{ho} < \sigma_{vo} < \sigma_h$ the Mohr circle of total stresses may be drawn as:

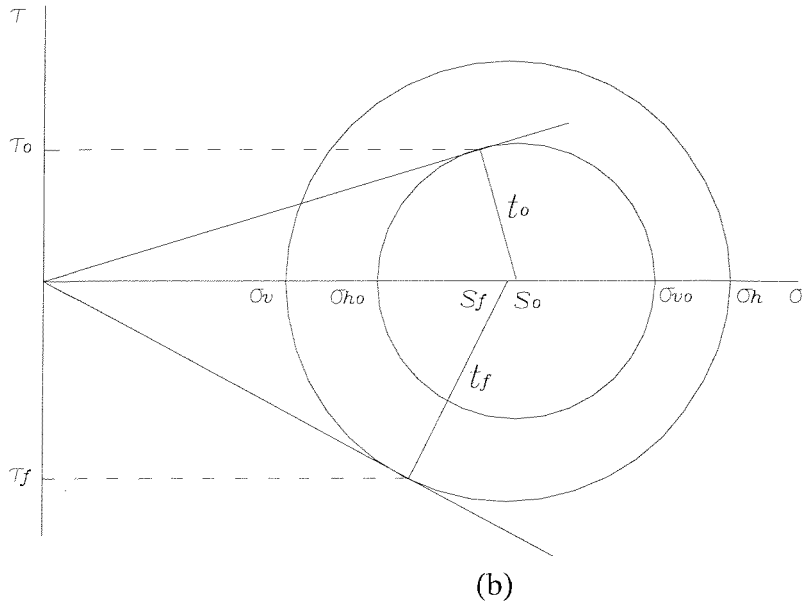


Figure 3.10a & b: Mohr circles of total stresses in front of a retaining wall before and after excavation ($K_o < 1$).

B. If $K_o > 1$, then $\tau_o < 0$, $\tau_f < 0$ and $\sigma_h > \sigma_{ho} > \sigma_{vo} > \sigma_v$. Therefore, $\tau_o - \tau_f > 0$ and the Mohr circle of total stresses may be drawn as:

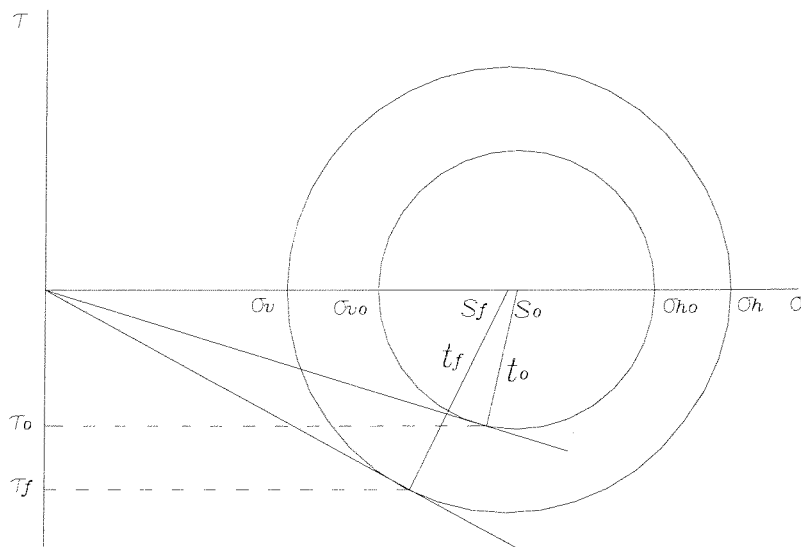


Figure 3.11: Mohr circles of total stresses in front of a retaining wall before and after excavation ($K_o > 1$).

C. If $K_o = 1$, then $\tau_o = 0$, $\tau_f < 0$ and $\tau_o - \tau_f > 0$.

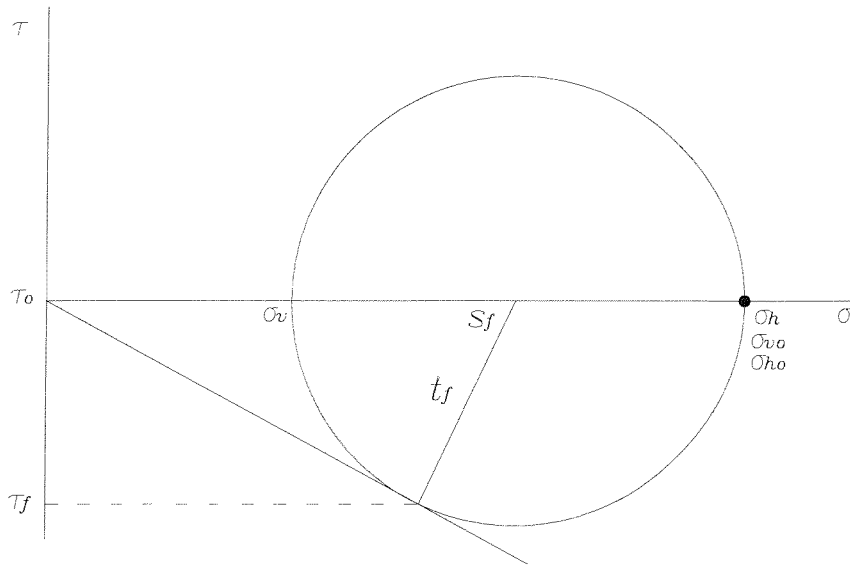


Figure 3.12: Mohr circle of total stresses in front of a retaining wall before and after excavation ($K_o = 1$).

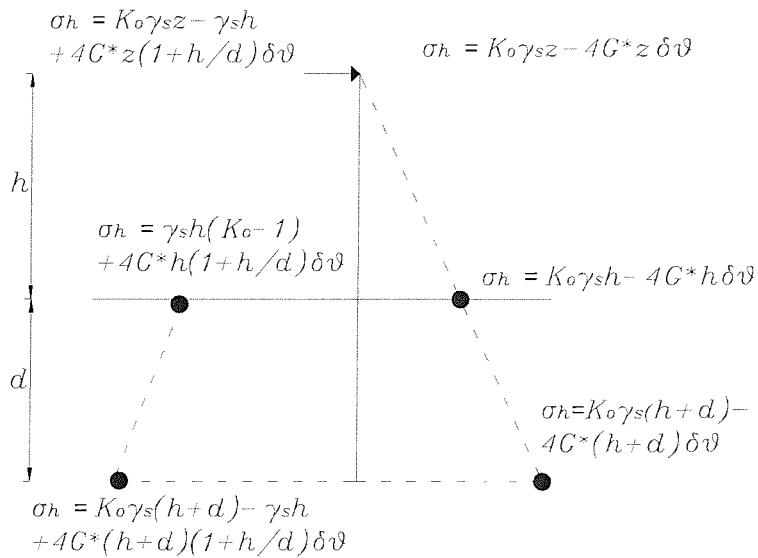


Figure 3.13: Lateral total stress distributions behind and in front of a retaining wall.

3.4 WALL ROTATION

Assuming that the total stress distribution behind and in front of the wall are described by Equations (3.25) and (3.38) respectively, the wall rotation $\delta\theta$ required to maintain stability can be calculated by considering the moment equilibrium about the prop:

$$\delta\theta = \gamma_s m [(2 K_o - 3) m^2 + 3] / 8 G^* (m^2 + m + 2) \quad (3.39)$$

where m is the retained height ratio, which is defined as the ratio of the retained height to the retaining wall's overall height. The detailed calculations are carried out in Mathematica and are presented in the Appendix.

The above relationship specifies the wall rotation $\delta\theta$ in relation to the initial *in situ* earth pressure coefficient K_o , the retained height ratio m and the ratio of the bulk soil unit weight to the rate of increase of the shear modulus γ_s / G^* . In Figures 3.14, 3.15 and 3.16 $\delta\theta$ is plotted against m for different values of γ_s / G^* and $K_o = 0.5, 1.0$ and 2.0 respectively. The values of γ_s / G^* vary from 0.005 to 0.02 , whereas m varies from 0 to 1 . In figures 3.17 and 3.18 $\delta\theta$ is plotted against K_o for different values of γ_s / G^* and for $m = 0.6$ and 0.7 respectively. Figures 3.19 and 3.20 show $\delta\theta$ against γ_s / G^* for $K_o = 0.5, 1.0, 2.0$ and $m = 0.6$ and 0.7 .

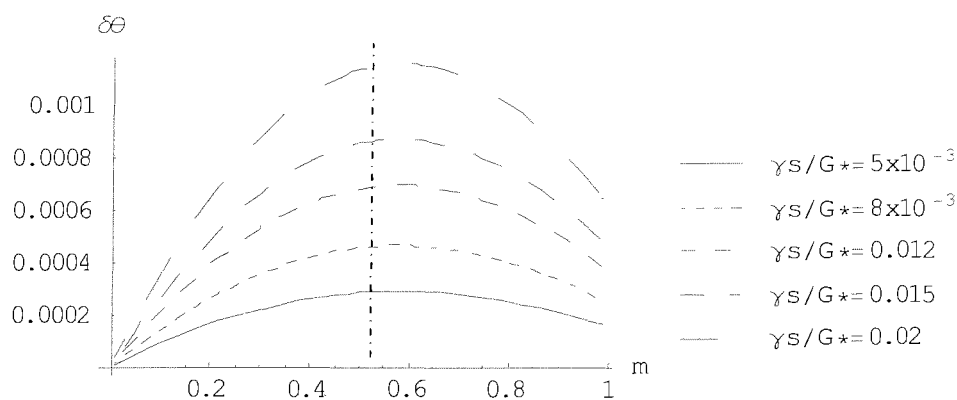


Figure 3.14: Variation of the wall rotation $\delta\theta$ with m for $K_o = 0.5$ and $\gamma_s / G^* = 0.005, 0.008, 0.012, 0.015$ and 0.02 .

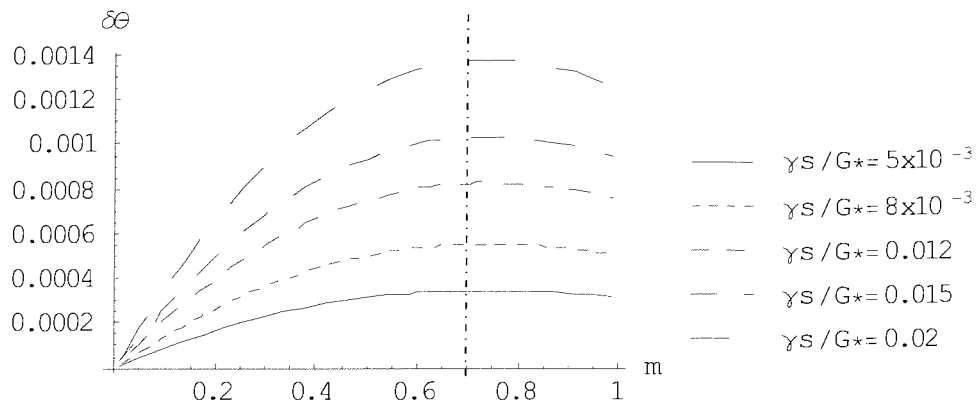


Figure 3.15: Variation of the wall rotation $\delta\theta$ with m for $K_o = 1.0$ and $\gamma_s / G^* = 0.005, 0.008, 0.012, 0.015$ and 0.02 .

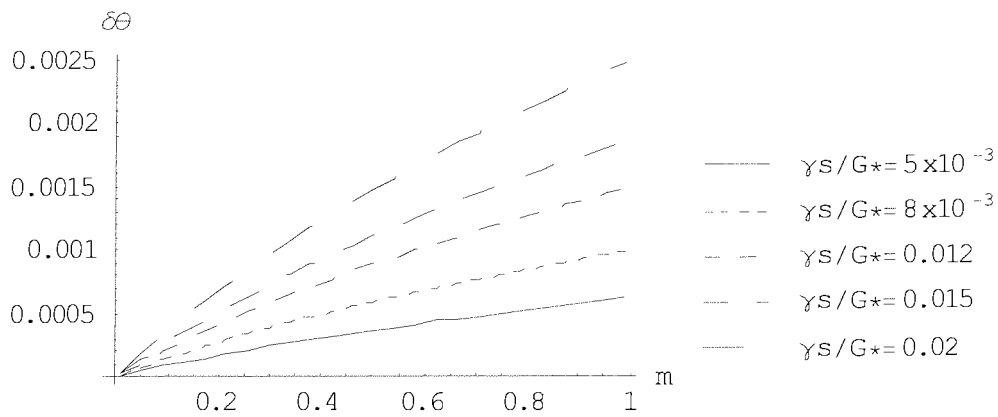


Figure 3.16: Variation of the wall rotation $\delta\theta$ with m for $K_o = 2.0$ and $\gamma_s / G^* = 0.005, 0.008, 0.012, 0.015$ and 0.02 .

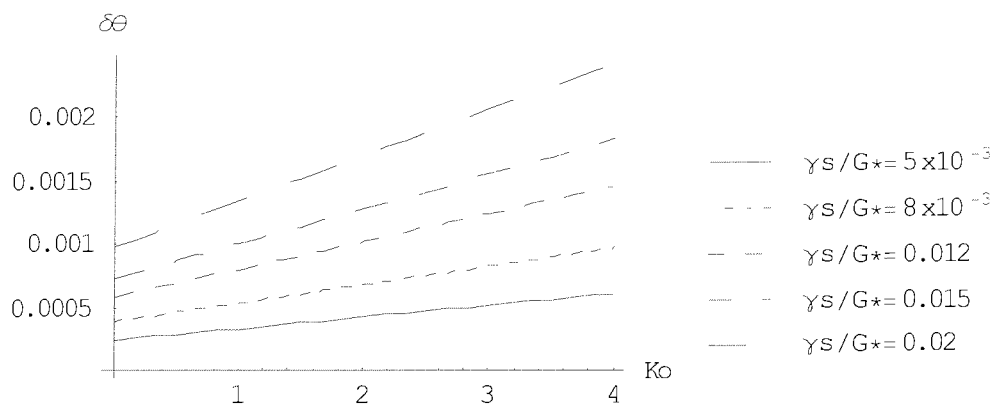


Figure 3.17: Variation of the wall rotation $\delta\theta$ with K_o for $m = 0.6$ and $\gamma_s / G^* = 0.005, 0.008, 0.012, 0.015$ and 0.02 .

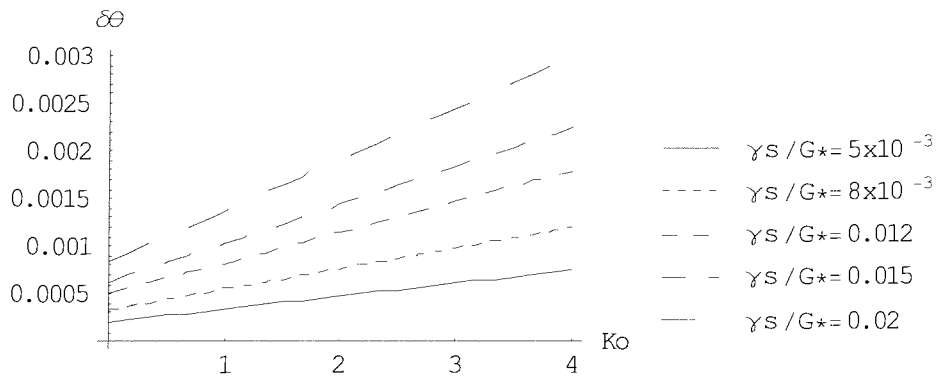


Figure 3.18: Variation of the wall rotation $\delta\theta$ with K_o for $m = 0.7$ and $\gamma_s / G^* = 0.005, 0.008, 0.012, 0.015$ and 0.02 .

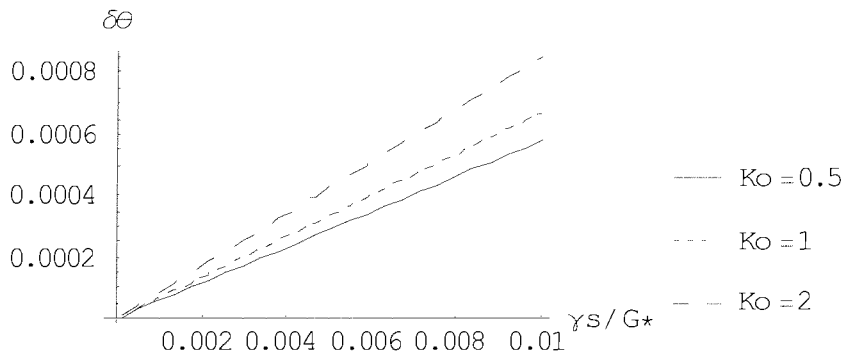


Figure 3.19: Variation of the wall rotation $\delta\theta$ with γ_s / G^* for $m = 0.6$ and $K_o = 0.5, 1.0$ and 2.0 .

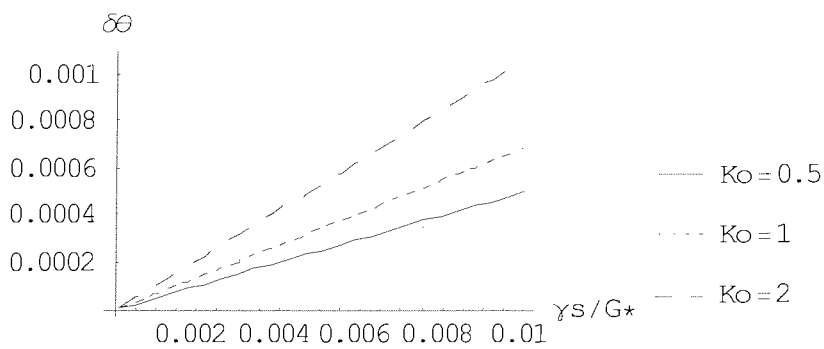


Figure 3.20: Variation of the wall rotation $\delta\theta$ with γ_s / G^* for $m = 0.8$ and $K_o = 0.5, 1.0$ and 2.0 .

According to the Figures, the wall rotation about the prop increases with decreasing soil stiffness and increasing earth pressure coefficient. The rate of the increase in the wall rotation with increasing K_o is less for high soil stiffness than for low. The relationship between the wall rotation and the retained height is approximately linear for $K_o=2$. It would be expected that as the retained height ratio, m , approaches unity the wall would fail. However, this is not obvious in Figures 3.14 and 3.15. An explanation could be that maybe there is a failure cut off at some value of m , indicated by a dashed line in Figures 3.14 and 3.15, that depends on the maximum principal stress difference; hence, the results for bigger values of m than this wouldn't apply. Moreover, it should be noted that the assumption of a perfectly rigid wall is followed herein; in reality retaining walls may not exhibit such a stiff response.

3.5 PROP LOADS

From the condition of horizontal equilibrium, the stress distributions and the wall rotation $\delta\theta$ deduced from equation (3.39), the prop force can be calculated:

$$F = \gamma_s m H^2 [-m^3 - 2 m^2 (K_o - 3) + m (4 K_o - 7) + 2] / 4 (m^2 + m + 2) \quad (3.40)$$

The normalised prop load is given by:

$$F / \gamma_s H^2 = [-m^3 - 2 m^2 (K_o - 3) + m (4 K_o - 7) + 2] / 4 (m^2 + m + 2) \quad (3.41)$$

In Figure 3.21 the normalised prop load $F / \gamma_s H^2$ is plotted against m and K_o , with m varying from 0 to 1.0 and K_o from 0.5 to 4.0. Figure 3.22 shows the variation of the normalized prop load with m for $K_o = 0.5, 1.0$ and 2.0 . In Figure 3.23 the normalized prop load is plotted against K_o for $m = 0.6, 0.7$ and 0.8 .

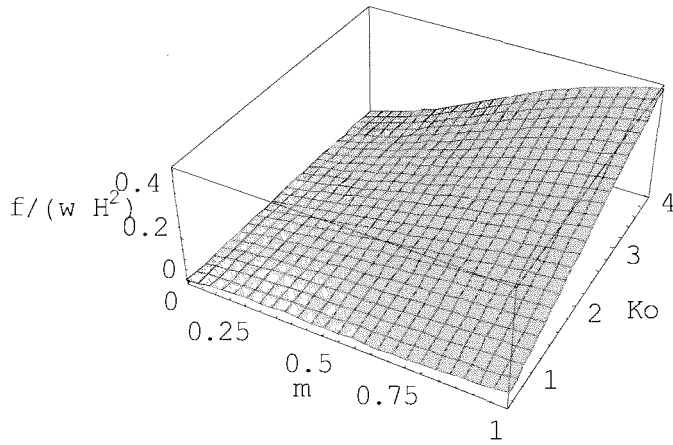


Figure 3.21: The variation of the normalised prop load $F / w H^2$ with m and K_o .

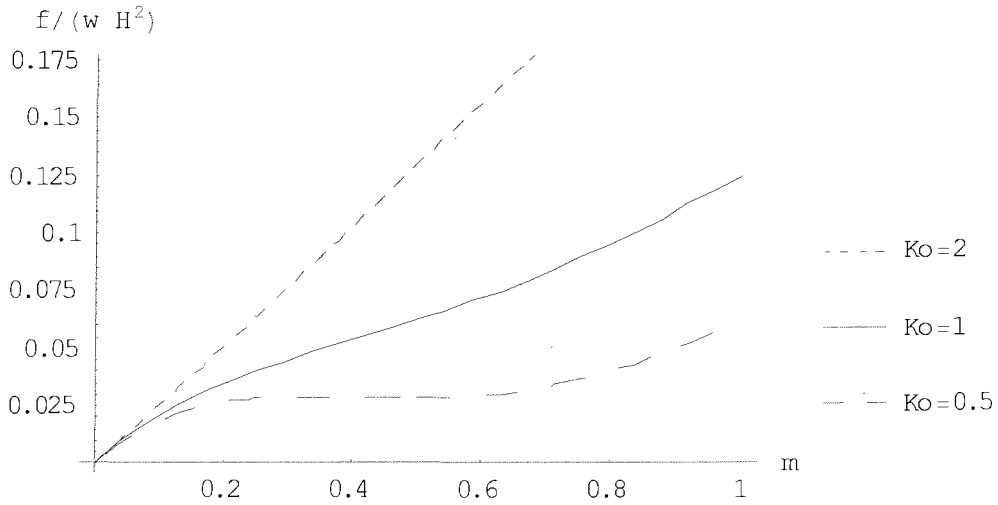


Figure 3.22: The variation of the normalised prop load $F / w H^2$ with m for $K_o = 0.5, 1.0$ and 2.0 .

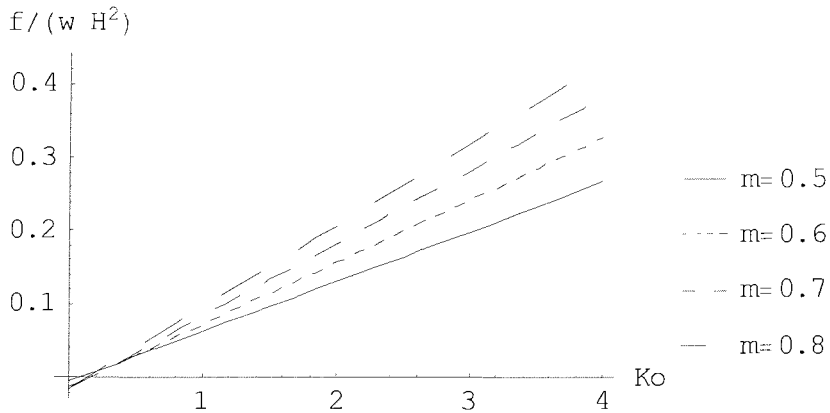


Figure 3.23: The variation of the normalised prop load $F / w H^2$ with m for $K_o = 0.5, 1.0,$ and 2.0 .

From the Figures, the normalized prop load increases with increasing K_o and m . For very low K_o values, negative prop loads are shown in Figure 3.23. The physical meaning of this might be that very low K_o values could result in a backward wall movement instead of a movement into the excavation. From the empirical relationship $K_o=1-\sin\phi$, for very low values of K_o the soil strength ϕ would be significantly increased; however, such high values of soil strength might not be realistic.

3.6 BENDING MOMENTS

The normalised bending moments along the wall at a depth z from the ground surface is:

$$M / \gamma_s H^3 = A (z / H) + B (z / H)^3 + C [z / H - m]^2 + D [z / H - m]^3 \quad (3.42)$$

where A , B , C and D are constants that depend on the retained height ratio m and the initial in situ earth pressure coefficient K_o , and they are defined by equations (3.43), (3.44), (3.45) and (3.46). If $z / H < m$, then $[z / H - m] = 0$.

$$A = -\{m [m^3 + 2 m^2 (K_o - 3) + m (7 - 4 K_o) - 2]\} / \{4 [m^2 + m + 2]\} \quad (3.43)$$

$$B = -K_o / 6 + \{m [m^2 (2 K_o - 3) + 3]\} / [12 (m^2 + m + 2)] \quad (3.44)$$

$$C = \{m [m^3 - 5 m + 4 + 2 K_o (m - 2)]\} / [4 (m^3 + m - 2)] \quad (3.45)$$

$$D = [2 K_o (m - 2) + 3 m (m^2 - 1)] / [12 (m^3 + m - 2)] \quad (3.46)$$

3.7 DEFORMATIONS

The wall deflection δ is calculated from the differential equation:

$$d^2 \delta / dz^2 = -M / EI \quad (3.47)$$

After double integrating equation (3.47) the normalised wall deflection is:

$$\delta / H = -\gamma_s H^4 / EI [A / 6 (z / H)^3 + B (z / H)^5 + C / 12 (z / H - m)^4 + D / 20 (z / H - m)^5 + J_1 (z / H) + J_2] \quad (3.48)$$

Where $E I$ is the retaining wall flexural rigidity and J_1, J_2 are constants of integration. From the boundary condition at the prop at $z=0 \rightarrow \delta=0$, J_2 can be calculated:

$$J_2 = -C / 12 m^4 + D / 20 m^5 \quad (3.49)$$

According to the geostrophical mechanism, the maximum deflection for a rigid wall propped at the crest is at the toe of the wall and is related to the wall rotation $\delta\theta$ required to maintain stability by the relationship:

$$\delta_{toe} / H = \delta\theta = \gamma_s m [(2 K_o - 3) m^2 + 3] / 8 G^* (m^2 + m + 2) \quad (3.50)$$

Therefore, the boundary condition at the toe at $z = H \rightarrow \delta = \delta_{toe}$ defines J_1 :

$$J_1 = -EI \delta\theta / \gamma_s H^4 - A / 6 - B / 20 - C (1 - m)^4 / 12 + C m^4 / 12 - D (1 - m)^5 / 20 - D m^5 / 20 \quad (3.51)$$

By substituting the integration constants J_1 and J_2 in equation (3.48):

$$\begin{aligned} \delta / H = & -\gamma_s H^4 / EI [A / 6 (z / H)^3 + B / 20 (z / H)^5 + C / 12 (z / H - m)^4 + D / 20 \\ & (z / H - m)^5 - EI \delta\theta / \gamma_s H^4 (z / H) - A / 6 (z / H) - B / 20 (z / H) - C (1 - m)^4 / 12 (z / H) \\ & + C m^4 / 12 (z / H) - D (1 - m)^5 / 20 (z / H) - D m^5 / 20 (z / H) - C m^4 / 12 + D m^5 / 20] \end{aligned} \quad (3.52)$$

Equation (3.52) enables the calculation of the deformations of a rigid wall for different initial earth pressure coefficients K_o and retained height ratios m , if the wall flexibility $E I$ and the rate of increase of the soil shear modulus G^* are known.

3.8 CRITICAL FLEXIBILITY RATIO

Considering the definition of the critical flexibility ratio R_{crit} , the deflection at the dredge level should be equal to the deflection at the toe of the retaining wall:

$$\delta_{dredge} = \delta_{toe} \rightarrow \delta_{dredge} / H = \delta_{toe} / H \quad (3.53)$$

From the geostrophical mechanism the wall rotation $\delta\theta$ will be related to the deflections, so:

$$\delta_{dredge} / H = \delta_{toe} / H = \delta\theta \quad (3.54)$$

At the dredge level the depth z equals the retained height h , so:

$$z = h \rightarrow z / H = h / H = m \quad (3.55)$$

From equations (3.52), (3.54) and (3.55):

$$\begin{aligned} \delta\theta &= m \delta\theta - \gamma_s H^4 / EI [A / 6 m^3 + B / 20 m^5 - A / 6 m - B / 20 m - C / 12 m \\ & (1 - m)^4 + C m^5 / 12 - D m (1 - m)^5 / 20 - D m^6 / 20 - C m^4 / 12 + D m^5 / 20] \\ \rightarrow (m - 1) \delta\theta - \gamma_s H^4 / EI \{ & A m (m^2 - 1) / 6 + B m (m^4 - 1) / 20 + C m [m^4 - m^3 - \\ & (1 - m)^4] / 12 + D m [m^4 - m^5 - (1 - m)^5] / 20 \} = 0 \end{aligned} \quad (3.56)$$

Equation (3.56) can be rewritten in the form:

$$\delta\theta = \gamma_s / G^* x L \quad (3.57)$$

$$\text{where } L = \{m [(2 K_o - 3) m^2 + 3]\} / \{8 (m^2 + m + 2)\} \quad (3.58)$$

From equations (3.56), (3.57) and (3.58):

$$L (m-1) / \{ [A m (m^2 - 1) / 6] + [B m (m^4 - 1) / 20] + [C m (m^4 - m^3 - (1 - m^4)) / 12] + [D m (m^4 - m^5 - (1 - m^5)) / 20] \} = G^* H^4 / EI = R_{crit} \quad (3.59)$$

Substituting A , B , C , D and L which are given by Equations (3.43), (3.44), (3.45), (3.46) and (3.58) respectively, Equation (3.59) can be rewritten in the form:

$$30 (m - 1) [m^2 (2 K_o - 3) + 3] / \{ m [m^6 (2 K_o - 3) - m^5 (2 K_o + 7) - 22 m^4 (K_o - 3) + 2 m^3 (29 K_o - 65) + m^2 (-44 K_o + 83) - 3 m - 6] \} = G^* H^4 / EI = R_{crit} \quad (3.60)$$

Equation (3.60) specifies the value of the critical flexibility ratio for different initial earth pressure coefficients K_o and retained height ratios m . Therefore, depending on the values of R_{crit} obtained from the above equation a stiff system can be distinguished from a flexible one. The advantages of this solution are that both the wall flexibility and the soil stiffness are considered in the same calculation and it can be applied in a general manner if the retained height ratio and the initial earth pressure coefficient are known. Moreover, a clear and consistent parameter for the soil stiffness is used, which can be obtained from laboratory tests on representative soil samples. Most of the calculations were carried out in Mathematica and can be found in the Appendix.

R_{crit} is plotted against m and K_o in Figure 3.24, against m for $K_o = 0.5, 1.0$ and 2.0 in Figures 3.25 and 3.26 and against K_o , for $m = 0.4, 0.5, 0.6, 0.7$ and 0.8 in Figure 3.27.

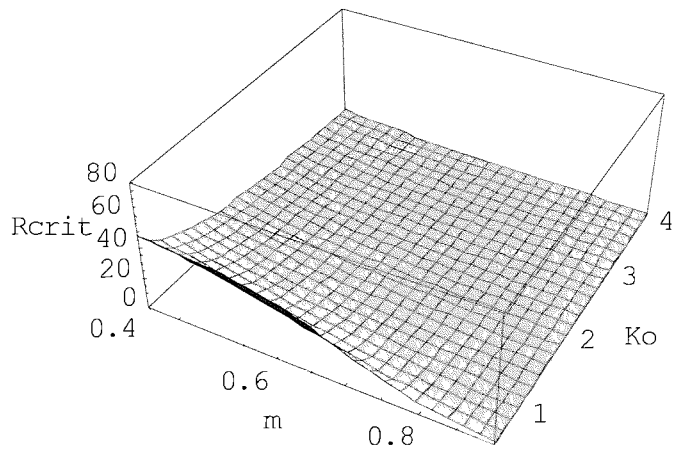


Figure 3.24: The variation of the critical flexibility ratio R_{crit} with m and K_o .

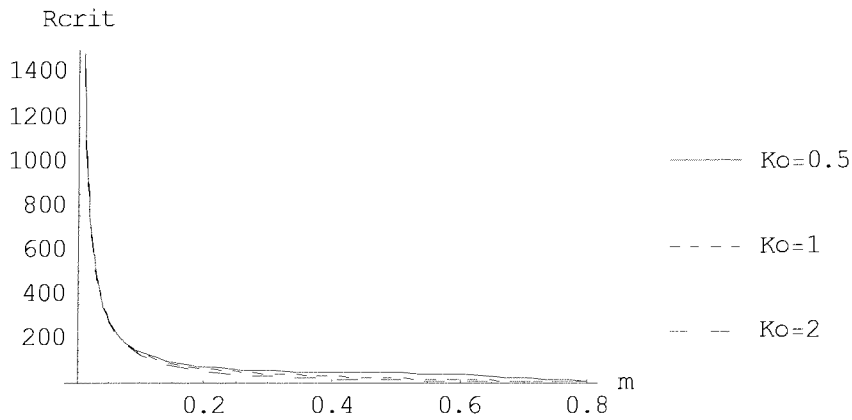


Figure 3.25: The variation of the critical flexibility ratio R_{crit} with m for $K_o = 0.5, 1.0$ and 2.0 .

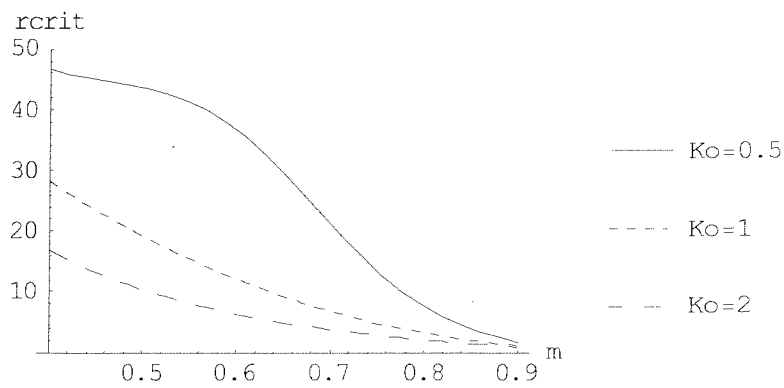


Figure 3.26: The variation of the critical flexibility ratio R_{crit} with m for $K_o = 0.5, 1.0$ and 2.0 , where m is in the range of 0.4 to 0.8.

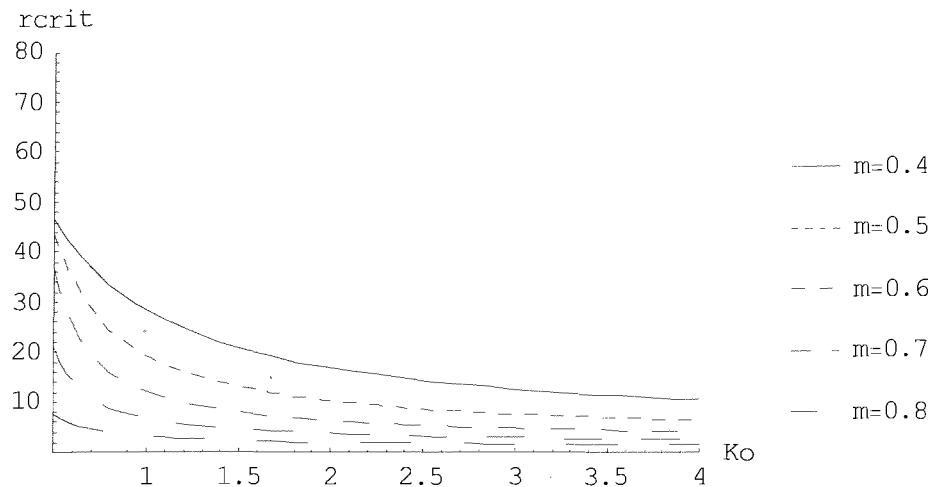


Figure 3.27: The variation of the critical flexibility ratio R_{crit} with K_o for $m = 0.4, 0.5, 0.6, 0.7$ and 0.8 , where K_o is in the range of 0.3 to 4.0 .

The critical flexibility ratio increases when K_o and m decrease. A system may be characterized stiff for values of $G^* H^4 / EI, K_o$ and m below the critical flexibility curve, whereas flexible for values of $G^* H^4 / EI, K_o$ and m above the critical flexibility curve. For a stiff system, the prop loads, bending moments, wall rotations and deformations may be calculated by the method presented in this Chapter. For a combination of values which lie on the critical flexibility curve, the wall movement at the toe of the wall will be the same with the wall movement at dredge level.

3.8. SUMMARY

The critical flexibility curves presented in this Chapter enable the designer to distinguish a stiff from a flexible system taking into account the relative soil/wall stiffness, the in situ earth pressure coefficient and the retained height ratio. For stiff systems, curves and relationships are given for the estimation of the prop loads, bending moments, wall rotations and deformations incorporating the relative soil/wall stiffness and the mobilized shear strength behind and in front of a retaining wall. For flexible systems, the application of the MSD method is examined in Chapter 4. Simple and reasonably accurate predictions may be obtained by this simple design framework.

4. ANALYSIS AND DESIGN OF FLEXIBLE RETAINING WALLS PROPPED AT THE CREST

4.1 INTRODUCTION

Some aspects of the soil behaviour and its theoretical modeling are reviewed and discussed in the beginning of this chapter. The hyperbolic relationship, introduced by Duncan and Cheng (1970) to represent the soil non-linear stress-strain relationship, is presented in detail and compared to other soil models.

The mobilised strength method for stiff walls, as presented earlier in this thesis, is extended, modified and applied to flexible retaining walls propped at the crest. New deformation patterns are proposed, the mobilized shear strain is associated with the mobilized shear strength by a modified version of the hyperbolic relationship introduced by Duncan and Cheng (1970) and the wall flexibility is idealized into a simple mechanism.

Finally, the potential of the method to serve as a design tool for flexible retaining walls propped at the crest in drained conditions is examined and the effects of the wall flexibility, the soil stiffness and the soil shear strength before excavation on the predicted deformations are investigated.

4.2 SOIL BEHAVIOUR

Soil behaviour is generally complicated and a substantial number of parameters may be required to describe it adequately. Previous research studies have been focused on investigating these parameters and developing constitutive models to achieve a better understanding of soil behaviour and its importance to the calculation of realistic ground

deformations. However, the complexity and extent of the problem allows only for a brief discussion here.

4.2.1 Soil stress-strain behaviour

The stress-strain behaviour of most soils is non-linear, with the soil stiffness depending on various parameters which are related to the type of soil, the soil current state and its stress history. Some of these parameters are real, whereas others are artifacts of the sampling process. The soil stiffness is quantified by means of the Young's modulus E or the shear modulus G , expressed as a tangent or secant, on a stress-strain curve.

The type of soil may be described by the grading and plasticity. An example of the effect of these parameters on soil stiffness can be found in the results of undrained triaxial tests on various soils carried out by Jardine, Symes and Burland (1984) with the accurate measurement of local axial strains. Low plasticity clays were found to exhibit the most non-linear but stiff initial behaviour, whereas cemented chalk samples showed the nearest approximation to linear stress-strain behavior. A summary of their results is presented in Figure 4.1, where the stiffness is expressed as the undrained secant Young's modulus normalized by the undrained shear strength, E_u / c_u , and plotted against the local axial strain ε_L .

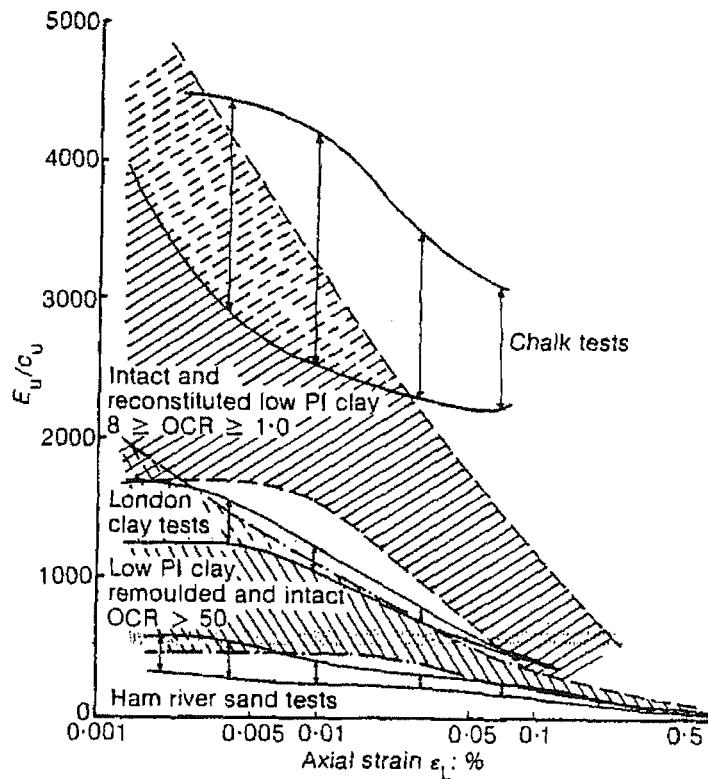
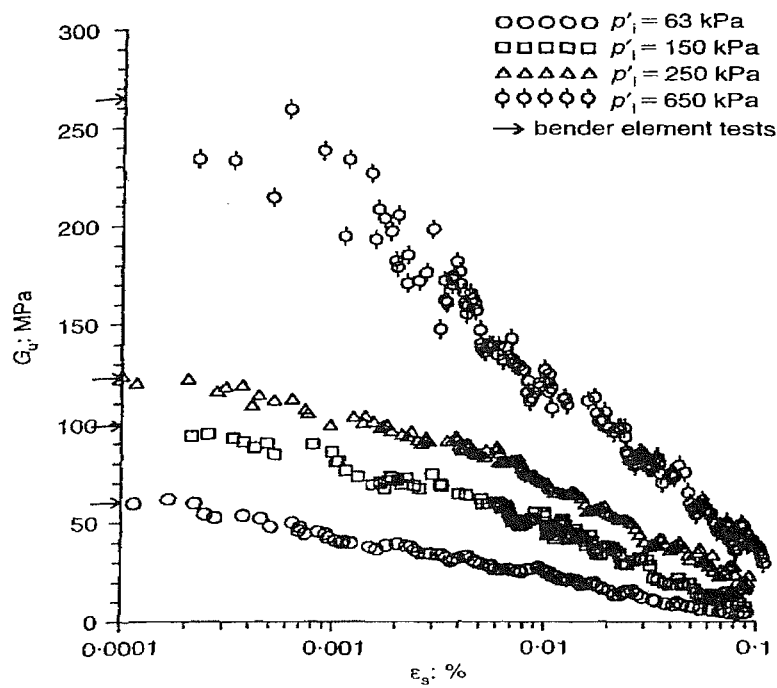
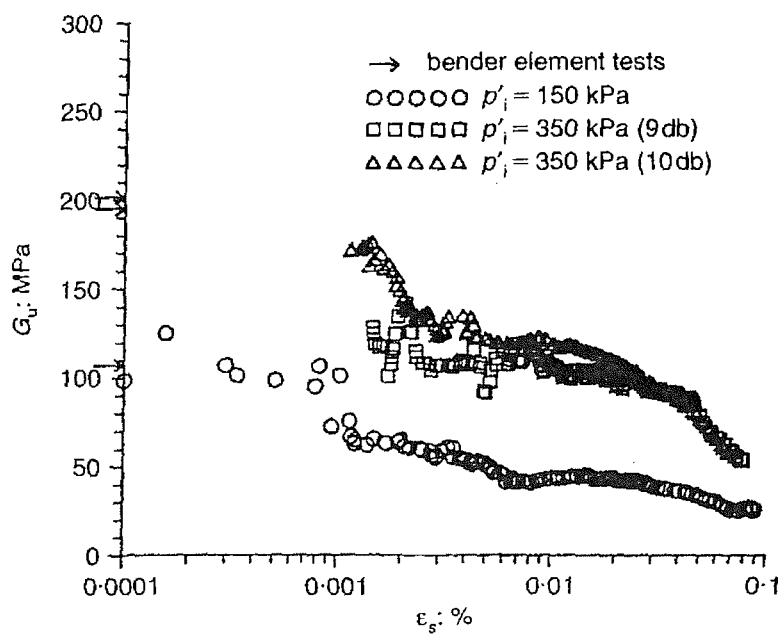


Figure 4.1: Normalised secant stiffness E_u / c_u against axial strain for all the undrained triaxial tests (Jardine, Symes and Burland, 1984).

The state of a soil may be described by its current stress state, which together with the current strain will affect the soil stiffness considerably. Jovičić and Coop (1997) carried out undrained triaxial tests on different types of sand. Some of their results are shown in Figures 4.2a and b in which the dependence of the tangent shear modulus G_{tan} on the initial mean effective stress before shearing, p'_i , is obvious, particularly for very small strains. Soil stiffness is usually normalized with respect to the initial mean effective stress before shearing, p'_o or p'_i .



(a)



(b)

Figure 4.2: Variation of tangent shear stiffness with strain and initial effective stress for undrained triaxial tests on: (a) compacted samples; (b) overconsolidated samples (Jovičić and Coop 1997).

The graph in Figure 4.3 represents the typical soil stiffness-strain relationship which has been in use for many years and is referred to as the S-shaped curve. The soil stiffness is high at small strains and reduces at larger strains. Simpson (1992) redrew the S-shaped curve, as shown in Figure 4.4, to indicate what proportion of the soil behaves elastically at each strain level. From this graph soil may be viewed 100% elastic at very small strains and the proportion of soil that behaves plastically increases with reducing stiffness.

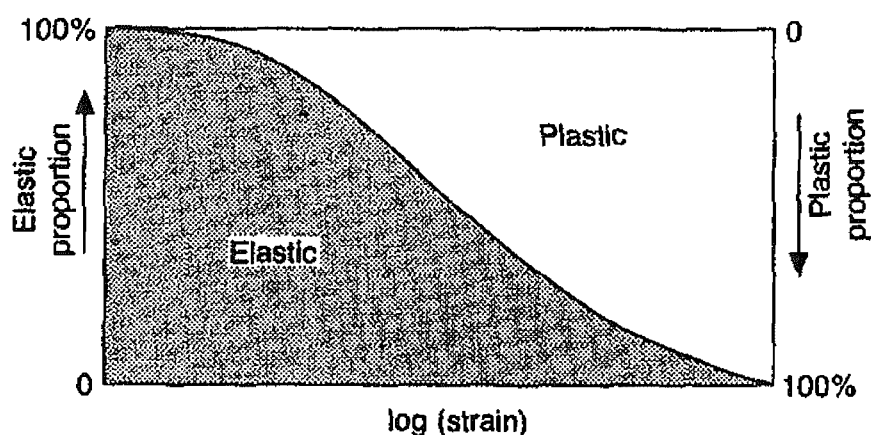


Figure 4.3: Proportions of elastic and plastic soil behaviour on the S-shaped curve (Simpson 1992).

Georgiannou et al (1991) measured the soil stiffness of several overconsolidated clays at very small strains using dynamic techniques. Figure 4.4, presented by Georgiannou et al (1991), shows that the typical stiffness-strain relationship for a monotonic loading path at any particular strain, with G being the tangent shear modulus, could be divided into three different strain regions which correspond to very small, small and larger strain levels. The shear strains dividing each zone are approximately 0.001% and 1% respectively. The importance of the very small to small strain region is pronounced; Jardine, Potts, Fourie and Burland (1986) found that in footings and excavations, the small strain characteristics appear to have the greatest influence on the deflection profiles around a loaded boundary, while Burland (1989) showed that the strains around many geotechnical structures are usually within this range.

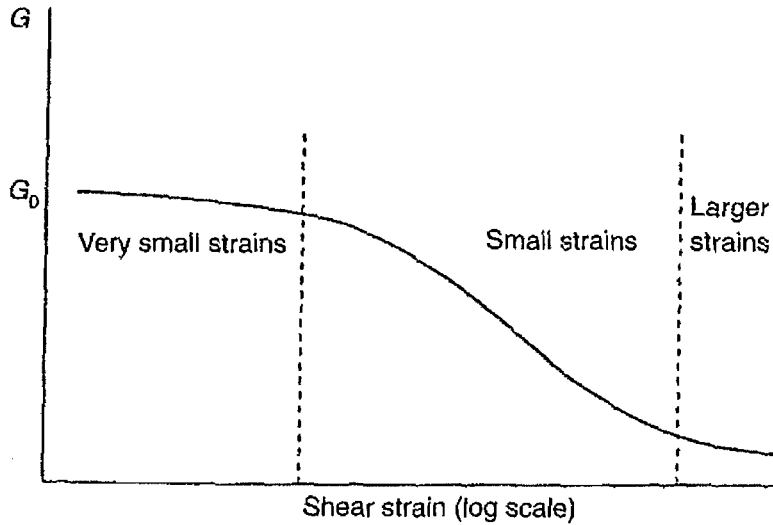


Figure 4.4: Typical shear stiffness-shear strain curve (Georgiannou et al,1991).

At the range of very small strains, strains may be considered as recoverable and elastic (Atkinson and Salfors, 1991) and the soil stiffness is proportional to $\sqrt{p_o'}$, while at small to large stains G is proportional to p_o' . This agrees with previous work for sands carried out by Wroth and Houlsby (1985), who related G to the mean effective stress p' by Equation (4.1)

$$G / p_r = A (p' / p_r)^n \quad (4.1)$$

where p_r is a reference pressure of 1 kPa, used to make Equation (4.1) dimensionless, and A and n are material parameters (constants) in the very small strain region. At the range of larger strains, strains are irrecoverable and may be considered as inelastic and A and n are not constants but will depend on the strain level and the stress path. Wroth et al (1979) found from experimental data that n is equal to 0.5 at small strains and increases to unity at large strains, while A decreased to zero. Allman and Atkinson (1992) investigated the basic behaviour of Bothkennar soil by drained and undrained triaxial tests. They rewrote Equation (4.2) between the shear stiffness and the initial mean effective stress in the form of Equation (4.3)

$$G = A p_o'^n \quad (4.2)$$

$$\ln G = \ln A + n \ln p_o' \quad (4.3)$$

where the parameters A and n depend on the soil, the overconsolidation ratio and the strain level. Their results from drained and undrained tests on normally consolidated samples are shown in Figure 4.5, where $\ln G$ is plotted against $\ln p_o'$ for strain levels from 0.01% to 1%. The parameter n was again found to vary from 0.5 at small strains to unity at larger strains.

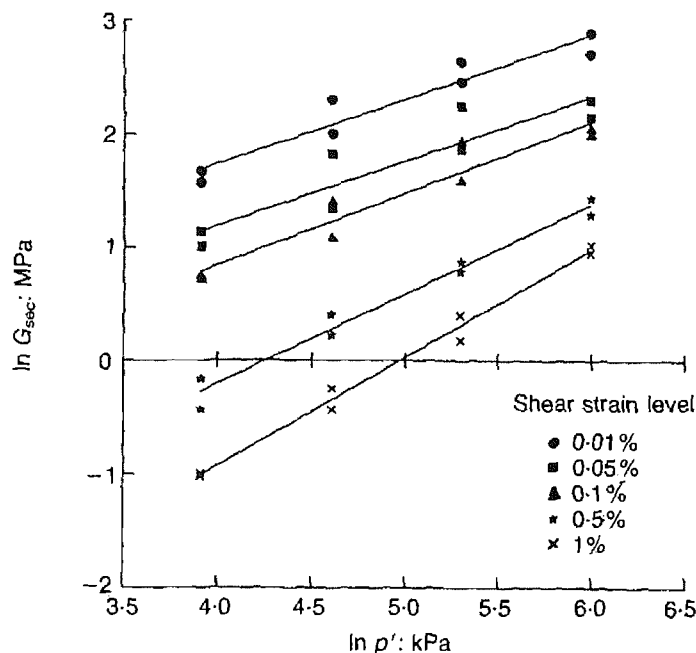


Figure 4.5: Variation of stiffness with initial effective stress and strain for normally consolidated samples (Allman and Atkinson 1992).

The soil consolidation history can be represented by the overconsolidation ratio OCR , and the soil stress-strain relationship is considered to be particularly dependent on it. Jardine, Symes and Burland (1984) found that the strain required to achieve peak strength steadily increased with increasing OCR , as shown in Figure 4.6, where R1, R1.4, R2, R4, R8 represent reconstituted samples of North Sea clay with OCR increasing from sample R1 to R8. Figure 4.7 shows that the normalised secant stiffness E_u / c_u at 0.01% axial strain is higher for lightly overconsolidated test conditions (e.g. tests R1 and R1.4), while it is lower for heavily overconsolidated conditions (e.g. test I3). In this figure, I1, I2, I3 and RM1, RM2 correspond to intact and remoulded samples respectively of North Sea clay, LC1, LC2 represent intact samples of London clay, HRS1, HRS2 are pluviated samples of Ham river sand and C1, C2 are intact samples of upper chalk. However, these results could be influenced by the different values of c_u for each test and the dependence

of c_u on other parameters, such as stress history, sample disturbance and soil microfabric. The initial mean effective stress p_o' may be a more appropriate parameter to normalise the secant stiffness, since it can be measured in the laboratory quite accurately. In Figure 4.8, E_u which is normalized with respect to p_o' , is plotted against OCR for several test conditions. In this case, the difference between the lightly and heavily overconsolidated samples is less pronounced.

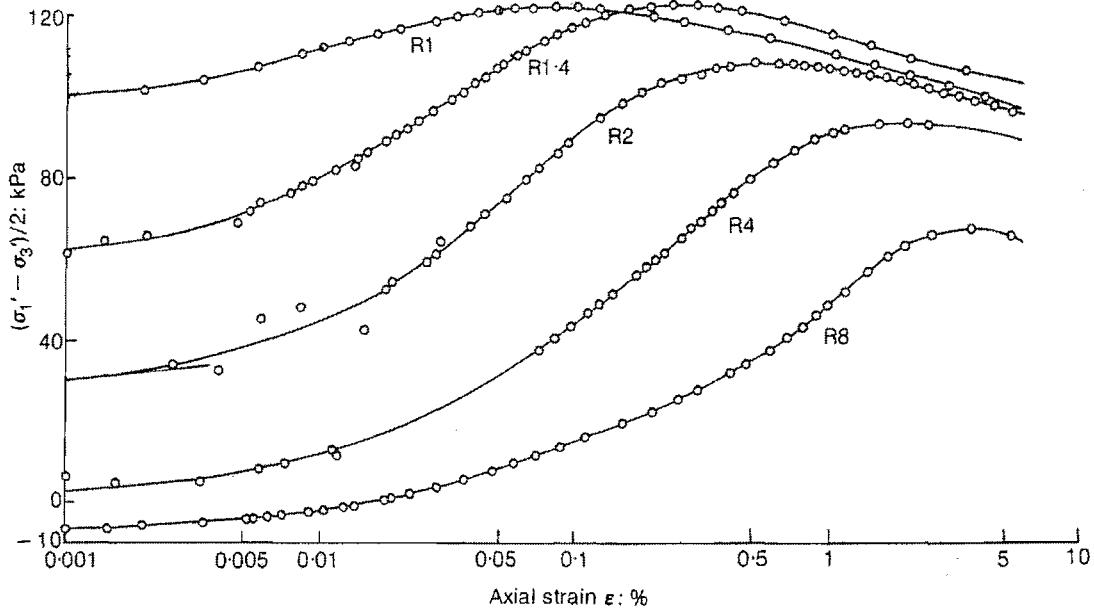


Figure 4.6: Stress-strain data for reconstituted samples of North Sea clay with OCR increasing from sample R1 to R8 (Jardine, Symes and Burland, 1984).

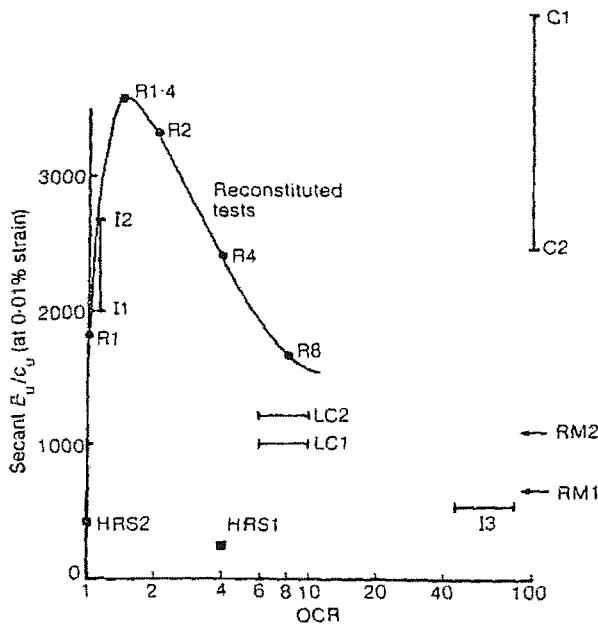


Figure 4.7: Variation of normalized secant axial stiffness with overconsolidation ratio for undrained triaxial tests on different soil samples (Jardine, Symes and Burland, 1984).

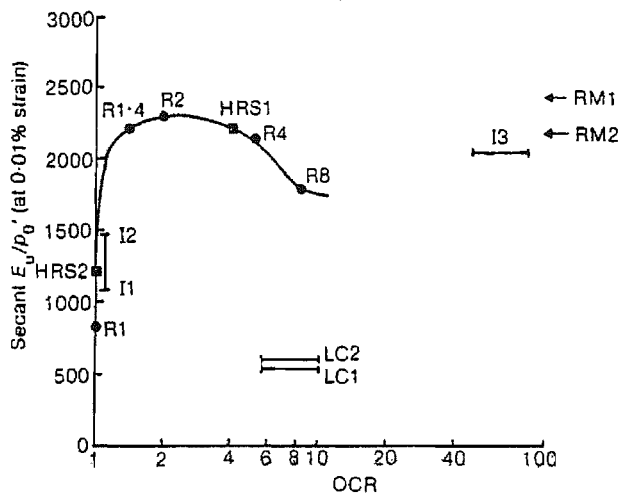


Figure 4.8: Variation of normalized secant axial stiffness with overconsolidation ratio for undrained triaxial tests on different soil samples (Jardine, Symes and Burland, 1984).

The results from drained and undrained tests on Bothkennar soil obtained by Allman and Atkinson (1992) show a similar trend. Figures 4.9 and 4.10 depict the variation of the normalised secant shear modulus G_{sec} / p_o' with shear strain for different overconsolidation ratios (expressed as R_p on the graphs).

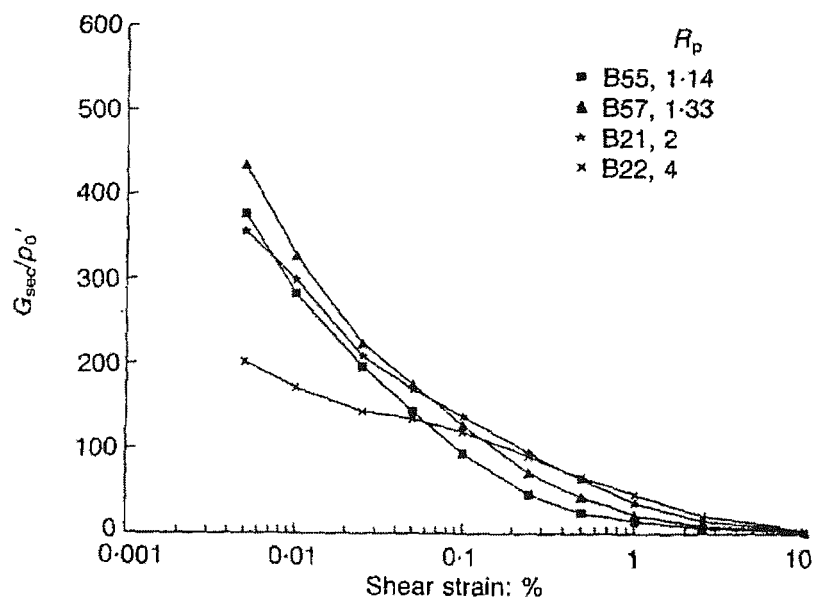


Figure 4.9: Normalised secant stiffness against shear strain for samples with different overconsolidation ratios in drained triaxial tests (Allman and Atkinson 1992).

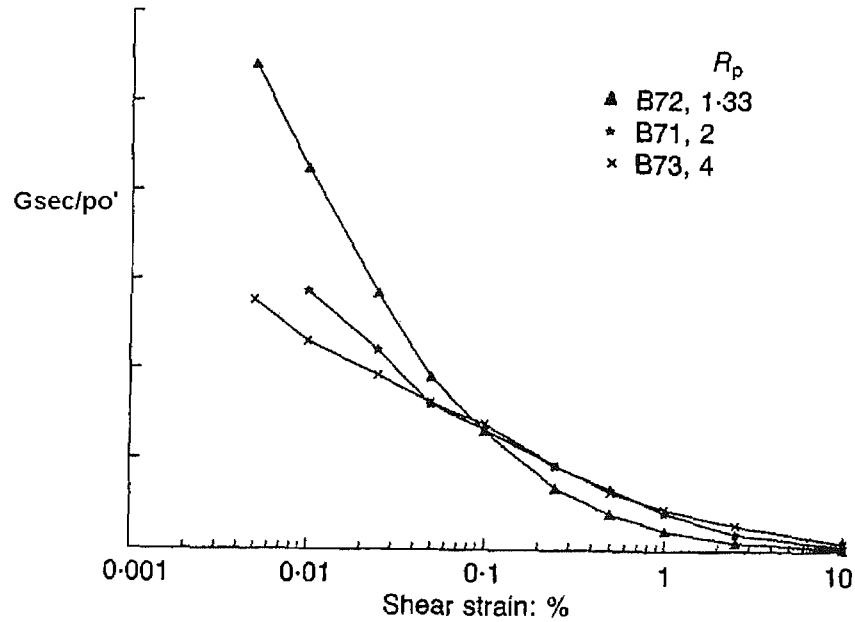


Figure 4.10: Normalised secant stiffness against shear strain for samples with different overconsolidation ratios in undrained triaxial tests (Allman and Atkinson 1992).

Viggiani and Atkinson (1995) suggested that the relationship between the initial tangent shear modulus G_0 and the overconsolidation ratio is given by Equation (4.4)

$$G_0 / p_r = A_0 (p' / p_r)^{n_0} (OCR)^m \quad (4.4)$$

where A_0 , n_0 and m are parameters related to the soil plasticity.

Atkinson, Richardson and Stallebrass (1990) investigated the effects of recent loading on the stiffness of overconsolidated soil by means of triaxial tests on reconstituted samples of London Clay. They suggested that the recent loading of a soil might consist of a relatively long period of time at constant stress state or a sudden change in the direction of the stress path and used the term “recent stress history” to describe both. Richardson (1988) found that stiffness increased logarithmically with time spent at constant stress, independently of any changes in stress path direction; therefore, these effects can be additive. Figure 4.11 shows the different stress paths followed at constant mean effective stress p' or constant deviatoric stress q , during triaxial tests carried out by Atkinson, Richardson and Stallebrass (1990). The samples had been brought to stress state O along

different stress paths from stress states P, Q, R or S, before they were loaded drained along stress paths OA or AB. The change in the direction of the stress path is denoted in Figure 4.11 by the symbol θ , which can take positive or negative values. Stress paths OA represented a change in q with constant p' ; stress paths OB represented a change in p' with $\Delta q = 0$.

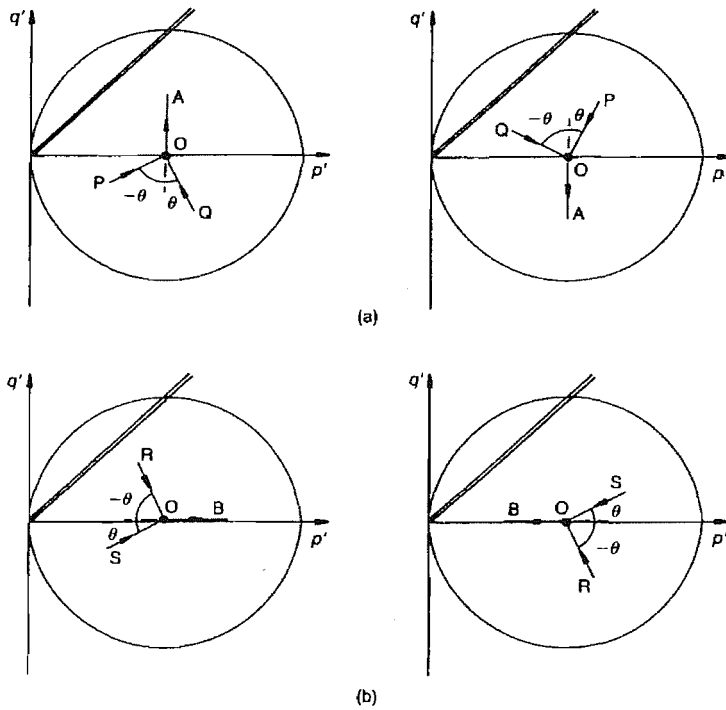


Figure 4.11: Different stress paths for triaxial tests at (a) constant p' (b) constant q (Atkinson, Richardson and Stallebrass 1990).

In Figure 4.12 $d q / d \epsilon_s$, which corresponds to $3 G_{tan}$, is plotted against shear strain for different rotations of the direction of initial stress path. The influence of the change in the stress paths on stiffness is obvious, especially at small strains. At 0.01% strain level the stiffness for $\theta = 180^\circ$ is approximately an order of magnitude larger than the stiffness for $\theta = 0^\circ$, while at 0.5% strain level there is almost no difference. Figure 4.13 illustrates the variation of $3 G_{tan}$ with the rotation of the stress path measured in constant p' tests for two stages of loading. At the beginning of the loading, when $q / p_o' = 0.05$, a significant increase of stiffness is noticed as the change in direction of the stress path varies from $\theta = 0^\circ$ to $\theta = 180^\circ$. During the second stage of loading, when $q / p_o' = 0.40$, the corresponding change in stiffness is very small.

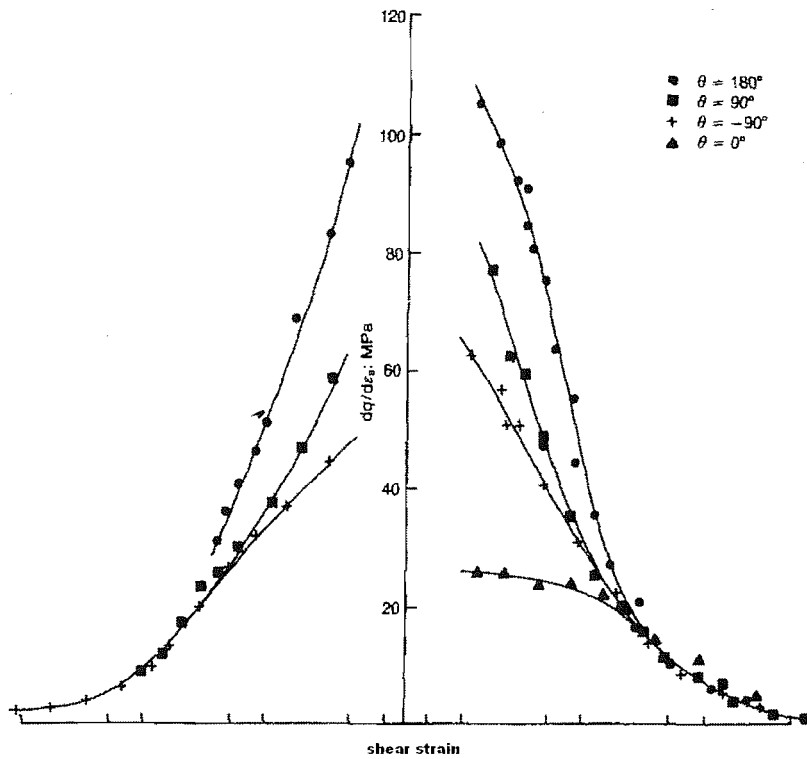


Figure 4.12: Shear stiffness of reconstituted London clay samples from triaxial constant p' tests (Atkinson, Richardson and Stallebrass 1990).

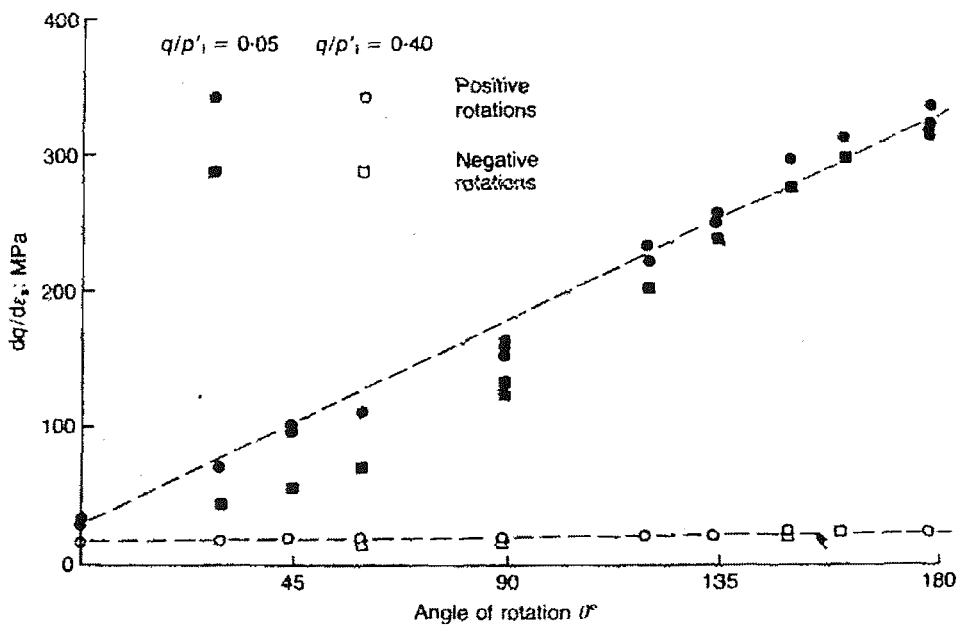


Figure 4.13: Variation of shear stiffness of reconstituted London clay samples with stress path rotation in triaxial constant p' tests (Atkinson, Richardson and Stallebrass 1990).

Powrie, Pantelidou and Stallebrass (1998) investigated the stress-strain relationship of clay soils appropriate to diaphragm walls by carrying out triaxial tests on samples of speswhite kaolin. Their results emphasize the importance of recent stress history during wall installation on the soil behaviour during excavation, which was found to be outside the influence of the soil geological or prewall-installation history. They suggested that during wall installation a reversal in the direction of the stress path in the soil behind the wall can result in a stiff response during excavation. For the soil in front of the wall, the change in the stress path direction during wall installation was smaller, resulting in a significantly less stiff response during excavation in comparison with the retained soil. Figure 4.14 shows the normalised stiffness G / p_o' plotted against triaxial shear strain for elements K5, K7, K8, M1A, NK1 in front the wall and KA1 behind the wall.

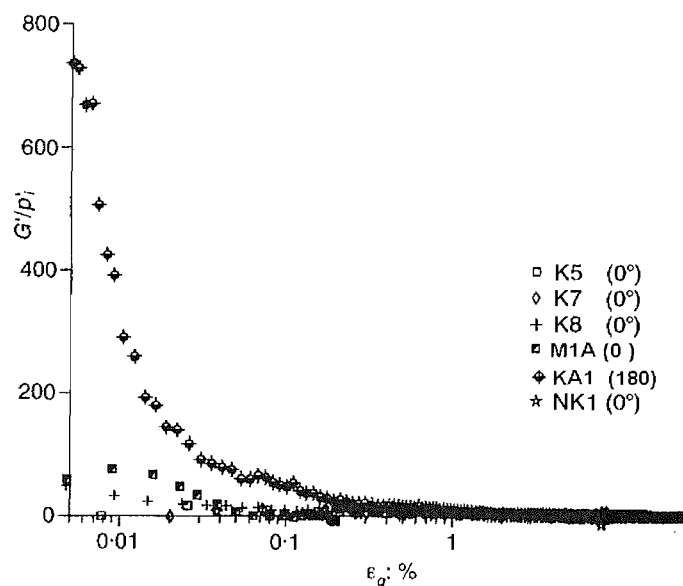


Figure 4.14: Normalised shear stiffness against triaxial shear strain for different total stress path rotations (Powrie, Pantelidou & Stallebrass, 1998).

Additionally, ageing or creep can affect soil stiffness. Allman and Atkinson (1992) plotted the variation of the normalized secant shear modulus G_{sec} / p_o' against shear strain for normally consolidated samples of Bothkennar clay that had been allowed different periods of rest before shearing. In Figure 4.15 sample B49 was sheared immediately, while samples B33 and B70 were sheared after 20 and 200 hours respectively. Sample B49 showed significantly lower stiffness than the other two samples. Allman and Atkinson (1992) noticed that the stress-strain behaviour of samples sheared after periods of rest was similar to that for a lightly overconsolidated soil.

Therefore, they suggested that the effects of creep or ageing might be equivalent to overconsolidation, at least for short periods of ageing.

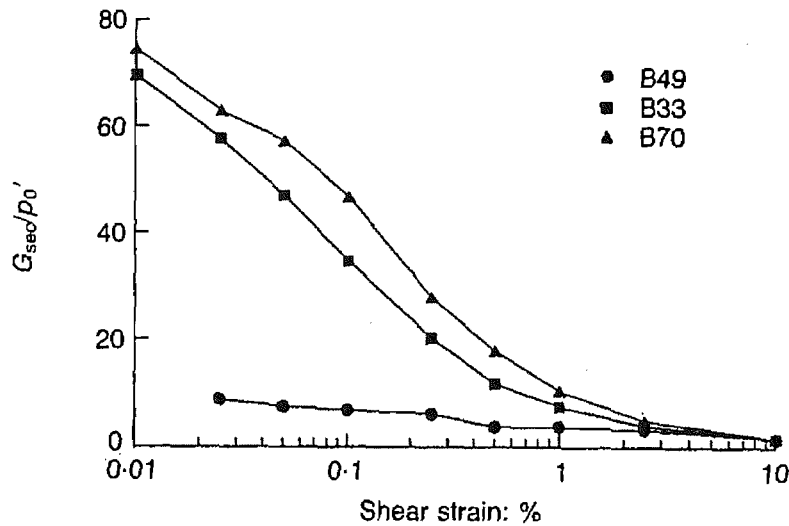


Figure 4.15: The effect of ageing on normalized secant shear stiffness of normally consolidated samples (Allman and Atkinson 1992).

It becomes obvious from the results of previous studies, as presented above, that the soil stress-strain relationship is rather complicated and depends on various parameters. The influence of even one parameter on soil stiffness may be difficult to evaluate accurately, due to the interaction with other parameters. Therefore, the values for each parameter should be selected carefully, allowing for possible uncertainty.

4.2.2 Theoretical modeling of soil behaviour

Roscoe and Schofield (1963) introduced a state boundary surface in stress space which embodies yield and is based on the concept of critical states. This model, which is known as Cam Clay, is shown in Figure 4.17. The yield locus is given by Equation (4.5) and separates elastic states inside the surface from elasto-plastic states on the boundary for a soil effectively preconsolidated isotropically to an average effective stress of p_o' . The value of p_o' defines the size of the state boundary surface. More details can be found in Schofield and Wroth (1968).

$$q / M p' + \ln (p' / p_o') = 0 \quad (4.5)$$

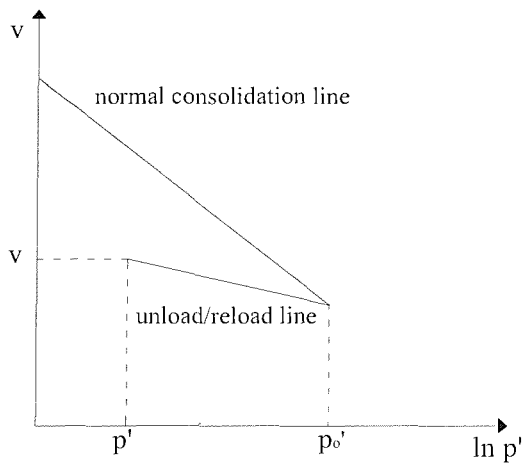


Figure 4.16: Current state and isotropic consolidation history.

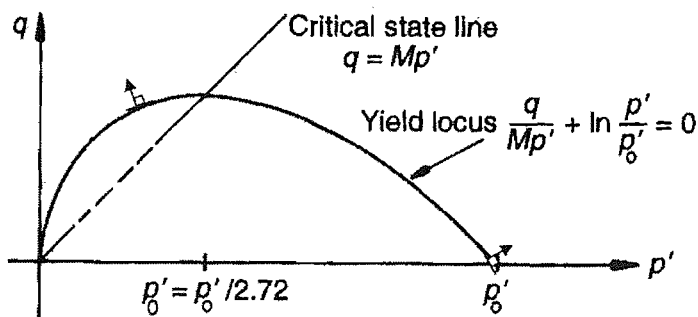


Figure 4.17: Cam Clay model (Osman, 2004).

Roscoe and Burland (1968) proposed a revised form of this model, known as Modified Cam Clay (Figure 4.18). In the yield locus expression, η stands for the stress ratio q / p' . In Figures 4.16 and 4.17 the vectors indicate the direction of the plastic strain increments.

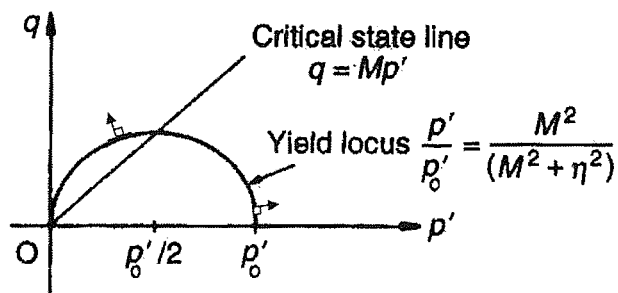


Figure 4.18: Modified Cam Clay model (Osman, 2004).

Al Tabaa (1987) and Al Tabaa and Wood (1989) introduced the “bubble” model using a single kinematic surface within the Modified Cam Clay state boundary surface. Stallebrass and Taylor (1997), based on the concept of multiple kinematic yield surfaces introduced by Mroz, Norris and Zienkiewicz (1979), employed three kinematic surfaces to take account of both the effect of recent stress history and yield at small strains or changes in stress. Simpson (1992) developed a brick analogue, known as the “brick model”, to simulate the effect of non-linearity and recent stress history.

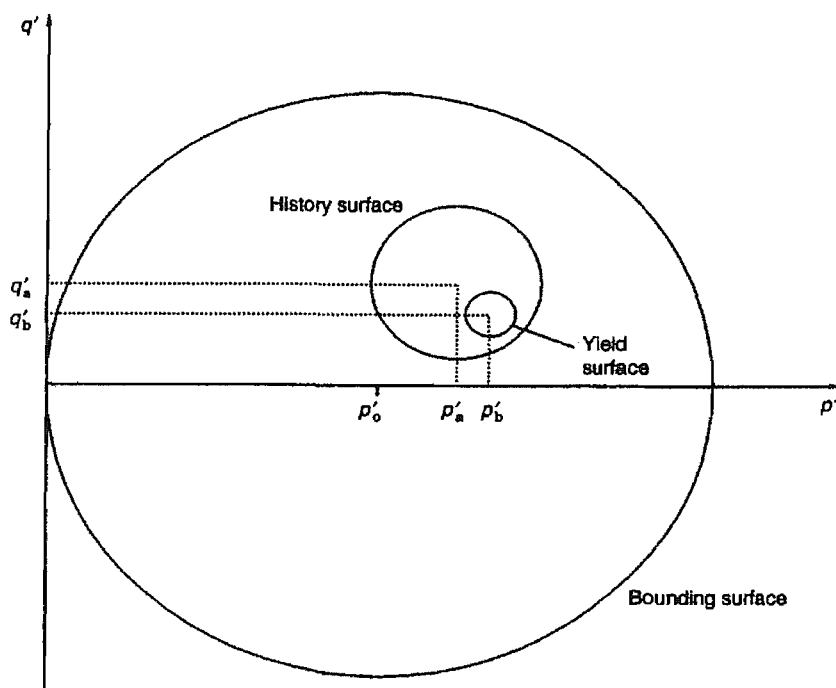


Figure 4.19: Soil model with three kinematic yield surfaces in triaxial stress space (Stallebrass and Taylor, 1997).

Jardine (1992) using a different experimental approach, observed two zones of behaviour in normalised stress space within a bounding yield surface which can be repositioned and modified if the soil is subjected to different stress histories.

Despite developments in theoretical soil modeling, soil behaviour still remains difficult to simulate accurately with a single constitutive model. Some of the models are complex, have many parameters and the calibration of their values may be difficult. In addition, some models are inherently fitted to a certain sample preparation procedure and testing process (e.g. during isotropic compression the triaxial shear strain is defined at constant confining pressure); this factor should be taken into consideration when such soil models are used. Therefore, a simple soil model that takes account of the soil inelasticity and its input parameters could be easily determined would be a useful design tool; such a soil model is used to represent the soil stress-strain behaviour in this thesis since it is consistent with the objective of achieving a practical and reasonably accurate solution and is presented in the next Section. Other simple soil models (e.g. power law) may also be incorporated in the method developed herein.

4.2.3 Hyperbolic stress-strain relationship

Duncan and Cheng (1970) proposed a simplified, practical relationship for representing the non-linear, inelastic and stress dependent behaviour of soils. The simplicity of the relationship derives from the relatively straightforward determination of the required parameters from laboratory triaxial tests. It is adopted in this project since it contributes to the objective of a practical design solution. According to this approach, the non-linear stress-strain relationship may be approximated by the hyperbolic equation proposed by Kodner (1963)

$$(\sigma_1 - \sigma_3) = \varepsilon / (a + b \varepsilon) \quad (4.6)$$

where σ_1 and σ_3 are the major and minor principal stresses respectively, ε is the axial strain and a and b are constants which can be derived from experimental data. In Figure 4.20 where the hyperbolic Equation (4.6) is plotted, the physical meaning of constants a and b is illustrated. The constant a is the reciprocal of the initial tangent Young's modulus E_i and the constant b is the reciprocal of the asymptotic value of stress difference, $(\sigma_1 - \sigma_3)_{ult}$, which the stress-strain curve approaches at infinite strain. Equation (4.6) can be written in the form of Equation (4.7):

$$\varepsilon / (\sigma_1 - \sigma_3) = a + b \varepsilon \quad (4.7)$$

The values of the constants a and b may be derived from triaxial test results and can be fitted to the plot of Equation (4.7) on transformed axes as shown in Figure 4.21, where a is the intercept and b is the slope of the straight line.

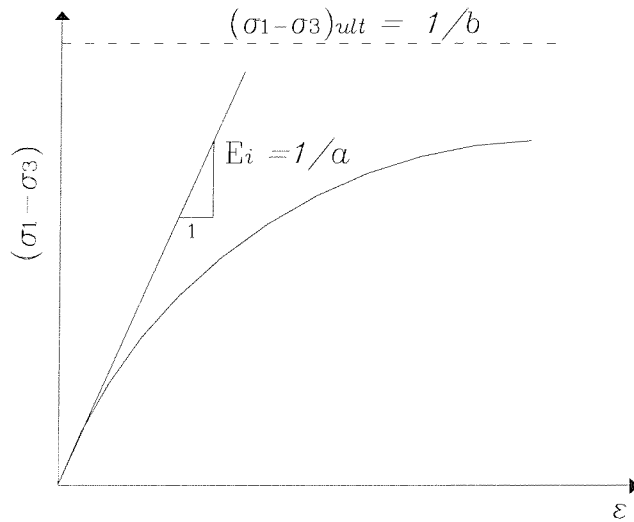


Figure 4.20: Hyperbolic stress-strain curve.

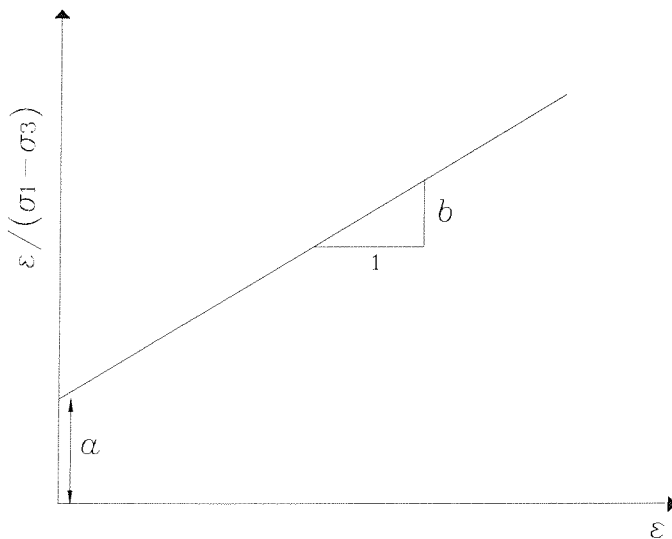


Figure 4.21: Transformed hyperbolic stress-strain curve.

The stress difference in the soil $(\sigma_1 - \sigma_3)$ at failure is usually found to be slightly less than its asymptotic value $(\sigma_1 - \sigma_3)_{ult}$ at infinite strain and a factor R_f can be used to relate them in Equation (4.8):

$$(\sigma_1 - \sigma_3)_f = R_f(\sigma_1 - \sigma_3)_{ult} \quad (4.8)$$

Duncan and Cheng (1970) found that factor R_f is generally in the range of 0.75 to 1.00 and is independent of the confining pressure σ_3 . They derived an expression for the tangent Young's modulus in terms of stresses

$$E_t = [1 - R_f(1 - \sin\phi) (\sigma_1 - \sigma_3) / (2c \cos\phi + 2\sigma_3 \sin\phi)]^2 K p_a (\sigma_3 / p_a)^n \quad (4.9)$$

where c is the true cohesion, ϕ is the effective friction angle, σ_3 is the confining pressure, p_a is the atmospheric pressure expressed in the same pressure units as E_t and σ_3 , K is a dimensionless modulus number and n is an exponent determining the rate of variation of the initial tangent Young's modulus E_i with σ_3 . The analytical calculations are presented in the Appendix. The advantage of equation (4.9) is that it facilitates the determination of the tangent Young's modulus for any stress condition if data from triaxial tests are available. However, it was assumed that the soil might be characterised by a single constant value of Poisson's ratio and the volume changes were not related to shear stresses.

It may be argued that the dilation of the soil due to shearing might be less significant than the dilation due to soil consolidation. Therefore, the approximation of zero volumetric strains may be allowed. In reality, pure volumetric strains might occur; these could be super imposed in the kinematic mechanism presented in this thesis assuming that they might not cause additional shear. The hyperbolic Equation (4.6), which relates the total principal stresses to axial strain, can then be transformed into the hyperbolic Equation (4.10) to relate the shear stress τ to shear strain γ :

$$\tau = (\gamma / 3) / (a + b \gamma / 1.5) \quad (4.10)$$

In Equation (4.10) the parameters a and b are related to the initial shear modulus G_i and the shear stresses at failure τ_f and at infinite strain τ_{ult} respectively by appropriate substitutions. The shear modulus G_i is related to the Young's modulus by the expression

$$G = E / [2(1 + \nu)] \quad (4.11)$$

where ν is the Poisson's ratio. The shear stresses at failure τ_f are related to those at infinite strain τ_{ult} by the parameter R_f :

$$R_f = \tau_f / \tau_{ult} \quad (4.12)$$

Therefore the parameters a and b in equation (4.10) may be defined as:

$$a = 1 / E_i = 1 / [2 G_i (1 + \nu)] \quad (4.13)$$

$$b = 1 / (\sigma_1 - \sigma_3)_{ult} = R_f / (\sigma_1 - \sigma_3)_f = R_f / (2 \tau_f) \quad (4.14)$$

Following the necessary substitutions and calculations as presented in Appendix A, the tangent shear modulus G for drained conditions may be represented by an Equation similar to Equation (4.9) in the form

$$G_{tan} = [1 - R_f \tau (1 - \sin\phi) / (c \cos\phi + \sigma_3 \sin\phi)]^2 [G_i (1 + \nu) / 1.5] \quad (4.15)$$

where G_i is the initial tangent shear modulus. In relationships (4.13) and (4.15) a single value of Poisson's ratio has been chosen, $\nu=0.5$, in an effort to keep consistent with the assumptions followed by Duncan and Cheng (1970). The tangent shear modulus G_{tan} can then be calculated from equation (4.15) for any stress condition if data from triaxial tests are available.

4.2.4 Comparison with other soil models

In previous research, different stress-strain relationships have been adopted to represent non-linear soil behaviour. A comparison between some of these relationships and the hyperbolic relationship introduced by Duncan and Cheng (1970) is presented in this section to investigate the order of approximation when the simplified approach is adopted.

According to the generalized Hooke's law, a change in shear stress in an isotropic elastic material is related to the change in shear strain by Equation (4.16):

$$\delta\tau = G \delta\gamma \quad (4.16)$$

From Equations (4.10) and (4.16) and assuming that the Poisson's ratio is equal to 0.5 (constant volume conditions), the secant shear modulus is given by the relationship (4.17).

$$G_{sec} = 1 / (3 a + 2 b \gamma) \quad (4.17)$$

If $A_I = 3 a$ and $B_I = 2 b$, Equation (4.17) can be rewritten in the simpler form:

$$G_{sec} = 1 / (A_I + B_I \gamma) \quad (4.18)$$

Equation (4.18) is plotted in Figure 4.22 for the data presented in Table 4.1, which were obtained from triaxial tests on dense and loose silica sand carried out by Duncan and Cheng (1970) with constant confining pressure to examine whether it can provide a good approximation of the soil stiffness-strain behaviour in drained conditions.

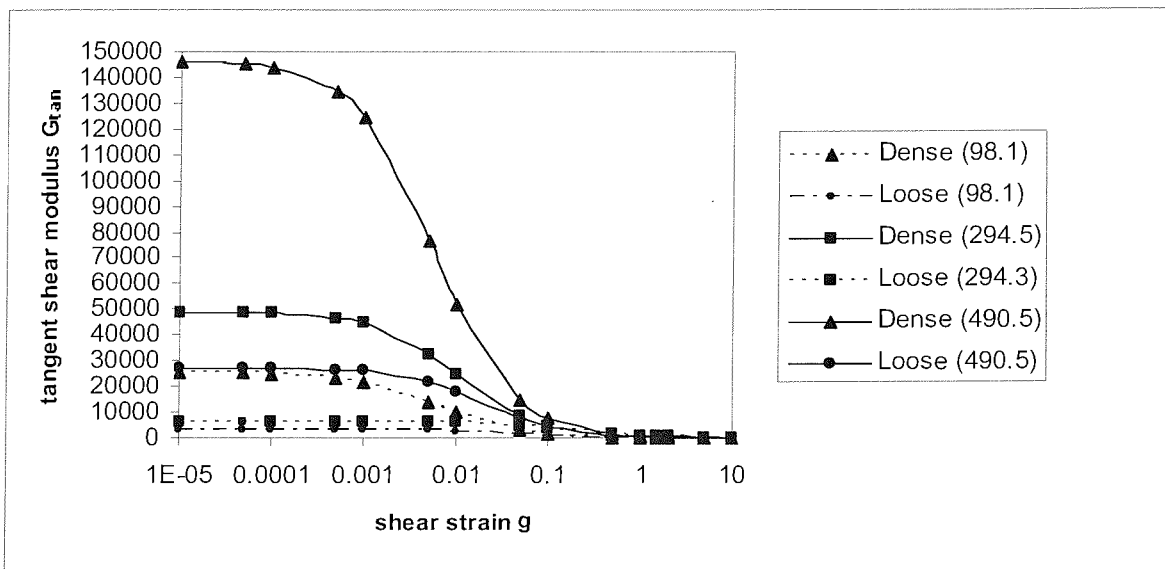


Figure 4.22: Shear modulus-shear strain curves for dense and loose fine silica sand at different confining pressures (in kN/m^2 . Data after Duncan and Cheng, 1970).

	Dense	Loose
D_r (Relative density)	100%	38%
R_f	0.91	0.90
K	2,000	295
n	0.54	0.65
σ_3 (KN/m ²)	• 98.1 • 294.3 • 490.5	• 98.1 • 294.3 • 490.5
a (m ² /KN)	• $1.315 \cdot 10^{-5}$ • $6.796 \cdot 10^{-6}$ • $2.273 \cdot 10^{-6}$	• $1.059 \cdot 10^{-4}$ • $5.097 \cdot 10^{-5}$ • $1.223 \cdot 10^{-5}$
b (m ² /KN)	• $3.092 \cdot 10^{-3}$ • $1.019 \cdot 10^{-3}$ • $6.178 \cdot 10^{-4}$	• $4.587 \cdot 10^{-3}$ • $3.202 \cdot 10^{-3}$ • $9.439 \cdot 10^{-4}$
$A_I=3a$	• $3.945 \cdot 10^{-5}$ • $2.039 \cdot 10^{-5}$ • $6.819 \cdot 10^{-6}$	• $3.177 \cdot 10^{-4}$ • $1.529 \cdot 10^{-4}$ • $3.669 \cdot 10^{-5}$
$B_I=2b$	• $6.184 \cdot 10^{-3}$ • $2.038 \cdot 10^{-3}$ • $1.236 \cdot 10^{-3}$	• $9.174 \cdot 10^{-3}$ • $6.405 \cdot 10^{-3}$ • $1.888 \cdot 10^{-3}$

Table 4.1: Triaxial tests on dense and loose silica sand carried out by Duncan and Cheng (1970).

To derive Equation (4.18), it was assumed that $\gamma = 1.5 \varepsilon_a$, where ε_a is the axial strain and γ is the shear strain, and the Poisson's ratio is equal to 0.5 which is valid for undrained conditions. For drained conditions, slightly different parameters of A_I and B_I may need to be applied. However, the shape of the diagram in Figure (4.22) is similar in shape to the S-shaped curve which is typically used to represent soil stiffness-strain relationship for a monotonic loading path (Figure 4.4). Therefore, the hyperbolic function may be used to characterize the soil stiffness-strain or mobilized shear strength-strain behaviour in drained conditions with acceptable accuracy. Its applicability to other types of soils will be investigated by fitting data from triaxial tests carried out in previous research studies to the hyperbolic Equation (4.18) and comparing the results.

Jardine, Symes and Burland (1984) presented the results of undrained triaxial tests on reconstituted and intact soil samples with different overconsolidation ratios and initial mean effective stresses and determined the axial stiffness by measurements of the local axial strain. The shear modulus G is related to the axial strain ε_a and Young's modulus E by Equation (4.11), whereas ε_a is related to γ by Equation (4.19)

$$\gamma = 1/2 (3 \varepsilon_a - \varepsilon_{vol}) \quad (4.19)$$

where ε_{vol} is the volumetric strain. In an undrained triaxial test $\varepsilon_{vol} = 0$; hence, $\gamma = 1.5 \varepsilon_a$. Jardine, Symes and Burland (1984) measured the secant Young's modulus E_{sec} ; this is related to the secant shear modulus G_{sec} by Equation (4.11), taking the Poisson's ratio ν equal to 0.5. Some of their results have been fitted to Equation (4.18) and are plotted in Figure 4.23. In Table 4.2 some of the parameters employed in their tests together with the values of A_I and B_I , which appear in Equation (4.18), are presented.

Tests	R ₁	R ₂	I ₁	I ₂	LC ₁	LC ₂
Material	North Sea clay	North Sea clay	North Sea clay	North Sea clay	London clay	London clay
Sample preparation	Reconstituted	Reconstituted	intact	intact	intact	intact
OCR	1.0	2.05	1.1	1.1	-	-
p_o' (KN/m ²)	267	158	474	508	226	199
τ (KN/m ²)	122	108	255	275	123	100
A_I (m ² /KN)	1.540 10 ⁻⁵	8.390 10 ⁻⁶	4.810 10 ⁻⁶	3.961 10 ⁻⁶	2.103 10 ⁻⁵	1.760 10 ⁻⁵
B_I (m ² /KN)	7.787 10 ⁻³	8.800 10 ⁻³	3.730 10 ⁻³	3.450 10 ⁻³	7.720 10 ⁻³	9.501 10 ⁻³

Table 4.2: Summary of some of the triaxial tests carried out by Jardine, Symes and Burland (1984).

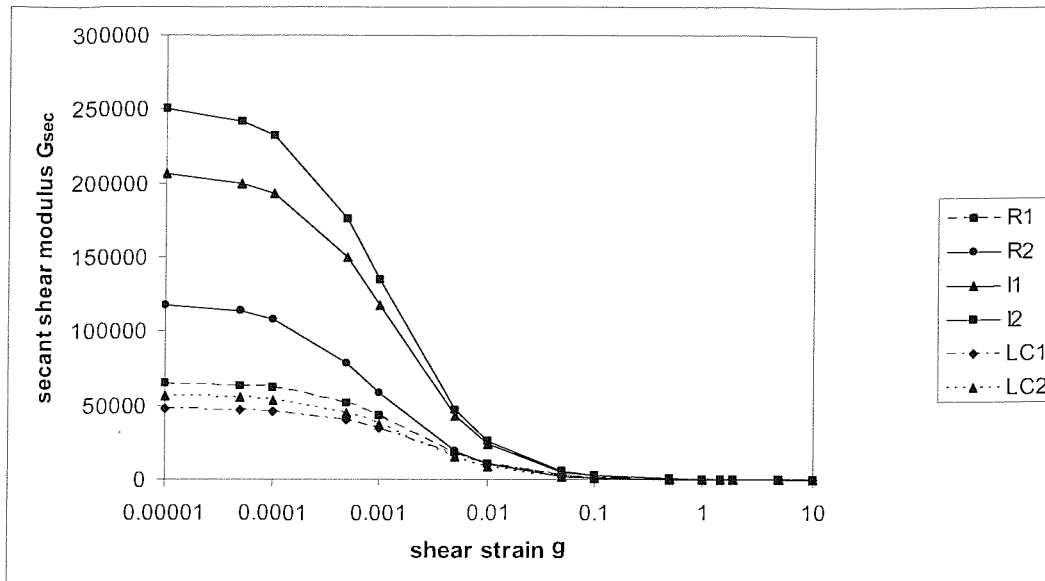


Figure 4.23: Secant shear modulus-shear strain curves clays at different initial mean effective stresses (p_o') and overconsolidation ratios (OCR) as indicated in Table 4.2 (Data after Jardine, Symes and Burland, 1984)

In Tables 4.3 the results of drained and undrained triaxial tests on Bothkennar soil are presented. The tests were carried out by Allman and Atkinson (1992) on one-dimensionally normally consolidated and lightly overconsolidated samples, which were reconstituted from a slurry and compressed and swelled to different states. The drained tests were carried out with constant mean effective stress, p' , while the undrained tests were carried out with constant cell pressure σ_3' ; an external displacement transducer was used to measure the axial strains. The results shown in Table 4.4 were presented by Smith, Jardine and Hight (1992) from triaxial tests on undisturbed Laval and Sherbrooke samples of Bothkennar clay. Plots of the secant shear modulus G_{sec} and tangent shear modulus, G_t , normalized with respect to the mean effective stress at the start of shearing p_o' , against shear strain γ were produced. In order to evaluate the hyperbolic stress-strain relationship proposed by Duncan and Cheng (1970), all the results are fitted to Equation (4.18) and are plotted in Figures 4.24 and 4.25a&b. The values of the parameters A_l and B_l are indicated in Tables 4.3 and 4.4.

Tests	B ₅₅	B ₅₇	B ₇₃	B ₇₅
Material	Bothkennar clay	Bothkennar clay	Bothkennar clay	Bothkennar clay
Sample preparation	reconstituted	reconstituted	reconstituted	reconstituted
OCR	1.14	1.33	4.0	1.0
Loading	Compression	Compression	Compression	Compression
Drainage	Drained	Drained	Undrained	Undrained
p_o' (KN/m ²)	175	150	50	200
τ (KN/m ²)	115.06	99.75	38.16	144.7
A_1 (m ² /KN)	$1.520 \cdot 10^{-5}$	$1.543 \cdot 10^{-5}$	$7.520 \cdot 10^{-5}$	$6.410 \cdot 10^{-5}$
B_1 (m ² /KN)	$8.256 \cdot 10^{-3}$	$9.254 \cdot 10^{-3}$	$2.490 \cdot 10^{-2}$	$6.570 \cdot 10^{-3}$

Table 4.3: Summary of some of the triaxial tests carried out by Allman and Atkinson (1992).

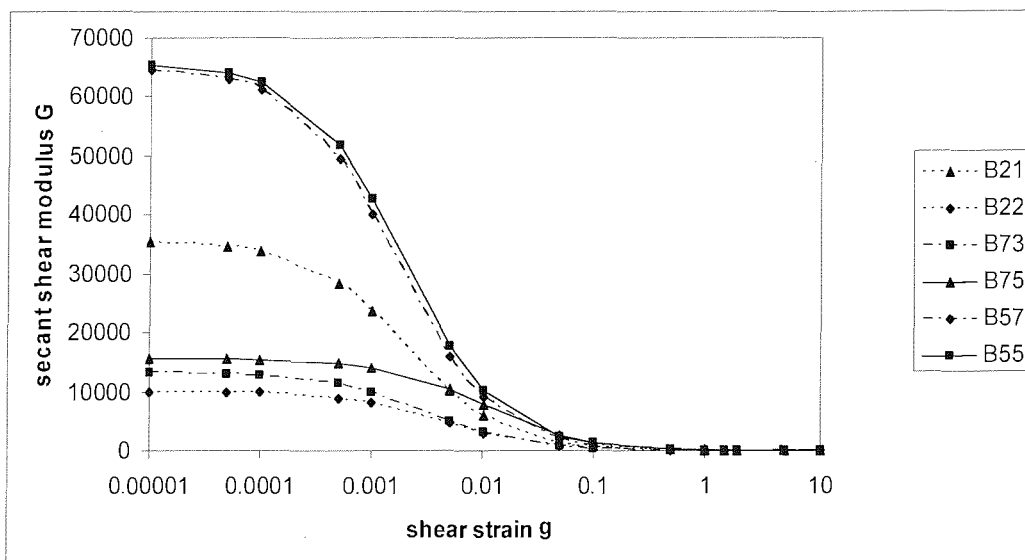


Figure 4.24: Secant shear modulus-shear strain curves for Bothkennar clay at different initial mean effective stresses (p_o') and overconsolidation ratios (OCR) as indicated in Table 4.3. (Data after Allman and Atkinson, 1992)

Tests	B ₅₅	B ₅₇
Material	Laval samples	Sherbrooke samples
Sample preparation	Undisturbed	Undisturbed
Drainage	Undrained	Undrained
p_o' (KN/m ²)	34	35.67
τ (KN/m ²)	25.89	31.57
B_I (m ² /KN)	$3.670 \cdot 10^{-2}$	$3.009 \cdot 10^{-2}$
A_I (m ² /KN) (for G_{sec})	$5.882 \cdot 10^{-5}$	$5.610 \cdot 10^{-5}$
A_I (m ² /KN) (for G_I)	$6.077 \cdot 10^{-5}$	$5.792 \cdot 10^{-5}$

Table 4.4: Summary of some of the triaxial tests for the characterization of Bothkennar clay (Smith, Jardine and Hight ,1992).

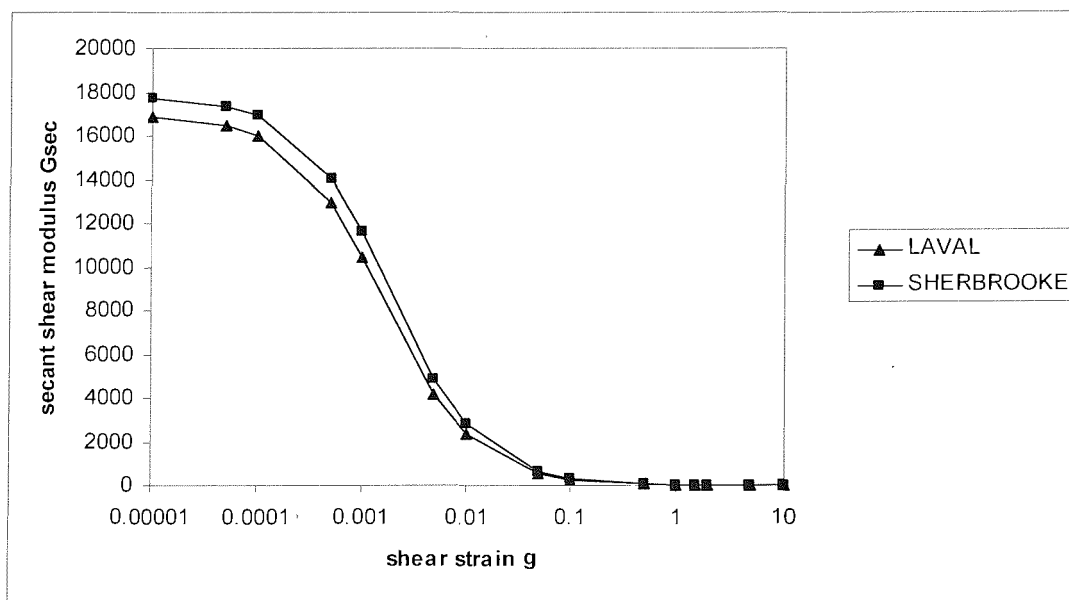


Figure 4.25a: Secant shear modulus-shear strain curves for undisturbed Laval and Sherbrooke samples of Bothkennar clay. (Data after Smith, Jardine and Hight ,1992)

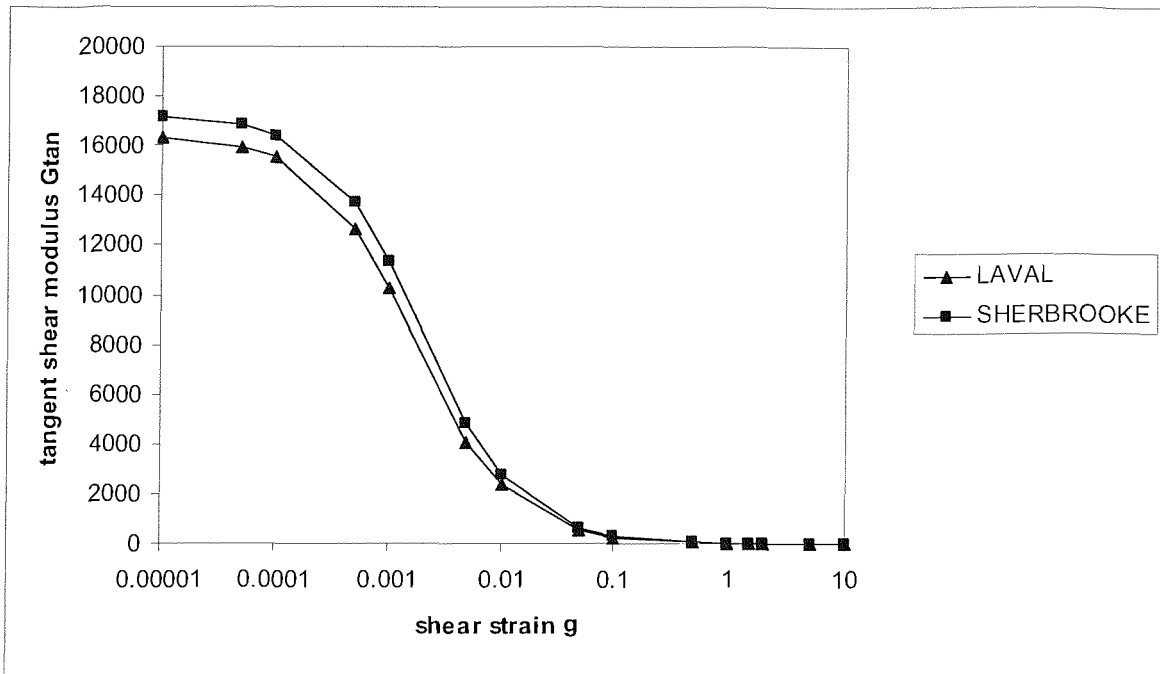


Figure 4.25b: Tangent shear modulus-shear strain curves for undisturbed Laval and Sherbrooke samples of Bothkennar clay. (Data after Smith, Jardine and Hight ,1992)

From Figures 4.22, 4.23, 4.24 and 4.25a&b the initial shear modulus at small strains is high. The shear modulus then decreases, following an S-shaped curve, to approximately zero at large strains. The shape of the diagram is similar for different types of soil, different sampling procedures and consolidation history as indicated by Tables 4.2, 4.3 and 4.4 and is in agreement with the results of more recent research work on the soil stiffness – strain behaviour, as discussed in the previous paragraph. Therefore, the hyperbolic Equation (4.18) may be used for a variety of soils with reasonable accuracy. In addition, Equation (4.18) has a relatively simple form and allows the determination of shear modulus for any stress condition if data from triaxial tests are available.

4.3 APPLICATION OF THE MSD METHOD TO FLEXIBLE WALLS

4.3.1 Assumptions

The mobilized strength method, described in Section 2.4, idealizes soil behaviour by means of simplified kinematically admissible strain fields. The active and passive soil zones are subdivided into triangles, the verticals and horizontals of which are frictionless displacement discontinuities, while the hypotenuse of each is a zero extension line. Mobilisation of a uniform shear strength is assumed which is consistent with the development of a uniform shear strain in each triangle. From a deformation geostructural mechanism, the mobilized strains are related to wall deformations.

According to the simplified geostructural mechanism, the maximum wall deflection will be at the toe of a rigid wall propped at the crest. However, flexible walls deform in a more complicated mode and the maximum wall deflection will possibly be close to dredge level. In this case, further kinematically admissible strain fields may be added to better represent the soil behaviour. Therefore, the active and passive soil zones are subdivided into a number of triangles as shown in Figure 4.26. The soil is divided in four zones behind the wall and two zones in front of the wall for the analysis presented in the thesis. In principle, the soil may be divided into more zones to achieve higher accuracy. The soil behind the wall and above the dredge level is divided into triangles OAE and AEK with heights equal to half the retained height, $h / 2$ and triangles BOF and BFJ with heights equal to the retained height, h . The soil behind the wall and below the dredge level is divided into triangles OPC and PCI, with heights equal to $h + d / 2$, where d is the penetration depth, and triangles ODG and DGH with heights equal to the overall height, $h + d$. For the soil in front of the wall two deforming triangles, FPL and LPN, are assumed with heights equal to half the penetration depth, $d / 2$ and two deforming triangles, FMG and MGQ, with heights equal to the penetration depth, d .

The triangles are free to slide on vertical and horizontal surfaces, which are assumed to be frictionless and can be attached to the surrounding rigid zones through zero extension lines. Zero extension lines are at 45° to the principal axes of strain, since the angle of dilation is taken as zero. The mobilised shear strength and the shear strain are assumed to

be uniform within each triangle. The use of additional kinematically admissible strain fields permits the incorporation of different mobilised shear strengths and hence mobilised strains in each zone of the soil surrounding the retaining wall. Strains can then be related to the wall deformations by a geostructural mechanism. The strain increment within a triangle should be consistent with the relative rotation of the same triangle and then the total strain is estimated by adding the strain increments of the adjacent triangles. The rotation of a triangle is related to the wall displacement by means of a geometrical relationship. The appropriate relationships, between the shear strains and the rotations, developed for each triangle will be presented later in this chapter.

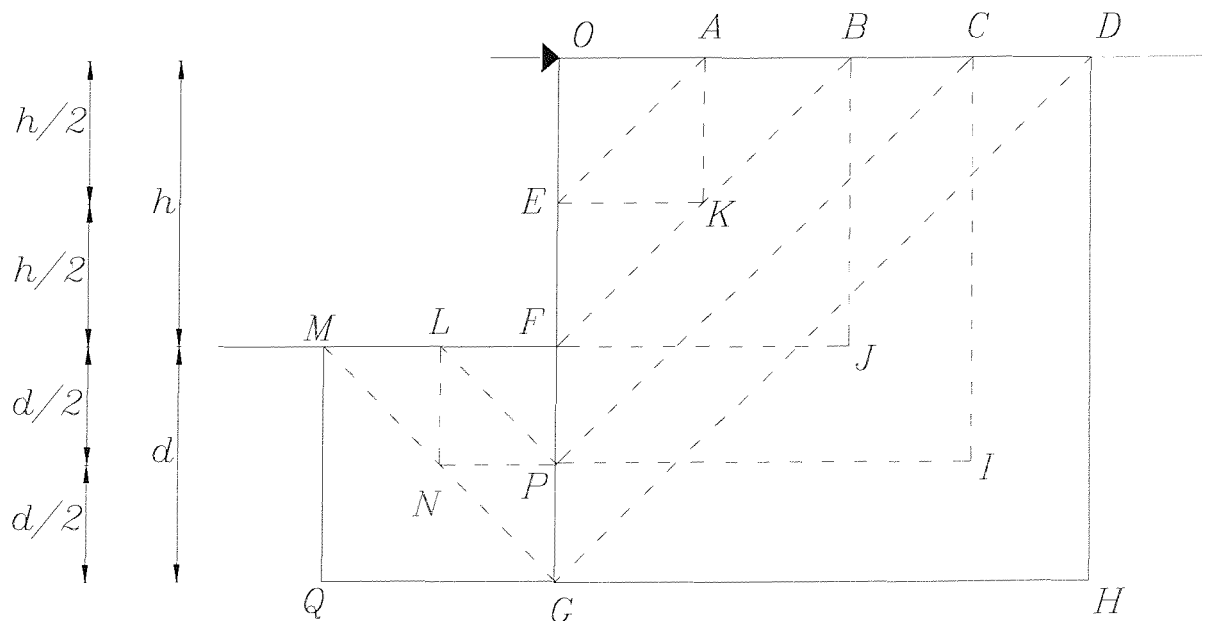


Figure 4.26: Admissible strain fields for a flexible retaining wall propped at the crest.

4.3.2 Wall rotations

Assuming that the wall movement takes place in four successive stages, then Figure 4.27 depicts the first stage, which consists of the movement of triangle OGD behind the wall to its new position OG'D' and of triangle FMG in front of the wall to its new position FM'G'.

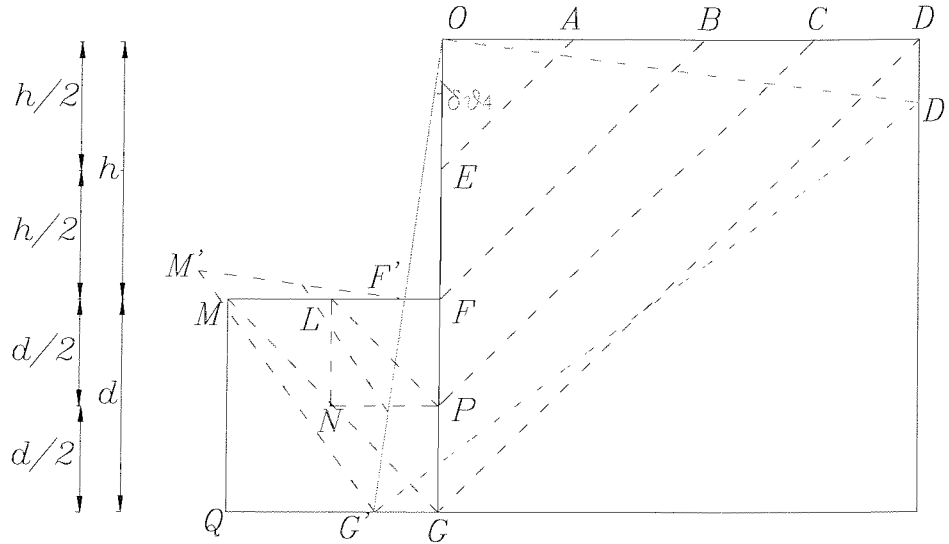


Figure 4.27: Stage 1 of the assumed wall movement – rotation of triangles ODG behind the wall and FMG in front of the wall.

The rotation of triangle ODG is $\delta\theta_4$ and its horizontal $\delta u_{(ODG)}$ and vertical $\delta v_{(ODG)}$ movements, taking compression positive, are:

$$\delta u_{(ODG)} = -\delta\theta_4 (h+d) \quad (4.20)$$

$$\delta v_{(ODG)} = \delta\theta_4 (h+d) \quad (4.21)$$

Therefore, the increments in horizontal (u) and vertical (v) strains are:

$$\delta\varepsilon_{u(ODG)} = \delta u_{(ODG)} / (h+d) = -\delta\theta_4 \quad (4.22)$$

$$\delta\varepsilon_{v(ODG)} = \delta v_{(ODG)} / (h+d) = \delta\theta_4 \quad (4.23)$$

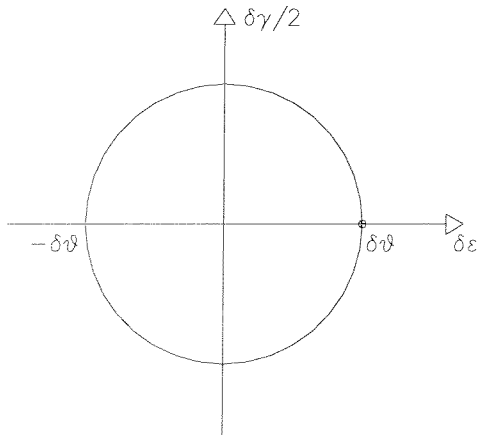


Figure 4.28: Mohr circle of strain increments.

Inward rotation would cause the signs of the vertical and horizontal strain increments to reverse. If $\delta\gamma$ is the shear strain increment, then from the Mohr circle of strain increments in Figure 4.28:

$$\delta\gamma_4 = 2 \delta\theta_4 \quad (4.24)$$

Triangle MFG in front of the wall will be compressed and the horizontal and vertical strain increments within it are related to the rotation of triangle ODG by Equation (4.25).

$$\delta\varepsilon_{u(MGQ)} + \delta\varepsilon_{v(MGQ)} = 0 \rightarrow \delta\theta_4 (h + d) / d - \delta\theta_4 (h + d) / d = 0 \quad (4.25)$$

Therefore, the maximum shear strain increment is given by Equation (4.26).

$$\delta\gamma_{(MGQ)} = \delta\gamma_5 = 2 \delta\theta_4 (h + d) / d \quad (4.26)$$

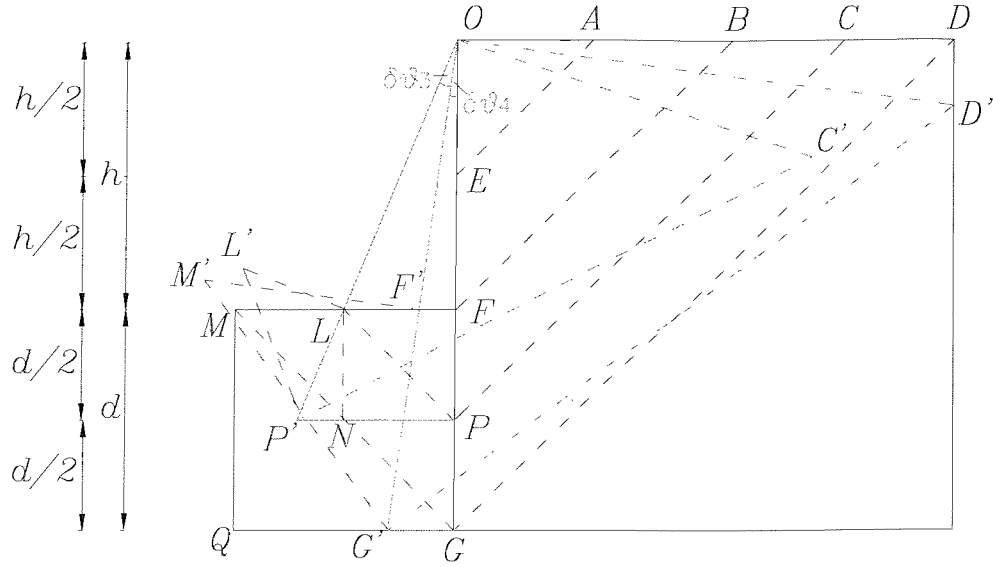


Figure 4.29: Stage 2 of the assumed wall movement – incremental rotation of triangles OCP behind the wall and FLP in front of the wall.

The second stage of the wall movement is illustrated in Figure 4.29. The shear strain increment $\delta\gamma_3$ within triangle OCP behind the wall is:

$$\delta\gamma_3 = 2 \delta\theta_3 \quad (4.27)$$

The horizontal and vertical strain increments within triangle LPN in front of the wall, which is compressed, are related to the rotation of triangle OCP by Equation (4.28) and the maximum shear strain increment is given by Equation (4.29).

$$\delta\varepsilon_{u(FLP)} = -\delta\varepsilon_{v(FLP)} = \delta\theta_3 (h + d/2) / (d/2) - \delta\theta_3 (h + d/2) / (d/2) \quad (4.28)$$

$$\delta\gamma_{(FLP)} = \delta\gamma_6 = 2 \delta\theta_3 (h + d/2) / (d/2) \quad (4.29)$$

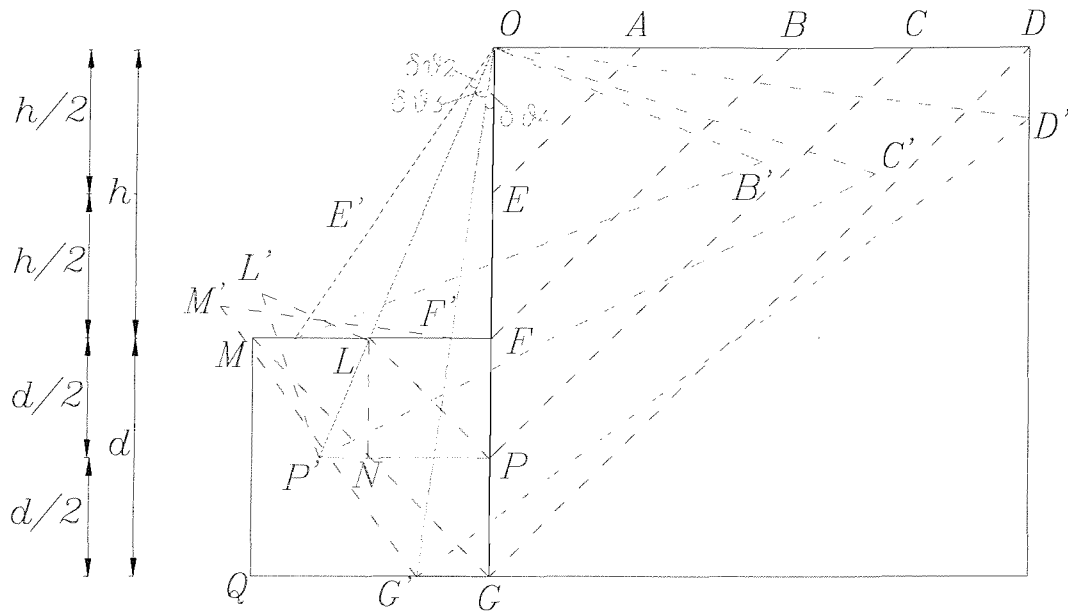


Figure 4.30: Stage 3 of the assumed wall movement – incremental rotation of triangle OBF.

During the third stage of the wall movement the incremental shear strain in triangle OBF behind the wall is:

$$\delta\gamma_2 = 2 \delta\theta_2 \quad (4.30)$$

Figure 4.31 shows the final stage of the wall movement.

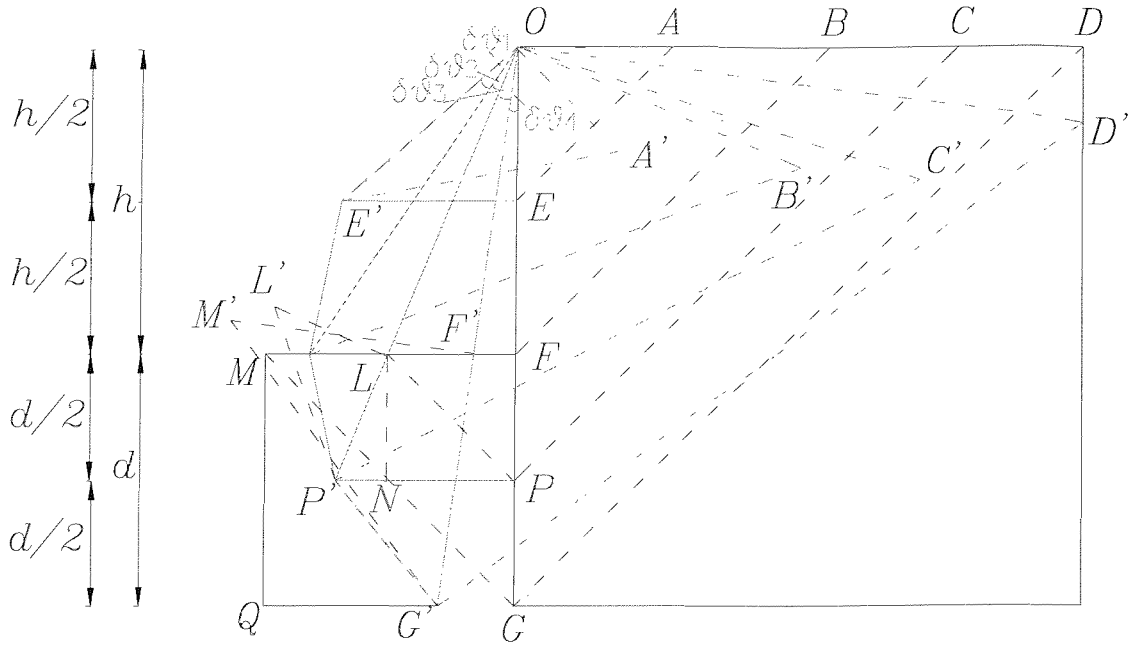


Figure 4.31: Stage 4 of the assumed wall movement - incremental rotation of triangle OAE.

The shear strain increment $\delta\gamma_1$ within triangle OAE behind the wall is:

$$\delta\gamma_1 = 2 \delta\theta_1 \quad (4.31)$$

In Figure 4.31 the total wall movement is shown. The total shear strain associated with the upper triangles is assumed to be the sum of the incremental shear strains associated with this triangle during each stage. Therefore, for triangles ODG, OCP, OBF and OAE behind the wall the total shear strains γ_4 , γ_3 , γ_2 and γ_1 are given by Equations (4.32), (4.33), (4.34) and (4.35) respectively:

$$\gamma_{(ODG)} = \gamma_4 = \delta\gamma_4 = 2 \delta\theta_4 \quad (4.32)$$

$$\gamma_{(OCP)} = \gamma_3 = \delta\gamma_4 + \delta\gamma_3 = 2 (\delta\theta_4 + \delta\theta_3) \quad (4.33)$$

$$\gamma_{(OBF)} = \gamma_2 = \delta\gamma_4 + \delta\gamma_3 + \delta\gamma_2 = 2 (\delta\theta_4 + \delta\theta_3 + \delta\theta_2) \quad (4.34)$$

$$\gamma_{(OAE)} = \gamma_1 = \delta\gamma_4 + \delta\gamma_3 + \delta\gamma_2 + \delta\gamma_1 = 2 (\delta\theta_4 + \delta\theta_3 + \delta\theta_2 + \delta\theta_1) \quad (4.35)$$

For triangles MFG and LPN in front of the wall the total shear strains γ_5 and γ_6 are given by Equations (4.36) and (4.37) respectively. The smaller triangle LPN in front of the wall will first be sheared by $\delta\gamma_5 = 2 \delta\theta_4 (h + d) / d$, due to the rotation of triangle FMG during the first stage. An additional amount of shear strain will then develop within triangle LPN during the second stage.

$$\gamma_{(MFG)} = \gamma_5 = \delta\gamma_5 = 2 \delta\theta_4 (h + d) / d \quad (4.36)$$

$$\gamma_{(LPN)} = \gamma_6 = \delta\gamma_5 + \delta\gamma_6 = 2 \delta\theta_4 (h + d) / d + 2 \delta\theta_3 (h + d / 2) / (d / 2) \quad (4.37)$$

4.3.3 Mobilised strength

If the increments of strain in a soil zone are known, then the mobilized strength can be estimated by a constitutive relationship measured in an element test on a representative sample of the soil. Bolton and Powrie (1988) used plots of mobilized friction angle φ'_{mob} against shear strain γ , derived from plane strain tests, as the means of expressing the mobilized strength and stiffness of the soil surrounding the wall. The rate of change of φ'_{mob} with shear strain is a useful tool for expressing strength and stiffness at the same time, providing information on the soil state relative to its critical state.

From the Mohr circle of stress (Figure 4.32) the mobilised angle of friction is given by relationship (4.38):

$$\varphi'_{mob} = \sin^{-1} [t / s'] = \sin^{-1} [(\sigma_1' - \sigma_3') / (\sigma_1' + \sigma_3')] \quad (4.38)$$

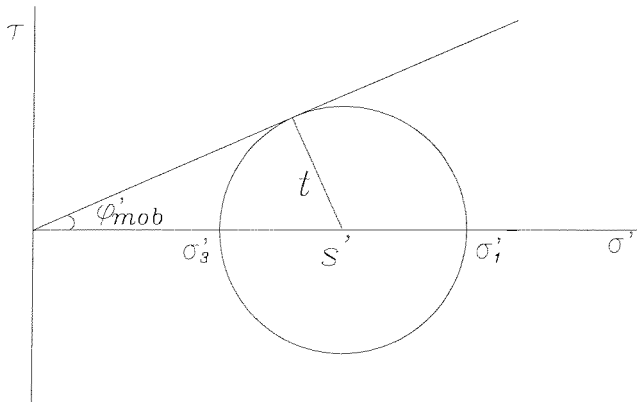


Figure 4.32: The Mohr circle of stress.

The use of the $\varphi'_{mob} - \gamma$ relationship, instead of the conventional way of presenting soil stiffness by the shear modulus G , has the advantage of being comparatively insensitive to small changes of OCR and initial effective stress (Bolton & Powrie, 1988) and will be adopted in the present project. Application of more kinematically admissible strain fields, as described in Sections 4.3.1 and 4.3.2, enables the use of different values of φ'_{mob} for the active and passive soil zone and for different depths from the crest.

The hyperbolic relationship introduced by Duncan and Cheng (1970) and described in Section 4.2.2, can be rewritten in terms of $\varphi'_{mob} - \gamma$. Their results from triaxial tests on dense and loose uniform fine silica sand samples by Duncan and Cheng (1970) can be transformed to fit this form (Equation 4.40) and are plotted in Figure 4.33a and b respectively, for different confining pressures. A list of the values of the parameters involved is presented in Table 4.5.

From Equation (4.10) in section 4.2.2 and Equation (4.38):

$$\varphi'_{mob} = \sin^{-1} \left\{ \gamma / [3 a \sigma_3 + \gamma (1 + 2 \sigma_3 b)] \right\} \quad (4.39)$$

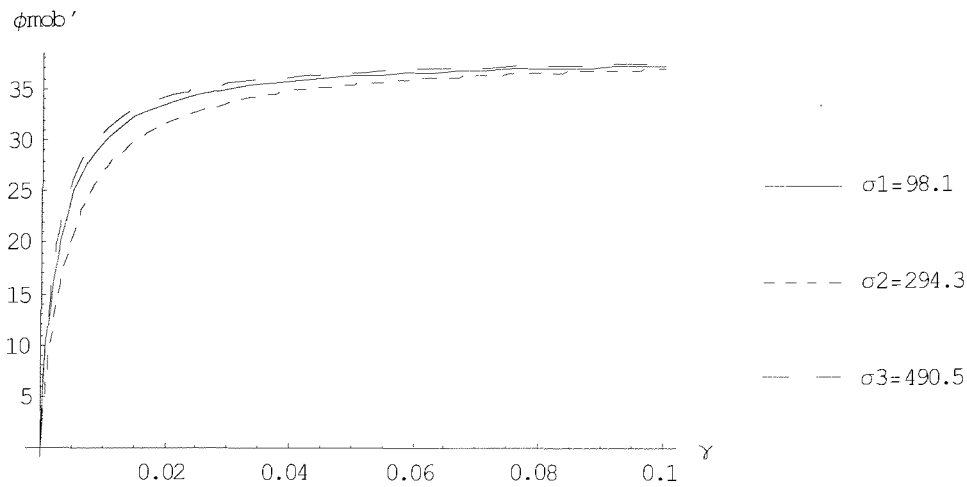
Equation (4.39) can be written in the simpler form

$$\varphi'_{mob} = \sin^{-1} [\gamma / (A + B \gamma)] \quad (4.40)$$

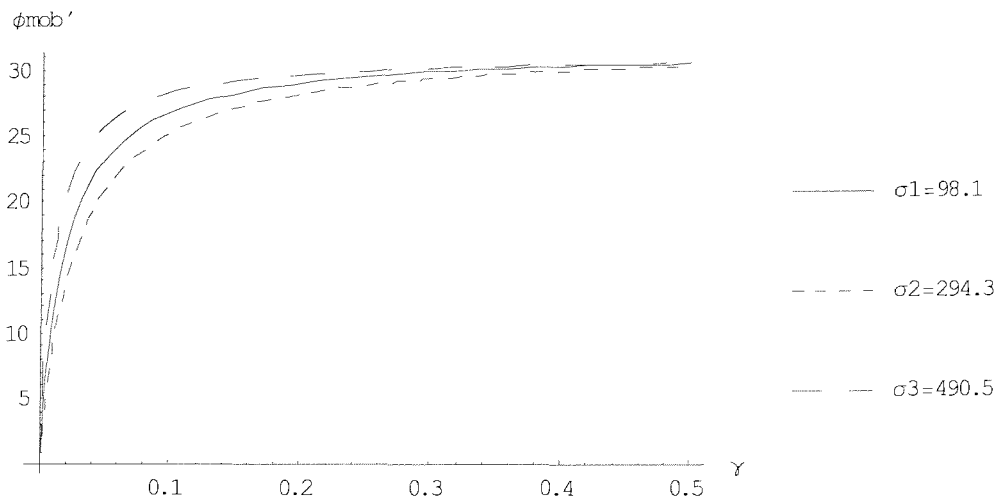
where $A = 3 a \sigma_3$, $B = (1 + 2 \sigma_3 b)$ and a , b are constants of the hyperbolic relationship as defined in section 4.2.2. As already mentioned, the parameters A and B might differ for drained conditions but the aim here is to show that Equation (4.40) can approximate satisfactorily the function of $\phi'_{mob} - \gamma$. The analytical calculations are presented in the Appendix.

Silica sand	Dense			Loose		
D_r (Relative density)	100%			38%		
R_f	0.91			0.90		
K	2,000			295		
n	0.54			0.65		
σ_3 (KN/m ²)	• 98.1	• 294.3	• 490.5	• 98.1	• 294.3	• 490.5
a (m ² /KN)	• 1.315 10 ⁻⁵	• 6.796 10 ⁻⁶	• 2.273 10 ⁻⁶	• 1.059 10 ⁻⁴	• 5.097 10 ⁻⁵	• 1.223 10 ⁻⁵
b (m ² /KN)	• 3.092 10 ⁻³	• 1.019 10 ⁻³	• 6.178 10 ⁻⁴	• 4.587 10 ⁻³	• 3.202 10 ⁻³	• 9.439 10 ⁻⁴
$A=3a \sigma_3$	• 3.87 10 ⁻³	• 6 10 ⁻³	• 3.35 10 ⁻³	• 0.0312	• 0.045	• 0.018
$B=1+2\sigma_3 b$	• 1.61	• 1.6	• 1.606	• 1.9	• 1.885	• 1.926

Table 4.5: Triaxial tests on dense and loose silica sand carried out by Duncan and Cheng (1970) together with the values of parameters A and B .



(a)



(b)

Figure 4.33: Mobilised friction angle against shear strain for (a) dense silica sand, (b) loose silica sand for results obtained from triaxial tests by Duncan and Cheng (1970).

4.4 WALL FLEXURAL RIGIDITY ANALYSIS

In Figure 4.34, the continuous curvature of the wall is idealized into a number of rotations at discrete points, corresponding to the triangles in the active and passive soil zones. The total length of the wall, $h + d$, is divided into four parts with lengths of $h / 2$,

$h/2$, $d/2$ and $d/2$, where h is the retained height of the wall and d its embedment depth (Figure 4.31).

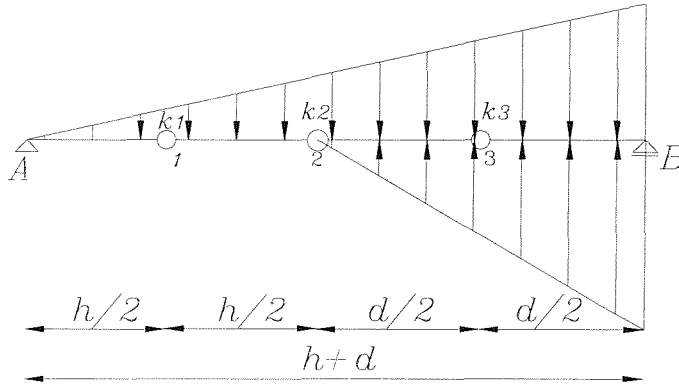


Figure 4.34: Discretisation of wall into four rigid parts connected by rotational springs.

The flexural rigidity of the beam, $E I$, is modeled by rotational springs of stiffness k_1 , k_2 and k_3 , where $k = M / \theta$, at points 1, 2 and 3 respectively. The first component at point 1 has a value k_1 equal to $E I$ divided by half the lengths of parts A-1 and 1-2:

$$k_1 = E I / (h/4 + h/4) = 2 E I / h \quad (4.41)$$

Component k_2 at point 2 is equal to $E I$ divided by half the lengths of parts 1-2 and 2-3:

$$k_2 = E I / (h/4 + d/4) = 4 E I / (h + d) \quad (4.42)$$

Following the same approach, component k_3 at point 3 has a value of:

$$k_3 = E I / (d/2) = 2 E I / d \quad (4.43)$$

The assumption that the flexural rigidity of a beam can be represented by a number of rotational springs concentrated on different points with rotational stiffness equal to $E I$ divided by half the lengths of the adjacent sections, will now be examined with reference to examples of beams with different boundary conditions subject to uniform and triangular loads.

- **Simply supported beam subject to uniform loading**

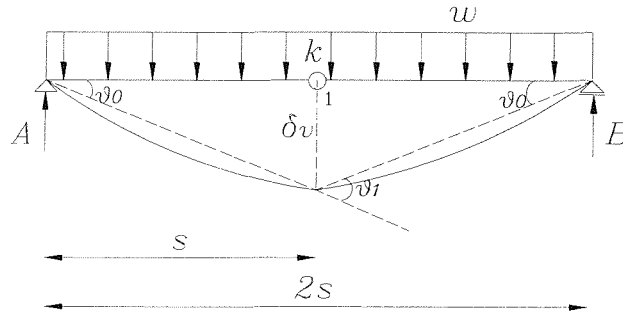


Figure 4.35: Simply supported beam subject to uniform loading.

The simply supported beam in Figure 4.35 is divided into two parts of equal length s . According to standard beam theory, the bending moment at any distance x from the support A is given by Equation (4.44), where w is the uniform load acting on the beam per meter of its length:

$$M(x) = w (2s)^2 \left\{ \frac{x}{2s} - \left[\frac{x}{2s} \right]^2 \right\} / 2 \quad (4.44)$$

If k is the component of flexural rigidity concentrated on point 1 and θ_1 is the rotation at this point, then the bending moment at the same point is:

$$M(s) = M_1 = k \theta_1 \quad (4.45)$$

From Equations (4.44) and (4.45) θ_1 can be calculated:

$$\theta_1 = w s^2 / (2k) \quad (4.46)$$

From standard beam theory, the deformation at any distance x from the support A is given by Equation (4.47):

$$\delta(x) = [w (2s)^4 / 24 E I] \left\{ \left[\frac{x}{2s} \right] - 2 \left[\frac{x}{2s} \right]^3 + \left[\frac{x}{2s} \right]^4 \right\} \quad (4.47)$$

If θ_0 is the rotation at point A, then the deformation at point 1 is:

$$\delta(s) = \delta_1 = \theta_0 s \quad (4.48)$$

From Equations (4.47) and (4.48):

$$\theta_0 = 5 w s^3 / (24 E I) \quad (4.49)$$

Considering the symmetry of the beam:

$$\theta_0 = 1/2 \theta_1 \quad (4.50)$$

From Equations (4.46), (4.49) and (4.50), component k can be calculated:

$$k = 1.2 E I / s \quad (4.51)$$

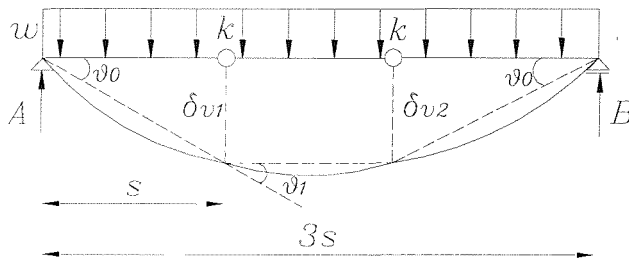


Figure 4.36: Simply supported beam subject to uniform loading with two rotational springs.

In Figure 4.36 a beam with the same loading and boundary conditions is divided in three parts of equal lengths s and its flexural rigidity is assumed to consist of two equal components, k , at points 1 and 2. The bending moments at any distance x from support A and at point 1 are given by Equations (4.52) and (4.53) respectively:

$$M(x) = w (3s)^2 \{x / (3s) - [x / (3s)]^2\} / 2 \quad (4.52)$$

$$M(s) = M_1 = k \theta_1 \quad (4.53)$$

Then, the rotation at point 1, θ_1 , can be calculated:

$$\theta_1 = w s^2 / k \quad (4.54)$$

From the standard beam theory, if θ_0 is the rotation at point A, the deformations at any distance x from support A and at point 1 are given by Equation (4.55) and (4.56) respectively:

$$\delta(x) = [w (3 s)^4 / (24 E I)] \{ x / (3 s) - 2 [x / (3 s)]^3 + [x / (3 s)]^4 \} \quad (4.55)$$

$$\delta(s) = \delta_1 = \theta_0 s \quad (4.56)$$

From Equations (4.55) and (4.56), θ_0 is calculated:

$$\theta_0 = 11 w s^3 / (12 E I) \quad (4.57)$$

From the symmetry of the beam:

$$\theta_0 = \theta_1 \quad (4.58)$$

From Equations (4.54), (4.57) and (4.58):

$$k = 1.09 E I / s \quad (4.59)$$

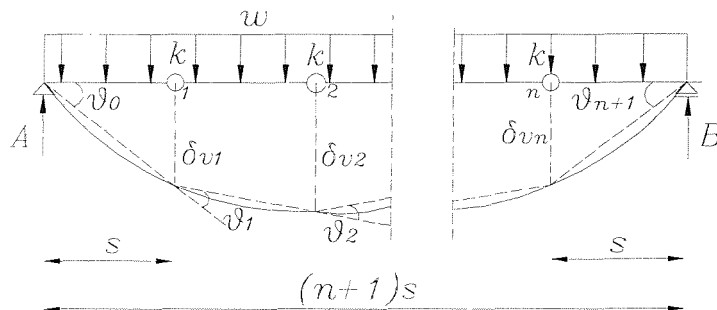


Figure 4.37: Simply supported beam subject to uniform loading with n rotational springs.

Figure 4.37 shows a simply supported beam subject to uniform loading, divided in $(n+1)$ parts of equal length s ; hence its total length is $(n+1) s$. Its flexural rigidity is assumed to consist of n equal components, k . In equations (4.60) and (4.61) the bending moments at any distance x from support A and at point 1 according to standard beam theory are respectively:

$$M(x) = w (n+1)^2 s^2 \{2 x / [(n+1) s] - [x / ((n+1) s)]^2\} / 2 \quad (4.60)$$

$$M_1 = k \theta_1 \quad (4.61)$$

The rotation at point 1, θ_1 , is:

$$\theta_1 = -w n s^2 / (2 k) \quad (4.62)$$

The general expression for the deformations at any point along the beam is given by Equation (4.63) and the deformations at points 1 and 2 are calculated by Equations (4.64) and (4.65):

$$\delta(x) = w (n+1)^4 s^4 / (24 E I) \{ x / [(n+1) s] - 2 [x / ((n+1) s)]^3 + [x / ((n+1) s)]^4 \} \quad (4.63)$$

$$\delta(s) = \delta_1 = \theta_0 s \rightarrow \theta_0 = w s^3 n (n^2 + 3 n + 1) / (24 E I) \quad (4.64)$$

$$\delta(2s) = \delta_2 = 2 \theta_0 s - \theta_1 s \quad (4.65)$$

Substituting Equation (4.62) into Equation (4.65):

$$\theta_0 = w s^2 [k s (n^3 + 3 n^2 - 5 n + 1) + 6 E I n] / (24 k E I) \quad (4.66)$$

From Equations (4.64) and (4.66):

$$k = 6 n E I / [s (6 n - 1)] \rightarrow k s / E I = 6 n / (6 n - 1) \quad (4.67)$$

It is obvious from Equation (4.67) that k depends on the number of points that the flexural rigidity is assumed to be concentrated on, n , and the distance, s , between these points. In Figure 4.38, where $k s / (E I)$ is plotted against n , $k s / (E I)$ tends to unity as the number of components of flexural rigidity increases. Hence, the assumption $k = E I / s$ is justified for $n > 1$.

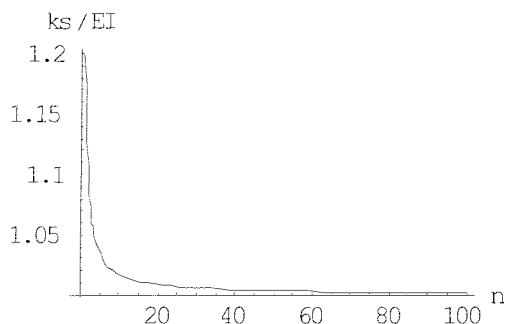


Figure 4.38: Plot of the quantity $k s / (E I)$ against the number of flexural rigidity components n .

Following the same approach the quantity $k s / (E I)$ is given by Equations (4.68) to (4.74) and is plotted against n in Figures (4.39) to (4.52) for beams with different boundary conditions subject to uniform and triangular loads. The analytical calculations have been carried out in Mathematica and are presented in the Appendix.

- **Built in beam subject to uniform loading**

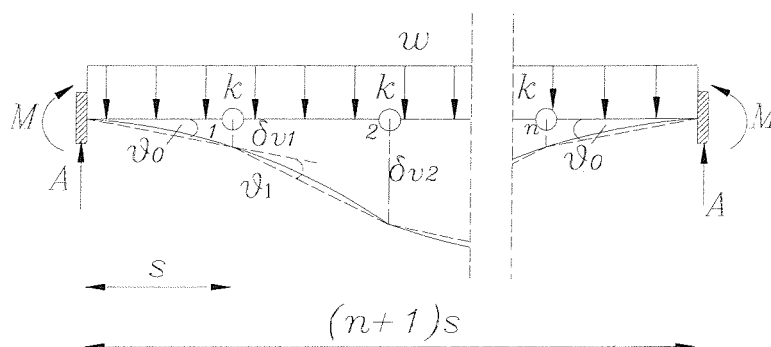


Figure 4.39: Built-in beam subject to uniform loading with n rotational springs.

$$k s / (E I) = (n^2 - 4 n + 1) / (n^2 - 4 n + 2) \quad (4.68)$$

In Figure 4.40, $k s / (E I)$ is plotted against n , for $n > 4$. As n increases, $k s / (E I)$ tends to unity. Hence, $k = E I / s$ for $n > 4$.

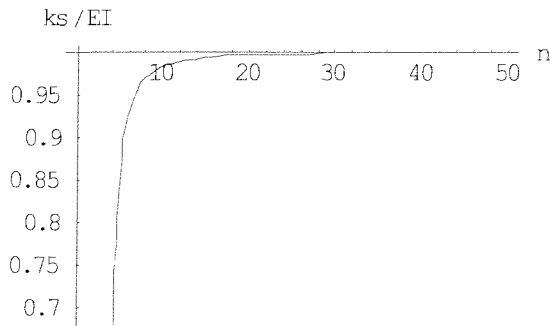


Figure 4.40: Plot of the quantity $k s / (E I)$ against the number of the flexural rigidity components n for a built in beam subject to uniform loading.

- **Cantilever beam subject to uniform loading**

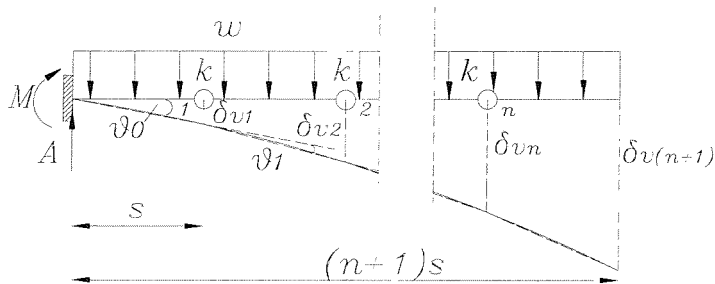


Figure 4.41: Cantilever beam subject to uniform loading with n rotational springs.

$$k = 6 n^2 E I / [(1 + 6 n^2) s] \rightarrow k s / E I = 6 n^2 / (1 + 6 n^2) \quad (4.69)$$

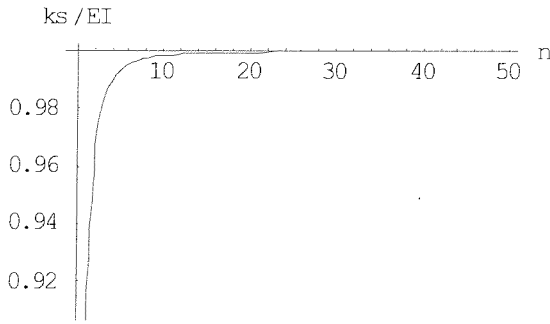


Figure 4.42: Plot of the quantity $ks / (EI)$ against the number of the flexural rigidity components n for a cantilever beam subject to uniform loading.

- **Built in – simply supported beam subject to uniform loading**

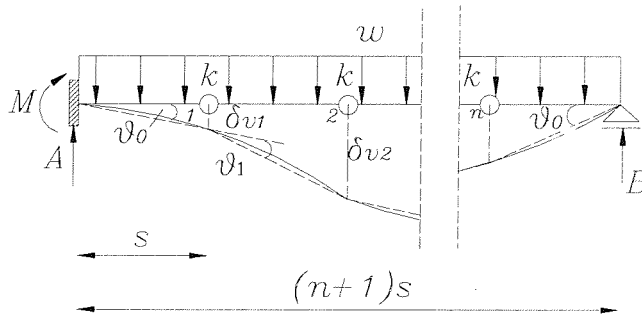


Figure 4.43: Built-in simply supported beam subject to uniform loading with n rotational springs.

$$ks / (EI) = 3n(n - 3) / (3n^2 - 9n + 2) \quad (4.70)$$

From Figure 4.44, where ks / EI is plotted against n for $n > 3$, as n increases ks / EI tends to unity.

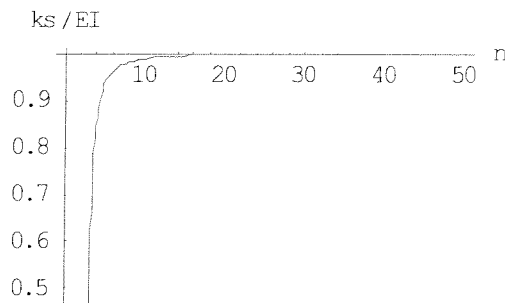


Figure 4.44: Plot of the quantity $ks / (EI)$ against the number of the flexural rigidity components n for a built in – simply supported beam subject to uniform loading.

- Simply supported beam subject to triangular loading

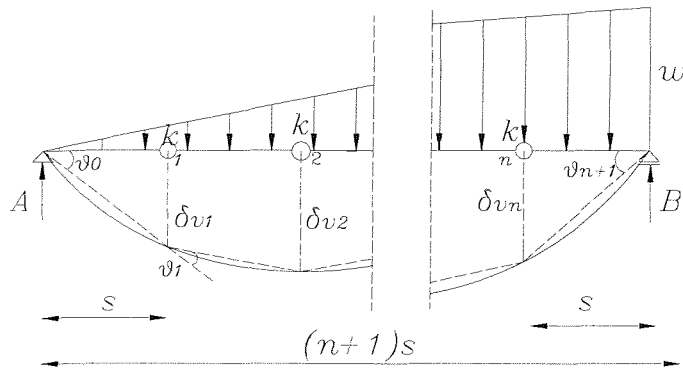


Figure 4.45: Simply supported beam subject to triangular loading with n rotational springs.

For the beam shown in Figure (4.45):

$$k s / (E I) = 2n (n+2) / (2n^2 + 4n - 1) \quad (4.71)$$

In Figure 4.46, where $k s / (E I)$ is plotted against n , $k s / (E I)$ tends to unity as n increases.

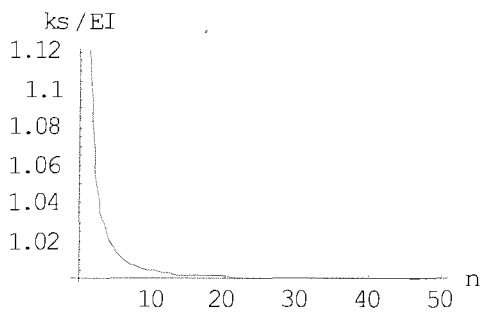


Figure 4.46: Plot of the quantity $k s / (E I)$ against the number of the flexural rigidity components n for a simply supported beam subject to triangular loading.

- Built in beam subject to triangular loading

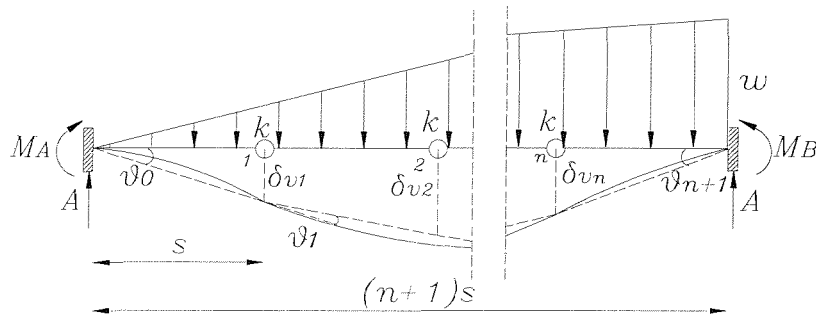


Figure 4.47: Built-in beam subject to triangular loading with n rotational springs.

$$k s / (E I) = (2n^3 - 3n^2 - 12n + 3) / (2n^3 - 3n^2 - 12n + 8) \quad (4.72)$$

In Figure 4.48 $k s / (E I)$ is plotted against n , for $n > 4$. According to this plot, $k s / (E I)$ tends to unity as n increases.

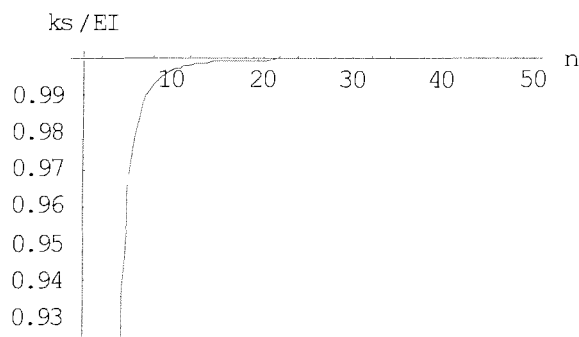


Figure 4.48: Plot of the quantity $k s / (E I)$ against the number of the flexural rigidity components n for a built in beam subject to triangular loading.

- **Cantilever beam subject to triangular loading**

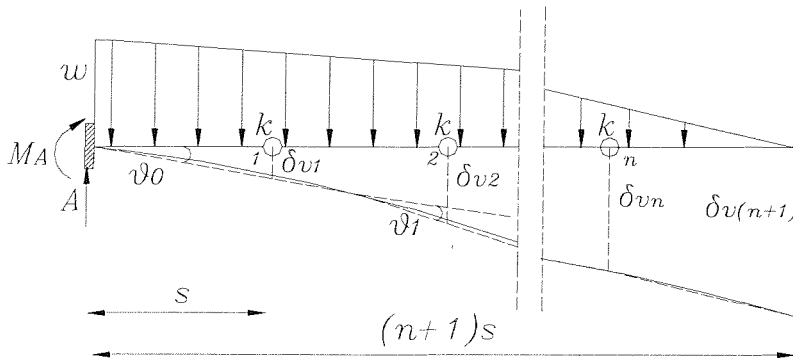


Figure 4.49: Cantilever beam subject to triangular loading with n rotational springs.

The quantity $k s / (E I)$ is given by Equation (4.71) and is plotted against n in Figure 4.50.

$$k s / (E I) = 2 n^2 / (1 + 2 n^2) \quad (4.73)$$

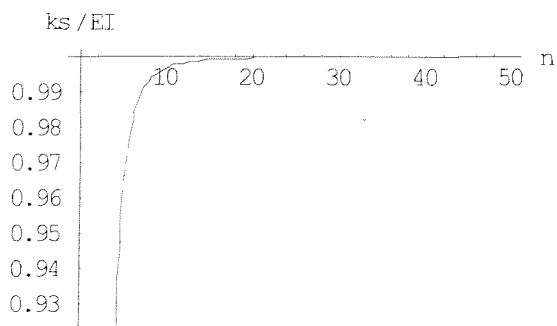


Figure 4.50: Plot of the quantity $k s / (E I)$ against the number of the flexural rigidity components n for a cantilever beam subject to triangular loading.

- **Built in - simply supported beam subject to triangular loading**

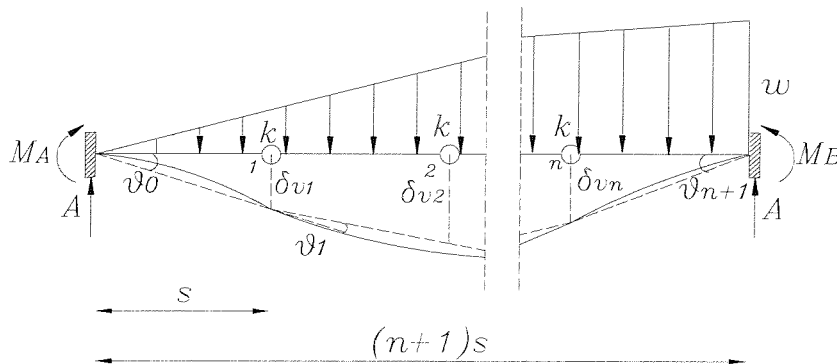


Figure 4.51: Built-in beam subject to triangular loading with n rotational springs.

$$k s / E I = 2 (2 n^2 - 6 n - 3) / (4 n^2 - 12 n - 1) \quad (4.74)$$

In Figure 4.52 $k s / E I$ is plotted against n for $n > 4$. It is obvious from the graph that $k = E I / s$ for $n > 4$.

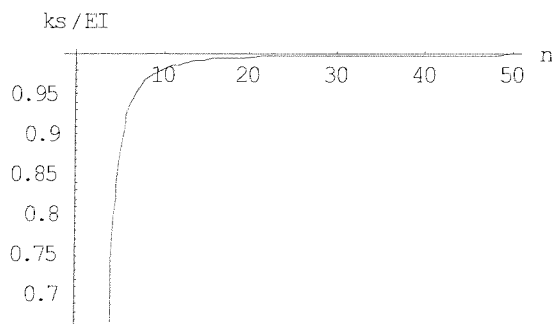


Figure 4.52: Plot of the quantity $k s / (E I)$ against the number of the flexural rigidity components n ($n > 4$) for a built in – simply supported beam subject to triangular loading.

The behaviour of a retaining wall propped at the crest is likely to resemble the behaviour of a simply supported or cantilever beam, since the point at the crest, where the prop force acts, can be considered as a simple support and the toe of the wall is free to move laterally. The discretised flexural rigidity approach, as described in this section, has been applied both to a cantilever and a simply supported beam and it has been shown that their flexural rigidity can be analysed in components with values of $k = E I / s$. Therefore, the flexural rigidity of a retaining wall propped at the crest can be approximated in this way. More examples of beams are presented in the Appendix.

4.4.1 Flexural rigidity analysis for a retaining wall propped at the crest

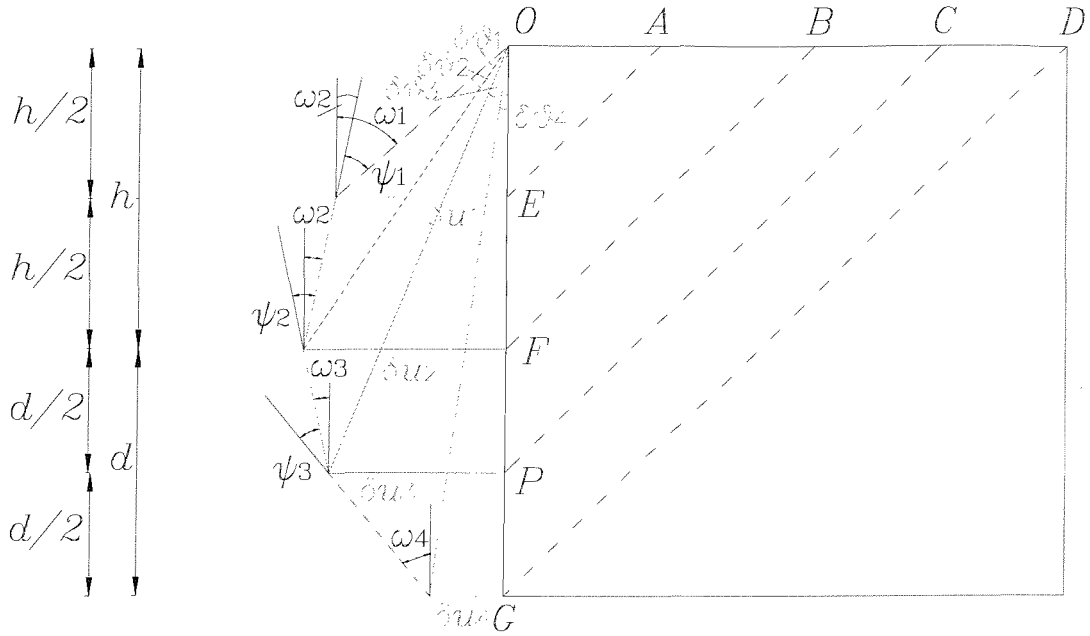


Figure 4.53: Rotations and displacements at discretised points along a retaining wall propped at the crest.

Figure 4.53 shows the rotations and displacements of a retaining wall propped at the crest according to the discretised flexural rigidity approach presented in the previous section. The continuous curvature of the wall is idealized into three rotations at discrete points, corresponding to the triangles in the active and passive soil zones.

The horizontal displacement at point G is δu_4 and at point P it is δu_3 . From the geostrophical mechanism described in section 4.3.1, the displacements δu_4 and δu_3 are related to the wall rotations $\delta\theta_4$ and $\delta\theta_3$ by Equations (4.75) and (4.76):

$$\delta u_4 = (h + d) \delta\theta_4 \quad (4.75)$$

$$\delta u_3 = (h + d/2) (\delta\theta_4 + \delta\theta_3) \quad (4.76)$$

From Figure 4.53, ω_i is the rotation of the wall at the i_{th} discrete point from its vertical position, while ψ_i is the rotation of the $(i+1)_{th}$ discrete point relevant to the rotation of the i_{th} discrete point. Hence, Equation (4.76) may be written:

$$\delta u_3 = (h + d) \delta \theta_4 + \omega_4 d / 2 \quad (4.77)$$

From Equations (4.76) and (4.77):

$$\omega_4 = [(h + d / 2) \delta \theta_3 - d / 2 \delta \theta_4] / d / 2 \quad (4.78)$$

The displacement at point F , δu_2 , is given by Equations (4.79) and (4.80):

$$\delta u_2 = h (\delta \theta_4 + \delta \theta_3 + \delta \theta_2) \quad (4.79)$$

$$\delta u_2 = \delta u_3 + \omega_3 d / 2 \quad (4.80)$$

From Equations (4.76), (4.79) and (4.80), the angle ω_3 may be calculated:

$$\omega_3 = [h \delta \theta_2 - d / 2 (\delta \theta_4 + \delta \theta_3)] / d / 2 \quad (4.81)$$

Similarly the horizontal displacement at point E , δu_1 , is given by Equations (4.82), (4.83) and (4.84):

$$\delta u_1 = h / 2 (\delta \theta_4 + \delta \theta_3 + \delta \theta_2 + \delta \theta_1) \quad (4.82)$$

$$\delta u_1 = \delta u_2 - \omega_2 h / 2 \quad (4.83)$$

$$\delta u_1 = \omega_1 h / 2 \quad (4.84)$$

Therefore, the angles ω_1 and ω_2 may be calculated and are given by Equations (4.85) and (4.86) respectively:

$$\omega_2 = \delta \theta_4 + \delta \theta_3 + \delta \theta_2 - \delta \theta_1 \quad (4.85)$$

$$\omega_1 = \delta\theta_4 + \delta\theta_3 + \delta\theta_2 + \delta\theta_1 \quad (4.86)$$

The rotation of the wall at the $(i+1)_th$ discrete point along its length relative to the rotation of the i_{th} discrete point, ψ_1 , ψ_2 and ψ_3 , can be calculated geometrically from Figure 4.53:

$$\psi_1 = \omega_1 - \omega_2 = 2 \delta\theta_1 \quad (4.87)$$

$$\psi_2 = \omega_2 + \omega_3 = 2 [\theta_2 (h + d/2) - \theta_1 d/2] / d \quad (4.88)$$

$$\psi_3 = \omega_4 - \omega_3 = 2 [\theta_3 (h + d) - \theta_2 h] / d \quad (4.89)$$

In the previous section it was shown that the flexural rigidity of a retaining wall, $E I$, can be modelled by three rotational springs of stiffness k_1 , k_2 and k_3 , where $k_i = M_i / \psi_i$. Therefore, considering Equations (4.41) and (4.87) the bending moment M_1 at point E at the retaining wall shown in Figure 4.53 is given by Equation (4.90):

$$k_1 = M_1 / \psi_1 = 2 E I / h \rightarrow M_1 = 2 \delta\theta_1 2 E I / h \rightarrow M_1 = 4 \delta\theta_1 E I / h \quad (4.90)$$

Similarly, the bending moments at points F and P are given by Equations (4.91) and (4.92) respectively:

$$\begin{aligned} k_2 &= M_2 / \psi_2 = 4 E I / (h + d) \rightarrow \\ &\rightarrow M_2 = 2 [\theta_2 (h + d/2) - \theta_1 d/2] 4 E I / [d (h + d)] \rightarrow \\ &\rightarrow M_2 = 4 E I [\theta_2 (2 h / d + 1) - \theta_1] / (h + d) \end{aligned} \quad (4.91)$$

$$\begin{aligned} k_3 &= M_3 / \psi_3 = 2 E I / d \rightarrow M_3 = 2 (2 E I / d) [\theta_3 (h + d) - \theta_2 h] / d \rightarrow \\ &\rightarrow M_3 = 4 E I / d^2 [\theta_3 (h + d) - \theta_2 h] \end{aligned} \quad (4.92)$$

The normalized bending moments are:

$$M_1 / (\gamma_s H^3) = 4 E I \delta\theta_1 / (m \gamma_s H^4) \quad (4.93)$$

$$M_2 / (\gamma_s H^3) = 4 E I / (\gamma_s H^4) [\delta\theta_2 (1+m) / (1-m) - \delta\theta_1] \quad (4.94)$$

$$M_3 / (\gamma_s H^3) = 4 E I / [\gamma_s H^4 (1-m)^2] (\delta\theta_3 - m \delta\theta_2) \quad (4.95)$$

The normalised bending moments can be rewritten in the form of Equations (4.96) to (4.98) where ρ is the wall flexibility defined by Rowe (1952):

$$M_1 / (\gamma_s H^3) = 4 \delta\theta_1 / (m \gamma_s \rho) \quad (4.96)$$

$$M_2 / (\gamma_s H^3) = 4 / (\gamma_s \rho) [\delta\theta_2 (1+m) / (1-m) - \delta\theta_1] \quad (4.97)$$

$$M_3 / (\gamma_s H^3) = 4 / [\gamma_s \rho (1-m)^2] (\delta\theta_3 - m \delta\theta_2) \quad (4.98)$$

4.5 ULS CALCULATIONS FOR A RETAINING WALL PROPPED AT THE CREST IN CONDITIONS OF ZERO PORE WATER PRESSURES

In Figure 4.54 the horizontal stress distributions together with the pore water pressures, assuming linear seepage, are shown behind and in front of a retaining wall, which is in limiting equilibrium. The active and passive stresses at the toe of the wall are written in Figure 4.54.

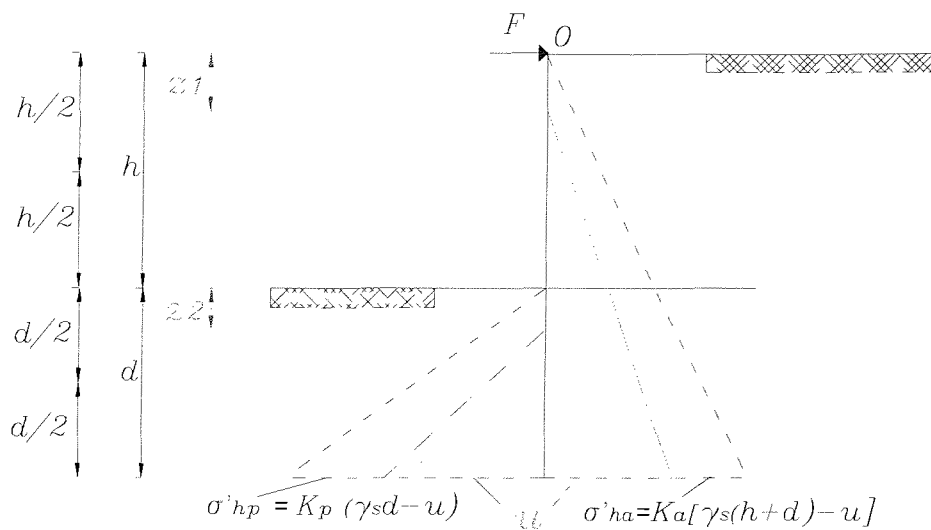


Figure 4.54: Stress and pore water pressure distribution in limit equilibrium behind and in front of a retaining wall propped at the crest.

Conditions of steady state seepage are often assumed; hence, the pore water pressures at the toe are given by Equation (4.99), where z_1 and z_2 are the distances between the ground surface and the ground water level behind and in front of the wall respectively:

$$u = \gamma_w [(d - z_2) + (h + z_2 - z_1) (d - z_2) / (h + 2d - z_2 - z_1)] \quad (4.99)$$

For simplicity and to emphasize the effect of soil stresses, since u is unaffected by soil/wall stiffness, the analysis is now focused on conditions of zero pore water pressures. Therefore:

$$z_1 = h + d \text{ and } z_2 = d \quad (4.100)$$

From the condition of horizontal stress equilibrium, the prop force F may be calculated:

$$\begin{aligned}\sum R_h = 0 &\rightarrow 1/2 K_a \gamma_s (h + d)^2 = 1/2 K_p \gamma_s d^2 + F \rightarrow \\ F &= 1/2 K_a \gamma_s (h + d)^2 - 1/2 K_p \gamma_s d^2\end{aligned}\quad (4.101)$$

If m is the retained height ratio ($m = h/H$), the normalized prop force $F/\gamma_s H^2$, where H is the overall height of the wall, is given by Equation (4.102):

$$F/\gamma_s H^2 = 1/2 K_a - 1/2 K_p (1 - m)^2 \quad (4.102)$$

Taking the moments at the point O at the crest, m may be calculated by Equation (4.103):

$$\begin{aligned}\sum M_h = 0 &\rightarrow 1/2 K_a \gamma_s (h + d)^3 \cdot 2/3 = 1/2 K_p \gamma_s d^2 (h + 2/3 d) \rightarrow \\ K_a &= K_p (1 - m)^3 + 3/2 K_p m (1 - m)^2\end{aligned}\quad (4.103)$$

According to Eurocode (EC7, 1997) the design soil strength φ'_{design} should be equal to $\tan^{-1}\{(\tan \varphi')/1.25\}$, where φ' is a moderately conservative estimate of the effective angle of friction relevant to the ultimate limit state. Taking into account wall friction, the active and passive earth pressure coefficients are given by Equations (4.104) and (4.105)

$$K_a = \left\{ [1 - \sin \varphi'_{design} \cos (\Delta - \delta)] / (1 + \sin \varphi'_{design}) \right\} e^{-\delta(\Delta - \delta) \tan \varphi'_{design}} \quad (4.104)$$

$$K_p = \left\{ [1 - \sin \varphi'_{design} \cos (\Delta - \delta)] / (1 + \sin \varphi'_{design}) \right\} e^{-\delta(\Delta - \delta) \tan \varphi'_{design}} \quad (4.105)$$

where $\sin \Delta = \sin \delta / \sin \varphi'_{design}$.

Equations (4.103), (4.104) and (4.105) relate the design soil strength φ'_{design} to the retained height ratio m . Therefore, if the retained height ratio is known, the soil strength required to maintain stability may be calculated. Similarly, if the design soil strength is known, the retained height ratio required to avoid collapse of the wall may be derived from the Equations above.

4.6 SLS CALCULATIONS FOR A RETAINING WALL PROPPED AT THE CREST IN CONDITIONS OF ZERO PORE WATER PRESSURES

The design of a retaining wall should not merely ensure avoidance of collapse but should also meet specific criteria in terms of displacement, damage and appearance. The required retained height ratio m may be calculated from the ULS calculations using the factored (design) strength, as shown in Section 4.5, and the soil and wall deformations can be estimated using the mobilised strength method.

Figures 4.27, 4.29, 4.30 and 4.31 in section 4.3.2 show four successive stages of a small wall movement into the excavation. According to the mobilised strength method for a wall with a retained height ratio m calculated from the ULS calculations, wall rotation about the crest will mobilise different amounts of soil strength, φ'_{mob_i} , in each soil zone. The transformed form (Equation 4.40) of the hyperbolic relationship introduced by Duncan and Cheng (1970) and described in Section 4.2.2, is used to relate the mobilised soil strength φ'_{mob_i} to the shear strain γ_i developed in each soil zone. The shear strain γ_i can be related to the wall rotations $\delta\theta_i$ as shown Section 4.3.2. The active and passive earth pressure coefficients, K_{ai} and K_{pi} will be different in each soil zone because the mobilised strengths φ'_{mob_i} are different and may be calculated by Equations (4.104) and (4.105) (Powrie, 1997), assuming full wall friction ($\varphi' = \delta$):

$$K_{ai} = \{[1 - \sin \varphi'_{mob} \cos (\Delta - \delta)] / (1 + \sin \varphi'_{mob})\} e^{-\{(\Delta - \delta) \tan \varphi'_{mob}\}} \quad (4.106)$$

$$K_{pi} = \{[1 - \sin \varphi'_{mob} \cos (\Delta - \delta)] / (1 + \sin \varphi'_{mob})\} e^{-\{(\Delta - \delta) \tan \varphi'_{mob}\}} \quad (4.107)$$

The distribution of the active and passive pressures behind and in front of the retaining wall is assumed to be different but linear in each soil zone as shown in Figure 4.55.

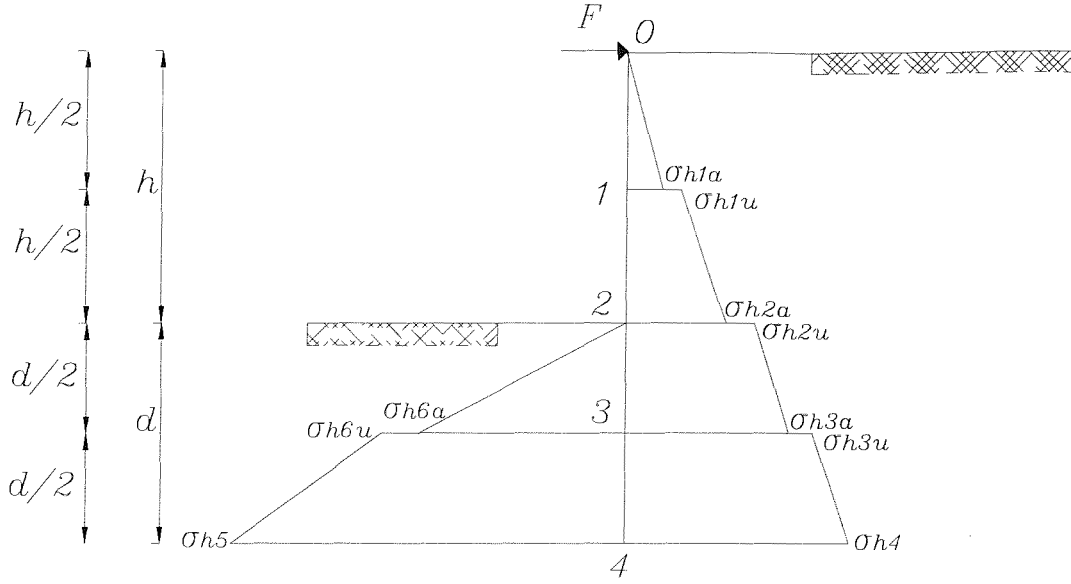


Figure 4.55: Redistribution of the active and passive stresses after a small movement of a retaining wall propped at the crest.

The mobilised soil strength, φ'_{mob_i} , is assumed to be uniform within each soil zone. For a wall with a retained height ratio m calculated from the ULS calculations using factored (design) strength, the soil strength mobilised in the soil zones 0-1, 1-2, 2-3 and 3-4 behind the wall and 2-3 and 3-4 in front (Figure 4.55) after a small wall rotation at the crest is given by Equations (4.108), (4.109), (4.110), (4.111), (4.112) and (4.113) respectively:

$$\varphi'_{mob1} = \sin^{-1} [\gamma_1 / (A + B \gamma_1)] \rightarrow$$

$$\rightarrow \varphi'_{mob1} = \sin^{-1} \{2 [\delta\theta_4 + \delta\theta_3 + \delta\theta_2 + \delta\theta_1] / [A + 2 B (\delta\theta_4 + \delta\theta_3 + \delta\theta_2 + \delta\theta_1)]\} \quad (4.108)$$

$$\varphi'_{mob2} = \sin^{-1} [\gamma_2 / (A + B \gamma_2)] \rightarrow$$

$$\rightarrow \varphi'_{mob2} = \sin^{-1} \{2 [\delta\theta_4 + \delta\theta_3 + \delta\theta_2] / [A + 2 B (\delta\theta_4 + \delta\theta_3 + \delta\theta_2)]\} \quad (4.109)$$

$$\varphi'_{mob3} = \sin^{-1} [\gamma_3 / (A + B \gamma_3)] \rightarrow$$

$$\rightarrow \varphi'_{mob3} = \sin^{-1} \{2 [\delta\theta_4 + \delta\theta_3] / [A + 2 B (\delta\theta_4 + \delta\theta_3)]\} \quad (4.110)$$

$$\begin{aligned} \varphi'_{mob4} &= \sin^{-1} [\gamma_4 / (A + B \gamma_4)] \rightarrow \\ \rightarrow \varphi'_{mob4} &= \sin^{-1} [2 \delta\theta_4 / (A + 2 B \delta\theta_4)] \end{aligned} \quad (4.111)$$

$$\begin{aligned} \varphi'_{mob5} &= \sin^{-1} [\gamma_5 / (A + B \gamma_5)] \rightarrow \\ \varphi'_{mob5} &= \sin^{-1} \{ [2 \delta\theta_4 (h + d) / d] / [A + 2 B \delta\theta_4 (h + d) / d] \} \end{aligned} \quad (4.112)$$

$$\begin{aligned} \varphi'_{mob6} &= \sin^{-1} [\gamma_6 / (A + B \gamma_6)] \rightarrow \\ \varphi'_{mob6} &= \sin^{-1} \{ 2 [\delta\theta_4 (h + d) / d + \delta\theta_3 (h + d/2) / (d/2)] / \\ &\quad [(A + 2 B [\delta\theta_4 (h + d) / d + \delta\theta_3 (h + d/2) / (d/2)])] \} \end{aligned} \quad (4.113)$$

It is shown in the Appendix that parameters A and B are given by:

$$A = \gamma_s / G^* \quad (4.114)$$

$$B = 1 + 0.5 (1 - \sin \varphi) / \sin \varphi \quad (4.115)$$

where G^* is the rate of increase of the shear modulus with depth and φ is the angle of shearing resistance at failure. The analytical calculations for the derivation of Equations (4.114) and (4.115) are presented in Appendix B.

The active and passive stresses just above and below each of the points along the wall, with a retained height ratio m calculated from the ULS calculations using the uniform factored (design) strength, can then be determined:

$$\sigma_{hla} = K_{ala} \gamma_s z = 1 / 2 K_{ala} \gamma_s h \quad (4.116)$$

$$\sigma_{hlu} = K_{alu} \gamma_s z = 1 / 2 K_{alu} \gamma_s h \quad (4.117)$$

$$\sigma_{h2a} = K_{a2a} \gamma_s z = K_{a2a} \gamma_s h \quad (4.118)$$

$$\sigma_{h2u} = K_{a2u} \gamma_s z = K_{a2u} \gamma_s h \quad (4.119)$$

$$\sigma_{h3a} = K_{a3a} \gamma_s z = K_{a3a} \gamma_s (h + d/2) \quad (4.120)$$

$$\sigma_{h3u} = K_{a3u} \gamma_s z = K_{a3u} \gamma_s (h + d/2) \quad (4.121)$$

$$\sigma_{h4} = K_{a4} \gamma_s z = K_{a4} \gamma_s (h + d) \quad (4.122)$$

$$\sigma_{h5} = K_{p5} \gamma_s z = K_{p5} \gamma_s d \quad (4.123)$$

$$\sigma_{h6u} = K_{p6u} \gamma_s z = K_{p6u} \gamma_s d / 2 \quad (4.124)$$

$$\sigma_{h6a} = K_{p6a} \gamma_s z = K_{p6a} \gamma_s d / 2 \quad (4.125)$$

If we assume that after a small wall rotation into the excavation a new equilibrium condition is reached, the prop force is equal to the sum of the stresses behind and in front of the wall:

$$\begin{aligned} F + \sigma_{h6a} d / 4 + (\sigma_{h5a} + \sigma_{h6u}) d / 4 - \sigma_{h1a} h / 4 - (\sigma_{h2a} + \sigma_{h1u}) h / 4 - (\sigma_{h3a} \\ + \sigma_{h2u}) d / 4 - (\sigma_{h4a} + \sigma_{h3u}) d / 4 = 0 \end{aligned} \quad (4.126)$$

If m is the retained height ratio ($m = h / H$), Equation (4.126) can be rewritten in the form:

$$\begin{aligned} F / (\gamma_s H^2) = 1 / (4 \gamma_s H) [m (\sigma_{h1a} + \sigma_{h2a} + \sigma_{h1u}) - (1 - m) (\sigma_{h6a} + \sigma_{h5a} + \sigma_{h6u} - \\ \sigma_{h3a} - \sigma_{h2u} - \sigma_{h3u} - \sigma_{h4a})] \end{aligned} \quad (4.127)$$

Taking the moments about the crest O:

$$\Sigma M_o = 0 \rightarrow 1 / (24 \gamma_s H) [2 m^2 \sigma_{h1a} + 4 m^2 \sigma_{h1u} + 5 m^2 \sigma_{h2a} + (1 - m) (5 m + 1)$$

$$\begin{aligned} & \sigma_{h2u} + (1-m) (4 m+2) \sigma_{h3a} + (1-m) (2 m+4) \sigma_{h3u} + (1-m) (m+5) \sigma_{h4a} - (1-m) \\ & (m+5) \sigma_{h5a} - (1-m) (4 m+2) \sigma_{h6a} - (1-m) (2 m+4) \sigma_{h6u} = 0 \end{aligned} \quad (4.128)$$

The normalized bending moments at points 1, 2 and 3 along the wall are given by Equations (4.129), (4.130) and (4.131) respectively.

$$M_1 / (\gamma_s H^3) = 1/2 m F / (\gamma_s H^2) - m^2 \sigma_{h1a} / (24 \gamma_s H) \quad (4.129)$$

$$M_2 / (\gamma_s H^3) = m F / (\gamma_s H^2) - m^2 / (24 \gamma_s H) (4 \sigma_{h1a} + 4 \sigma_{h1u} + 5 \sigma_{h2a}) \quad (4.130)$$

$$M_3 / (\gamma_s H^3) = m^2 / (24 \gamma_s H) (\sigma_{h6u} + 2 \sigma_{h5a} - 2 \sigma_{h4a} - \sigma_{h3u}) \quad (4.131)$$

Combining Equations (4.129), (4.130) and (4.131) with Equations (4.96), (4.97) and (4.98) from Section 4.4.1, where ρ is the wall flexibility ρ defined by Rowe (1952) and is equal to H^4 / EI :

$$1/2 m F / (\gamma_s H^2) - m^2 \sigma_{h1a} / (24 \gamma_s H) = 4 \delta\theta_1 / (m \gamma_s \rho) \quad (4.132)$$

$$\begin{aligned} & m F / (\gamma_s H^2) - m^2 / (24 \gamma_s H) (4 \sigma_{h1a} + 4 \sigma_{h1u} + 5 \sigma_{h2a}) = \\ & = 4 / (\gamma_s \rho) [\delta\theta_2 (1+m) / (1-m) - \delta\theta_1] \end{aligned} \quad (4.133)$$

$$\begin{aligned} & m^2 / (24 \gamma_s H) (\sigma_{h6u} + 2 \sigma_{h5a} - 2 \sigma_{h4a} - \sigma_{h3u}) = \\ & = 4 / [\gamma_s \rho (1-m)^2] (\delta\theta_3 - m \delta\theta_2) \end{aligned} \quad (4.134)$$

The active and passive pressures are related to the wall rotations at discrete points by Equations (4.108) to (4.125). Substitution of their values into Equations (4.127), (4.128), (4.132), (4.133) and (4.134) gives a system of five unknowns: $\delta\theta_1$, $\delta\theta_2$, $\delta\theta_3$, $\delta\theta_4$ and F . The solution of this system requires the determination of parameters A and B . Parameter B can be easily obtained from triaxial tests on soil samples and parameter A depends on G^* , the rate of increase of the shear modulus G with depth. To explore the rotations of a retaining wall propped at the crest for a range of wall flexibility numbers embedded in a

variety of soil conditions, the system of five unknowns is solved numerically for values of φ' from 20° to 40° ; values of $\log(\gamma_s \rho)$ from -4 to 2, where the quantity $(\gamma_s \rho)$ is dimensionless and values of $\log(\gamma_s / G^*)$ from -6 to -1, where the quantity (γ_s / G^*) is dimensionless, assuming full wall friction ($\delta = \varphi'$). The in service normalized maximum bending moments $M_{max} / (\gamma_s H^3)$ and prop loads $F / (\gamma_s H^2)$ and the normalized deformations at points 1 (δ_1/H), 2 (δ_2/H), 3 (δ_3/H) and 4 (δ_4/H) along the wall can then be determined. The in service maximum bending moments and prop loads are divided by the respective values $M_{max,EC7} / (\gamma_s H^3)$ and $F_{EC7} / (\gamma_s H^2)$ calculated from the ULS calculations according to Eurocode 7 (1995). The programming of the numerical calculations was carried out in Mathematica and can be found in the electronic copy of the Appendices. The results are presented in tables in Appendix C. Some of the numerical results are plotted in Figures 4.56 to 4.91.

The ratio of the serviceability maximum bending moments to the bending moments calculated according to Eurocode 7 (1995) ($M_{max} / M_{max,EC7}$), the ratio of the serviceability prop loads to the prop loads calculated according to Eurocode 7 (1995) (F/F_{EC7}) and the normalised displacements ($\delta_1/H, \delta_2/H, \delta_3/H, \delta_4/H$) are plotted in Figures 4.56 to 4.61 when A is equal to 10^{-4} and in Figures 4.62 to 4.67 when A is equal to 10^{-3} against $(\gamma_s \rho)$ for different values of φ' ; in Figures 4.68 to 4.73 when $\gamma_s \rho$ is equal to 10^{-1} and in Figures 4.74 to 4.79 when $\gamma_s \rho$ is equal to 10 against the parameter A for different values of φ' ; in Figures 4.80 to 4.85 when φ' is equal to 20° and in Figures 4.86 to 4.91 when φ' is equal to 25° against $\gamma_s \rho$ for different values of A . Tables and figures for a wider range of values can be found in Appendix D.

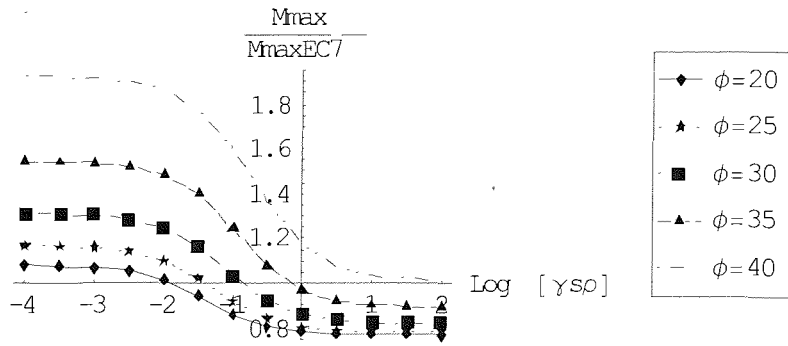


Figure 4.56: The ratio of $M_{max} / M_{max,EC7}$ against $(\gamma_s \rho)$ for different values of ϕ' when $A = 10^{-4}$.

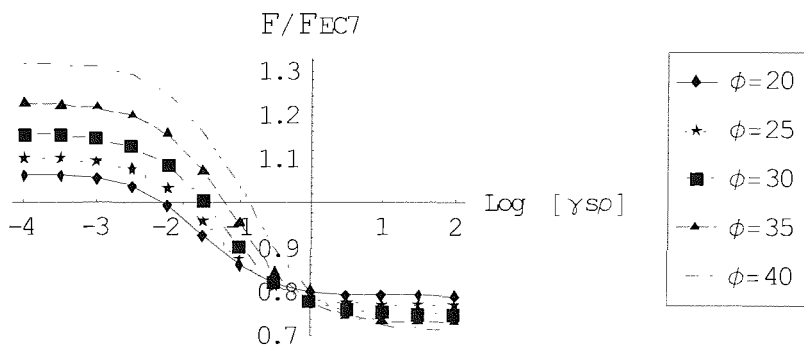


Figure 4.57: The ratio of F / F_{EC7} against $(\gamma_s \rho)$ for different values of ϕ' when $A = 10^{-4}$.

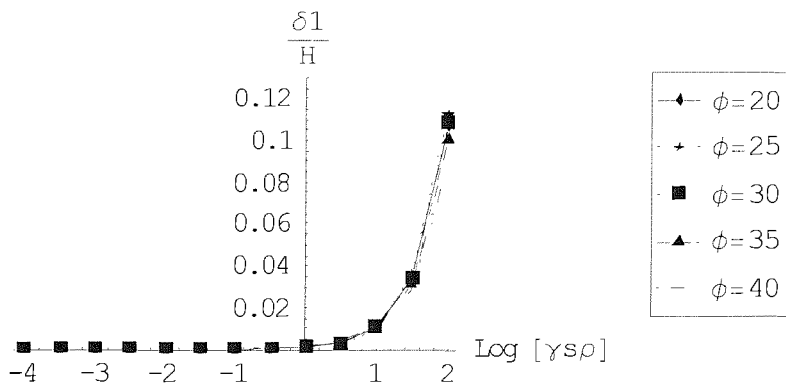


Figure 4.58: Normalized deformations at depth $h/2$ from the crest against $(\gamma_s \rho)$ for different values of ϕ' when $A = 10^{-4}$.

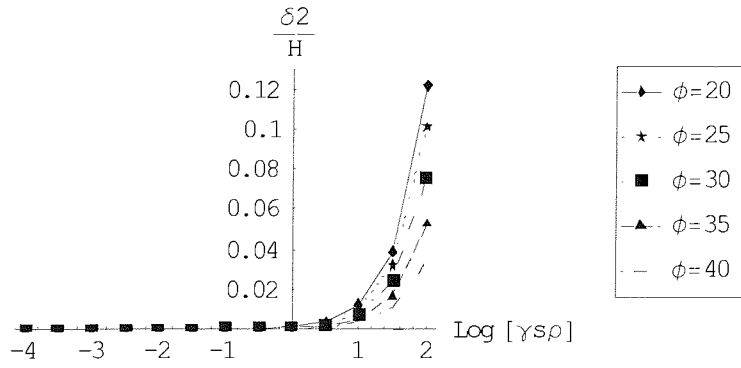


Figure 4.59: Normalized deformations at depth h from the crest against $(\gamma_s \rho)$ for different values of ϕ' when $A = 10^{-4}$.

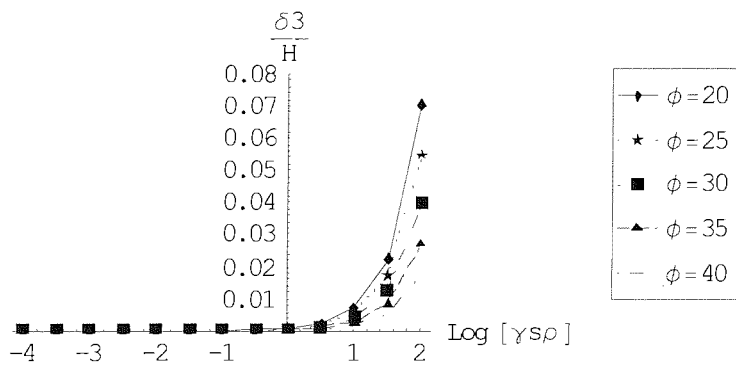


Figure 4.60: Normalized deformations at depth $h+d/2$ from the crest against $(\gamma_s \rho)$ for different values of ϕ' when $A = 10^{-4}$.

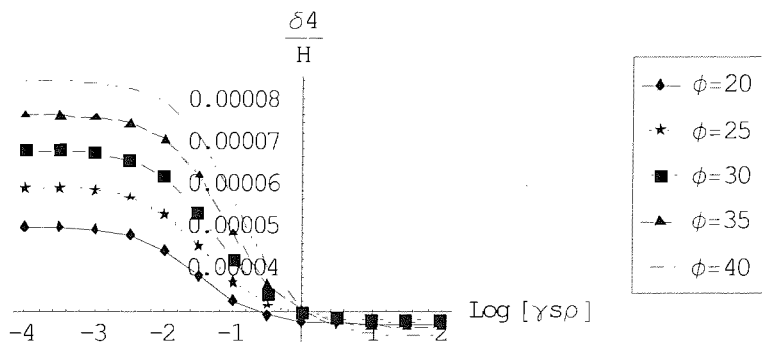


Figure 4.61: Normalized deformations at depth H from the crest against $(\gamma_s \rho)$ for different values of ϕ' when $A = 10^{-4}$.

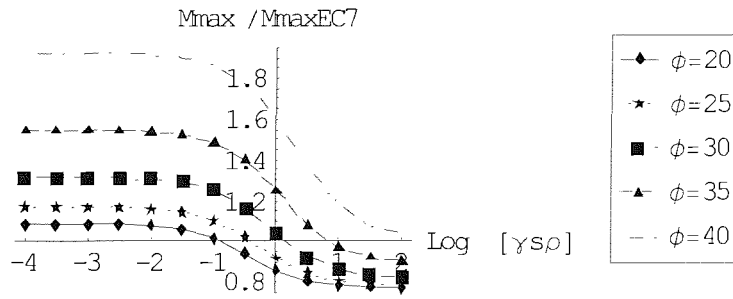


Figure 4.62: The ratio of $M_{max} / M_{max,EC7}$ against $(\gamma_s \rho)$ for different values of ϕ' when $A = 10^{-3}$.

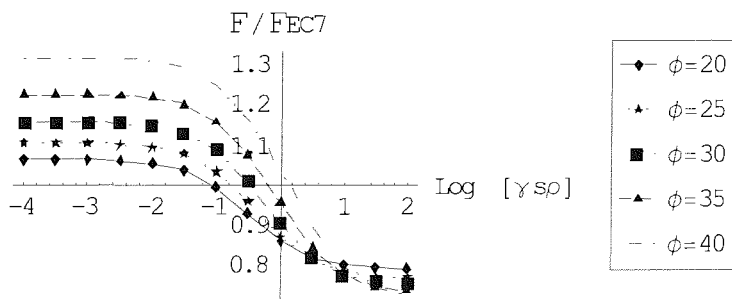


Figure 4.63: The ratio of F / F_{EC7} against $(\gamma_s \rho)$ for different values of ϕ' when $A = 10^{-3}$.

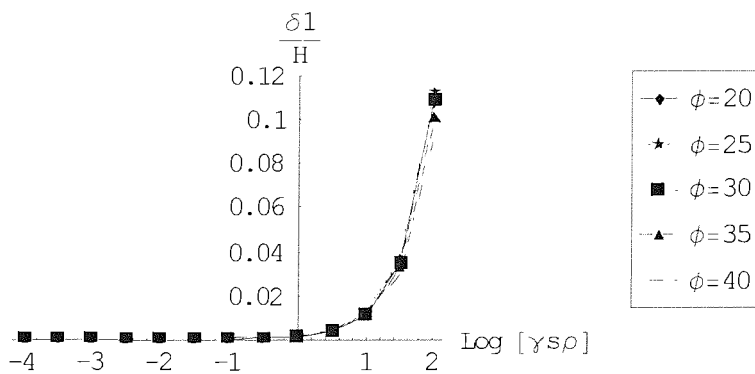


Figure 4.64: Normalized deformations at depth $h/2$ from the crest against $(\gamma_s \rho)$ for different values of ϕ' when $A = 10^{-3}$.

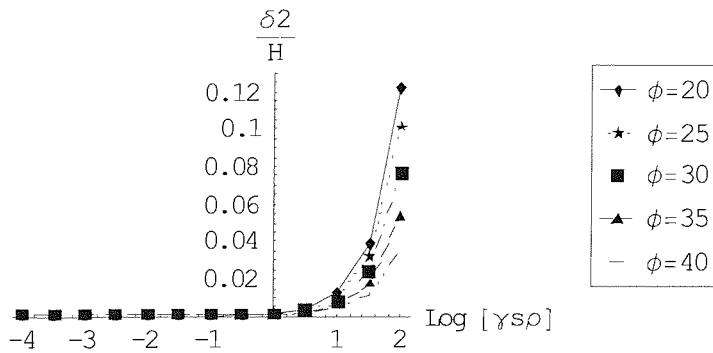


Figure 4.65: Normalized deformations at depth h from the crest against $(\gamma_s \rho)$ for different values of ϕ' when $A = 10^{-3}$.

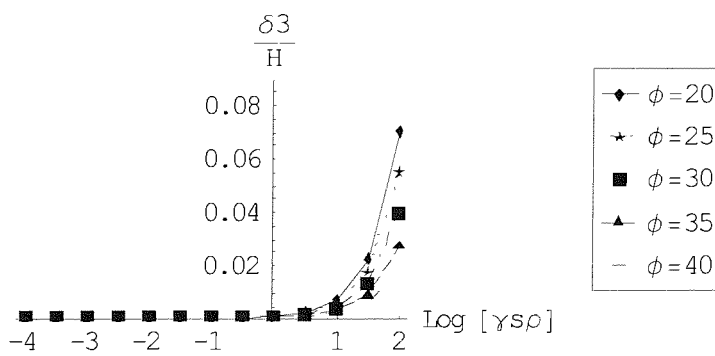


Figure 4.66: Normalized deformations at depth $h+d/2$ from the crest against $(\gamma_s \rho)$ for different values of ϕ' when $A = 10^{-3}$.

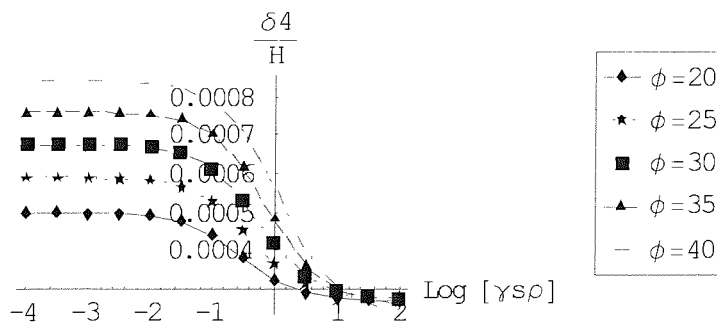


Figure 4.67: Normalized deformations at depth H from the crest against $(\gamma_s \rho)$ for different values of ϕ' when $A = 10^{-3}$.

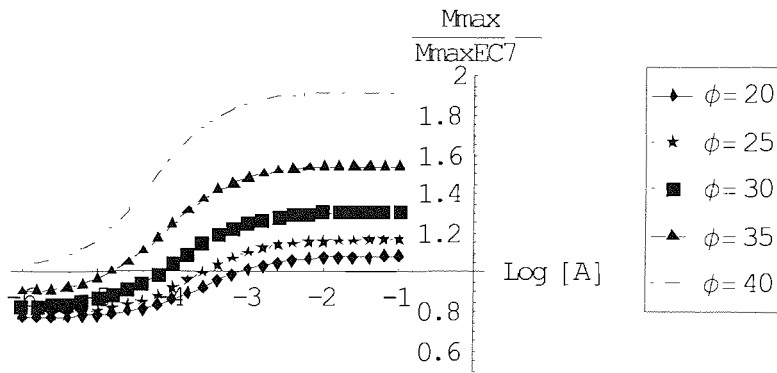


Figure 4.68: The ratio of $M_{max}/M_{max,EC7}$ against parameter A for different values of ϕ' when $(\gamma_s \rho)=10^{-1}$.

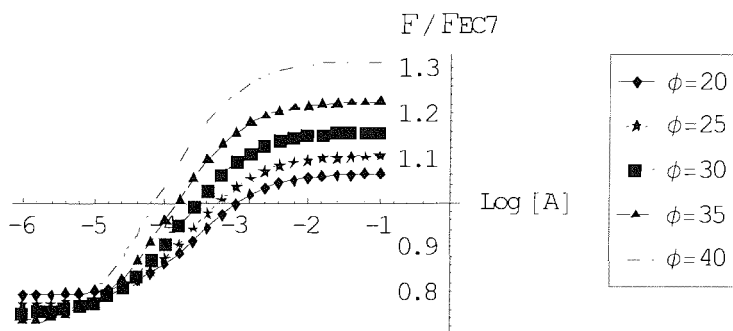


Figure 4.69: The ratio of F/F_{EC7} against parameter A for different values of ϕ' when $(\gamma_s \rho)=10^{-1}$.

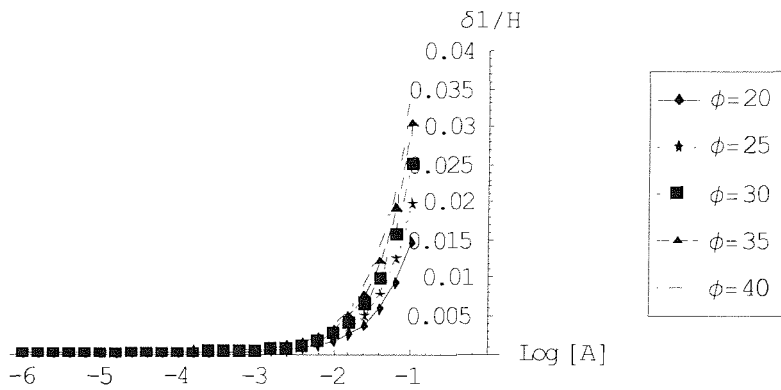


Figure 4.70: Normalized deformations at depth $h/2$ from the crest against parameter A for different values of ϕ' when $(\gamma_s \rho)=10^{-1}$.

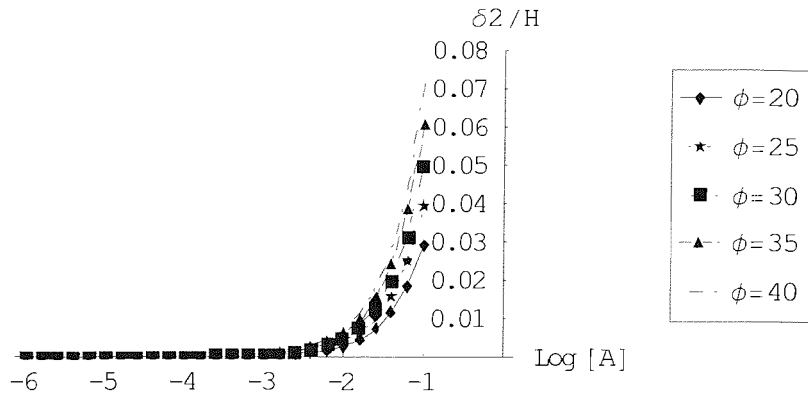


Figure 4.71: Normalized deformations at depth h from the crest against parameter A for different values of ϕ' when $(\gamma_s \rho) = 10^{-1}$.

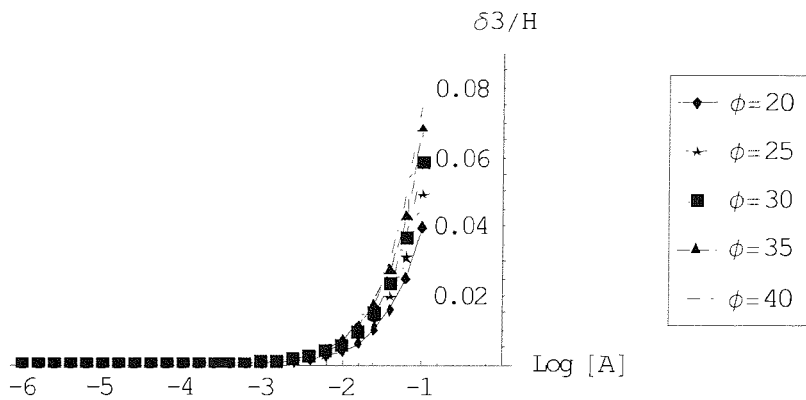


Figure 4.72: Normalized deformations at depth $h + d/2$ from the crest against parameter A for different values of ϕ' when $(\gamma_s \rho) = 10^{-1}$.

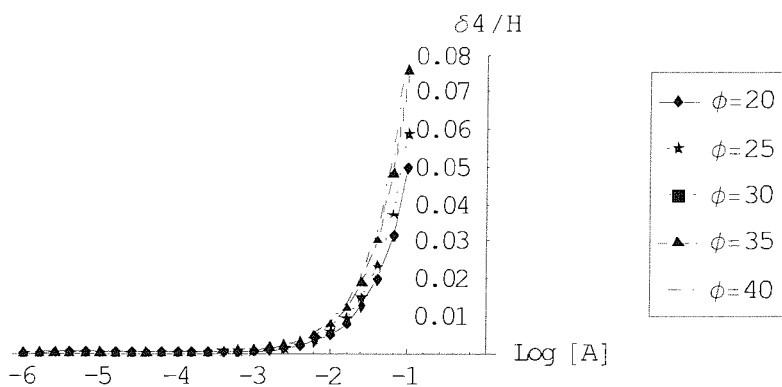


Figure 4.73: Normalized deformations at depth H from the crest against parameter A for different values of ϕ' when $(\gamma_s \rho) = 10^{-1}$.

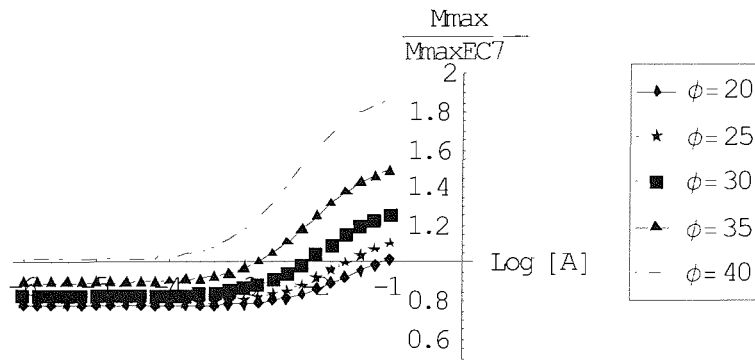


Figure 4.74: The ratio of $M_{max}/M_{max,EC7}$ against parameter A for different values of ϕ' when $(\gamma_s \rho)=10$.

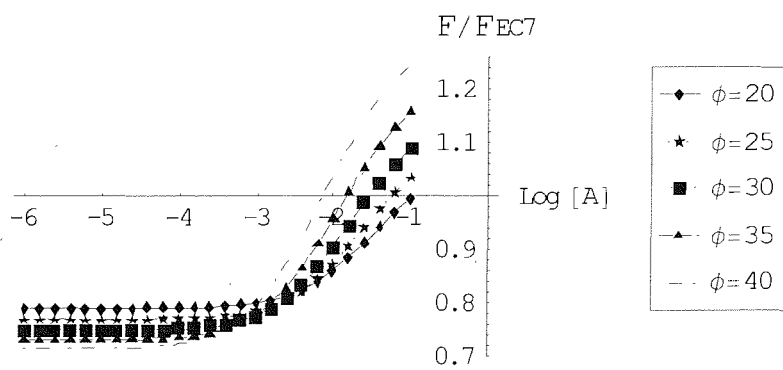


Figure 4.75: The ratio of F/F_{EC7} against parameter A for different values of ϕ' when $(\gamma_s \rho)=10$.

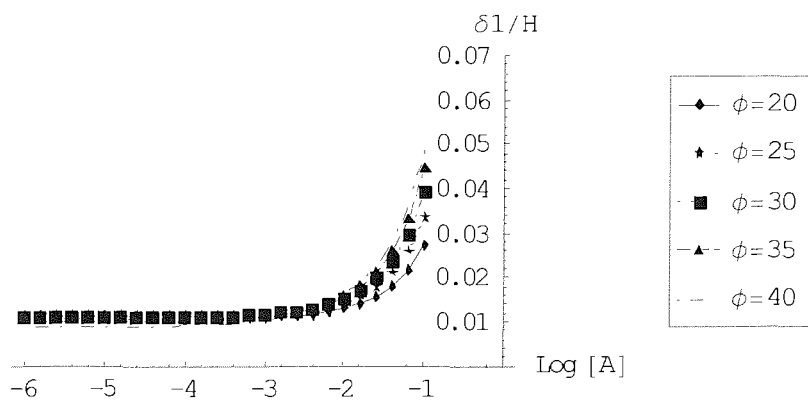


Figure 4.76: Normalized deformations at depth $h/2$ from the crest against parameter A for different values of ϕ' when $(\gamma_s \rho)=10$.

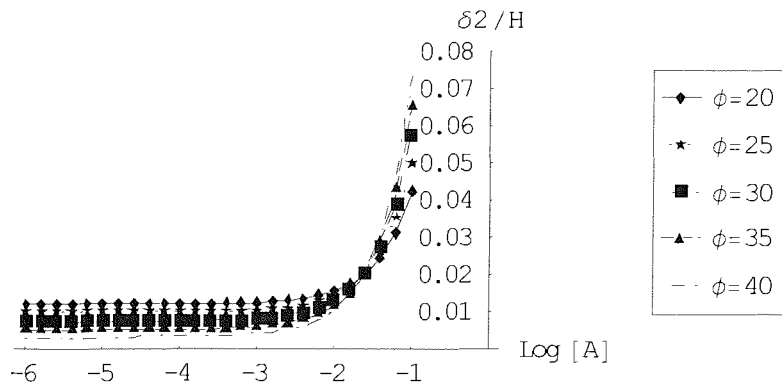


Figure 4.77: Normalized deformations at depth h from the crest against parameter A for different values of ϕ' when $(\gamma_s \rho)=10$.

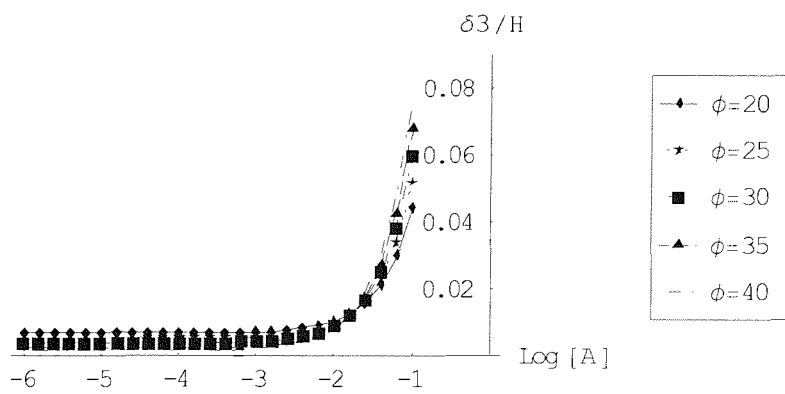


Figure 4.78: Normalized deformations at depth $h+d/2$ from the crest against parameter A for different values of ϕ' when $(\gamma_s \rho)=10$.

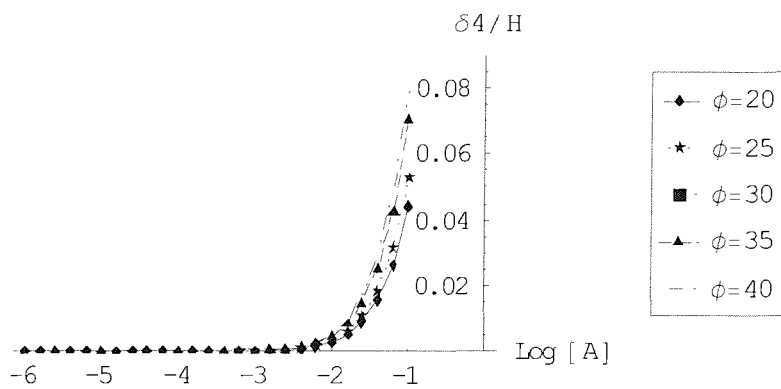


Figure 4.79: Normalized deformations at depth H from the crest against parameter A for different values of ϕ' when $(\gamma_s \rho)=10$.

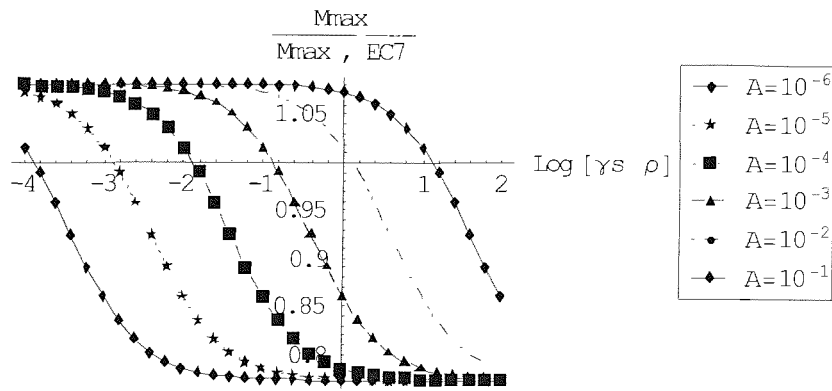


Figure 4.80: The ratio of $M_{max}/M_{max,EC7}$ against $(\gamma_s \rho)$ for different values of A when $\varphi' = 20^\circ$.

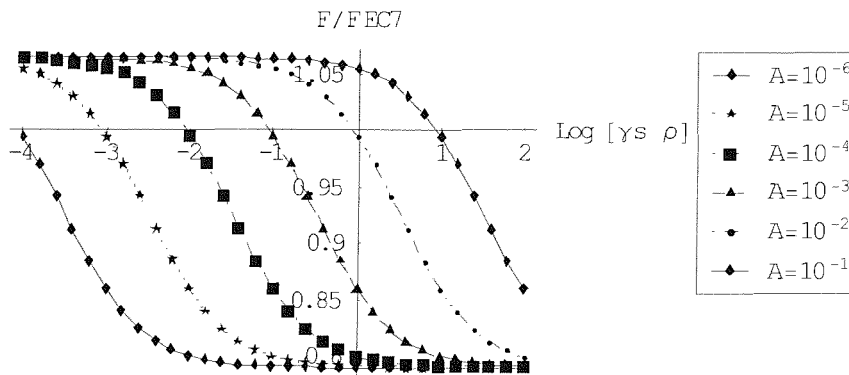


Figure 4.81: The ratio of F/F_{EC7} against $(\gamma_s \rho)$ for different values of A when $\varphi' = 20^\circ$.

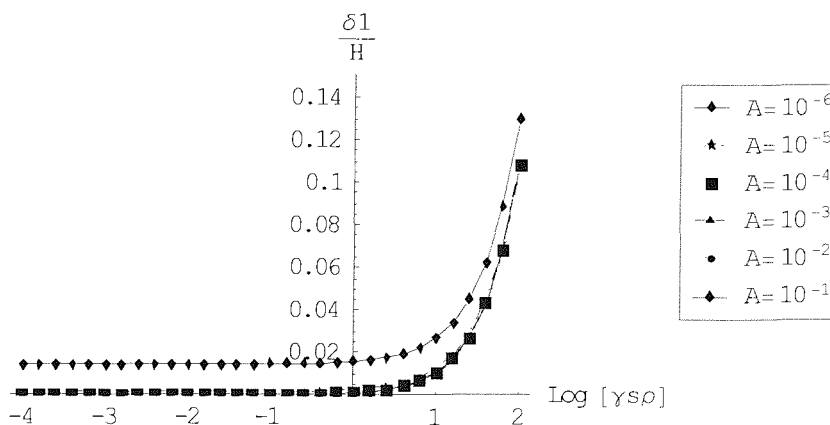


Figure 4.82: Normalized deformations at depth $h/2$ from the crest against $(\gamma_s \rho)$ for different values of A when $\varphi' = 20^\circ$.

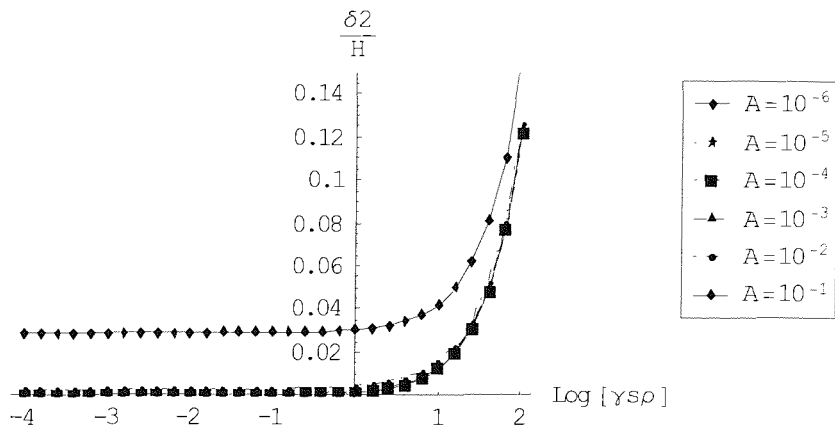


Figure 4.83: Normalized deformations at depth h from the crest against $(\gamma_s \rho)$ for different values of A when $\varphi' = 20^\circ$.

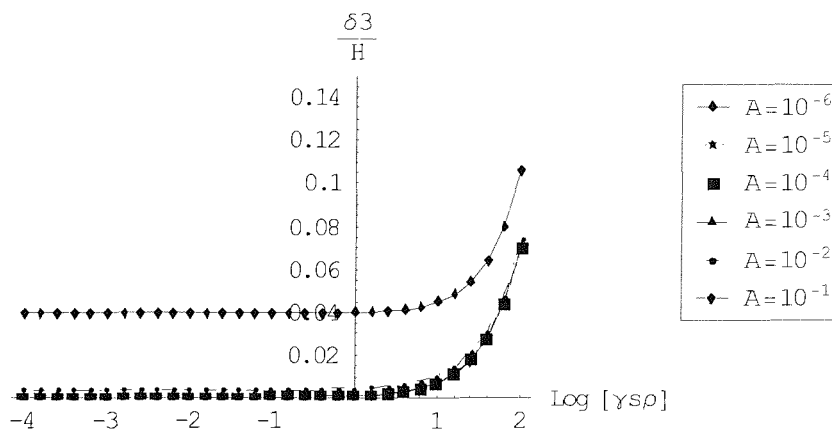


Figure 4.84: Normalized deformations at depth $h+d/2$ from the crest against $(\gamma_s \rho)$ for different values of A when $\varphi' = 20^\circ$.

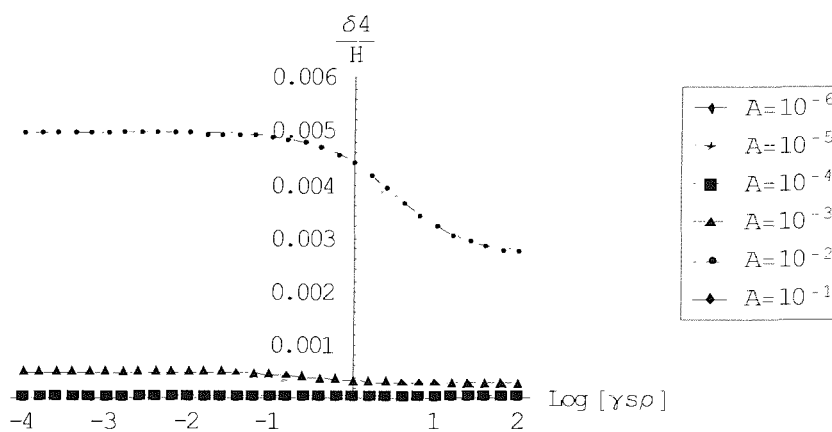


Figure 4.85: Normalized deformations at depth H from the crest against $(\gamma_s \rho)$ for different values of A when $\varphi' = 20^\circ$.

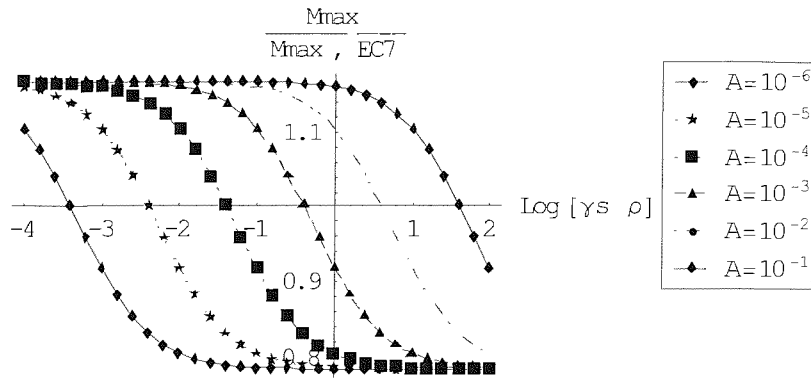


Figure 4.86: The ratio of $M_{max}/M_{max,EC7}$ against $(\gamma_s \rho)$ for different values of A when $\phi' = 25^\circ$.

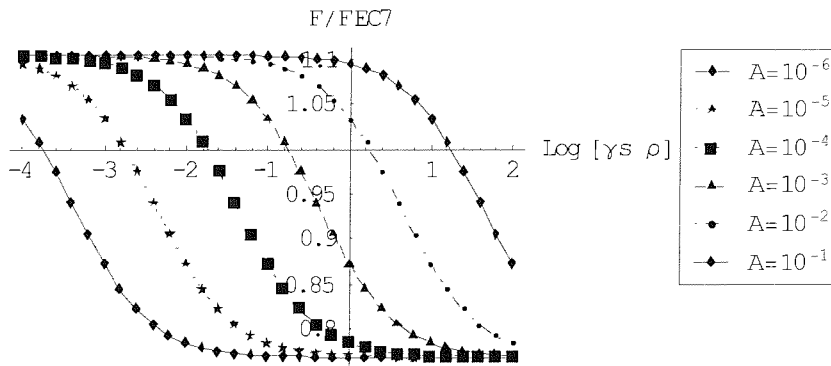


Figure 4.87: The ratio of F/F_{EC7} against $(\gamma_s \rho)$ for different values of A when $\phi' = 25^\circ$.

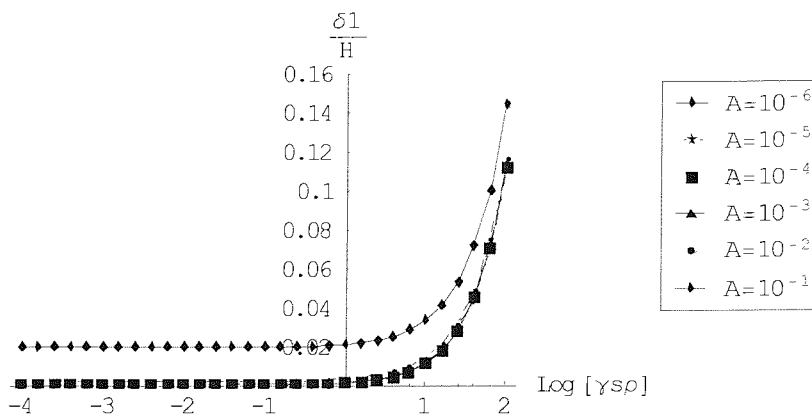


Figure 4.89: Normalized deformations at depth $h/2$ from the crest against $(\gamma_s \rho)$ for different values of A when $\phi' = 25^\circ$.

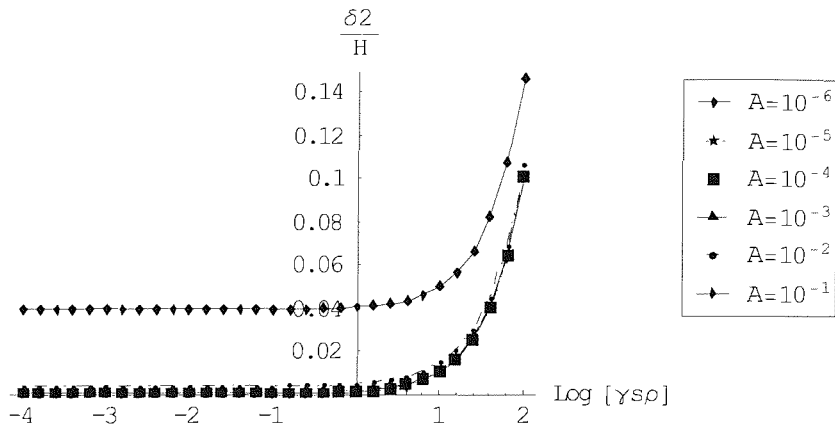


Figure 4.90: Normalized deformations at depth h from the crest against $(\gamma_s \rho)$ for different values of A when $\phi' = 25^\circ$.

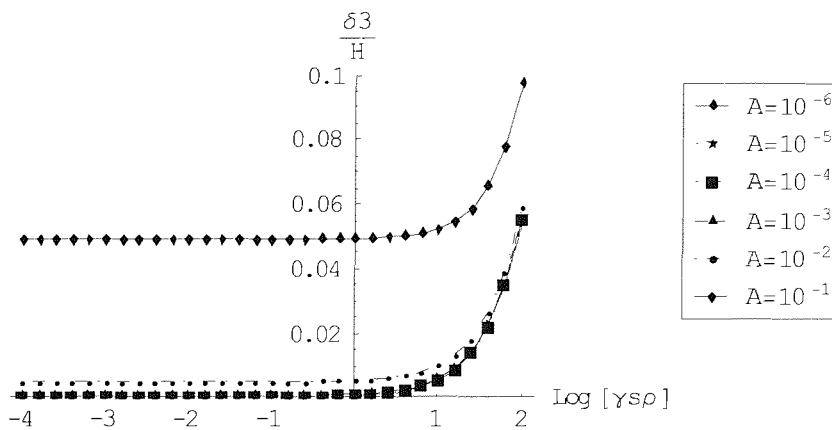


Figure 4.91: Normalized deformations at depth $h+d/2$ from the crest against $(\gamma_s \rho)$ for different values of A when $\phi' = 25^\circ$.

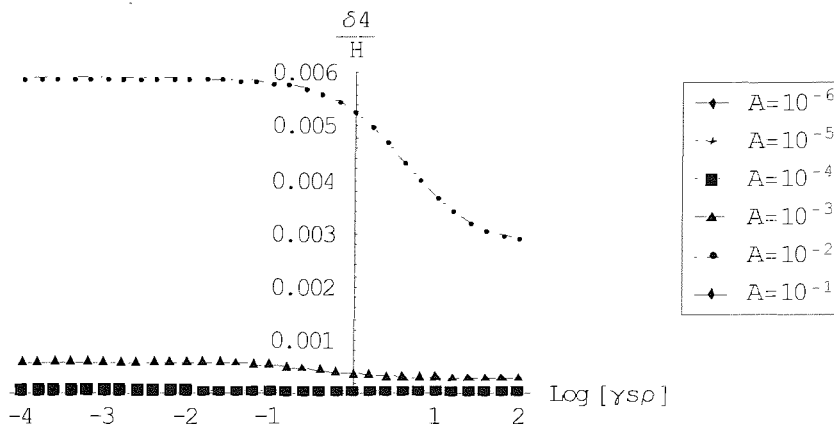


Figure 4.92: Normalized deformations at depth H from the crest against $(\gamma_s \rho)$ for different values of A when $\phi' = 25^\circ$.

The origin of axes for the $M_{max} / M_{max,EC7}$ and F / F_{EC7} graphs is at (0, 1). The $x-x'$ axis represents the case when the maximum bending moments and prop loads calculated according to the mobilized strength method is equal to the respective magnitudes calculated according to Eurocode 7 (1995). For the parts of the curves above the $x-x'$ axis Eurocode 7 (1995) might underpredict, whereas for the parts of the curves below the $x-x'$ axis might overpredict the maximum bending moments and the prop loads compared with the mobilized strength method. The figures show that as the wall flexibility or the soil stiffness increases, the maximum bending moments and the prop loads reduce below their limit equilibrium values. The pattern of the reduction is similar for different values of ϕ' . At very high or very low values of wall flexibility or soil stiffness there is insignificant change in the ratios $M_{max} / M_{max,EC7}$ and F / F_{EC7} and they tend to similar values. However, it should be noted that very high or low values of wall flexibility or soil stiffness might not be realistic, but are included to represent extreme conditions. According to the curves, as the soil becomes stiffer, the wall should be stiffer to get the same reduction in the bending moments. This is in agreement with the definition of $R_{crit} = G^* H^4 / EI$ as presented in Chapter 3; as G^* increases, $\rho = H^4 / EI$ should decrease to maintain the same value of R_{crit} . Moreover, greater values of soil stiffness or wall flexibility are needed for a given reduction of $M_{max} / M_{max,EC7}$ and F / F_{EC7} when ϕ' is high (40°) than when it is low (20°).

The normalized displacements increase with decreasing soil stiffness or increasing wall flexibility, with the exception of δ_4/H which decreases with increasing wall flexibility. This may be explained by attributing δ_4/H to rigid body rotation about the prop. Moreover, there is insignificant change in the values of the normalized displacements when $\log A < -2$.

It should be noted that the accuracy of the MSD method as presented in this Section may be improved if the soil behind and in front of the retaining wall is divided into a larger number of soil zones and a more complex model of the soil behaviour is adopted. In this thesis, the number of soil zones and the soil model incorporated in the MSD method can achieve reasonable accuracy and meet the objective for a simple approach.

4.7 SUMMARY

In Chapter 4, new kinematically admissible soil displacement fields have been introduced to apply the MSD method to flexible retaining walls propped at the crest in conditions of zero pore water pressures. The wall flexibility has been idealised into a simple mechanism and the hyperbolic relationship, introduced by Duncan and Cheng (1970), has been modified and is used to associate the mobilized shear strain with the mobilized shear strength. The ratios of the MSD maximum bending moments and prop loads to those calculated according to Eurocode 7 (EC7, 1995) and the displacements at characteristic points along the wall are plotted against the shear strength before excavation, wall flexibility and soil stiffness. According to the MSD results presented in this Chapter, the maximum bending moments and prop loads are significantly reduced from the values suggested by Eurocode 7 (EC7, 1995) for flexible walls or stiff soils. However, Eurocode 7 (EC7, 1995) might underpredict the maximum bending moments and prop loads for rigid walls or less stiff soils. Regarding the displacements, little change is noticed for large values of soil stiffness or small values of wall flexibility.

5. ANALYSIS AND DESIGN OF FLEXIBLE RETAINING WALLS PROPPED AT THE CREST IN CONDITIONS OF PORE WATER PRESSURES CORRESPONDING TO LINEAR SEEPAGE

5.1 INTRODUCTION

The pore water pressures may have a considerable effect on retaining structures. Therefore, their influence when excavating or constructing retaining walls should not be neglected. In this chapter, the MSD method is applied to flexible retaining walls propped at the crest in conditions of pore water pressures corresponding to an approximate state of linear seepage from an original ground water table at the ground level and at half the retained height level. Initially, the retained height ratio, m , is determined from the ULS calculations according to Eurocode 7 (EC7, 1995). The maximum bending moments and prop loads are calculated according to Eurocode 7 (EC7, 1995) and according to the MSD method. The ratios of the maximum bending moments and prop loads derived from the MSD method to those determined by Eurocode 7 ($M_{max} / M_{max,EC7}$, F / F_{EC7}) and the normalized bending moments at characteristic points along the wall (δ_1/H , δ_2/H , δ_3/H , δ_4/H) are plotted for different values of initial shear strength, wall flexibility and soil stiffness, similarly to the procedure described in Chapter 4.

5.2 ULS CALCULATIONS: ORIGINAL WATER TABLE AT GROUND LEVEL

Figure 5.1 shows the horizontal stress distributions together with the pore water pressures, assuming linear seepage from a water table at ground level, behind and in front of a retaining wall which is in limiting equilibrium. The normalized pore water pressures $u / (\gamma_s H)$ at the toe are given by Equation (5.1) and the normalized effective active $\sigma'_{ha} / (\gamma_s H)$ and passive stresses $\sigma'_{hp} / (\gamma_s H)$ at the toe of the wall are given by

Equations (5.2) and (5.3) respectively, where γ_s is the soil unit weight and H is the overall height of the wall.

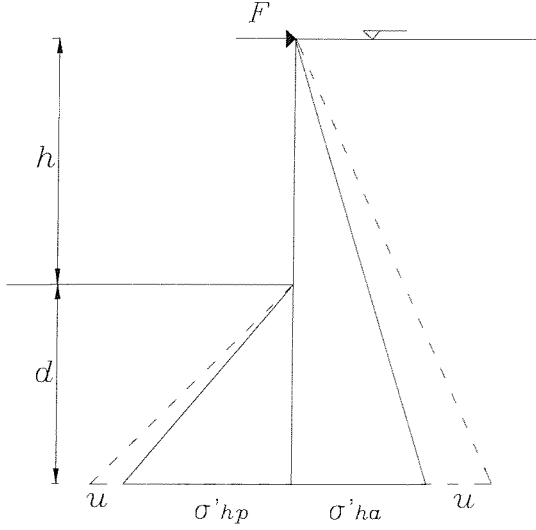


Figure 5.1: Stress and pore water pressure distribution in limit equilibrium behind and in front of a retaining wall propped at the crest in conditions of pore water pressures at ground level.

$$u = \gamma_w d [1 + h / (2d + h)] \rightarrow u / (\gamma_s H) = 2 \gamma_w (1-m) / [\gamma_s (2-m)] \quad (5.1)$$

$$\sigma'_{ha} / (\gamma_s H) = K_a [1 - u / (\gamma_s H)] = K_a \{1 - \gamma_w (1-m) / [\gamma_s (2-m)]\} \quad (5.2)$$

$$\sigma'_{hp} / (\gamma_s H) = K_p [1 - m - u / (\gamma_s H)] = K_p \{1 - m - \gamma_w (1-m) / [\gamma_s (2-m)]\} \quad (5.3)$$

From the condition of horizontal stress equilibrium, the normalized prop force $F / (\gamma_s H)$ may be calculated

$$\begin{aligned} F / (\gamma_s H^2) = & 1 / 2 K_a [1 - u / (\gamma_s H)] - 1 / 2 (1-m) K_p [1 - m - u / (\gamma_s H)] \\ & + 1 / 2 m u / (\gamma_s H) \end{aligned} \quad (5.4)$$

where m is the retained height ratio ($m = h / H$).

Taking the moments at the point O at the crest, m may be calculated by Equation (5.5):

$$\begin{aligned} \sum M_h = 0 \rightarrow & 1/3 \sigma'_{ha} / (\gamma_s H) - 1/6 \sigma'_{hp} / (\gamma_s H) (1-m) (2+m) + 1/3 u / (\gamma_s H) \\ & - 1/6 (1-m) (2+m) u / (\gamma_s H) = 0 \end{aligned} \quad (5.5)$$

Assuming full wall friction, the active and passive earth pressure coefficients are given by Equations (4.104) and (4.105). The determination of the retained height ratio m , enables the calculation of the maximum bending moment along the wall assuming a uniform value of φ'_{mob} according to Eurocode 7 (EC7, 1997).

5.3 SLS CALCULATIONS: ORIGINAL WATER TABLE AT GROUND LEVEL

For a wall with a retained height ratio m calculated from the ULS calculations using factored (design) strength and pore water pressures corresponding to a linear seepage from a water table at ground level, the distribution of total stresses in each soil zone is similar to that shown in Figure 4.55 and their normalised values are given by Equations (5.12) to (5.21). The normalised pore water pressures in each soil zone are determined by Equations (5.7) to (5.11), where $u/(\gamma_s H)$ are the pore water pressures at the toe of the wall given by Equation (5.6) and γ_w the unit weight of water:

$$u/(\gamma_s H) = \gamma_w d / \gamma_s [1 + h/(2d+h)] = 2 (1 - m) \gamma_w / [\gamma (2-m)] \quad (5.6)$$

$$u_1/(\gamma_s H) = h/2 \ 1/H \ u/(\gamma_s H) = 1/2 \ m \ u/(\gamma_s H) \quad (5.7)$$

$$u_2/(\gamma_s H) = h/H \ u/(\gamma_s H) = m \ u/(\gamma_s H) \quad (5.8)$$

$$u_3/(\gamma_s H) = (h+d/2)/H \ u/(\gamma_s H) = 1/2 (1+m) \ u/(\gamma_s H) \quad (5.9)$$

$$u_5/(\gamma_s H) = u/(\gamma_s H) \quad (5.10)$$

$$u_6/(\gamma_s H) = d/2 \ / \ d \ u/(\gamma_s H) = 1/2 \ u/(\gamma_s H) \quad (5.11)$$

$$\sigma_{h1a} = 1 / 2 \ K_{a1a} (\gamma_s h - u_1) + u_1 \rightarrow$$

$$\begin{aligned}\sigma_{h1a}/(\gamma_s H) &= 1/2 m K_{a1a} + u/(\gamma_s H) (1 - K_{a1a}) \\ &= 1/2 m K_{a1a} + 1/2 m u/(\gamma_s H) (1 - K_{a1a})\end{aligned}\quad (5.12)$$

$$\sigma_{h1u}/(\gamma_s H) = 1/2 m K_{a1u} + 1/2 m u/(\gamma_s H) (1 - K_{a1u}) \quad (5.13)$$

$$\sigma_{h2a}/(\gamma_s H) = m K_{a2a} + m u/(\gamma_s H) (1 - K_{a2a}) \quad (5.14)$$

$$\sigma_{h2u}/(\gamma_s H) = m K_{a2u} + m u/(\gamma_s H) (1 - K_{a2u}) \quad (5.15)$$

$$\sigma_{h3a}/(\gamma_s H) = 1/2(1+m) K_{a3a} + 1/2(1+m) u/(\gamma_s H) (1 - K_{a3a}) \quad (5.16)$$

$$\sigma_{h3u}/(\gamma_s H) = 1/2(1+m) K_{a3u} + 1/2(1+m) u/(\gamma_s H) (1 - K_{a3u}) \quad (5.17)$$

$$\sigma_{h4}/(\gamma_s H) = K_{a4} + u/(\gamma_s H) (1 - K_{a4}) \quad (5.18)$$

$$\sigma_{h5}/(\gamma_s H) = K_{p5} (1-m) + u/(\gamma_s H) (1 - K_{p5}) \quad (5.19)$$

$$\sigma_{h6a}/(\gamma_s H) = 1/2(1-m) K_{p6a} + 1/2 u/(\gamma_s H) (1 - K_{p6a}) \quad (5.20)$$

$$\sigma_{h6u}/(\gamma_s H) = 1/2(1-m) K_{p6u} + 1/2 u/(\gamma_s H) (1 - K_{p6u}) \quad (5.21)$$

Substituting the values of total stresses into Equations (4.127), (4.128), (4.132), (4.133) and (4.134), gives a system of five unknowns which is solved numerically for a range of values of ϕ' , $\log(\gamma_s \rho)$ and $\log(\gamma_s / G^*)$ as described in Section 4.6.

The results are presented in tables and figures in the Appendix. To enable comparison of the curves for zero pore water pressures to those with the original water table at ground level, some of the numerical results are presented in Figures 5.2 to 5.37 similarly to Figures 4.56 to 4.91 in Section 4.6.

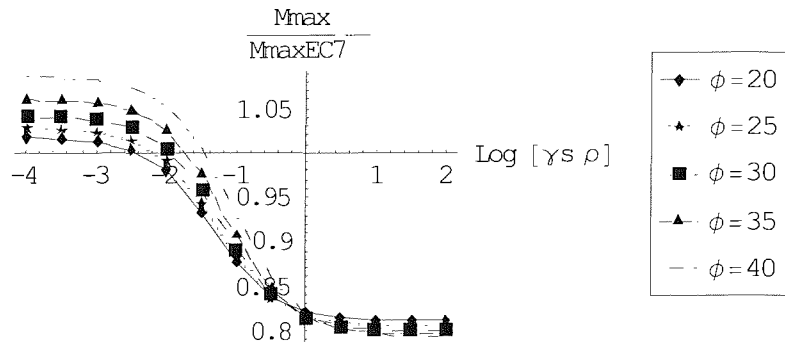


Figure 5.2: The ratio of $M_{max} / M_{max,EC7}$ against $(\gamma_s \rho)$ for different values of ϕ' when $A = 10^{-4}$ and the original water table is at ground level.

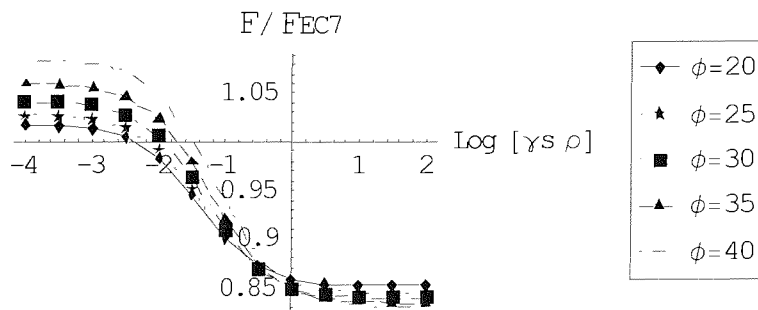


Figure 5.3: The ratio of F / F_{EC7} against $(\gamma_s \rho)$ for different values of ϕ' when $A = 10^{-4}$ and the original water table is at ground level.

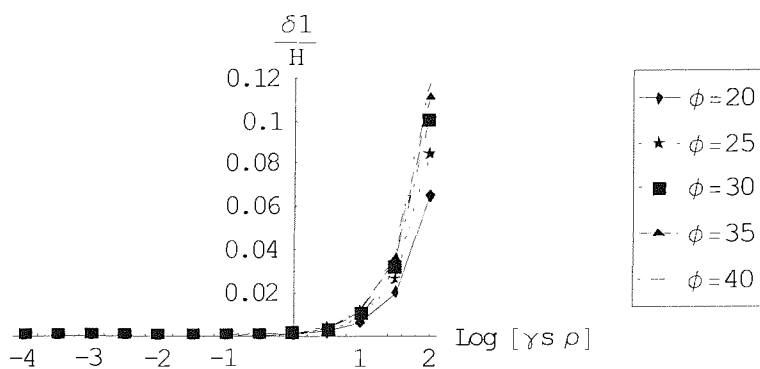


Figure 5.4: Normalized deformations at depth $h/2$ from the crest against $(\gamma_s \rho)$ for different values of ϕ' when $A = 10^{-4}$ and the original water table is at ground level.

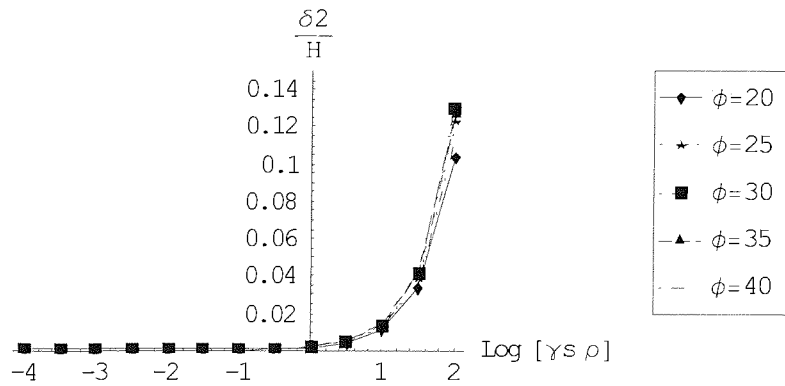


Figure 5.5: Normalized deformations at depth h from the crest against $(\gamma_s \rho)$ for different values of ϕ' when $A = 10^{-4}$ and the original water table is at ground level.

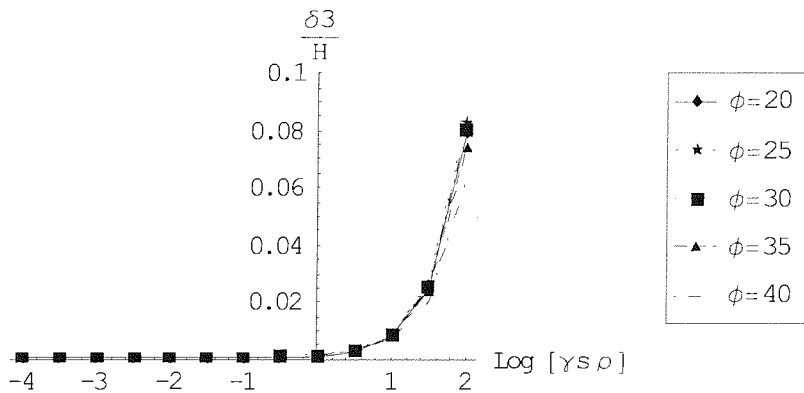


Figure 5.6: Normalized deformations at depth $h+d/2$ from the crest against $(\gamma_s \rho)$ for different values of ϕ' when $A = 10^{-4}$ and the original water table is at ground level.

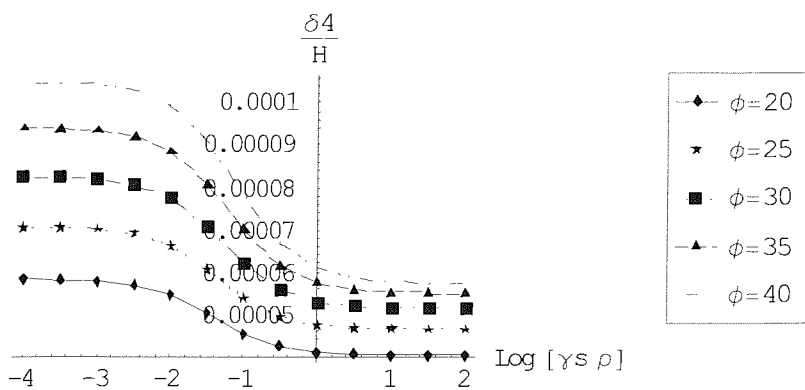


Figure 5.7: Normalized deformations at depth H from the crest against $(\gamma_s \rho)$ for different values of ϕ' when $A = 10^{-4}$ and the original water table is at ground level.

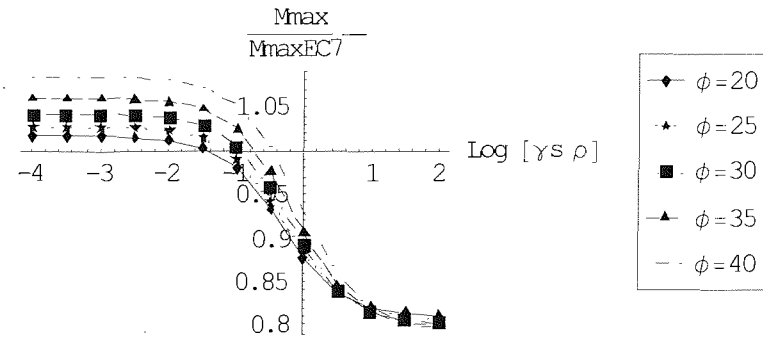


Figure 5.8: The ratio of $M_{max} / M_{max,EC7}$ against $(\gamma_s \rho)$ for different values of ϕ' when $A = 10^{-3}$ and the original water table is at ground level.

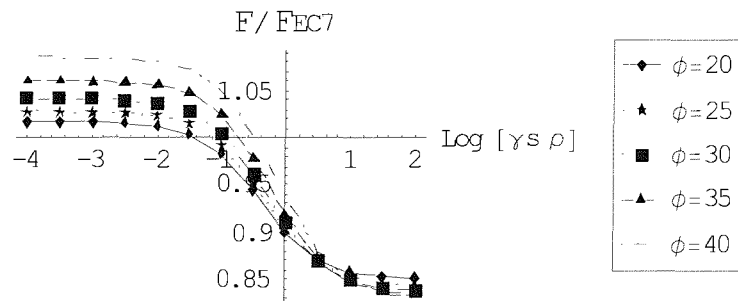


Figure 5.9: The ratio of F / F_{EC7} against $(\gamma_s \rho)$ for different values of ϕ' when $A = 10^{-3}$ and the original water table is at ground level.

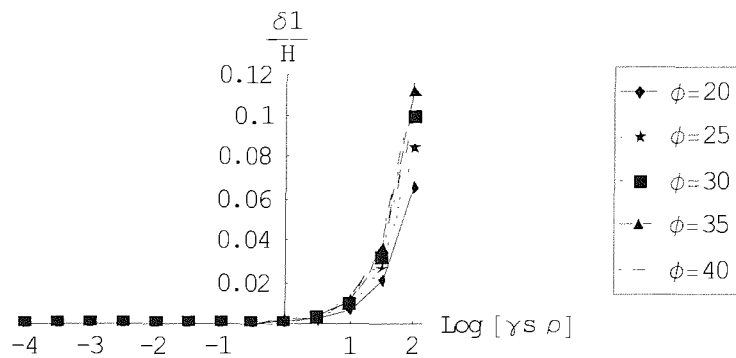


Figure 5.10: Normalized deformations at depth $h/2$ from the crest against $(\gamma_s \rho)$ for different values of ϕ' when $A = 10^{-3}$ and the original water table is at ground level.

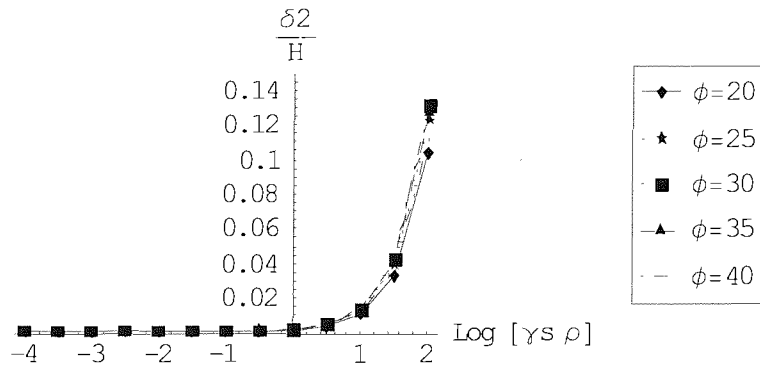


Figure 5.11 Normalized deformations at depth h from the crest against $(\gamma_s \rho)$ for different values of ϕ' when $A = 10^{-3}$ and the original water table is at ground level.

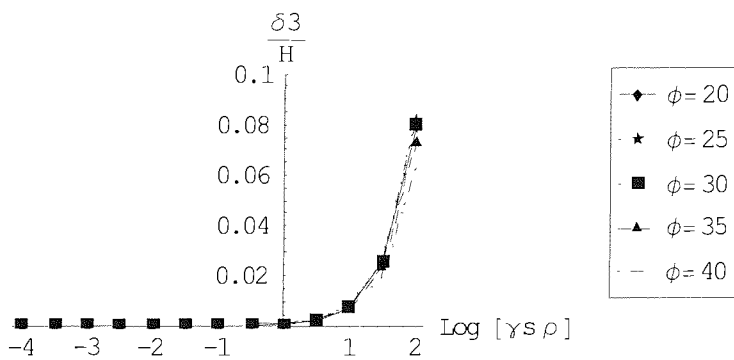


Figure 5.12: Normalized deformations at depth $h+d/2$ from the crest against $(\gamma_s \rho)$ for different values of ϕ' when $A = 10^{-3}$ and the original water table is at ground level.

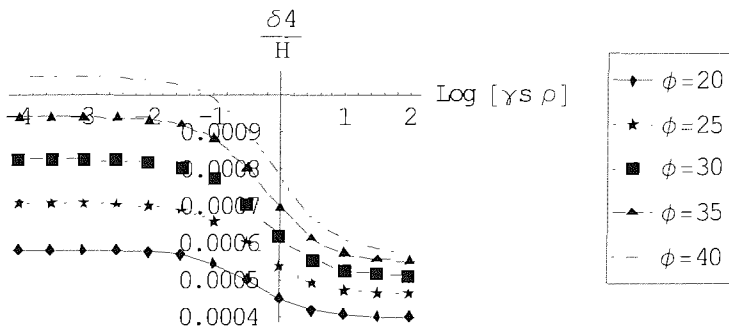


Figure 5.13: Normalized deformations at depth H from the crest against $(\gamma_s \rho)$ for different values of ϕ' when $A = 10^{-3}$ and the original water table is at ground level.

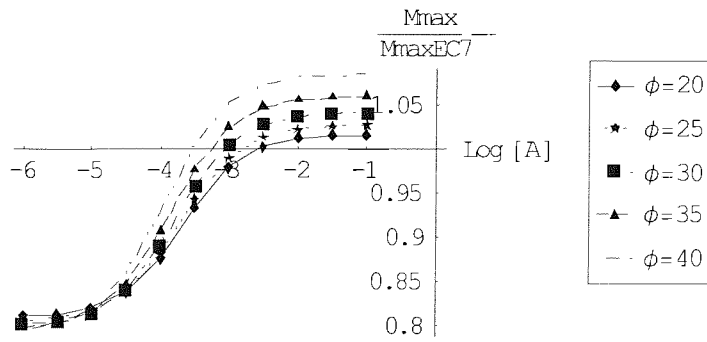


Figure 5.14: The ratio of $M_{max} / M_{max,EC7}$ against parameter A for different values of ϕ' when $(\gamma_s \rho) = 10^{-1}$ and the original water table is at ground level.

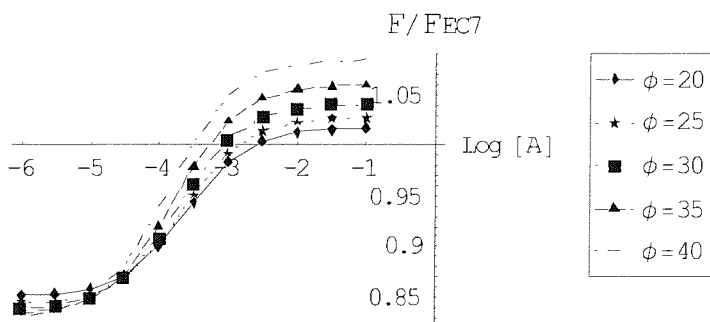


Figure 5.15: The ratio of F / F_{EC7} against parameter A for different values of ϕ' when $(\gamma_s \rho) = 10^{-1}$ and the original water table is at ground level.

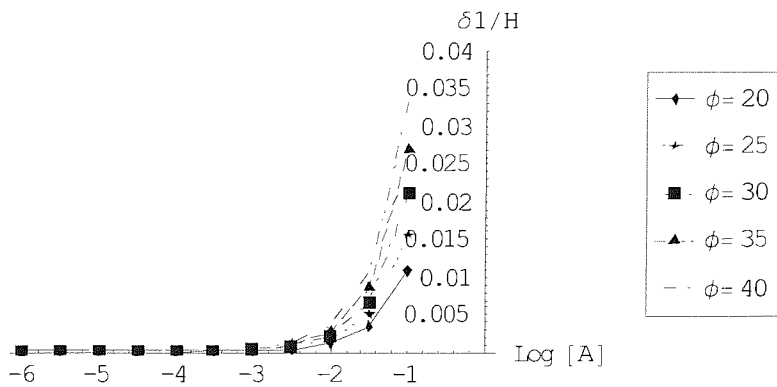


Figure 5.16: Normalized deformations at depth $h/2$ from the crest against parameter A for different values of ϕ' when $(\gamma_s \rho) = 10^{-1}$ and the original water table is at ground level.

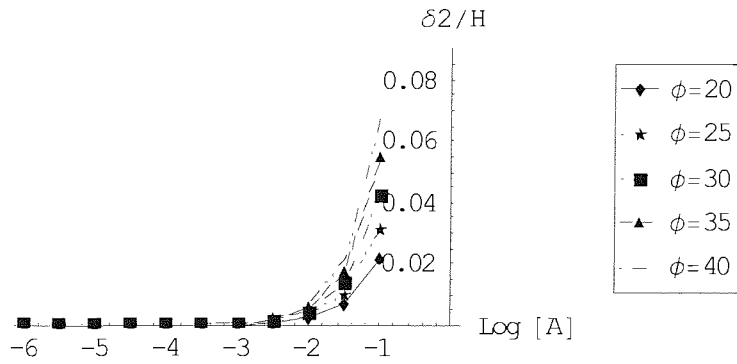


Figure 5.17: Normalized deformations at depth h from the crest against parameter A for different values of ϕ' when $(\gamma_s \rho) = 10^{-1}$ and the original water table is at ground level.

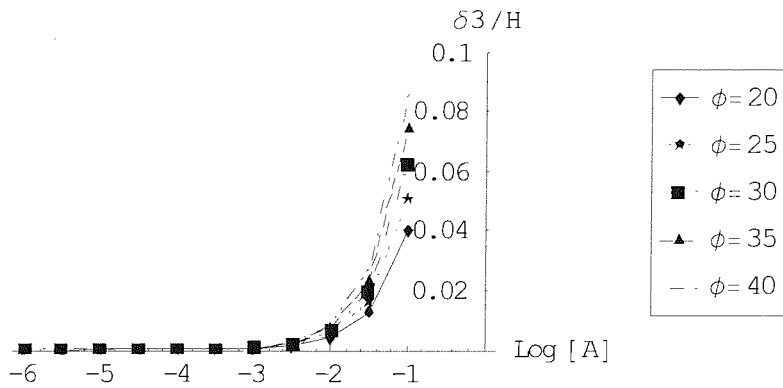


Figure 5.18: Normalized deformations at depth $h+d/2$ from the crest against parameter A for different values of ϕ' when $(\gamma_s \rho) = 10^{-1}$ and the original water table is at ground level.

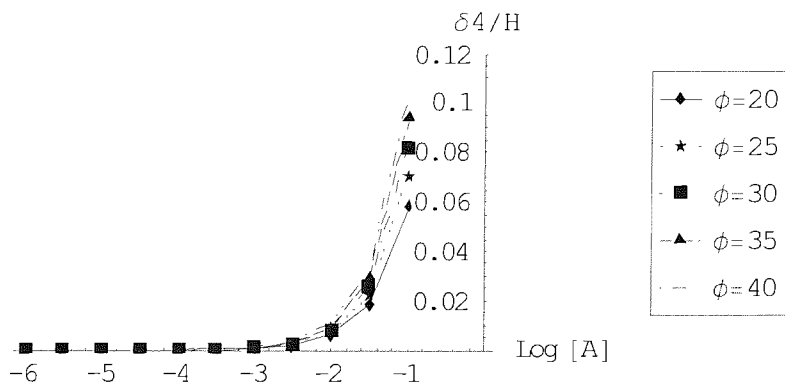


Figure 5.19: Normalized deformations at depth H from the crest against parameter A for different values of ϕ' when $(\gamma_s \rho) = 10^{-1}$ and the original water table is at ground level.

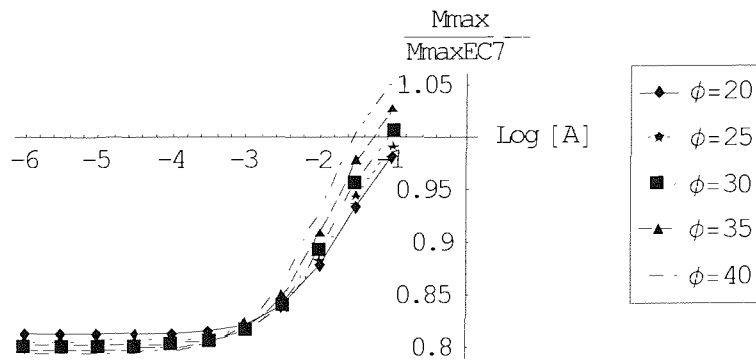


Figure 5.20: The ratio of $M_{max} / M_{max,EC7}$ against parameter A for different values of ϕ' when $(\gamma_s \rho) = 10$ and the original water table is at ground level.

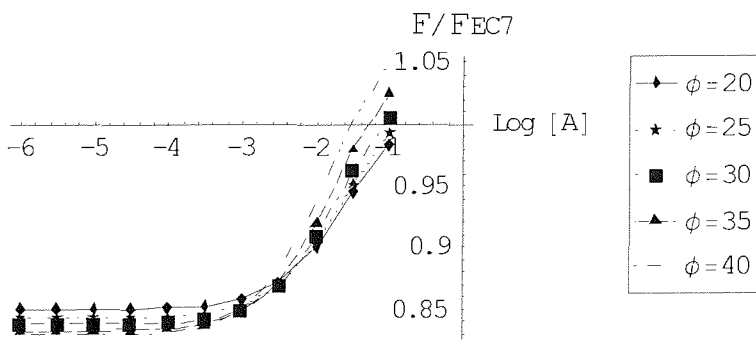


Figure 5.21: The ratio of F / F_{EC7} against parameter A for different values of ϕ' when $(\gamma_s \rho) = 10$ and the original water table is at ground level.

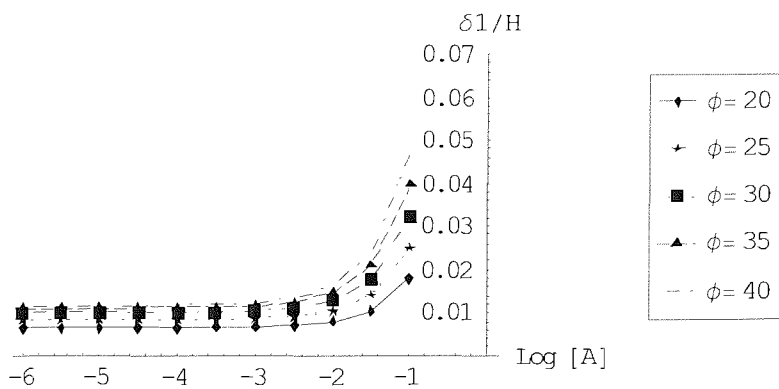


Figure 5.22: Normalized deformations at depth $h/2$ from the crest against parameter A for different values of ϕ' when $(\gamma_s \rho) = 10$ and the original water table is at ground level.

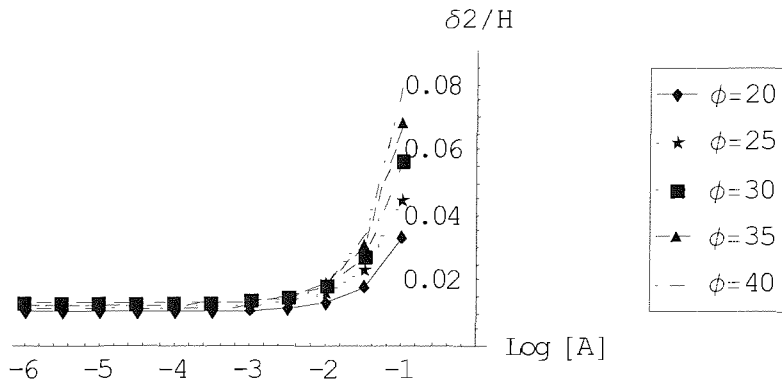


Figure 5.23: Normalized deformations at depth h from the crest against parameter A for different values of ϕ' when $(\gamma_s \rho) = 10$ and the original water table is at ground level.

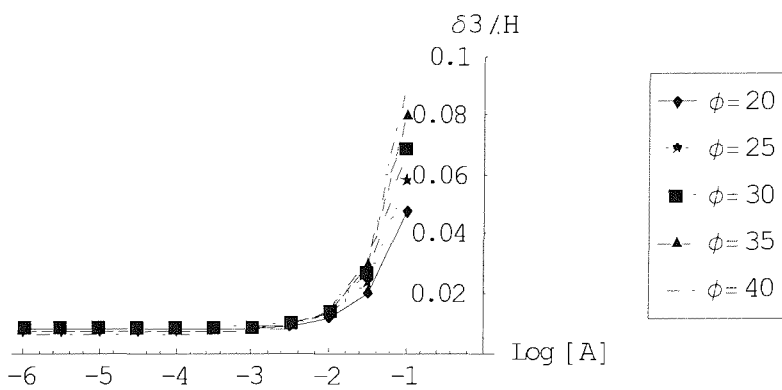


Figure 5.24: Normalized deformations at depth $h+d/2$ from the crest against parameter A for different values of ϕ' when $(\gamma_s \rho) = 10$ and the original water table is at ground level.

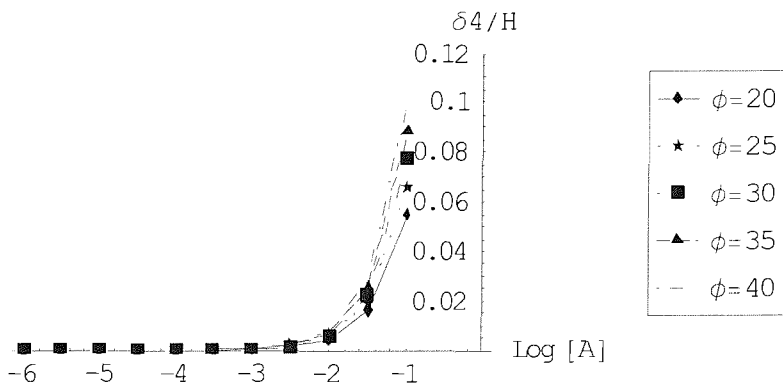


Figure 5.25: Normalized deformations at depth H from the crest against parameter A for different values of ϕ' when $(\gamma_s \rho) = 10$ and the original water table is at ground level.

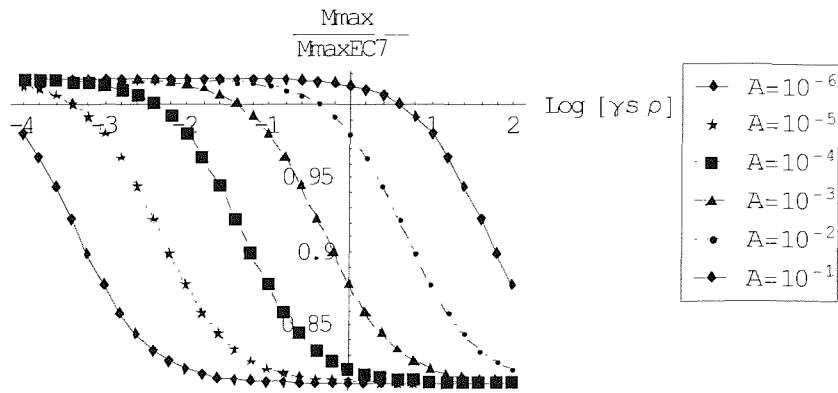


Figure 5.26: The ratio of $M_{max} / M_{max,EC7}$ against $(\gamma_s \rho)$ for different values of A when $\phi' = 20^\circ$ and the original water table is at ground level.

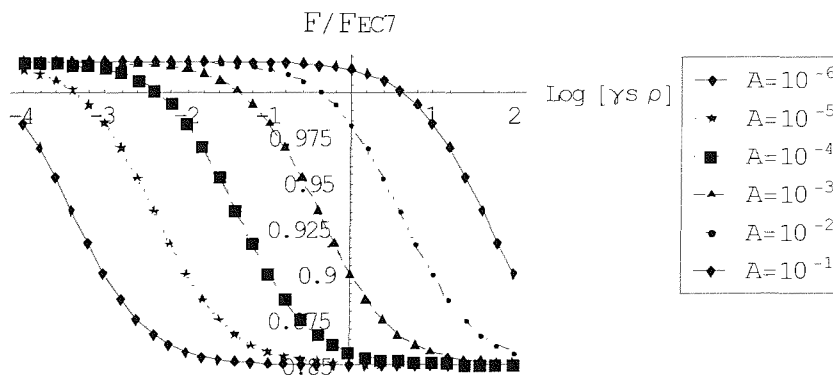


Figure 5.27: The ratio of F / F_{EC7} against $(\gamma_s \rho)$ for different values of A when $\phi' = 20^\circ$ and the original water table is at ground level.

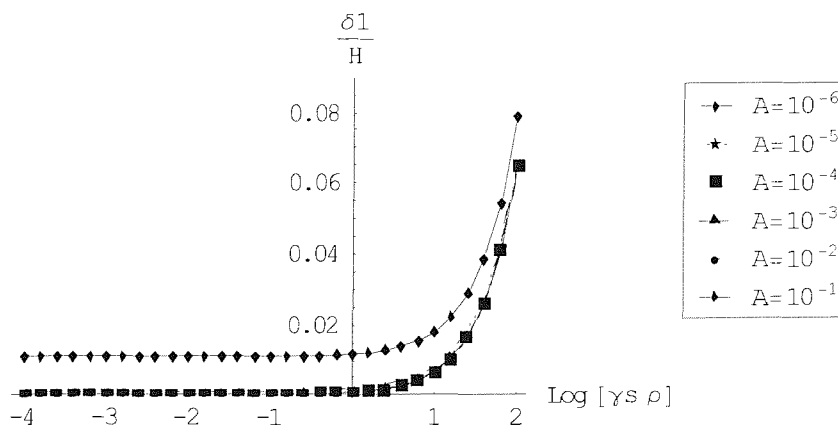


Figure 5.28: Normalized deformations at depth $h/2$ from the crest against $(\gamma_s \rho)$ for different values of A when $\phi' = 20^\circ$ and the original water table is at ground level.

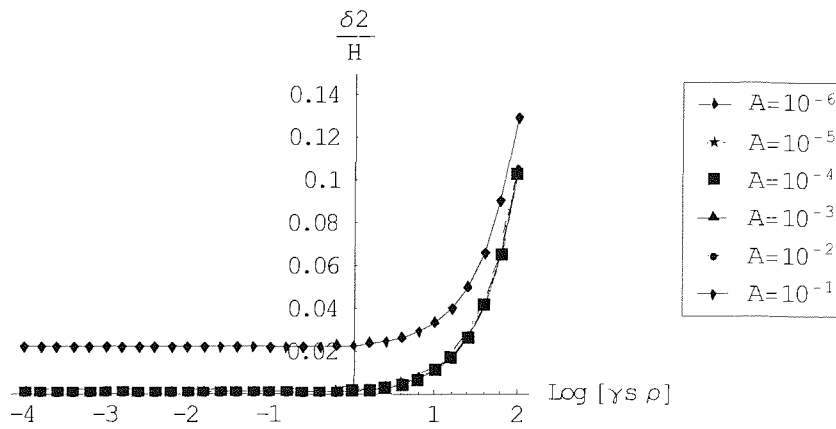


Figure 5.29: Normalized deformations at depth h from the crest against $(\gamma_s \rho)$ for different values of A when $\varphi' = 20^\circ$ and the original water table is at ground level.

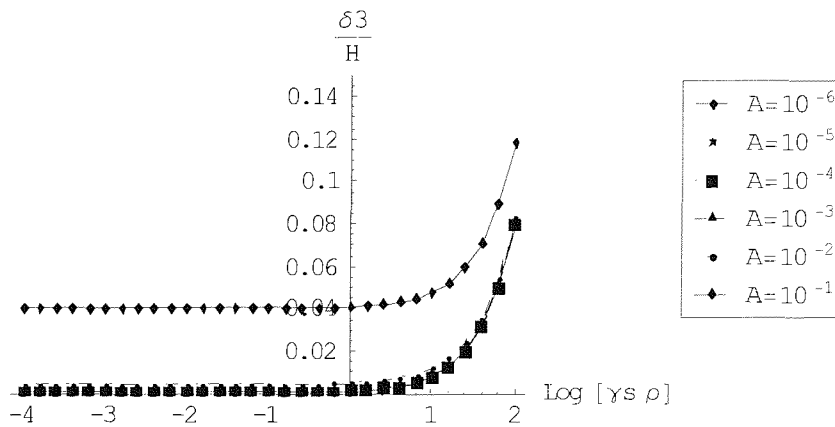


Figure 5.30: Normalized deformations at depth $h+d/2$ from the crest against $(\gamma_s \rho)$ for different values of A when $\varphi' = 20^\circ$ and the original water table is at ground level.

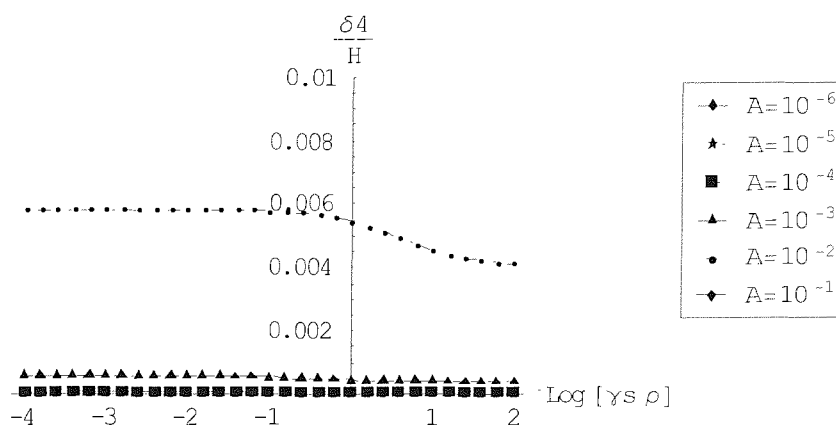


Figure 5.31: Normalized deformations at depth H from the crest against $(\gamma_s \rho)$ for different values of A when $\varphi' = 20^\circ$ and the original water table is at ground level.

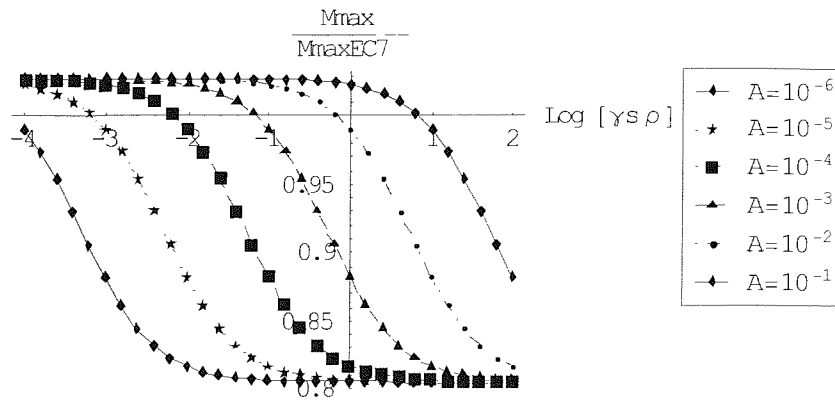


Figure 5.32: The ratio of $M_{max} / M_{max,EC7}$ against $(\gamma_s \rho)$ for different values of A when $\phi' = 25^\circ$ and the original water table is at ground level.

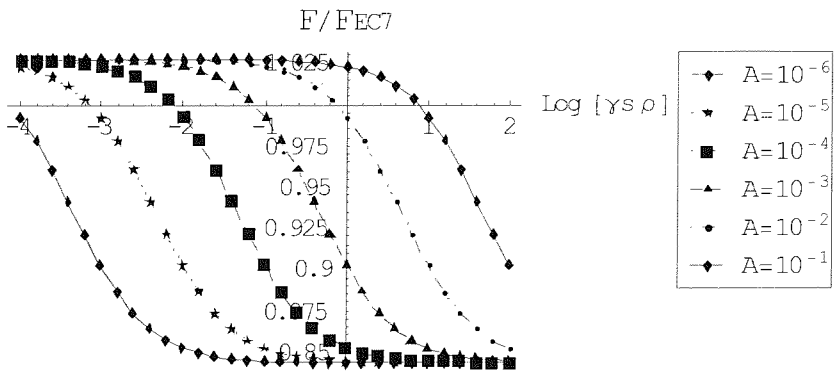


Figure 5.33: The ratio of F / F_{EC7} against $(\gamma_s \rho)$ for different values of A when $\phi' = 25^\circ$ and the original water table is at ground level.

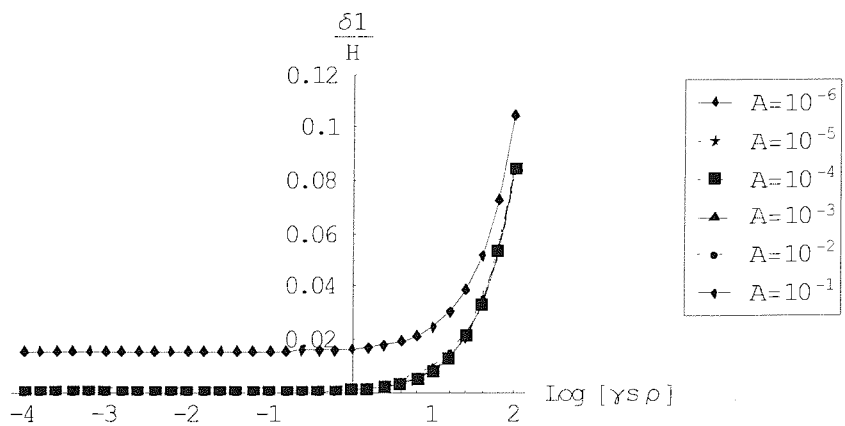


Figure 5.34: Normalized deformations at depth $h/2$ from the crest against $(\gamma_s \rho)$ for different values of A when $\phi' = 25^\circ$ and the original water table is at ground level.

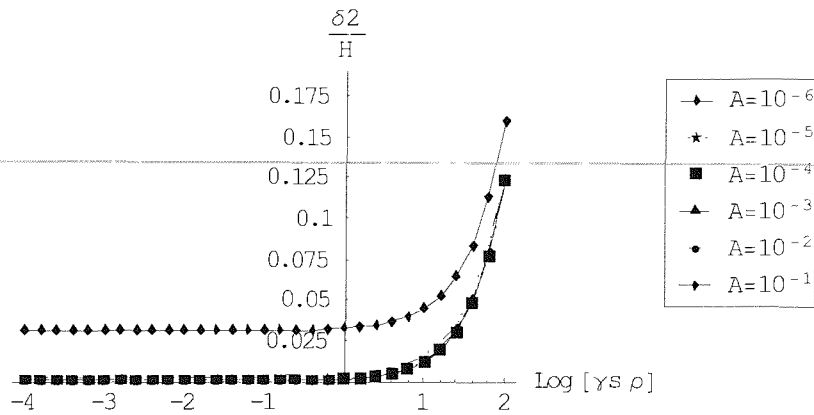


Figure 5.35: Normalized deformations at depth h from the crest against $(\gamma_s \rho)$ for different values of A when $\varphi' = 25^\circ$ and the original water table is at ground level.

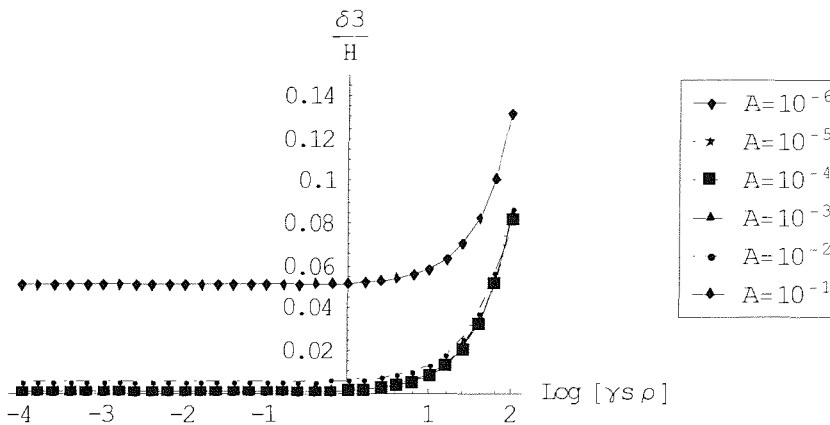


Figure 5.36: Normalized deformations at depth $h + d/2$ from the crest against $(\gamma_s \rho)$ for different values of A when $\varphi' = 25^\circ$ and the original water table is at ground level.

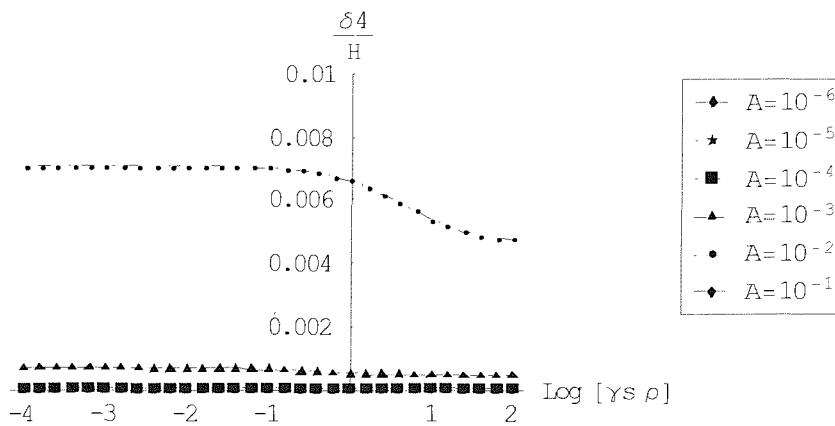


Figure 5.37: Normalized deformations at depth H from the crest against $(\gamma_s \rho)$ for different values of A when $\varphi' = 25^\circ$ and the original water table is at ground level.

From the figures, the curves for $M_{max} / M_{max,EC7}$ tend to a value of 0.8, while F / F_{EC7} tend to a value of 0.85 for large values of $\gamma_s \rho$ or very small values of A . The ratios $M_{max} / M_{max,EC7}$ and F / F_{EC7} are generally closer to unity, the influence of the different values of

ϕ' becomes less important and the rate of the reduction is slightly lower when the pore water pressures are included in the calculations; however, the pattern of the reduction is similar to the one presented in Chapter 4 for zero pore water pressures. The calculation of the maximum bending moments and prop loads for very stiff walls based on the Eurocode 7 (1995) might be more accurate when the pore water pressures are considered. The normalized displacements (δ_1/H , δ_2/H , δ_3/H and δ_4/H) are larger when the original water table is at ground level than in conditions of zero pore water pressures. Some of the results for a retaining wall with the water table at ground level are presented in Tables in Appendix D.

5.4 ULS CALCULATIONS: ORIGINAL WATER TABLE AT HALF THE RETAINED HEIGHT LEVEL

The effective stress distribution and pore water pressures for a retaining wall propped at the crest in limit equilibrium when the original ground water table is at a distance $h/2$ from the ground surface, where h is the wall retained height, are shown in Figure 5.38. The normalized pore water pressures $u / (\gamma_s H)$ at the toe of the wall are given by Equation (5.22) and the normalized effective active $\sigma'_{ha1} / (\gamma_s H)$, $\sigma'_{ha2} / (\gamma_s H)$ and passive stresses $\sigma'_{hp} / (\gamma_s H)$ are given by Equations (5.23), (5.24) and (5.25) respectively.

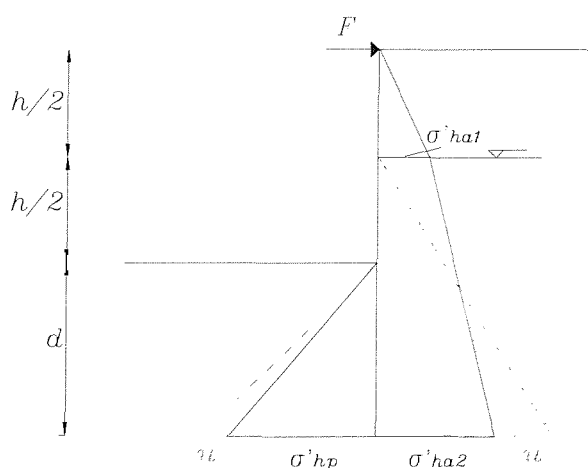


Figure 5.38: Stress and pore water pressure distribution in limit equilibrium behind and in front of a retaining wall propped at the crest with the original water table at half the retained height level.

$$u / (\gamma_s H) = \gamma_w (1-m) (2-m) / [\gamma_s (2-1.5m)] \quad (5.22)$$

$$\sigma'_{ha1} = K_a \gamma_s h/2 \rightarrow \sigma'_{ha1} / (\gamma_s H) = 1 / 2 m K_a \quad (5.23)$$

$$\sigma'_{ha2} / (\gamma_s H) = K_a [1 - 0.5 m - u / (\gamma_s H)] \quad (5.24)$$

$$\sigma'_{hp} = K_p (\gamma_s d - u) \rightarrow \sigma'_{hp} / (\gamma_s H) = K_p [1 - m - u / (\gamma_s H)] \quad (5.25)$$

The normalized prop force $F / (\gamma_s H)$ and the retained height ratio m may be calculated from Equations (5.26) and (5.27):

$$F / (\gamma_s H^2) = 1/8 m^2 K_a + (1-1/2 m) 1/2 m K_a + 1/2 (1-1/2 m) K_a [1-0.5 m - u / (\gamma_s H)] - 1/2 (1-m) K_p [1-m - u / (\gamma_s H)] + 1/4 m u / (\gamma_s H) \quad (5.26)$$

$$\begin{aligned} \sum M_h = 0 \rightarrow & 1/12 m^2 \sigma'_{ha1} / (\gamma_s H) + 1/2 (1-1/2m) (1+1/2m) \sigma'_{ha1} / (\gamma_s H) \\ & + 1/6 (1-1/2m) (1/2m+2) \sigma'_{ha2} / (\gamma_s H) - 1/6 (1-m) (m+2) \sigma'_{hp} / (\gamma_s H) \\ & + 1/6 (1-1/2m) (1/2m+2) u / (\gamma_s H) - 1/6 (1-m) (m+2) u / (\gamma_s H) = 0 \end{aligned} \quad (5.27)$$

The maximum bending moment along the wall may then be determined according to Eurocode (EC7, 1995).

5.5 SLS CALCULATIONS: ORIGINAL WATER TABLE AT HALF THE RETAINED HEIGHT LEVEL

The normalised pore water pressures at the toe and in each soil zone for a wall with a retained height ratio m , calculated from the ULS calculations using factored (design) strength are determined by Equation (5.22) and Equations (5.28) to (5.33) respectively; the normalised total stresses along the wall are given by Equations (5.34) to (5.43):

$$u_1 / (\gamma_s H) = 0 \quad (5.28)$$

$$u_2 / (\gamma_s H) = h/2 / (h/2+d) u / (\gamma_s H) = 0.5m / (1-1/2m) u / (\gamma_s H) \quad (5.29)$$

$$u_3 / (\gamma_s H) = (h+d/2) / (h/2+d) u / (\gamma_s H) = 1/2 (1+m) / (1-1/2m) u / (\gamma_s H) \quad (5.30)$$

$$u_4 / (\gamma_s H) = u / (\gamma_s H) \quad (5.31)$$

$$u_5 / (\gamma_s H) = u / (\gamma_s H) \quad (5.32)$$

$$u_6 / (\gamma_s H) = d/2 / d u / (\gamma_s H) = 1/2 u / (\gamma_s H) \quad (5.33)$$

$$\sigma_{h1a} / (\gamma_s H) = 0.5 m K_{a1a} \quad (5.34)$$

$$\sigma_{h1u} / (\gamma_s H) = 0.5 m K_{a1u} \quad (5.35)$$

$$\sigma_{h2a} / (\gamma_s H) = m K_{a2a} + 0.5m / (1-0.5m) u / (\gamma_s H) (1 - K_{a2a}) \quad (5.36)$$

$$\sigma_{h2u} / (\gamma_s H) = m K_{a2u} + 0.5m / (1-0.5m) u / (\gamma_s H) (1 - K_{a2u}) \quad (5.37)$$

$$\sigma_{h3a} / (\gamma_s H) = 0.5(1+m)K_{a3a} + 0.5(1+m) / (1-0.5m) u / (\gamma_s H) (1 - K_{a3a}) \quad (5.38)$$

$$\sigma_{h3u} / (\gamma_s H) = 0.5(1+m)K_{a3u} + 0.5(1+m) / (1-0.5m) u / (\gamma_s H) (1 - K_{a3u}) \quad (5.39)$$

$$\sigma_{h4}/(\gamma_s H) = K_{a4} + u/(\gamma_s H) (1 - K_{a4}) \quad (5.40)$$

$$\sigma_{h5}/(\gamma_s H) = K_{p5} (1-m) + u/(\gamma_s H) (1 - K_{p5}) \quad (5.41)$$

$$\sigma_{h6a'}/(\gamma_s H) = 0.5(1-m) K_{p6u} + 0.5 u/(\gamma_s H) (1 - K_{p6u}) \quad (5.42)$$

$$\sigma_{h6u}/(\gamma_s H) = 0.5(1-m) K_{p6a} + 0.5 u/(\gamma_s H) (1 - K_{p6a}) \quad (5.43)$$

Substitution of the total stresses into Equations (4.127), (4.128), (4.132), (4.133) and (4.134) given in Section 4.6, gives a system of five unknowns: $\delta\theta_1$, $\delta\theta_2$, $\delta\theta_3$, $\delta\theta_4$ and F . The system is solved numerically in Appendix D and some of the results are plotted in Figures 5.39 to 5.74 for the same range of parameters A , $\gamma_s \rho$ and ϕ' as in Section 4.6 and 5.2 for comparison between the different conditions of pore water pressures.

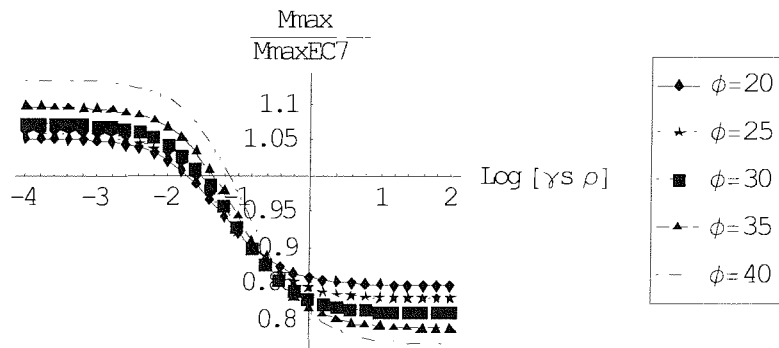


Figure 5.39: The ratio of $M_{max} / M_{max,EC7}$ against $(\gamma_s \rho)$ for different values of ϕ' when $A = 10^{-4}$ and the original water table is at half the retained height level.

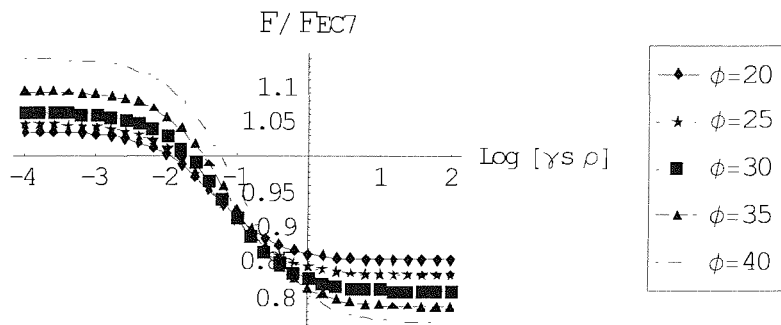


Figure 5.40: The ratio of F / F_{EC7} against $(\gamma_s \rho)$ for different values of ϕ' when $A=10^{-4}$ and the original water table is at half the retained height level.

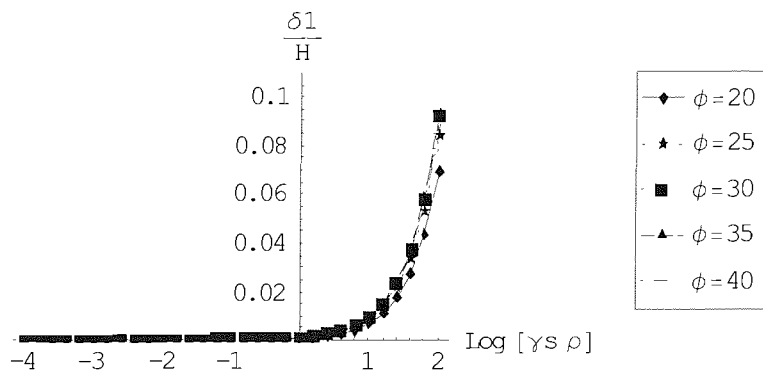


Figure 5.41: Normalized deformations at depth $h/2$ from the crest against $(\gamma_s \rho)$ for different values of ϕ' when $A = 10^{-4}$ and the original water table is at half the retained height level.

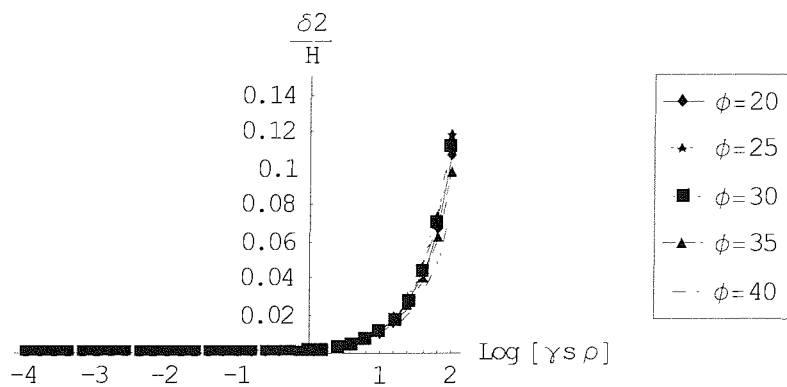


Figure 5.42: Normalized deformations at depth h from the crest against $(\gamma_s \rho)$ for different values of ϕ' when $A = 10^{-4}$ and the original water table is at half the retained height level.

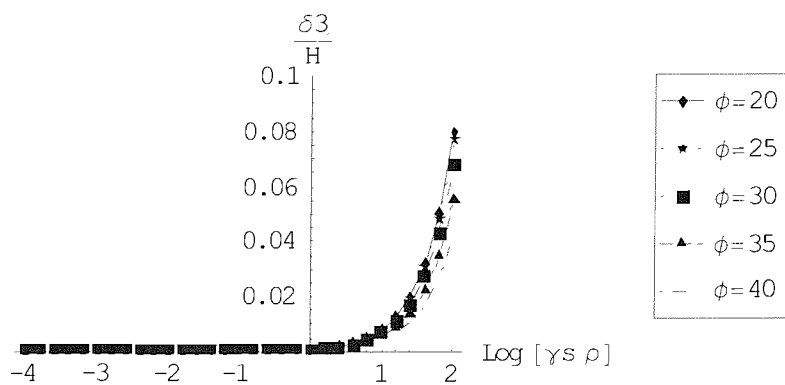


Figure 5.43: Normalized deformations at depth $h+d/2$ from the crest against $(\gamma_s \rho)$ for different values of ϕ' when $A = 10^{-4}$ and the original water table is at half the retained height level.

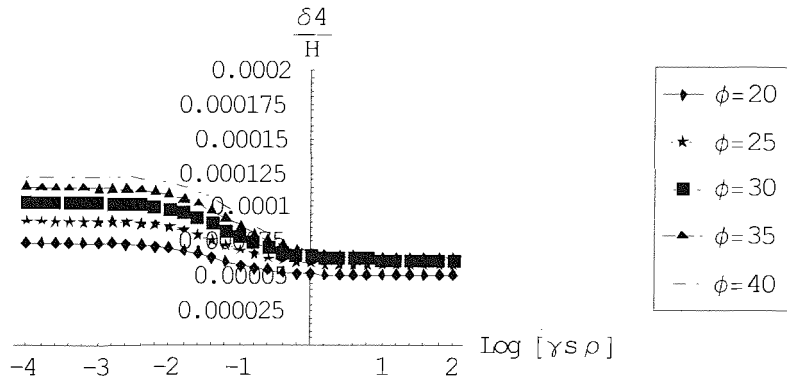


Figure 5.44: Normalized deformations at depth H from the crest against $(\gamma_s \rho)$ for different values of ϕ' when $A = 10^{-4}$ and the original water table is at half the retained height level.

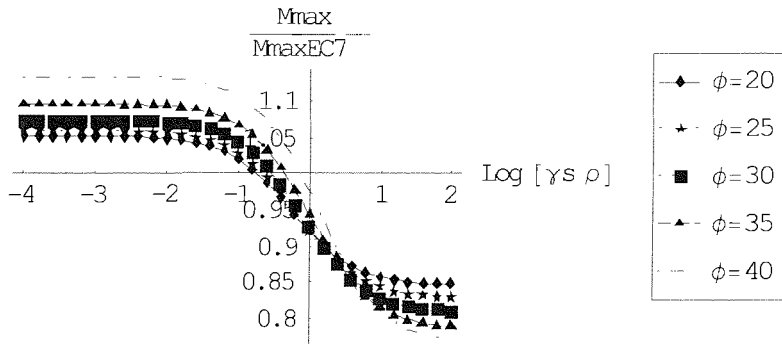


Figure 5.45: The ratio of $M_{max} / M_{max,EC7}$ against $(\gamma_s \rho)$ for different values of ϕ' when $A = 10^{-3}$ and the original water table is at half the retained height level.

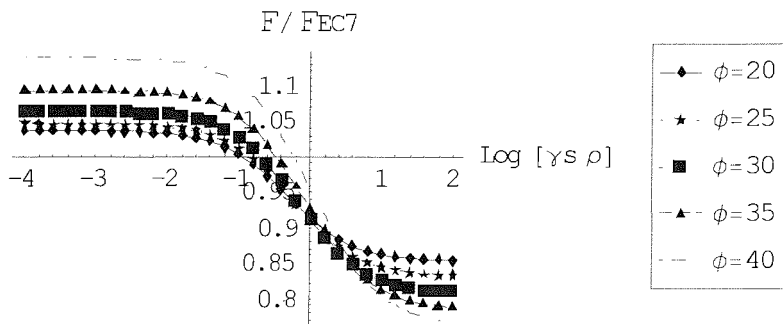


Figure 5.46: The ratio of F / F_{EC7} against $(\gamma_s \rho)$ for different values of ϕ' when $A = 10^{-3}$ and the original water table is at half the retained height level.

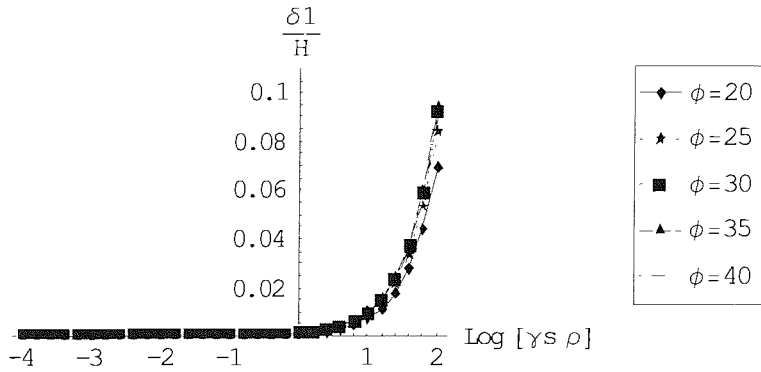


Figure 5.47: Normalized deformations at depth $h/2$ from the crest against $(\gamma_s \rho)$ for different values of ϕ' when $A = 10^{-3}$ and the original water table is at half the retained height level.

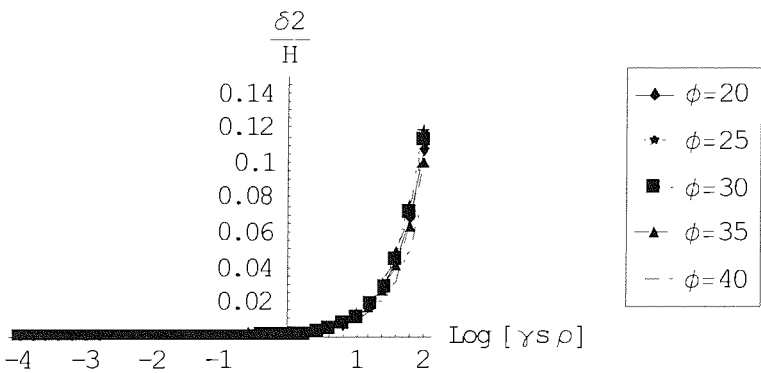


Figure 5.48: Normalized deformations at depth h from the crest against $(\gamma_s \rho)$ for different values of ϕ' when $A = 10^{-3}$ and the original water table is at half the retained height level.

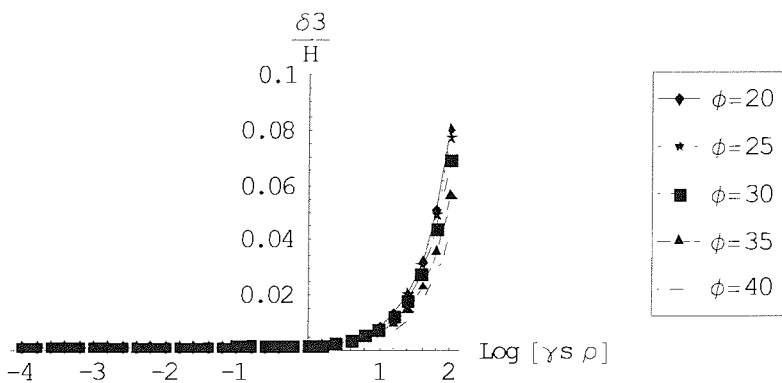


Figure 5.49: Normalized deformations at depth $h+d/2$ from the crest against $(\gamma_s \rho)$ for different values of ϕ' when $A = 10^{-3}$ and the original water table is at half the retained height level.

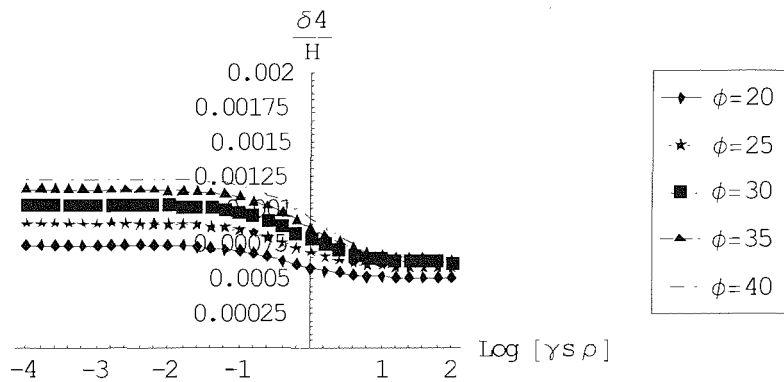


Figure 5.50: Normalized deformations at depth H from the crest against $(\gamma_s \rho)$ for different values of ϕ' when $A = 10^{-3}$ and the original water table is at half the retained height level.

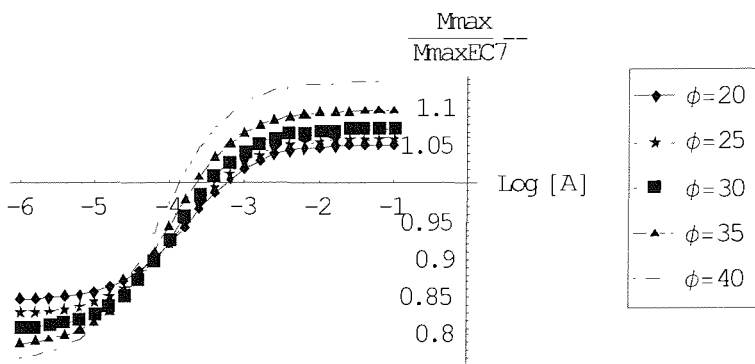


Figure 5.51: The ratio of $M_{max} / M_{max,EC7}$ against parameter A for different values of ϕ' when $(\gamma_s \rho) = 10^{-1}$ and the original water table is at half the retained height level.

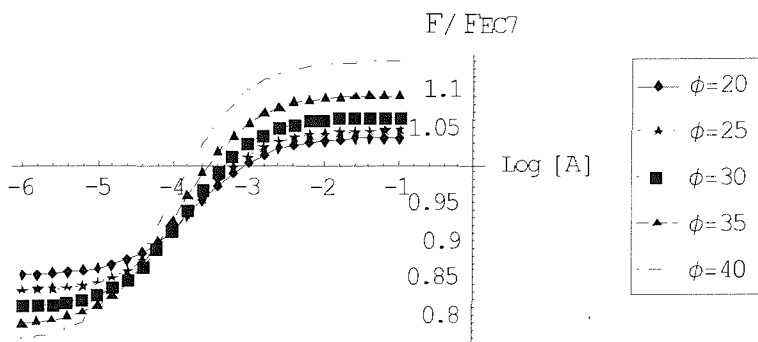


Figure 5.52: The ratio of F / F_{EC7} against parameter A for different values of ϕ' when $(\gamma_s \rho) = 10^{-1}$ and the original water table is at half the retained height level.

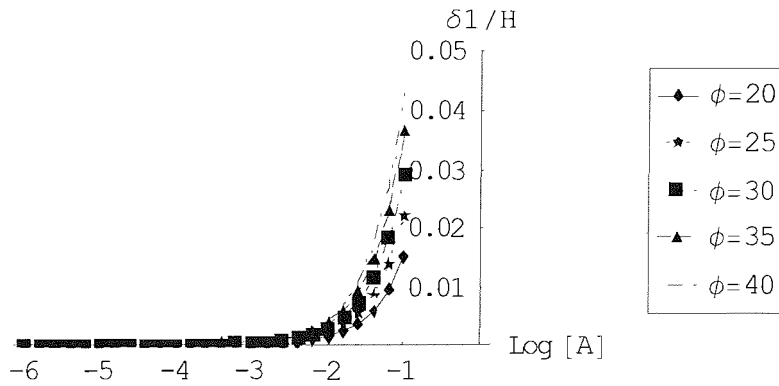


Figure 5.53: Normalized deformations at depth $h/2$ from the crest against parameter A for different values of ϕ' when $(\gamma_s \rho) = 10^{-1}$ and the original water table is at half the retained height level.

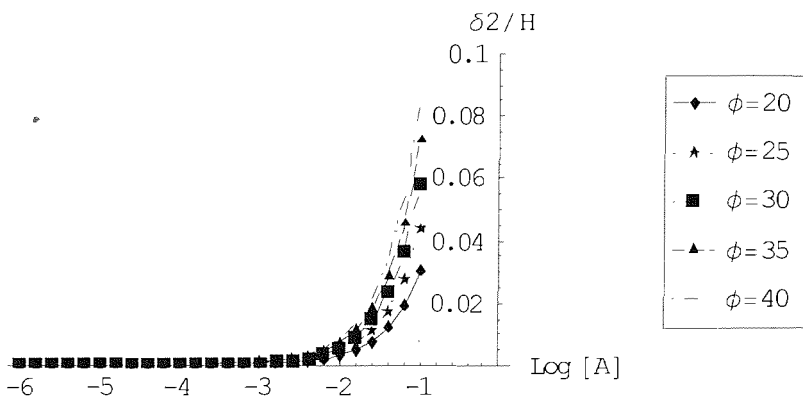


Figure 5.54: Normalized deformations at depth $h/2$ from the crest against parameter A for different values of ϕ' when $(\gamma_s \rho) = 10^{-1}$ and the original water table is at half the retained height level.

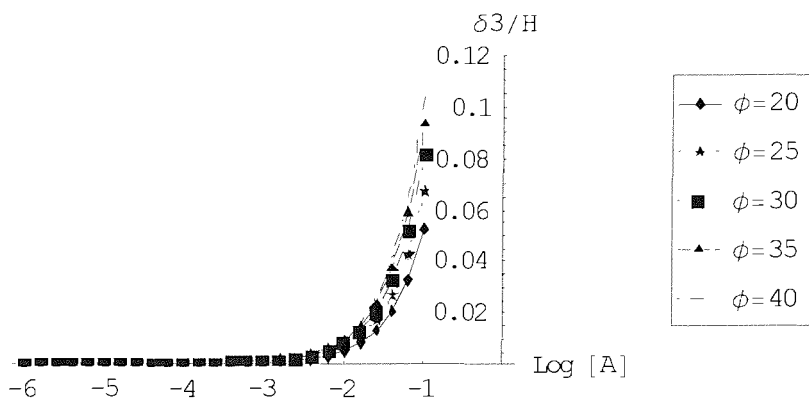


Figure 5.55: Normalized deformations at depth $h+d/2$ from the crest against $(\gamma_s \rho)$ for different values of ϕ' when $(\gamma_s \rho) = 10^{-1}$ and the original water table is at half the retained height level.

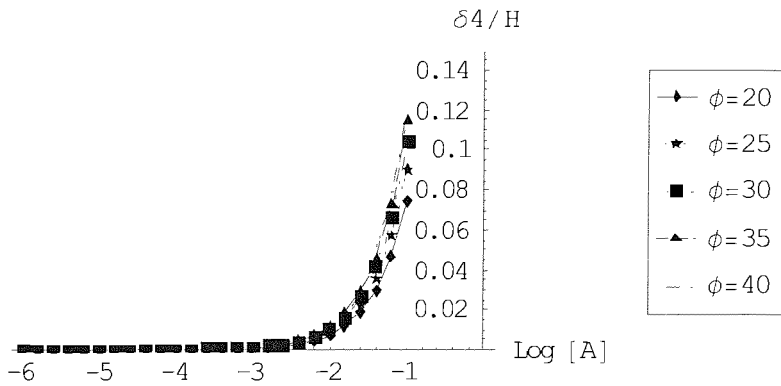


Figure 5.56: Normalized deformations at depth H from the crest against $(\gamma_s \rho)$ for different values of ϕ' when $(\gamma_s \rho) = 10^{-1}$ and the original water table is at half the retained height level.

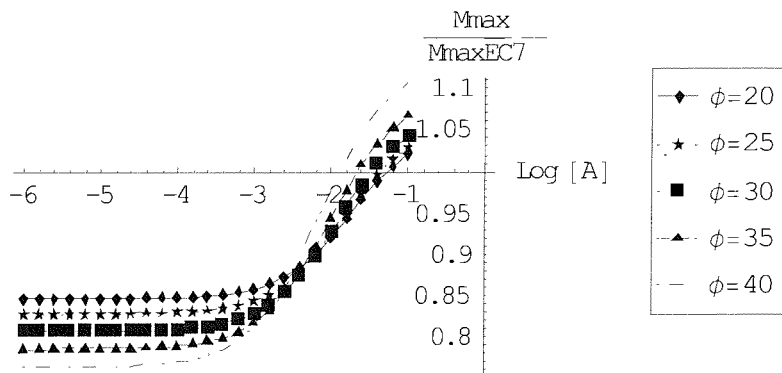


Figure 5.57: The ratio of $M_{max} / M_{max,EC7}$ against parameter A for different values of ϕ' when $(\gamma_s \rho) = 10$ and the original water table is at half the retained height level.

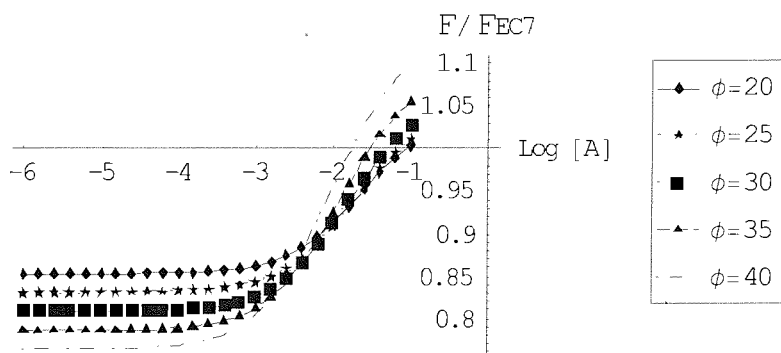


Figure 5.58: The ratio of F / F_{EC7} against parameter A for different values of ϕ' when $(\gamma_s \rho) = 10$ and the original water table is at half the retained height level.

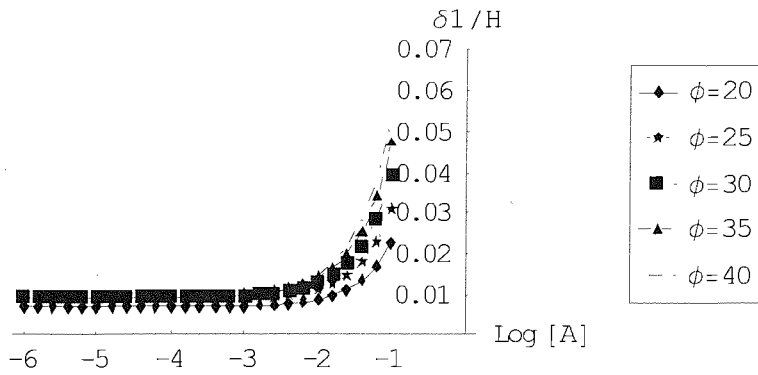


Figure 5.59: Normalized deformations at depth $h/2$ from the crest against parameter A for different values of ϕ' when $(\gamma_s \rho) = 10$ and the original water table is at half the retained height level.

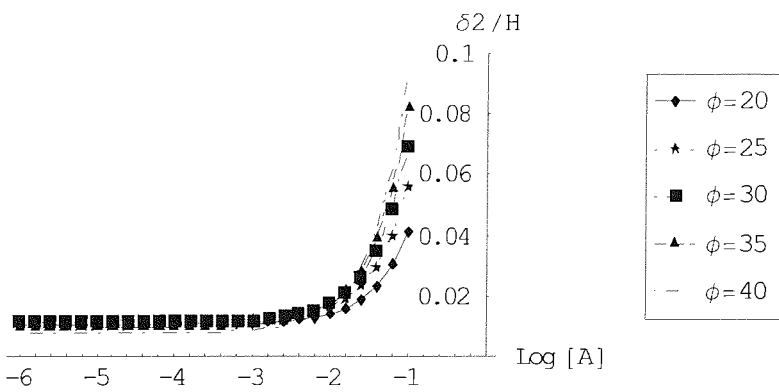


Figure 5.60: Normalized deformations at depth $h/2$ from the crest against parameter A for different values of ϕ' when $(\gamma_s \rho) = 10$ and the original water table is at half the retained height level.

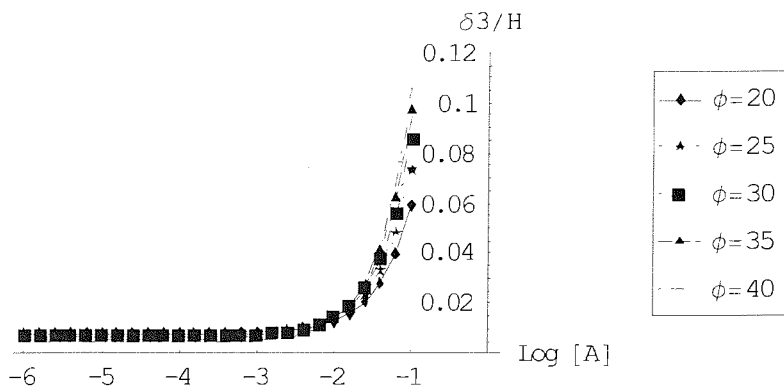


Figure 5.61: Normalized deformations at depth $h+d/2$ from the crest against $(\gamma_s \rho)$ for different values of ϕ' when $(\gamma_s \rho) = 10$ and the original water table is at half the retained height level.

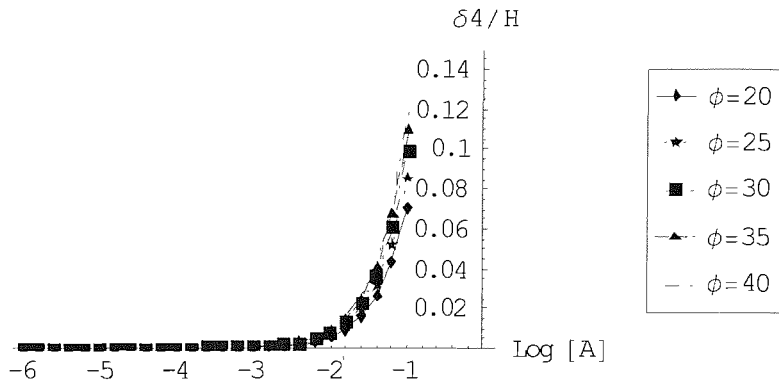


Figure 5.62: Normalized deformations at depth H from the crest against $(\gamma_s \rho)$ for different values of ϕ' when $(\gamma_s \rho) = 10$ and the original water table is at half the retained height level.

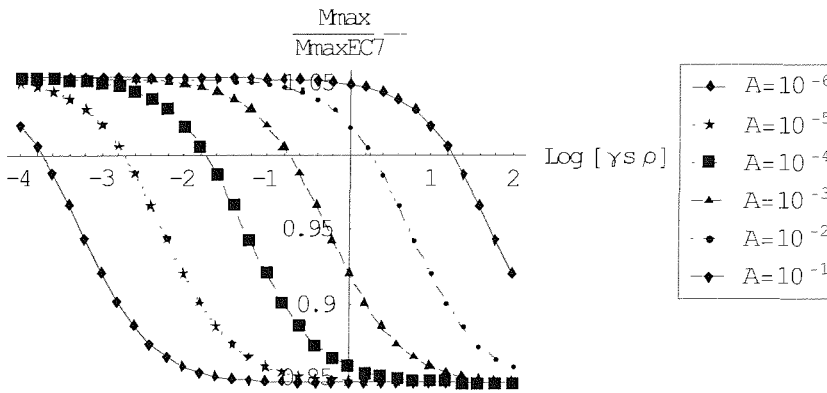


Figure 5.63: The ratio of $M_{max} / M_{max,EC7}$ against $(\gamma_s \rho)$ for different values of A when $\phi' = 20^\circ$ and the original water table is at half the retained height level.

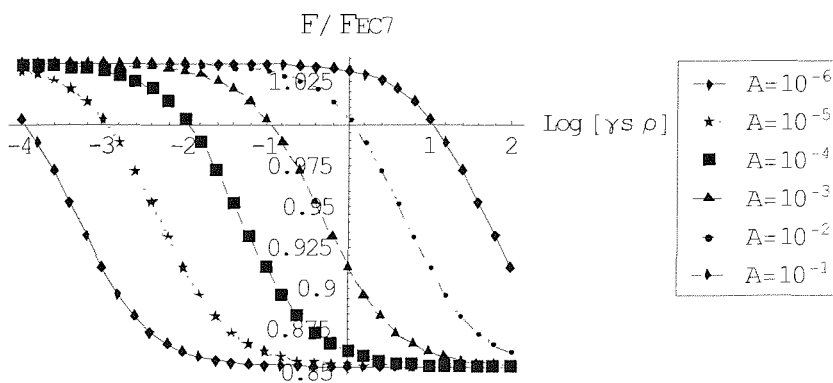


Figure 5.64: The ratio of F / F_{EC7} against $(\gamma_s \rho)$ for different values of A when $\phi' = 20^\circ$ and the original water table is at half the retained height level.

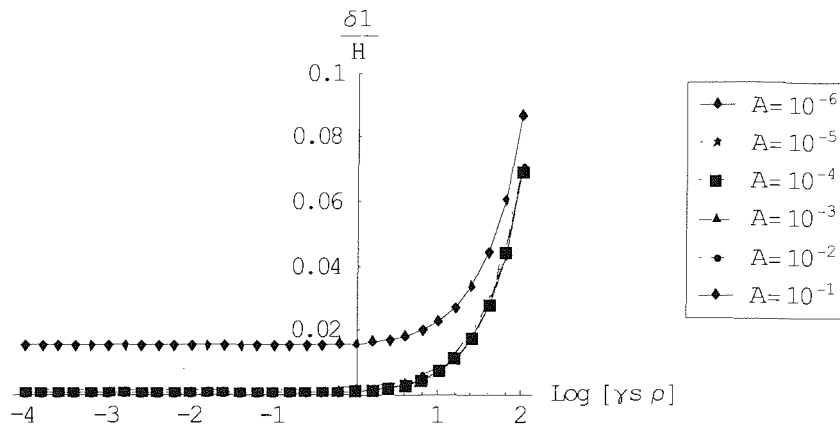


Figure 5.65: Normalized deformations at depth $h/2$ from the crest against $(\gamma_s \rho)$ for different values of A when $\phi' = 20^\circ$ and the original water table is at half the retained height level.

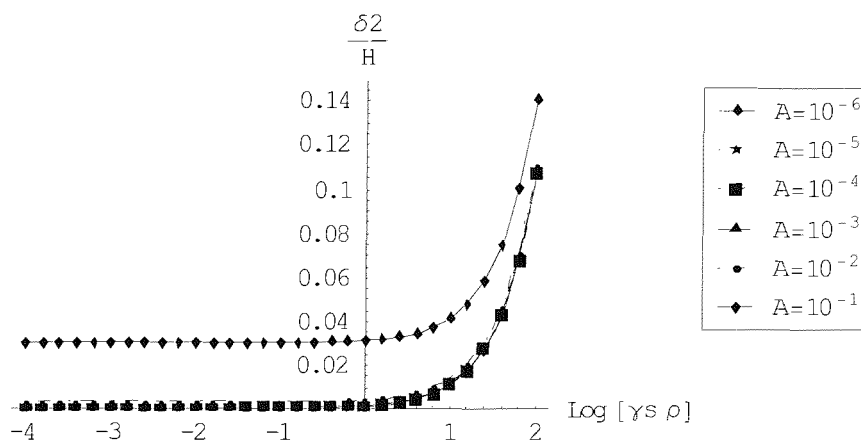


Figure 5.66: Normalized deformations at depth h from the crest against $(\gamma_s \rho)$ for different values of A when $\phi' = 20^\circ$ and the original water table is at half the retained height level.

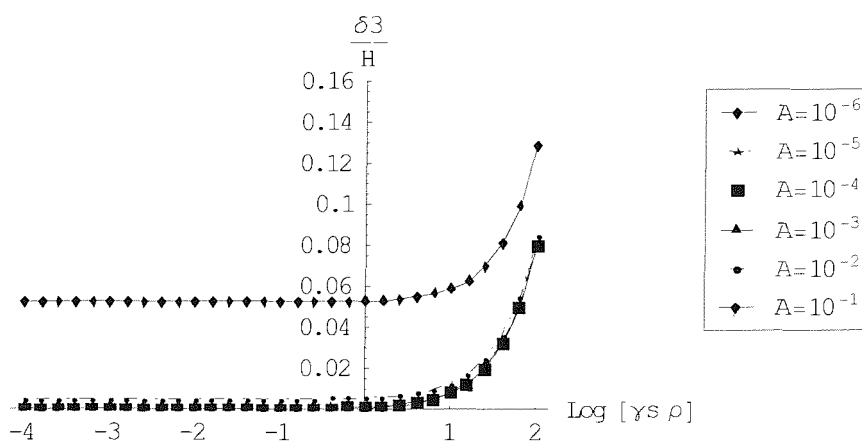


Figure 5.67: Normalized deformations at depth $h+d/2$ from the crest against $(\gamma_s \rho)$ for different values of A when $\phi' = 20^\circ$ and the original water table is at half the retained height level.

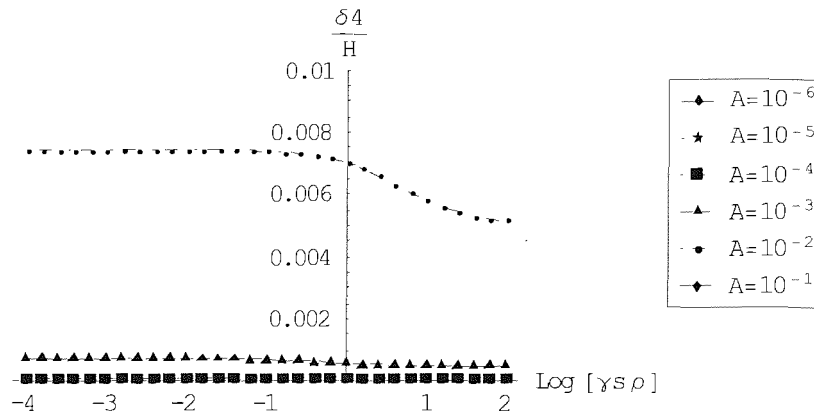


Figure 5.68: Normalized deformations at depth H from the crest against $(\gamma_s \rho)$ for different values of A when $\phi' = 20^\circ$ and the original water table is at half the retained height level.

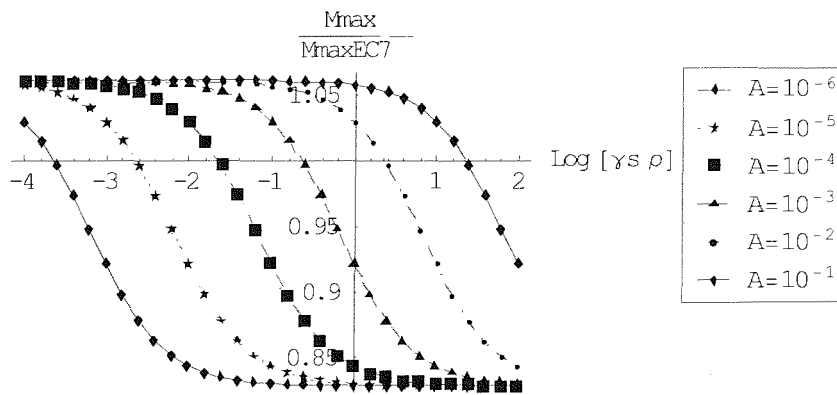


Figure 5.69: The ratio of $M_{max} / M_{max,EC7}$ against $(\gamma_s \rho)$ for different values of A when $\phi' = 25^\circ$ and the original water table is at half the retained height level.

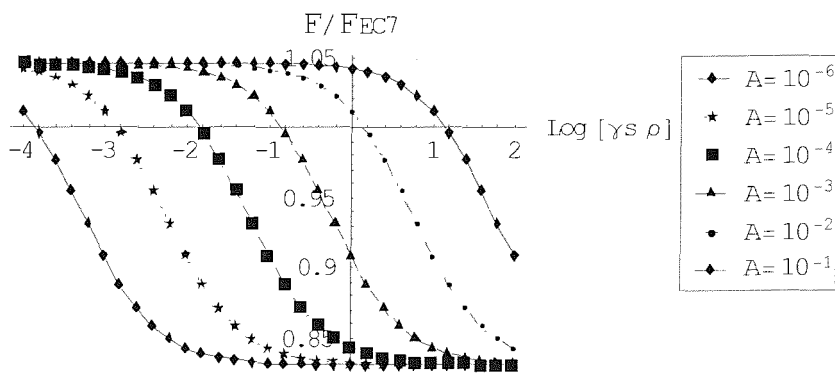


Figure 5.70: The ratio of F / F_{EC7} against $(\gamma_s \rho)$ for different values of A when $\phi' = 25^\circ$ and the original water table is at half the retained height level.

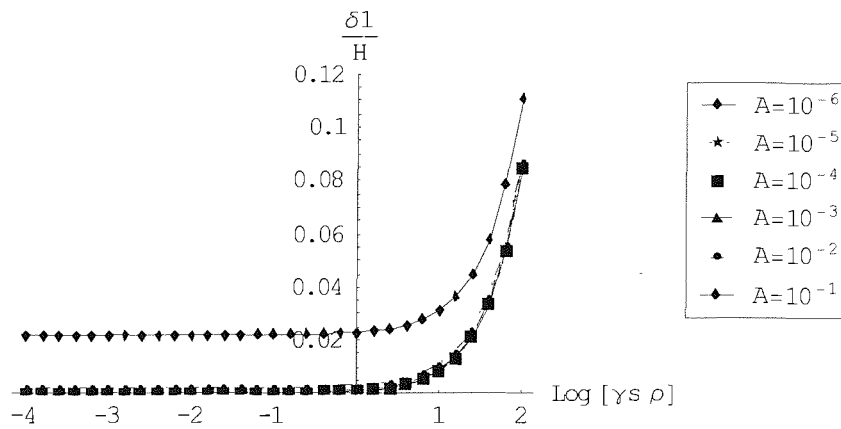


Figure 5.71: Normalized deformations at depth $h/2$ from the crest against $(\gamma_s \rho)$ for different values of A when $\phi' = 25^\circ$ and the original water table is at half the retained height level.

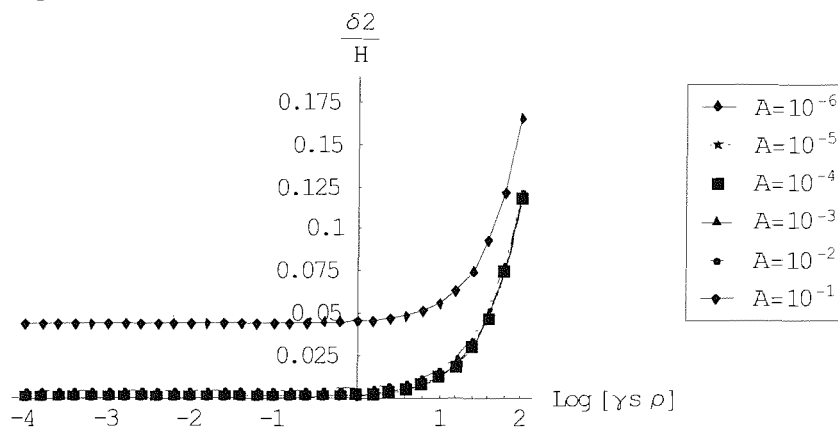


Figure 5.72: Normalized deformations at depth h from the crest against $(\gamma_s \rho)$ for different values of A when $\phi' = 25^\circ$ and the original water table is at half the retained height level.

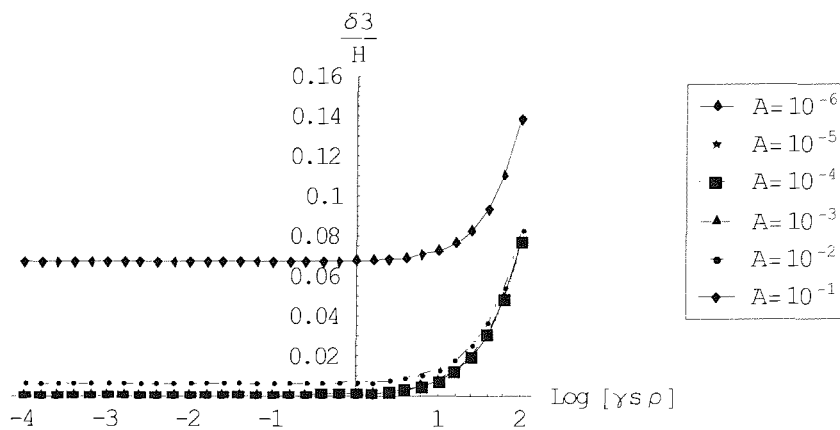


Figure 5.73: Normalized deformations at depth $h+d/2$ from the crest against $(\gamma_s \rho)$ for different values of A when $\phi' = 25^\circ$ and the original water table is at half the retained height level.

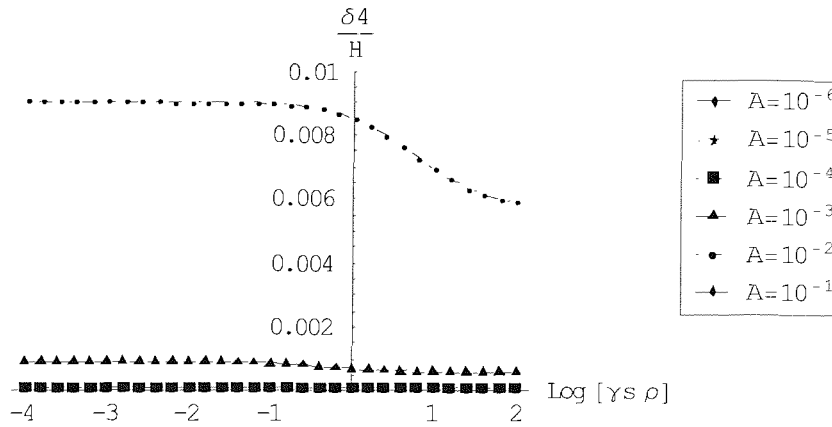


Figure 5.74: Normalized deformations at depth H from the crest against $(\gamma_s \rho)$ for different values of A when $\phi' = 25^\circ$ and the original water table is at half the retained height level.

From the figures, the ratios $M_{max} / M_{max,EC7}$ and F / F_{EC7} are closer to unity than in conditions of zero pore water pressures and slightly higher for small values of $\gamma_s \rho$ and large values of A , but slightly lower for large values of $\gamma_s \rho$ and small values of A than those with the water table at ground level; however, the pattern of the reduction is similar for all cases. The calculation of the maximum bending moments and prop loads for very stiff walls according to the Eurocode (EC7, 1995) might be more accurate when the water table is assumed to be at the ground level. When the water table is at half the retained height level the normalized displacements (δ_1/H , δ_2/H , δ_3/H and δ_4/H) are slightly higher than when the water table is at ground level.

5.6 REDUCTION CURVES FOR STIFF CLAYS AND SANDS

In Figures 5.75 and 5.76 the ratios $M_{max} / M_{max,EC7}$ and F / F_{EC7} are shown for values of A and ϕ' that are typically found in stiff clays, while in Figures 5.77 and 5.78 these values are chosen to represent the behaviour of sandy deposits. It should be noted that the selection of parameter A is not that straightforward and usually varies; however, the scope herein is to limit the number of curves to those that may be typical in current engineering practice in UK; hence, the selection of these values is based on the results of triaxial tests on samples from different locations as found in the literature.

In the Figures, curve 1 is drawn for conditions of zero pore water pressures, while curves 2 and 3 represent a water table at the ground surface and at half the retained height level respectively. The lines perpendicular to axis x-x show the typical wall flexibility values ($\text{Log} [\gamma_s \rho]$) for a rigid, diaphragm, sheet pile and soft retaining wall with a total length of 20m. The rigid and soft walls are included to represent extreme cases.

	RIGID	DIAPHRAGM	SHEET PILE	SOFT
EI (kNm^2/m)	2.33×10^9	2.33×10^6	7.8×10^4	3.2×10^4
ρ (m^3/kN)	6.96×10^{-5}	6.96×10^{-2}	2.05	5
$\text{Log} [\gamma_s \rho]$	-2.86	0.14	1.6	2.0

Table 5.1

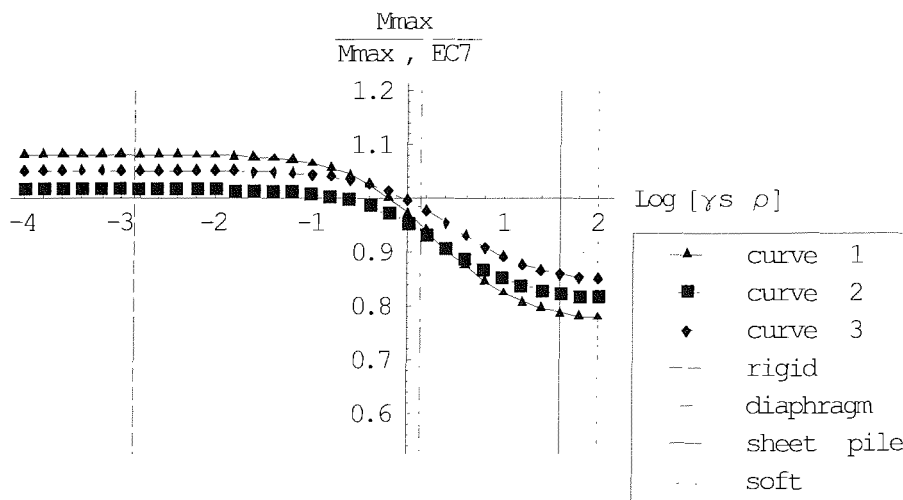


Figure 5.75: The ratio of $M_{max} / M_{max,EC7}$ against $(\gamma_s \rho)$ when $A=10^{-2.3}$ and $\phi' = 20^\circ$.

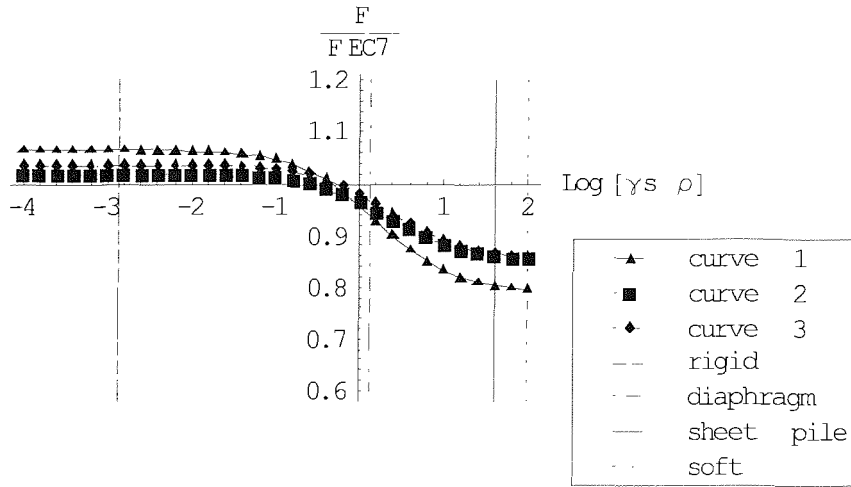


Figure 5.76: The ratio of F / F_{EC7} against $(\gamma_s \rho)$ when $A=10^{-2.3}$ and $\phi' = 20^\circ$.

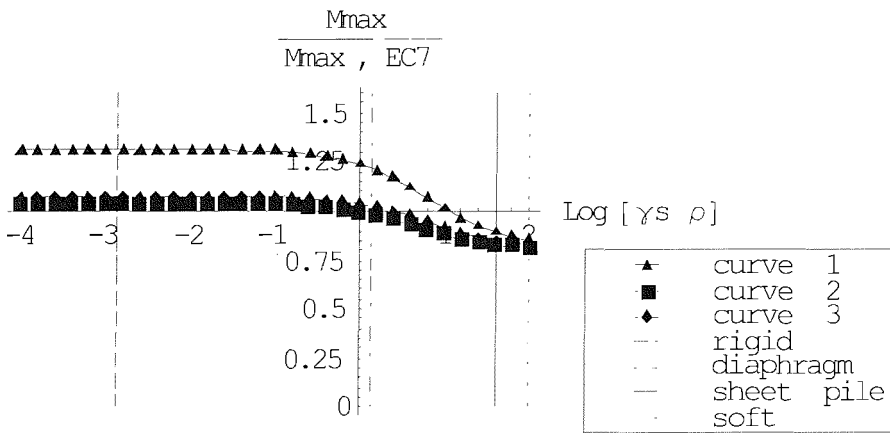


Figure 5.77: The ratio of $M_{max} / M_{max,EC7}$ against $(\gamma_s \rho)$ when $A=10^{-2.1}$ and $\phi' = 30^\circ$.

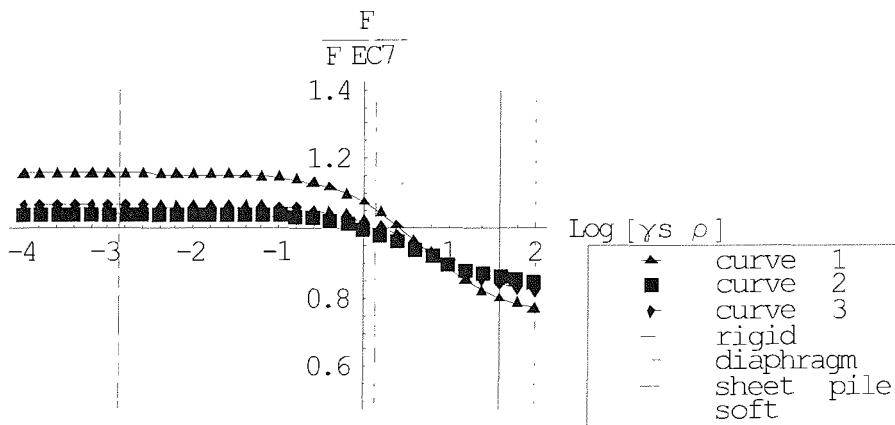


Figure 5.78: The ratio of F / F_{EC7} against $(\gamma_s \rho)$ when $A=10^{-2.1}$ and $\phi' = 30^\circ$.

According to the figures, the pattern of the reduction is similar in each case. Eurocode 7 (EC7, 1995) might underpredict the bending moments and prop loads for a rigid wall and the bending moments for a diaphragm wall embedded in sand assuming zero pore water pressures, while it might overpredict both the bending moments and prop loads for the other types of walls. For a diaphragm wall, the MSD results are in very good agreement with those derived from Eurocode 7 (EC7, 1995), while for a sheet pile wall the maximum reduction in the bending moments is about 23% in clays and 20% in sands. Regarding the prop loads of a sheet pile wall, a maximum reduction from the Eurocode 7 (EC7, 1995) results of about 20% in clays and 21% in sands is noticed. If these reduction curves are taken into account in engineering practice, together with a safe selection of parameter A as discussed, more economic designs might be feasible.

5.7 SUMMARY

In Chapter 5 the bending moment and prop load reduction curves together with the normalised displacements at characteristic points along a retaining wall are presented assuming a natural water table at the ground surface and at half the retained height level. The pattern of the reduction is similar to that presented in Chapter 4 for conditions of zero pore water pressures, but the magnitudes differ. A reduction in both the bending moments and the prop loads can be achieved when sheet pile walls are embedded in stiff clays or sands, while for diaphragm walls the MSD results are in good agreement with those calculated following Eurocode 7 (EC7, 1995). The advantage of the MSD method is that incorporates the effect of both the wall flexibility and soil stiffness in the design of retaining walls. The degree of safety in the design depends significantly on the selection of the appropriate value of parameter A for different types of soil.

6. COMPARISON BETWEEN THE MSD METHOD AND OTHER METHODS OF ANALYSIS

6.1 INTRODUCTION

In an early analysis, Rowe (1952) presented a number of reduction curves based on the results of a series of model tests on anchored sheet pile walls retaining loose and dense dry sand varying the flexibility ρ for various surcharge, anchor levels, anchor yield and dredge levels. In a later analysis by Rowe (1955) more reduction curves are presented based on an analytical solution in which both the wall flexibility and the soil stiffness are taken into account. The soil stiffness is described by means of a soil parameter m_r , which is assumed to increase linearly with depth. For the reasons discussed in Chapter 2 the soil parameter m_r may be considered as equivalent to the rate of increase of the Young's modulus with depth, E^* . However, a direct comparison between the reduction curves presented by Rowe and the curves showed in Chapter 4 could lead to misleading conclusions, since Rowe compared the anchor loads and the bending moments measured in his experiments or calculated theoretically to the values calculated by the free earth support method with the stress distributions estimated using Coulomb's theory and the passive pressures reduced by a factor of safety, F_p . This procedure was suggested in the former UK code of practice CP2 but, as already mentioned, modern codes of practice require the application of a factor of safety to the soil strength directly. Moreover, in Rowe's analysis the wall flexibility ρ is calculated in $ft^5 / lb \times in^2$ and the soil parameter m_r in lb / ft^3 . Therefore, Rowe's results for bending moments and prop loads need to be compared to values derived from calculations based on the current codes of practice and his curves need to be redrawn in consistent units to facilitate a valid comparison. In Section 6.3, an MSD analysis is carried out for stiff walls and the results are compared to values predicted by the geostructural mechanism proposed by Bolton and Powrie(1988), to check the consistency of the MSD method.

6.2 COMPARISON BETWEEN THE MSD METHOD AND ROWE'S ANALYSIS

6.2.1 Transformed axes

a. $x-x'$ axis

Rowe (1952) plotted the ratio of the experimental maximum bending moments per unit of model height (M_{max}/H^3) to the free earth support value against the logarithm of wall flexibility ρ for retained height ratios (h/H) in the range 0.6 to 0.8, surcharge coefficients ($q/\gamma_s H$) in the range 0 to 0.2 and anchor levels in the range 0 to $0.3H$. The values for $Log \rho$ varied from -4.5 to -2. If ρ is converted in *SI* units (m^3/kN), then the $x-x'$ axis should be redrawn for values of $Log \rho$ in the range -1.54 to 0.96. The friction angle φ' is taken by Rowe(1952) as 30° for loose and 40° for dense dry sand.

In his later analysis, Rowe (1955) plotted the ratio of the theoretical maximum bending moments to the free earth support value against the logarithm of parameter $m_r \rho$, where m_r is the soil parameter as defined by Rowe (1955), as already discussed. If $m_r \rho$ is converted in *SI* units, then the $x-x'$ axis should be redrawn for values of $Log(m_r \rho)$ in the range 2.16 to 6.16. For a specific soil, the parameter m_r is given by Rowe (1955); therefore, for loose sands $Log \rho$ is in the range -1.79 to 2.21 and for dense sands $Log \rho$ is in the range -2.79 to 1.21.

b. $y-y'$ axis

The ratios $M'_{fes} = M_{max,fes}/H^3$, $F'_{fes} = F_{fes}/H^2$ (Rowe, 1952) and $M_{max,fes}/K_{aR}\gamma_s H^3$, $F_{fes}/K_{aR}\gamma_s H^2$ (Rowe, 1955) based on the free earth support method are converted to those according to Eurocode 7 (1995) in the calculations presented in this section.

In Rowe's analysis, the free earth support calculations were carried out with an active earth pressure coefficient, K_{aR} , equal to the Coulomb value (Equation 6.1) for soil/ wall friction δ equal to $2/3 \varphi'$ and a passive earth pressure, σ'_{hpR} , equal to the Coulomb value

for soil/wall friction $\delta=0$ and divided by a factor $F_p=1.5$. The active and passive stresses for a wall in limit equilibrium according to Rowe are given by Equations (6.2) and (6.3), where m is the retained height ratio.

$$K_{aR} = \cos^2 \varphi / \{1 + [\sin (\varphi + \delta) \sin \varphi / \cos \delta]^{0.5}\}$$

$$= \cos^2 \varphi / \{1 + [\sin (5/3 \varphi) \sin \varphi / \cos (2/3 \varphi)]^{0.5}\} \quad (6.1)$$

$$\sigma'_{haR} = K_{aR} \gamma_s H^2 / 2 \quad (6.2)$$

$$\sigma'_{hpR} = K_{pR} \gamma_s d^2 / (2 F_p) \rightarrow K_{pR} \gamma_s (1-m)^2 H^2 / (2 F_p) \quad (6.3)$$

Taking the moments about the crest:

$$\sum M_h = 0 \rightarrow$$

$$(K_{aR} \gamma_s H^2 / 2) 2/3 H - K_{pR} \gamma_s (1-m)^2 H^2 / (2 F_p) [m H + 2/3 (1-m) H] = 0 \rightarrow$$

$$K_{pR} (1-m)^2 / (K_{aR} F_p) = 2 / (2+m) \quad (6.4)$$

From the condition of horizontal stress equilibrium, the normalized prop force F'_{fes}/K_{aR} may be calculated

$$F'_{fes}/K_{aR} = F / (K_{aR} H^2) = 1/2 \gamma_s [1 - K_{pR} (1-m)^2 / (K_{aR} F_p)]$$

$$= 1/2 \gamma_s m / (2+m) \quad (6.5)$$

In Rowe's analysis it is assumed that the maximum bending moments will occur above dredge level. If z_o is the depth where the maximum bending moment occurs divided by the wall height H , then for $z_o \leq m = h/H$, the normalised maximum bending moments are:

$$M'_{fes} = M_{max,fes} / H^3 = 1/3 K_{aR} \gamma_s [m / (2+m)]^{1.5} \rightarrow \quad (6.6)$$

$$M'_{fes}/K_{aR}=M_{max,fes}/K_{aR}H^3 = 1/3 \gamma_s [m/(2+m)]^{1.5} \quad (6.7)$$

The normalised bending moments in the form of Equation (6.6) are used in Rowe's earlier analysis (1952), whereas in his later analysis (1955) they are presented in the form of Equation (6.7) and are independent of the values of φ' .

The ULS calculations for zero pore water pressures according to Eurocode 7 (1995) are presented in Chapter 4. Taking the moments about the crest, Equation (6.8) is derived and the normalised prop loads and maximum bending moments are given by Equations (6.9), (6.10) and (6.11).

$$K_p/K_a = 1 / [(1-m)^2 (1+0.5m)] \quad (6.8)$$

$$F'_{EC7}/K_a = F_{EC7} / (K_a H^2) = 0.25 \gamma_s m / (1+0.5 m) \quad (6.9)$$

$$M'_{EC7} = M_{max,EC7} / H^3 = F_{EC7}/H^2 z_o - 1/6 K_a \gamma_s z_o^3 + 1/6 K_p \gamma_s (z_o - m)^3 \quad (6.10)$$

$$M'_{EC7}/K_a = M_{max,EC7} / K_a H^3 =$$

$$F_{EC7} / (K_a H^2) z_o - 1/6 \gamma_s z_o^3 + 1/6 \gamma_s K_p / K_a (z_o - m)^3 \quad (6.11)$$

The earth pressure coefficients K_a and K_p are given by Equations (4.104) and (4.105) in Chapter 4.

In Table 6.1 the ratio of the free earth support maximum bending moments to the respective values calculated according to Eurocode 7 (1995), M'_{fes} / M'_{EC7} , and the ratio $(M'_{fes}/K_{aR})/(M'_{EC7}/K_a)$ are calculated for different values of φ' and m and are plotted in Figures 6.1 and 6.2. The ratio $(M'_{fes}/K_{aR})/(M'_{EC7}/K_a)$ is independent of φ' .

φ'	m	M'_{fes}/M'_{EC7}	$(M'_{fes}/K_{aR})/(M'_{EC7}/K_d)$
20	0.6	0.879255	1.02176
20	0.65	0.900429	1.04636
20	0.7	0.93645	1.08822
20	0.75	0.996409	1.1579
20	0.8	1.0982	1.27618
25	0.6	0.853864	1.02176
25	0.65	0.874426	1.04636
25	0.7	0.909407	1.08822
25	0.75	0.967634	1.1579
25	0.8	1.06648	1.27618
30	0.6	0.831575	1.02176
30	0.65	0.851601	1.04636
30	0.7	0.885669	1.08822
30	0.75	0.942376	1.1579
30	0.8	1.03865	1.27618
35	0.6	0.812201	1.02176
35	0.65	0.83176	1.04636
35	0.7	0.865034	1.08822
35	0.75	0.92042	1.1579
35	0.8	1.01445	1.27618
40	0.6	0.795669	1.02176
40	0.65	0.81483	1.04636
40	0.7	0.847427	1.08822
40	0.75	0.901685	1.1579
40	0.8	0.993798	1.27618

Table 6.1: Comparison between the maximum bending moment ratios derived from the Free Earth Support method (Rowe, 1952) and those derived from Eurocode 7 (EC7, 1995).

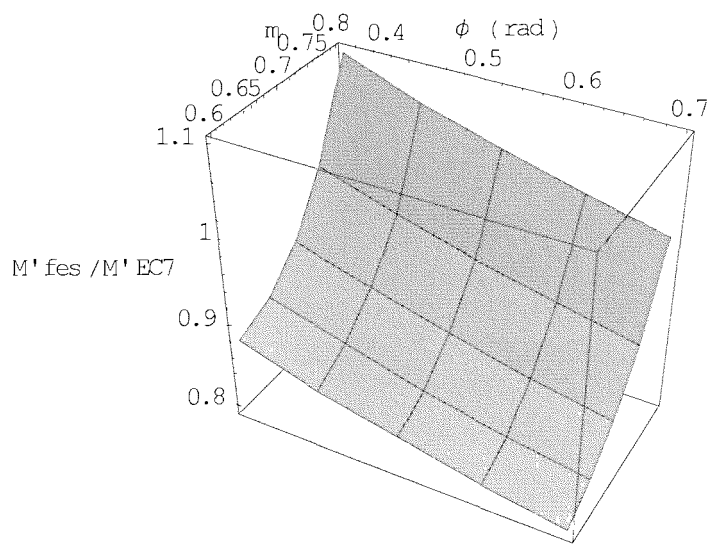


Figure 6.1: The ratio M'_{fes} / M'_{EC7} against ϕ and m .

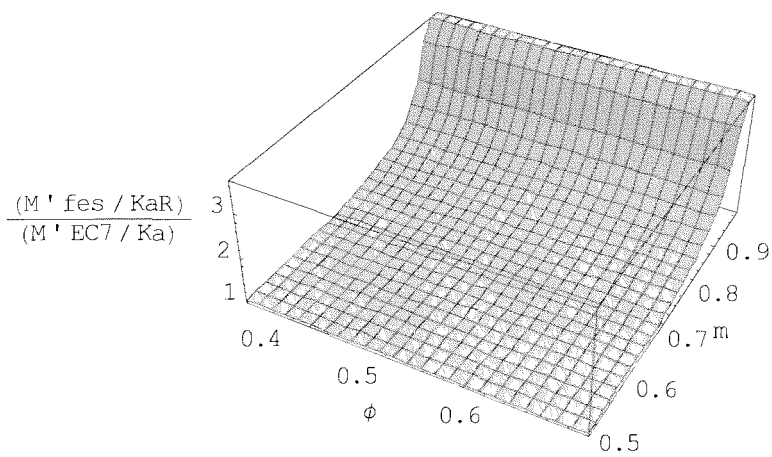


Figure 6.2: The ratio $(M'_{fes} / KaR) / (M'_{EC7} / Ka)$ against ϕ and m .

In Table 6.2 the ratio of the free earth support prop loads to the respective values calculated according to Eurocode 7 (1995), F'_{fes}/F'_{EC7} , and the ratio $(F'_{fes}/K_{aR}) / (F'_{EC7}/K_a)$ are calculated for different values of φ' and m . The ratio F'_{fes}/F'_{EC7} is plotted in Figure 6.5 and is independent of m . The values for (F'_{fes}/K_{aR}) are the same as those calculated according to Eurocode 7 (1995).

φ'	m	F'_{fes}/F'_{EC7}	$(F'_{fes}/K_{aR})/(F'_{EC7}/K_a)$
20	0.6	0.860534	1.
20	0.65	0.860534	1.
20	0.7	0.860534	1.
20	0.75	0.860534	1.
20	0.8	0.860534	1.
25	0.6	0.835683	1.
25	0.65	0.835683	1.
25	0.7	0.835683	1.
25	0.75	0.835683	1.
25	0.8	0.835683	1.
30	0.6	0.813869	1.
30	0.65	0.813869	1.
30	0.7	0.813869	1.
30	0.75	0.813869	1.
30	0.8	0.813869	1.
35	0.6	0.794907	1.
35	0.65	0.794907	1.
35	0.7	0.794907	1.
35	0.75	0.794907	1.
35	0.8	0.794907	1.
40	0.6	0.778728	1.
40	0.65	0.778728	1.
40	0.7	0.778728	1.
40	0.75	0.778728	1.
40	0.8	0.778728	1.

Table 6.2: Comparison between the prop load ratios derived from the Free Earth Support method (Rowe, 1952) and those derived from Eurocode 7 (EC7, 1995).

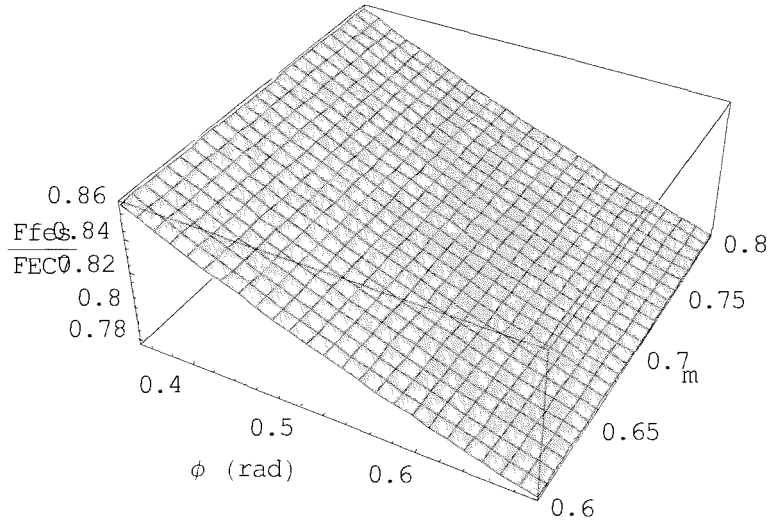


Figure 6.3: The ratio F'_{fes}/F'_{EC7} against ϕ and m .

If M'_{exp} , F'_{exp} and M'_{th} , F'_{th} are the experimental and theoretical maximum bending moments and prop loads according to Rowe, then the y - y' axis in Rowe's curves can be multiplied by M'_{fes}/M'_{EC7} and F'_{fes}/F'_{EC7} according to Equations (6.12) to (6.15):

$$M'_{exp} / M'_{fes} \times M'_{fes} / M'_{EC7} = M'_{exp} / M'_{EC7} \quad (6.12)$$

$$M'_{th} / M'_{fes} \times M'_{fes} / M'_{EC7} = M'_{th} / M'_{EC7} \quad (6.13)$$

$$F'_{exp} / F'_{fes} \times F'_{fes} / F'_{EC7} = F'_{exp} / F'_{EC7} \quad (6.14)$$

$$F'_{th} / F'_{fes} \times F'_{fes} / F'_{EC7} = F'_{th} / F'_{EC7} \quad (6.15)$$

6.2.2 Experimental curves

Rowe's reduction curves based on experiments are redrawn on transformed axes for dense and loose sands and for retained height ratios h/H from 0.6 to 0.8 in the Figures presented in this Section. Rowe used values of $\phi'=30^\circ$ and $\text{Log}m_r=4.75 \text{ lb/ft}^3$ for loose sands, while $\phi'=40^\circ$ and $\text{Log}m_r=5.75 \text{ lb/ft}^3$ for dense sands. As already discussed in Section 3.2, the definition of parameter m_r is quite unusual and might be considered as a measure of the rate of increase of Young's modulus with depth, E^* . Analyses according to the MSD method is carried out for $\phi'=30^\circ$ and $\text{Log}A=-2.25$ for loose sands and $\phi'=40^\circ$ and $\text{Log}A=-3.33$ for dense sands to compare with Rowe's results. For the values of parameter $A=\gamma_s/G^*$, it is assumed that parameter m_r in Rowe's analysis is equal to E^* ; hence, G^* may be estimated. It should be noted that in the MSD analysis the retained height ratio h/H is equal to 0.73 for $\phi'=30^\circ$ (loose sands) and equal to 0.82 for $\phi'=40^\circ$ (dense sands); this is because a unique value of h/H can be correlated to a specific value of ϕ' in the ULS calculations according to Eurocode 7 (EC7, 1995) as shown in Section 4.5 (Equations 4.103-4.105). The results based on the MSD method are presented in Figures 6.7, 6.10, 6.13 and 6.15.

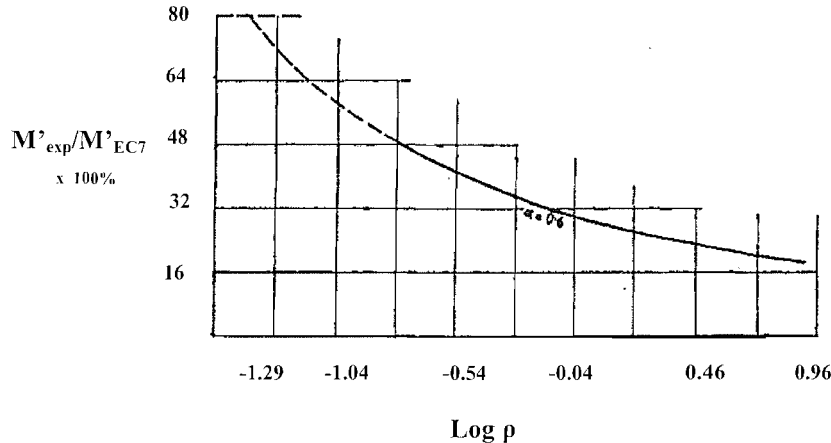


Figure 6.4: Rowe's experimental reduction curves for $h/H=0.6$ for dense sands on transformed axes.

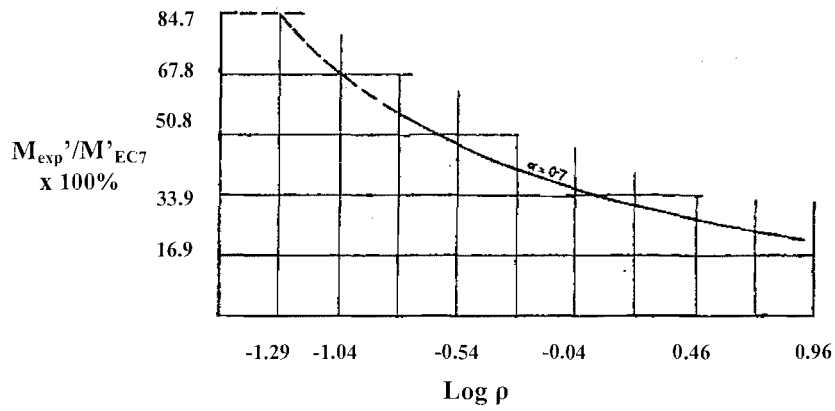


Figure 6.5: Rowe's experimental reduction curves for $h/H=0.7$ for dense sands on transformed axes.

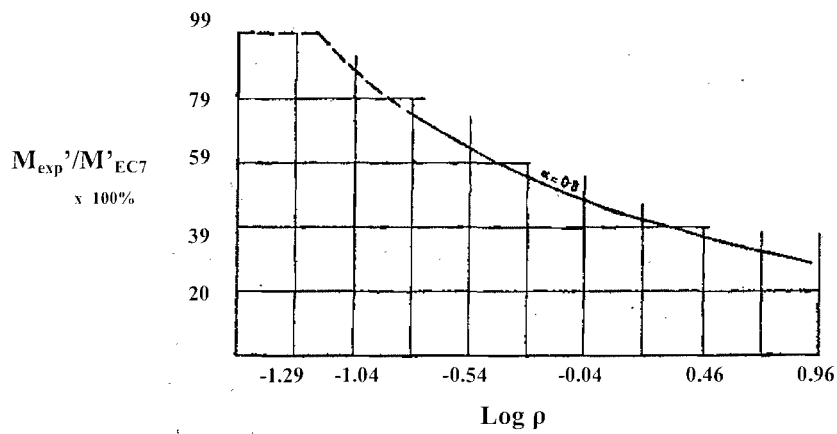


Figure 6.6: Rowe's experimental reduction curves for $h/H=0.8$ for dense sands on transformed axes.

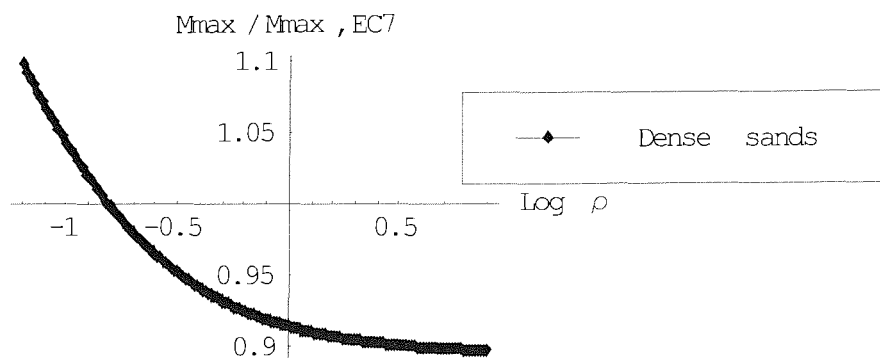


Figure 6.7: MSD reduction curve for $h/H=0.8$ for dense sands.

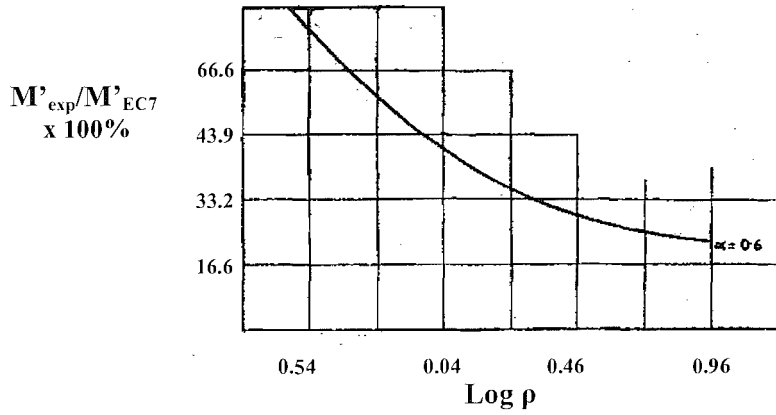


Figure 6.8: Rowe's experimental reduction curves for $h/H=0.6$ for loose sands on transformed axes.

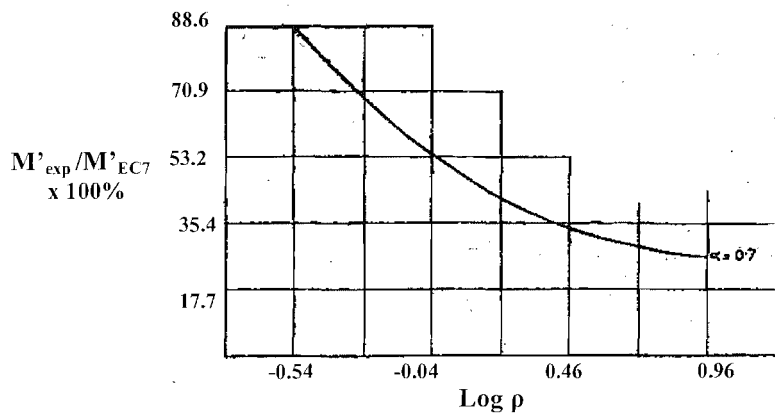


Figure 6.9: Rowe's experimental reduction curves for $h/H=0.7$ for loose sands on transformed axes.

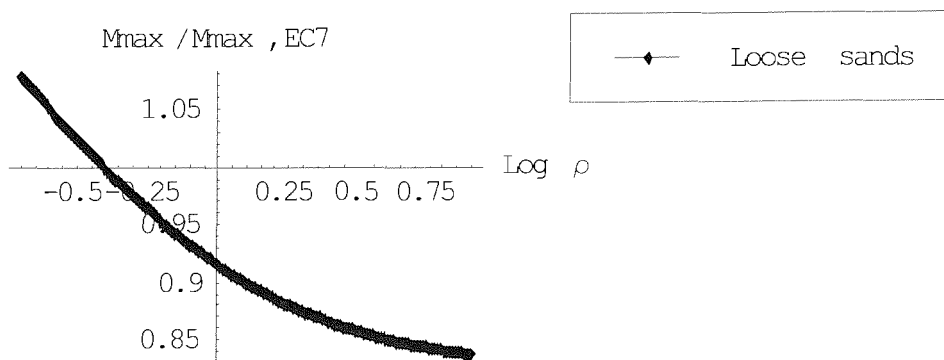


Figure 6.10: MSD reduction curve for $h/H=0.7$ for loose sands.

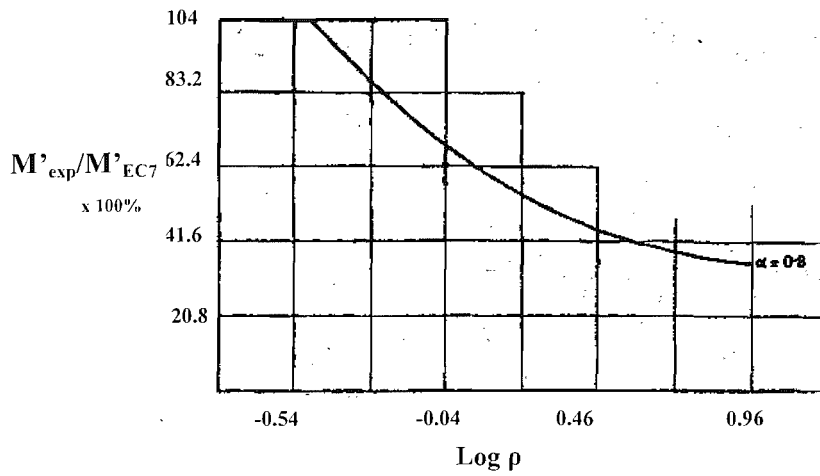


Figure 6.11: Rowe's experimental reduction curves for $h/H=0.8$ for loose sands on transformed axes.

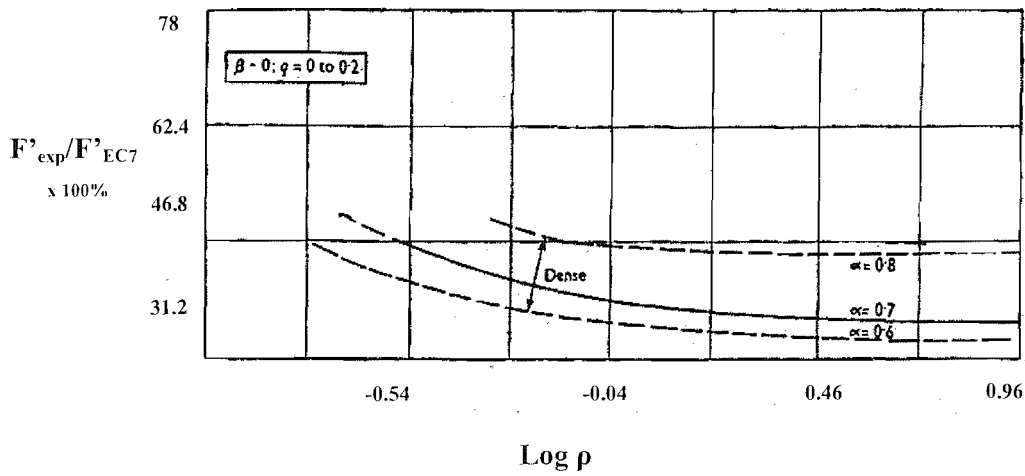


Figure 6.12: Rowe's experimental reduction curves for prop loads for dense sands for h/H from 0.6 to 0.8.

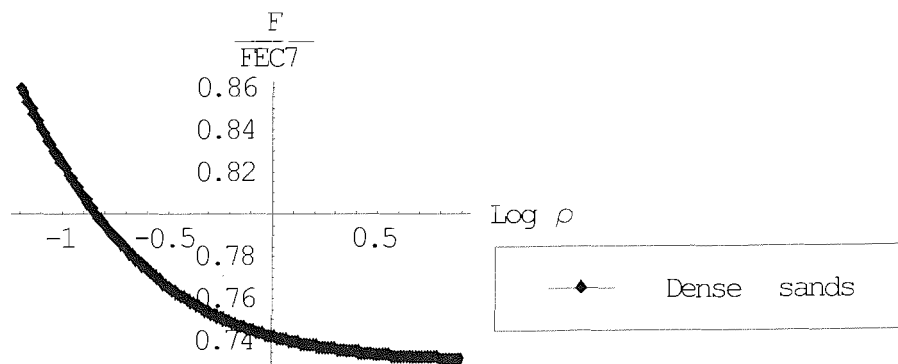


Figure 6.13: MSD reduction curve for $h/H=0.8$ for dense sands.

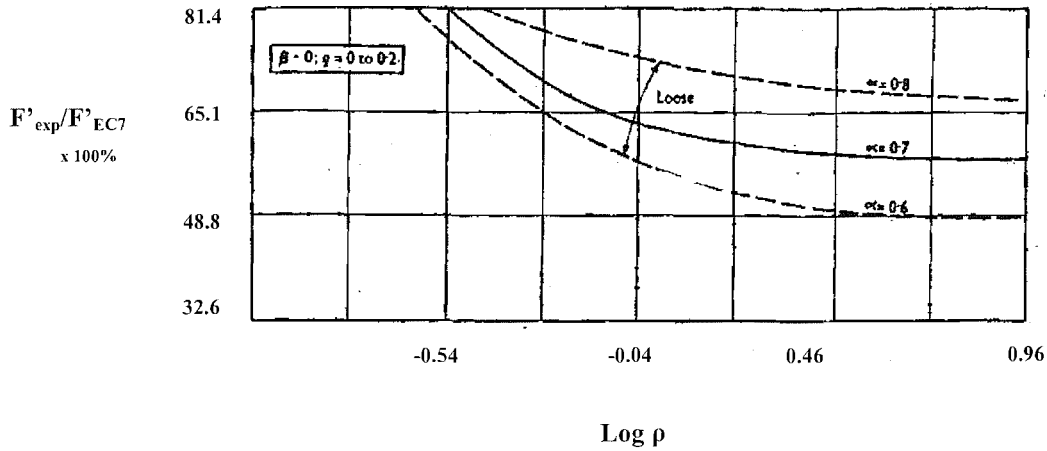


Figure 6.14: Rowe's experimental reduction curves for prop loads for loose sands for h/H from 0.6 to 0.8.

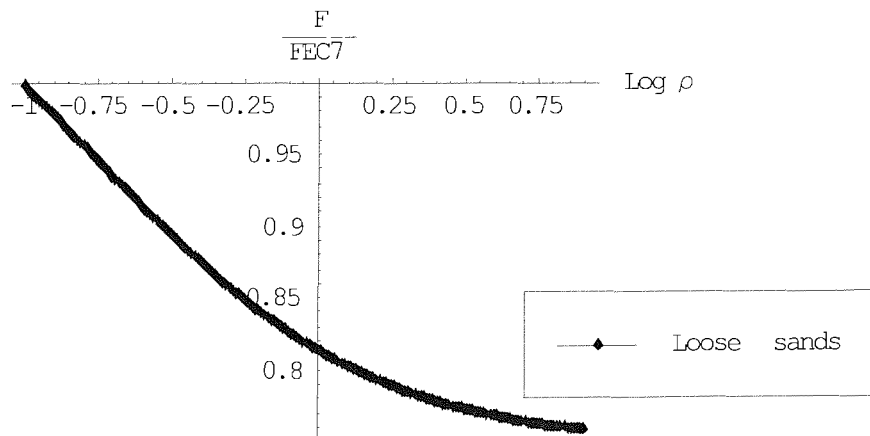


Figure 6.15: MSD reduction curve for $h/H=0.7$ for loose sands.

From Rowe's curves on transformed axis, the reduction in the maximum bending moments and prop loads is greater when the design procedure suggested in the Eurocode (EC7, 1995) is followed rather than the free earth support method. In Figures 6.7, 6.10, 6.13 and 6.15 the pattern of the reduction according to the MSD method is the same with that derived from Rowe's experiments. However, for increasing wall flexibility Rowe's experiments show larger reduction than the MSD method in both the maximum bending moments and the prop loads. According to the MSD method, Eurocode 7 (EC7, 1995) might underpredict the maximum bending moments and prop loads for stiffer walls; this is not noticed in Rowe's results. Rowe presented mean curves for the prop loads with surcharge coefficients ($q/\gamma_s H$) in the range from 0 to 0.2, whereas in the MSD method the

surcharge was assumed to be equal to 0; this might be a reason for the difference in the results. It should be noted that the soil parameter m_r used in Rowe's analysis is quite unusual and it is assumed to be equivalent to the rate of increase of the Young's modulus with depth, E^* to enable the comparison with the MSD results; however there might be some uncertainty in this assumption. Moreover, Powrie, Pantelidou and Stallebrass (1998) suggested that for the soil in front of a retaining wall propped at the crest, the change in the stress path direction during wall installation might be smaller, resulting in a significant less stiff response during excavation in comparison with the retained soil. Therefore, a more rapid rate of mobilisation of soil strength with mobilized strength may be used for the retained soil. This was not taken into account in the MSD method; hence it might be another reason for the divergence in the results.

6.2.3 Theoretical curves

Rowe's (1955) mean theoretical curves for the maximum bending moments and prop loads are redrawn on transformed axes in Figures 6.16 and 6.19 respectively, where M'_{th} , F'_{th} and M'_{EC7} , F'_{EC7} are the normalised maximum bending moments and the normalised prop loads according to the Free Earth Support method and Eurocode 7 (EC7, 1995) respectively.

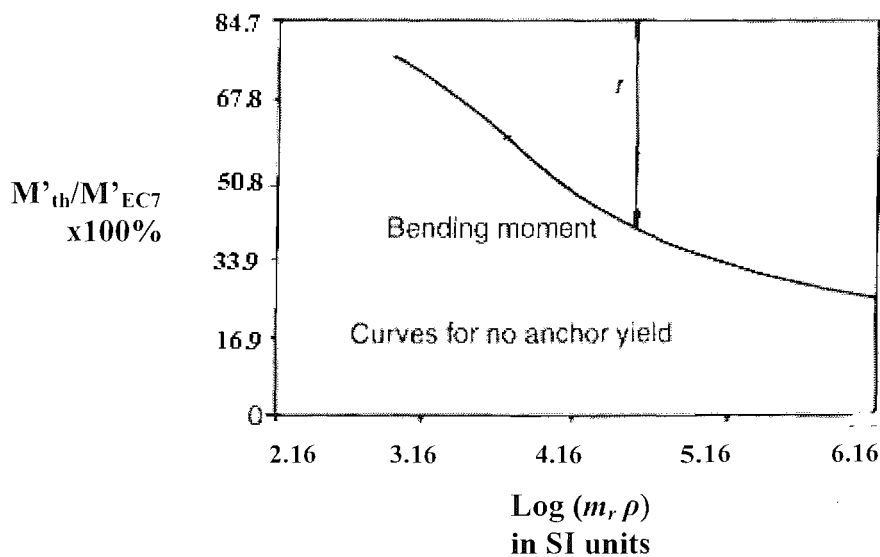


Figure 6.16: Rowe's theoretical mean reduction curve for dense sands on transformed axes.

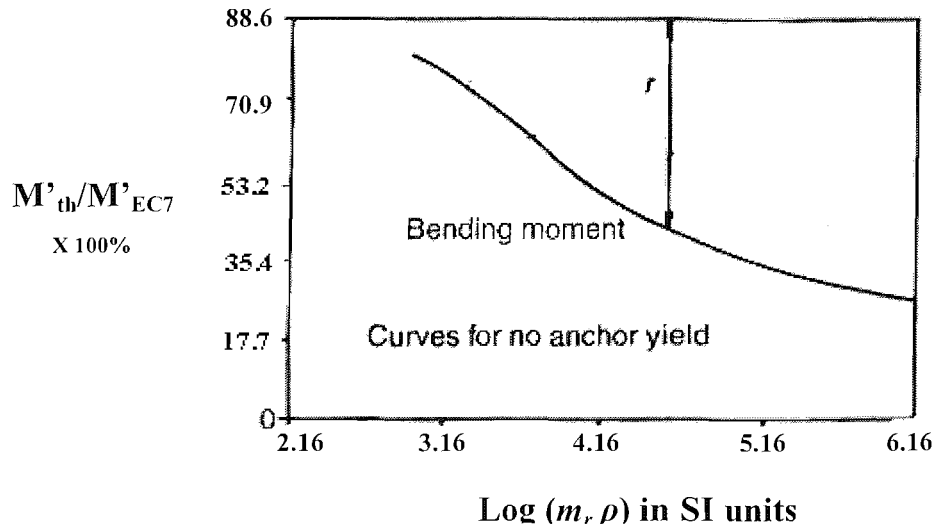


Figure 6.17: Rowe's theoretical mean reduction curve for loose sands on transformed axes.

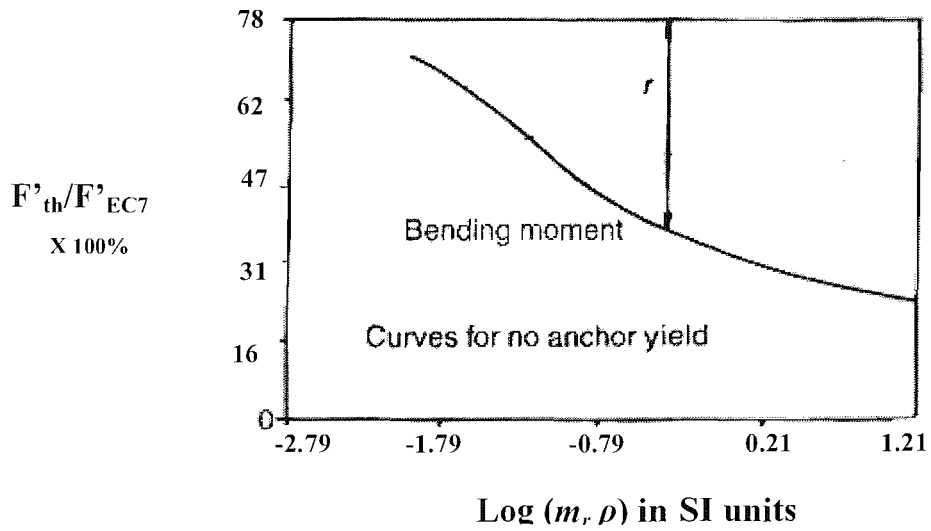


Figure 6.18: Rowe's theoretical mean reduction curve for dense sands on transformed axes.

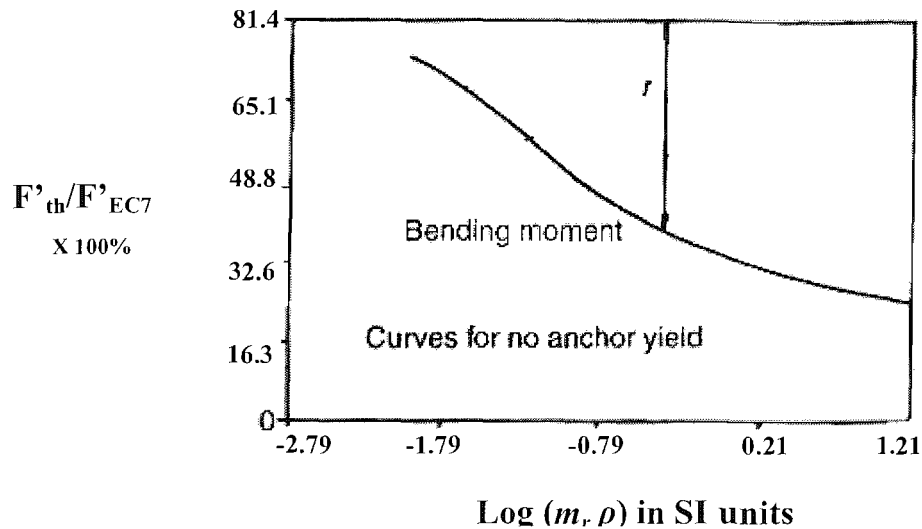


Figure 6.19: Rowe's theoretical mean reduction curve for loose sands on transformed axes.

The theoretical curves presented by Rowe (1955) and redrawn in transformed axes in the Figures are mean curves for walls with retained ratios from 0.6 to 0.8, anchor levels from 0 to 0.2 and surcharge coefficients from 0 to 0.2. According to Rowe's (1955) theoretical curves the reduction in the maximum bending moments and prop loads is greater when the design procedure suggested in the Eurocode (EC7, 1995) is followed rather than the free earth support method. Rowe (1955) notes that there is a wide divergence between his experimental and theoretical curves for stiff walls in dense and loose sands. This may be explained by the uncertainty in the soil parameter m_r used in the theoretical approach.

6.3 COMPARISON OF THE MSD METHOD BETWEEN STIFF AND FLEXIBLE WALLS

Bolton and Powrie (1988) introduced the mobilised strength method for stiff walls as described in Chapter 2. According to this approach, the active and passive soil zones are subdivided into two triangles, the mobilised soil strength, ϕ'_{mob} , is assumed to be uniform with depth and consistent with the development of a uniform shear strain in each triangle. For a wall propped at the crest, the shear strain on the retained side is equal to $2 \delta\theta$ and on the excavated side is equal to $2 \delta\theta (1 + h/d)$, where $\delta\theta$ is the rotation at the crest and the pattern of the deformations is presented in Figure 2.12.

The mobilised strength method for flexible walls, as presented in Chapter 4, assumes that the active soil zone is subdivided into four triangles and the passive into two triangles. The use of additional kinematically admissible strain fields permits the incorporation of different mobilised shear strengths and hence mobilized strains in each zone of the soil surrounding the retaining wall. The shear strains are related to the wall rotations at the crest as described in Chapter 4 and the pattern of the rotations and deformations is presented in Figure 4.31.

For a flexible wall, mobilisation of four different values of shear strength would be expected on the retained side of the wall and two on the excavated side. However, as the wall flexibility decreases the rotations $\delta\theta_1$, $\delta\theta_2$ and $\delta\theta_3$, which are attributed to wall bending, should decrease, while $\delta\theta_4$, which is attributed to rigid body rotation should increase. Ideally, for a very stiff wall the rotations $\delta\theta_1$, $\delta\theta_2$ and $\delta\theta_3$ would approach zero, the shear strains and mobilized shear strengths would become uniform in the active and passive soil zone and reach the values suggested by Bolton and Powrie (1988) and the pattern of deformations would resemble that shown in Figure 2.12; this is checked in the following examples.

6.3.1 Example 1

In Table 6.3 the mobilised shear strength in each triangle and the wall rotations at the crest are shown for a value of A equal to 10^{-2} and different values of $\text{Log } \rho$ and φ' . The mobilised strengths within the triangles OAE, OBF, OCP, ODG, FGM and FPL, as showed in Figure 4.31, are φ'_{mob1} , φ'_{mob2} , φ'_{mob3} , φ'_{mob4} , φ'_{mob5} and φ'_{mob6} respectively. From Table 6.3, it is obvious that for low wall flexibility values ($\text{Log } \rho = -6$) the mobilised strength becomes uniform on the retained and excavated side of the wall and the rotations $\delta\theta_1$, $\delta\theta_2$ and $\delta\theta_3$ tend to zero and are significantly lower than $\delta\theta_4$. For higher wall flexibility values different values of soil strength are mobilised and the rotations $\delta\theta_1$, $\delta\theta_2$ and $\delta\theta_3$ become higher than $\delta\theta_4$.

In the case of $A=10^{-2}$, $\varphi' = 20^\circ$ and $\text{Log } \rho = -6$, the mobilized strength on the retained side is uniform and equal to 0.219, while on the excavated side is equal to 0.333. For the same case, the shear strains behind (γ_b) and in front (γ_f) of the wall according to Bolton and Powrie (1988) are given by Equations (6.16) and (6.17)

$$\gamma_b = 2 \delta\theta_4 = 0.0038 \quad (6.16)$$

$$\gamma_f = 2 \delta\theta_4 (1+h/d) = 2 \delta\theta_4 / (1-m) = 0.0091 \quad (6.17)$$

where m is the retained height ratio and is equal to 0.582. The shear strains are related to the mobilised strengths behind ($\varphi'_{mob,b}$) and in front ($\varphi'_{mob,f}$) of the wall by the relationship (4.40) in Chapter 4.

$$\varphi'_{mob,b} = \sin^{-1} [\gamma_b / (A + B \gamma_b)] = 0.219 \quad (6.18)$$

$$\varphi'_{mob,f} = \sin^{-1} [\gamma_f / (A + B \gamma_f)] = 0.333 \quad (6.19)$$

Therefore, for low wall flexibility values the mobilized strength method as developed in Chapter 4 gives the same results with the geostructural mechanism proposed by Bolton and Powrie(1988).

$$A=w/G^*=10^{-2}$$

φ'	$\text{Log } \rho$	φ'_{mob1}	φ'_{mob2}	φ'_{mob3}	φ'_{mob4}	φ'_{mob5}	φ'_{mob6}	$\delta\theta_1$	$\delta\theta_2$	$\delta\theta_3$	$\delta\theta_4$
20	-6	0.257	0.257	0.257	0.257	0.303	0.303	4.403×10^{-8}	3.444×10^{-8}	2.622×10^{-8}	0.0049
20	-4	0.257	0.257	0.257	0.257	0.304	0.304	4.402×10^{-6}	3.443×10^{-6}	2.621×10^{-6}	0.005
20	-2	0.268	0.263	0.259	0.255	0.3026	0.308	0.0004	0.0003	0.0003	0.0048
20	0	0.342	0.337	0.323	0.219	0.279	0.341	0.0341	0.0259	0.0192	0.003
30	-6	0.374	0.374	0.374	0.374	0.473	0.473	6.002×10^{-8}	1.902×10^{-8}	1.563×10^{-8}	0.0068
30	-4	0.374	0.374	0.374	0.374	0.473	0.473	6.001×10^{-6}	1.902×10^{-6}	1.566×10^{-6}	0.0068
30	-2	0.385	0.377	0.374	0.372	0.472	0.473	0.0006	0.00019	0.00015	0.0066
30	0	0.504	0.477	0.4418	0.3004	0.4365	0.507	0.044	0.0137	0.0111	0.0036
40	-6	0.484	0.484	0.484	0.484	0.652	0.652	6.394×10^{-8}	8.591×10^{-9}	7.563×10^{-9}	0.0084
40	-4	0.484	0.484	0.484	0.484	0.652	0.652	6.393×10^{-6}	8.59×10^{-7}	7.562×10^{-7}	0.0084
40	-2	0.495	0.484	0.483	0.481	0.651	0.652	0.000633	0.000085	0.000075	0.0082
40	0	0.659	0.569	0.511	0.389	0.619	0.671	0.0478	0.0064	0.0055	0.0046

Table 6.3

6.3.2 Example 2

In Table 6.4 the mobilised shear strength in each triangle and the wall rotations at the crest are shown for a value of φ' equal to 20° and different values of $\text{Log } \rho$ and $\text{Log } A$. From Table 6.4, as the soil becomes stiffer ($\text{Log } A$ decreases), the wall has to become stiffer for the mobilised strength to become uniform on the retained and excavated side.

In the case of $\varphi' = 20^\circ$, $A = 10^{-4}$ and $\text{Log } \rho = -7$, the mobilized strength on the retained side is uniform and equal to 0.22, while on the excavated side is equal to 0.333. For the same case, the shear strains behind (γ_b) and in front (γ_f) of the wall according to Bolton and Powrie (1988) are given by Equations (6.20) and (6.21)

$$\gamma_b = 2 \delta\theta_4 = 3.8 \times 10^{-5} \quad (6.20)$$

$$\gamma_f = 2 \delta\theta_4 (1+h/d) = 2 \delta\theta_4 / (1-m) = 9.1 \times 10^{-5} \quad (6.21)$$

where m is the retained height ratio and is equal to 0.582. The mobilised strengths behind ($\varphi'_{mob,b}$) and in front ($\varphi'_{mob,f}$) of the wall are:

$$\varphi'_{mob,b} = \sin^{-1} [\gamma_b / (A + B \gamma_b)] = 0.22 \quad (6.22)$$

$$\varphi'_{mob,f} = \sin^{-1} [\gamma_f / (A + B \gamma_f)] = 0.333 \quad (6.23)$$

The values calculated in Equations (6.22) and (6.23) are the same as those shown in Table 6.4 for the specific case examined.

$\varphi'=20$

Log A	Log ρ	φ'_{mob1}	φ'_{mob2}	φ'_{mob3}	φ'_{mob4}	φ'_{mob5}	φ'_{mob6}	$\delta\theta_1$	$\delta\theta_2$	$\delta\theta_3$	$\delta\theta_4$
-6	-7	0.258	0.258	0.258	0.257	0.304	0.304	4.3955×10^{-9}	3.4386×10^{-9}	2.617×10^{-9}	4.97×10^{-7}
-6	-6	0.2575	0.2575	0.2575	0.2575	0.3038	0.3038	4.403×10^{-8}	3.444×10^{-8}	2.622×10^{-8}	4.84×10^{-7}
-6	-4	0.268	0.263	0.259	0.256	0.303	0.306	4.331×10^{-6}	3.39×10^{-6}	2.58×10^{-7}	0.000048
-6	-2	0.268	0.263	0.259	0.255	0.303	0.306	0.00043	0.00033	0.00026	0.00484
-6	0	0.349	0.349	0.351	0.211	0.274	0.349	0.0322	0.0241	0.0177	2.685×10^{-7}
-4	-7	0.257	0.257	0.257	0.257	0.303	0.303	4.403×10^{-9}	3.444×10^{-9}	2.622×10^{-9}	0.0000499
-4	-6	0.258	0.258	0.257	0.257	0.3037	0.3038	4.402×10^{-8}	3.443×10^{-8}	2.621×10^{-8}	0.00005
-4	-4	0.268	0.263	0.259	0.256	0.3027	0.3058	4.331×10^{-6}	0.000657708207	2.581×10^{-6}	0.000048
-4	-2	0.342	0.337	0.323	0.219	0.279	0.341	0.00034	0.00026	0.00019	0.00003
-4	0	0.349	0.349	0.348	0.211	0.274	0.349	0.0323	0.0241	0.0177	0.000027
-2	-7	0.257	0.257	0.257	0.257	0.304	0.304	4.4032×10^{-9}	3.444×10^{-9}	2.622×10^{-9}	0.005
-2	-6	0.257	0.257	0.257	0.257	0.304	0.304	4.403×10^{-8}	3.444×10^{-8}	2.622×10^{-8}	0.005
-2	-4	0.257	0.257	0.257	0.257	0.303	0.303	4.402×10^{-6}	3.443×10^{-6}	2.621×10^{-6}	0.005
-2	-2	0.268	0.263	0.259	0.255	0.302	0.305	0.00043	0.00033	0.00026	0.0048
-2	0	0.342	0.337	0.323	0.219	0.278	0.341	0.0341	0.0259	0.0192	0.003

Table 6.4

6.4 SUMMARY

Rowe's (1952, 1955) experimental and theoretical curves are redrawn on transformed axes to show the reduction in the maximum bending moments and displacements when the design procedure suggested in the Eurocode 7 (EC7, 1995) is followed; the reduction is generally greater compared to the free earth support method. The MSD curves display a similar reduction pattern; however, Rowe's experiments show larger reduction in both the maximum bending moments and the prop loads than the MSD method for increasing wall flexibility. According to the MSD method, Eurocode 7 (EC7, 1995) might underpredict the maximum bending moments and prop loads for stiffer walls; this is not noticed in Rowe's analysis. However, this may be justified to a certain extent since Rowe presented mean curves and used a rather ambiguous parameter to represent the soil behaviour. Furthermore, the change in the stress path direction during wall installation, which might result in a less stiff response of the soil in front of the retaining wall during excavation, has not been incorporated in the MSD method. This might be another reason for the divergence in the results.

To assess the consistency of the MSD method as presented in this thesis, an analysis for low wall flexibility values was carried out. For stiff walls, the MSD method tends to values predicted by the geosstructural mechanism proposed by Bolton and Powrie(1988).

7. VALIDATION OF THE MSD METHOD FOR FLEXIBLE WALLS WITH CASE HISTORIES

7.1 INTRODUCTION

The validity of the MSD method for flexible walls is assessed by comparison with data from five monitored case histories of deep excavations. In recent engineering practice, detailed data for singly propped at the crest embedded retaining walls are limited. Therefore, one case history of a singly propped retaining wall at Bell Common is presented. The rest of the case histories are retaining walls supported by temporary props near the crest and a permanent reinforced concrete prop slab at dredge level. The data used for comparison with the MSD method are those obtained during the period that followed the installation of the temporary props and before casting of the permanent prop slab; hence, for these stages the walls act as singly propped at the crest.

The MSD method is a simple and practical design framework which may also be used to check whether a further more complicated analysis is required. Therefore, the following simplifications are made in the calculations according to the MSD method:

- Lower bound parameters are used.
- The soil profile in the case histories is variable; hence the selection of a representative value for the soil parameter $A=\gamma_s/G^*$ used in the MSD calculations is complicated. In some case histories deposits of sand and gravel overlying clay are found, and London Clay extends to a greater depth than the other soil layers; therefore, it is assumed that the properties of clay will govern the behaviour, and the value of parameter $A=\gamma_s/G^*$ is chosen to be representative of the London clay. Jardine *et al* (1984) presented results of the ratio E_u/c_u against the axial strain, where E_u is the undrained Young's modulus and c_u the undrained shear strength, obtained from triaxial tests on London clay samples with different overconsolidation ratios. In this Section, parameter $A=\gamma_s/G^*$ is calculated from the results provided by Jardine *et al* (1984) for axial strains equal to 0.01% in conjunction with the undrained shear strength profile of the London Clay given in each case history with the exception of

case history 4. In case history 4, Atherfield Clay was found to extend to a great depth; hence, different values of parameter A were used as described in Section 7.5.

- In order to provide general results, the MSD method has been developed for conditions of pore water pressures at ground level or at half the retained height level as described in Chapter 5. Hence, for the case histories examined two solutions are presented and compared; the ground water table in the first one is assumed to be at ground level, while in the second one at a distance of half the retained height from the ground level.
- The temporary props are assumed to be installed at the crest, although in some case histories they were installed at a small distance from the crest.
- The value of the factor of safety applied to the soil strength and employed in the MSD calculations is derived from the limit equilibrium calculations according to Eurocode 7 (EC7, 1995), since the excavation geometry is already known.

7.2 CASE HISTORY 1: Propped contiguous bored pile wall at Walthamstow

The first case study is a propped contiguous bored pile retaining wall constructed as part of the A406 North Circular Road improvement scheme between Chingford Road and Hale End Road in Walthamstow, London (Project Report 10, E468A/BG, TRL, 1993). The instrumented section of the wall was formed from 17m deep by 1.5m diameter bored piles, spaced at 1.7m centres with a retained height of 8m, supported by temporary props at distance of 0.7m below the crest and a permanent prop slab at dredge level. Measurements of the wall bending moments and movements were obtained during and after construction. Ground instrumentation in the vicinity of the wall was installed before commencement of construction. The site location and the instrumented sections are shown in Figure 7.1.

The ground in the vicinity of the instrumented section comprised 1.5m made ground and a silty clay with coarse gravel overlying London Clay, which is weathered to a depth of between 5 and 6m. The ground water table is at a distance of 1.5m below the original ground level. The soil profile and the undrained shear strength from consolidated undrained triaxial tests are shown in Figure 7.2.

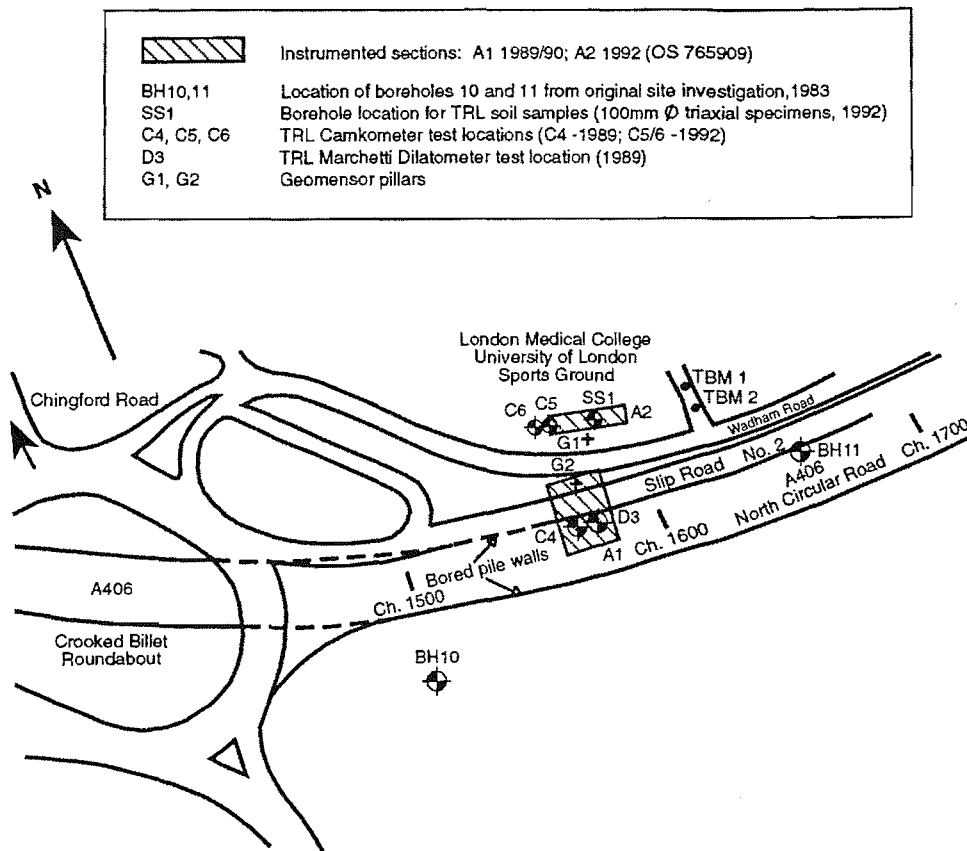


Figure 7.1: Location of site and instrumented sections (Project Report 10, E468A/BG, TRL, 1993).

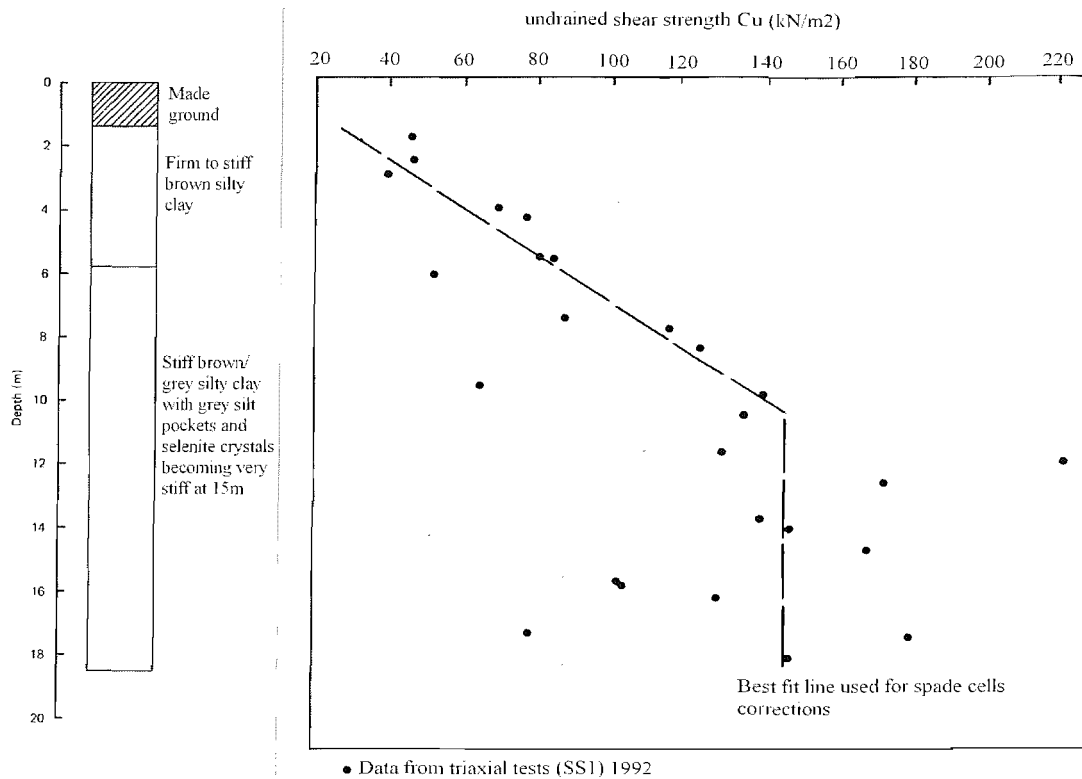


Figure 7.2: Soil profile and undrained shear strength (Project Report 10, E468A/BG, TRL, 1993).

The MSD results are validated against bending moment and movement data obtained after bulk excavation and just before the casting of the permanent prop slab. The values of the parameters used in the MSD calculations are listed in Table 7.1. For the parameter $A = \gamma_s / G^*$ a range of values is given. According to Jardine *et al* (1984), for intact samples of London Clay with initial mean effective stress equal to 226 kPa (sample LC1) and 199 kPa (sample LC2), the values of E_u / c_u at 0.01% axial strain were found equal to 1010 and 1200 respectively. The profile of the undrained shear strength with depth is given in Figure 7.2. Hence, the rate of increase of E_u with depth, E_u^* , can be determined. Assuming that the Poisson's ratio, ν_u is equal to 0.5 (undrained conditions) the rate of increase of the shear modulus with depth can be calculated from the relationship:

$$G_u^* = G_u / z = E_u / [2(1 + \nu_u)z] = E_u^* / 3 \tag{7.1}$$

Therefore, for a value of γ_s equal to 20 kN/m³, parameter A is in the range of values shown in Table 7.1.

	$\rho=H^4/EI$ (m ³ /KN)	$A= \gamma_s/G^*$ (dimensionless)	ϕ'_{peak} (degrees)	γ_s (KN/m ³)	γ_w (KN/m ³)
values	$10^{-1.73}$	$10^{-2.45} \sim 10^{-2.37}$	22°	20	10

Table 7.1

The bending moments as measured by vibrating wire strain gauges are showed in Figure 7.3. It has been checked and confirmed by the original authors that a negative sign is equivalent to a convex outwards bending of the wall towards the excavation.

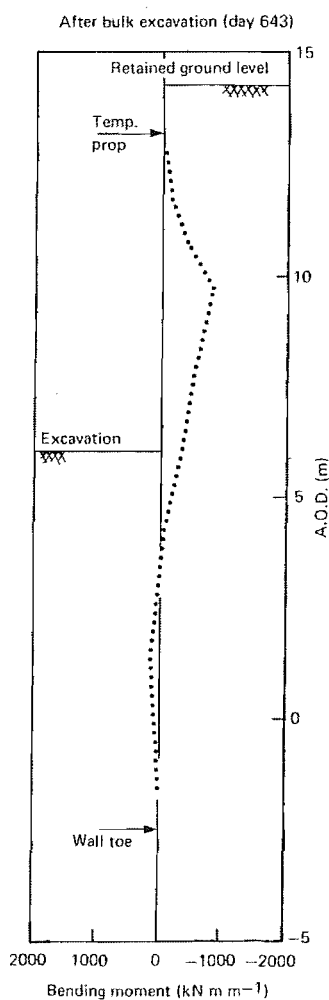


Figure 7.3: Bending moments measured by vibrating wire gauges after bulk excavation (Project Report 10, E468A/BG, TRL, 1993).

In the first column in Tables 7.2a & b the maximum bending moments estimated according to the MSD method and according to Gaba et al (2003), as described in Section 2.3.2, together with the measured values are showed. The displacements at characteristic points along the wall (Figure 4.55) are also presented. The pore water pressures are assumed to be

at ground level for the results in Table 7.2a, while at half the retained height level for the results in Table 7.2b.

Ground water table at $z = 0$	M_{max} (KNm)	δ_1 (mm)	δ_2 (mm)	δ_3 (mm)	δ_4 (mm)
Estimated (MSD)	1590~1610	15.3~16.9	28.4~30.1	26.2~27.5	8.2~9.5
Estimated (Gaba <i>et al</i>,2003)	1784				
Measured	1000	6.8	7.7	6.6	4.9

Table 7.2a

Ground water table at $z = 0.5 h$	M_{max} (KNm)	δ_1 (mm)	δ_2 (mm)	δ_3 (mm)	δ_4 (mm)
Estimated (MSD)	1505~1521	15.5~16.9	29.1~31.4	22.4~23.8	17~19.4
Estimated (Gaba <i>et al</i>,2003)	1207.8				
Measured	1000	6.8	7.7	6.6	4.9

Table 7.2b

The estimated maximum bending moments according to the MSD method is closer to the measured values when the pore water pressures are at half the retained height level. The empirical method suggested by Gaba *et al* (2003) gives a good estimation when conditions of pore water pressures at half the retained height level are assumed, but overestimates the maximum bending moments for conditions of pore water pressures at ground level; the MSD results appear to be closer to the measured ones in this case.

The displacements are over predicted by the MSD calculations. However, the measurements on the inclinometers were examined only for a short period of time until casting of the permanent prop slab. Higher horizontal movements would possibly develop

in the long term. Moreover, the displacements were obtained from the inclinometer readings assuming base fixity; hence, these values are possibly underestimated in comparison to those that occurred in reality. Generally, the MSD method gives a conservative estimation of the maximum bending moments and the displacements when compared to the measured values.

7.3 CASE HISTORY 2: Propped diaphragm wall at the A406/A10 junction

The second case study is a diaphragm retaining wall embedded in over-consolidated clay constructed as part of the A406 North Circular Road, Great Cambridge Road Junction improvement scheme in North London (Research Report 331, RR331, TRL, 1991). Field instrumentation was installed prior to any construction work to determine the initial ground conditions and instruments were installed in two of the wall panels to record measurements during and immediately after construction as showed in Figure 7.4.

At the instrumented section, made ground at the surface overlies a 1.3m thick deposit of firm sand and gravel, while firm silty clay, characteristic of the London clay formation was encountered below. The ground water table is at the top of the London clay layer which is at a distance of 2.6m from the original ground level. The soil profile together with the undrained shear strength obtained from triaxial tests is showed in Figure 7.5.

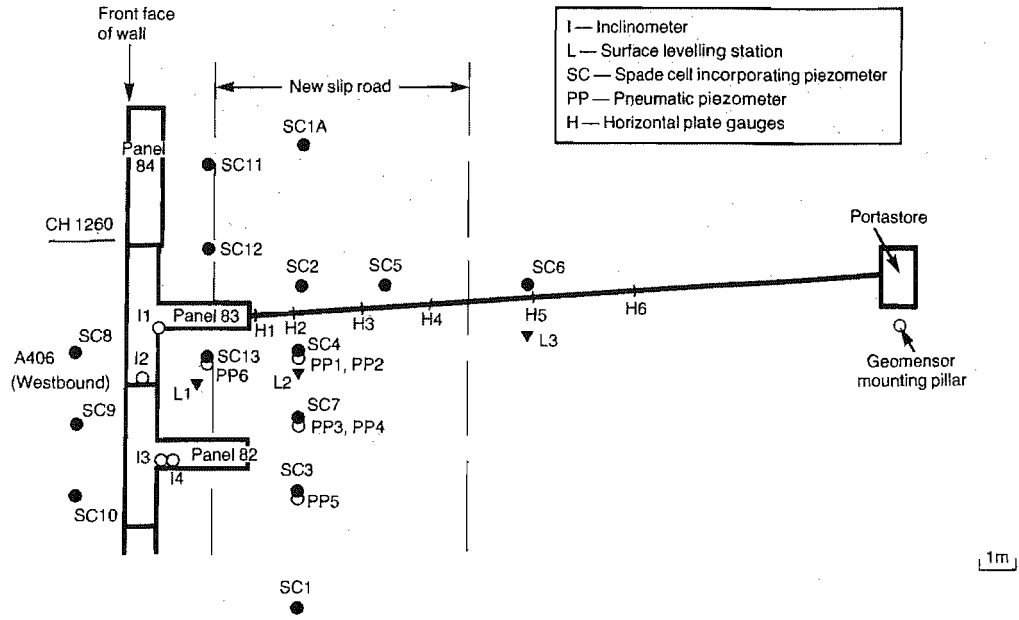


Figure 7.4: Plan of instrumentation (Research Report 331, RR331, TRL, 1991).

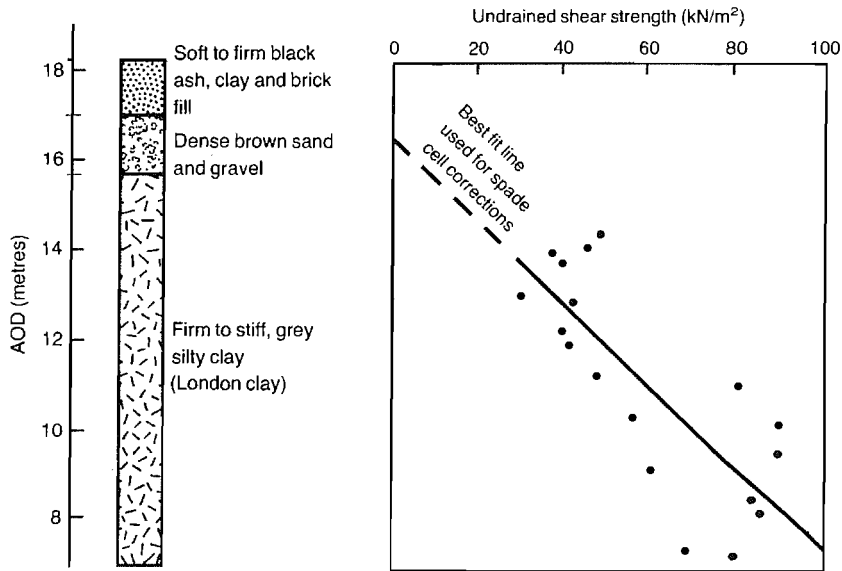


Figure 7.5: Soil profile and undrained shear strength (Research Report 331, RR331, TRL, 1991).

For the construction of the instrumented section of the wall, T-panels penetrated from original ground level to a depth of about 13.5m and excavation in front of the wall followed. Temporary props were installed near the crest retaining a height of 6m and a permanent reinforced concrete slab was later cast below the final carriageway level at 12.7m. The data obtained at the commencement of excavation and just before the casting

of the permanent slab are used for comparison with the MSD results. The construction sequence is shown in Table 7.3.

Construction sequence at instrumented section of south wall

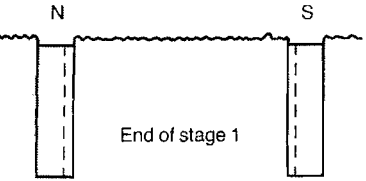
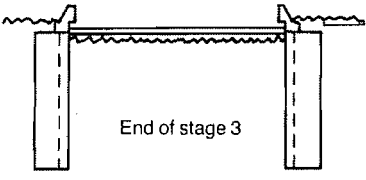
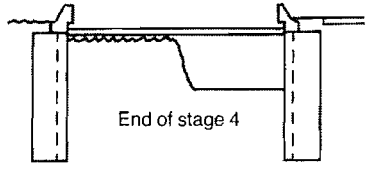
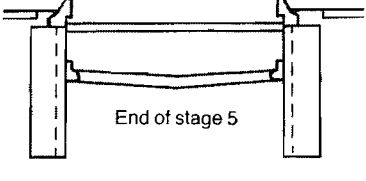
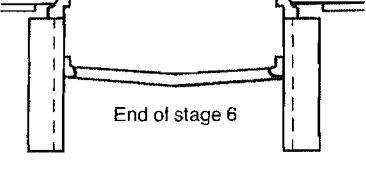
Stage	Description	Period	Schematic
1	Installation of guide walls	14-7-87	 <p>End of stage 1</p>
	Installation of wall panels under bentonite	11-9-87 to 11-4-88	
2	Temporary excavation to 2 m on both sides of wall: panels reduced to cut off levels.	5-2-88 to 9-2-88	 <p>End of stage 3</p>
	Retained side backfilled	12-4-88	
	Capping beam and parapet built	16-5-88 to 14-8-88	
	Construction of slip road on retained side	30-9-88 to 11-10-88	
	Slip road opened	16-10-88	
3	Excavation to 1.7 m	21-2-89	 <p>End of stage 4</p>
	Temporary props installed and concreted to wall	10-3-89 to 17-3-89	
4	Excavation to 5 m	20-3-89	 <p>End of stage 5</p>
	Excavation to 6 m	21-3-89	
	Excavation to 6.3 m	22-3-89	
5	Excavation completed to north wall	5-4-89	 <p>End of stage 6</p>
	Prop slab with hinges cast	12-7-89	
6	Temporary props released	2-8-89 to 3-8-89	
7	Carriageway construction	14-12-89	
	Road opened	25-2-90	

Table 7.3: Construction sequence (Research Report 331, RR331, TRL, 1991).

In Table 7.4 the values of the parameters used in the MSD calculations are listed. The values of the parameter $A = \gamma_s/G^*$ were obtained similarly to the procedure described in Section 7.2.

	$\rho = H^4/EI$ (m ³ /KN)	$A = \gamma_s/G^*$ (dimensionless)	ϕ'_{peak} (degrees)	γ_s (KN/m ³)	γ_w (KN/m ³)
values	$10^{-3.06}$	$10^{-2.34} \sim 10^{-2.27}$	24°	20	10

Table 7.4

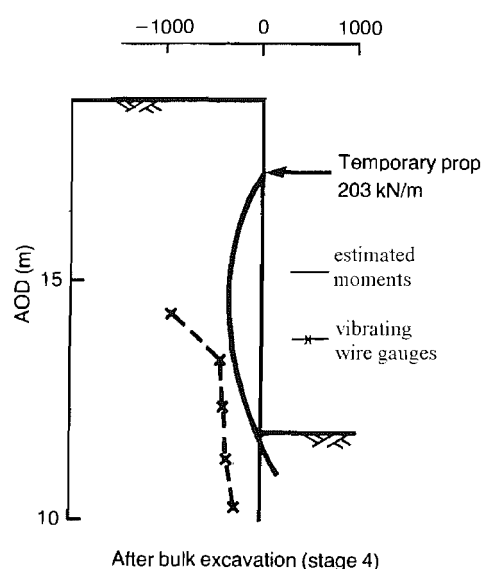


Figure 7.5: Bending moment distribution after bulk excavation (Research Report 331, RR331, TRL, 1991).

The bending moments determined from measurements on the vibrating wire strain gauges are showed in Figure 7.5. It has been checked and confirmed by the original authors that a negative sign is equivalent to a convex outwards bending of the wall towards the excavation. Some of the vibrating wire gauges stopped functioning after a specific stage; hence measurements were only available for the lower part of the wall. The estimated bending moments assuming a linear distribution of earth pressures corresponding to an earth pressure coefficient of unity on the retained side together with the prop load measured by the Contractor are shown in the same figure. The estimated values are reasonably close to those measured except for the maximum value; the maximum measured value was substantially different from the maximum estimated and it was considered suspect. However, the small number of measured values results in uncertainty.

Therefore, an average of the measured and estimated assuming $K=1$ values for the maximum bending moment was considered appropriate for comparison with the MSD results and is listed in Tables 7.5a & b, together with the maximum bending moments estimated according to the MSD method and according to Gaba *et al* (2003). The displacements at characteristic points along the wall (Figure 4.55) are also presented. The original water table is assumed to be at ground level for the results in Table 7.5a, and at half the retained height level for the results in Table 7.5b.

Ground water table at $z = 0$	M_{max} (KNm)	δ_1 (mm)	δ_2 (mm)	δ_3 (mm)	δ_4 (mm)
Estimated (MSD)	804.8~804.9	12.9~13.5	21.4~22.7	25.2~26.7	20.7~21.9
Estimated (Gaba <i>et al</i>,2003)	627.8				
Average value for measured and estimated with $K=1$	689.2	2.25	1.34	0.8	0

Table 7.5a

Ground water table at $z = 0.5 h$	M_{max} (KNm)	δ_1 (mm)	δ_2 (mm)	δ_3 (mm)	δ_4 (mm)
Estimated (MSD)	735.5~735.8	8.4~9.6	16.2~18.9	25.6~27	19.8~21.4
Estimated (Gaba <i>et al</i>,2003)	412.3				
Average value for measured and estimated with $K=1$	689.2	2.25	1.34	0.8	0

Table 7.5b

The MSD values for the maximum bending moments are reasonably close to the measured ones. However, the horizontal displacement profile is different from the one assumed in the MSD calculations and the values are overpredicted. This difference could be due to the assumption of a rigid prop in the MSD calculations. Moreover, the measurements were

examined only for a short period of time and higher horizontal movements would possibly develop in the long term.

7.4 CASE HISTORY 3: Propped secant pile wall at Hackney to M11 link

The secant pile wall being examined forms part of the south wall on the George Green tunnel which is located on the new alignment of the A12 to M11 link road. The instrumented wall section lies between Wanstead underground station and Blake Hall Road (Report 188, TRL, 1996).

The ground near the instrumented section consists of made ground to a depth of 1m and a 4.8m thick band of sandy gravel overlying a deposit of London clay. The London clay becomes stiffer with depth and some evidence of weathering was noticed in the upper 0.3m. The ground water table is at a depth of 4.5m below the ground level. The soil profile and the undrained shear strength measured from 100mm diameter triaxial specimens are shown in Figure 7.6.

Secant bored piles of 1.2m diameter were installed at 1m centres with a penetration depth of 18m at the instrumented part of the wall. A reinforced concrete capping beam was constructed on the pile tops. Temporary steel props were installed and bulk excavation was carried out. At completion of excavation the retained height was 7.5m. A reinforced concrete slab was constructed at the carriageway centre during a later stage. The main stages of the construction are given in Table 7.6. For comparison with the MSD results, the data obtained at Day 414 are examined.

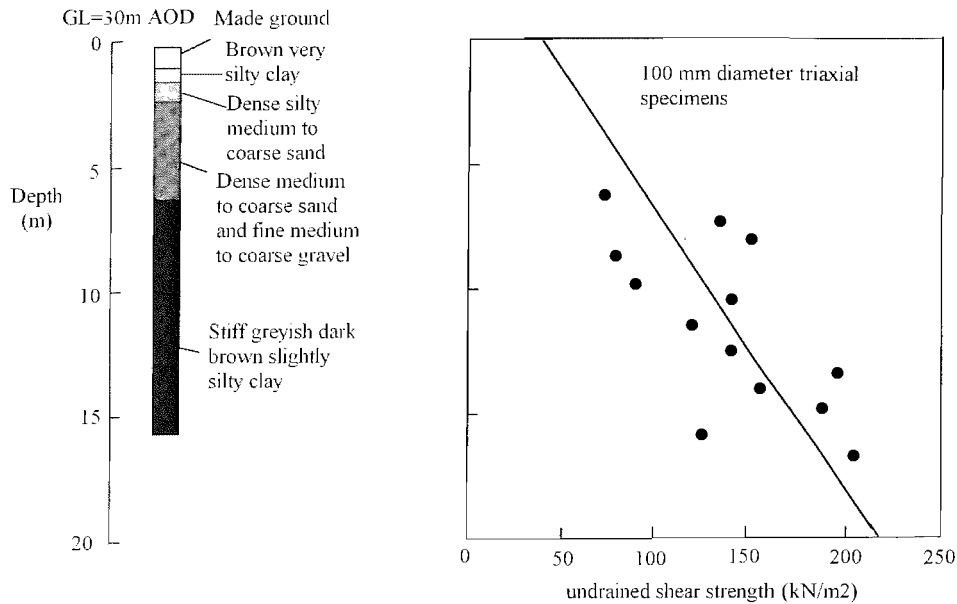


Figure 7.6: Soil profile and undrained shear strength (Report 188, TRL, 1996).

Construction sequence at instrumented area

Stage	Description	Period	Day Number
1	Installation of piles S209-S217	8/7/94 - 21/7/94	100-113
2	Capping beam constructed	30/9/94-17/11/94	184-232
3	Excavation to 4m depth Temporary props installed	16/12/94-19/12/94	261-264
		23/1/95-10/2/95	299-317
4	Excavation to 6.5m depth Excavation to formation (8m depth)	21/3/95-28/3/95	356-363
		11/4/95	377
5	Reinforced concrete slab cast	19/5/95-25/5/95	415-421
6	Jacks inserted in props	10/7/95-21/7/95	467-478
7	Temporary props released	21/7/95	478

Table 7.6: The construction sequence (Report 188, TRL, 1996).

The values of the parameters used in the MSD calculations are listed in Table 7.7. The values of the parameter $A = \gamma_s / G^*$ were obtained similarly to the procedure described in Section 7.2.

	$\rho = H^4 / EI$ (m ³ /KN)	$A = \gamma_s / G^*$ (dimensionless)	φ'_{peak} (degrees)	γ_s (KN /m ³)	γ_w (KN/m ³)
values	$10^{-1.39}$	$10^{-2.27} \sim 10^{-2.19}$	25.1°	20	10

Table 7.7

The bending moments as measured by vibrating wire strain gauges are showed in Figure 7.7. It has been checked and confirmed by the original authors that a negative sign is equivalent to a convex outwards bending of the wall towards the excavation.

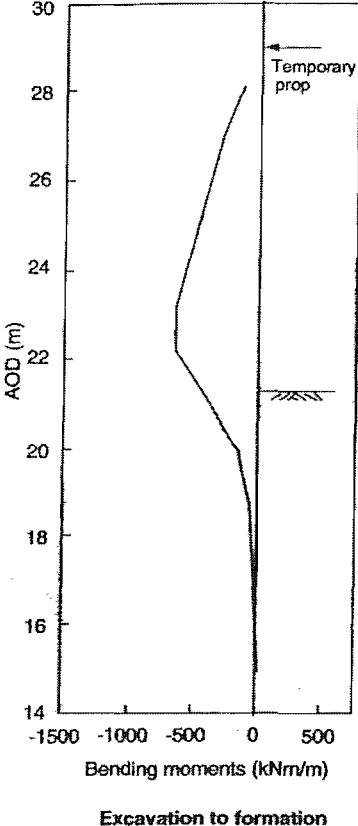


Figure 7.7: Bending moment distribution after excavation to formation and before casting of the reinforced concrete slab (Report 188, TRL, 1996).

In Tables 7.8a & b the maximum bending moments estimated according to the MSD method and according to Gaba et al (2003), as described in Section 2.3.2, together with the measured values are showed. The displacements at characteristic points along the wall (Figure 4.55) are also presented. The initial water table is assumed to be at ground level for the results in Table 7.8a, and at half the retained height level for the results in Table 7.8b.

Ground water table at $z = 0$	M_{max} (KNm)	δ_1 (mm)	δ_2 (mm)	δ_3 (mm)	δ_4 (mm)
Estimated (MSD)	1736~1787	21.9~23.5	29.8~31.2	35~36.7	33~35.9
Estimated (Gaba <i>et al</i> ,2003)	1394.8				
Measured	667	2.5	4.8	3.2	2.9

Table 7.8a

Ground water table at $z = 0.5 h$	M_{max} (KNm)	δ_1 (mm)	δ_2 (mm)	δ_3 (mm)	δ_4 (mm)
Estimated (MSD)	1559~1596	18.8~19.9	32.1~35.3	37.2~39.5	35~36.7
Estimated (Gaba <i>et al</i> ,2003)	908.7				
Measured	667	2.5	4.8	3.2	2.9

Table 7.8b

It is obvious from Tables 7.8a & b that the MSD calculations overpredict the maximum bending moments for both solutions. The estimated values according to Gaba *et al* (2003) are less than the MSD results for conditions of pore water pressures at the ground level, but are significantly different when the ground water table is assumed to be at half the retained height level. However, it should be mentioned that the magnitude of the bending moments is quite uncertain. The measured values were determined from the bending strains given by each pair of gauges based on the flexural rigidity (EI) per metre run of the secant pile wall and the same value of EI was employed in the MSD calculations. The value of parameter A was based on the experimental results on London clay presented by Jardine *et al* (1984). Therefore, the difference between the measured and the MSD values could possibly be caused by a slight divergence in the values of the parameters A or ρ used in the analysis. If the bending moments were estimated from the total lateral stress distribution as read from

spade pressure cells and piezometers before construction and summarised in Figure 7.8, higher values would be expected.

The MSD calculations result in overpredicted values of lateral displacement. However, it is noted in the relevant report that wall movement measurements were not taken at the extremes of temperature and larger movements may have actually occurred.

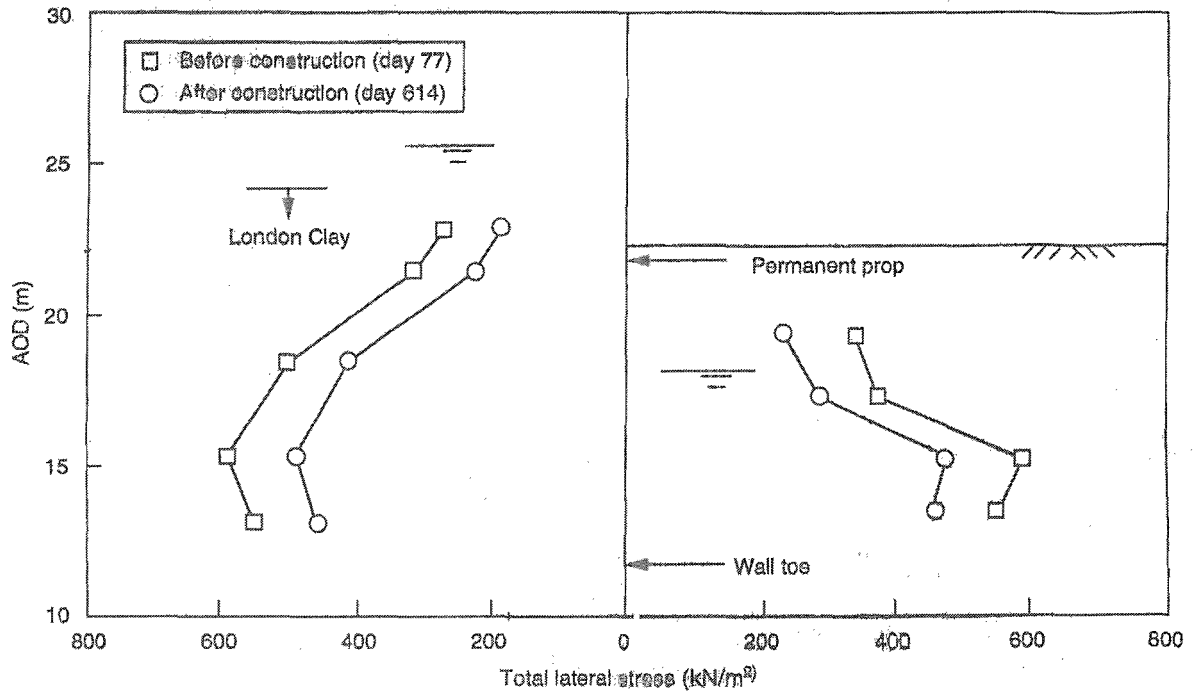


Figure 7.8: Total stress distribution measured by spade pressure cells and piezometers before and after construction (Report 188, TRL, 1996).

7.5 CASE HISTORY 4: A contiguous bored pile wall on the Channel Tunnel Rail Link at Ashford

The Channel Tunnel Rail Link (CTRL) consists of 109 km of high speed track linking the Channel Tunnel at Folkstone, Kent to the London terminus at St Pancras. At Ashford, Kent the railway runs through approximately 1.8km of cut and cover tunnels and associated retained cuttings to minimise the impact of noise and to avoid crossing existing road and rail routes at grade. The sides of the tunnels and propped retained cuttings were constructed between contiguous bored pile retaining walls (Richards *et al*, 2006). An 11m long section of a retaining wall that forms part of a propped cutting between Gasworks Lane to Beaver Road constructed has been comprehensively instrumented. The instrumented section has been constructed from bored pile walls using 1.05m diameter piles approximately 20m long and spaced at 1.35m centres. Preliminary assessment of the geology in the area was collected from borehole records and laboratory tests. The location of the examined section together with the instrumentation in the area is showed in Figure 7.9.

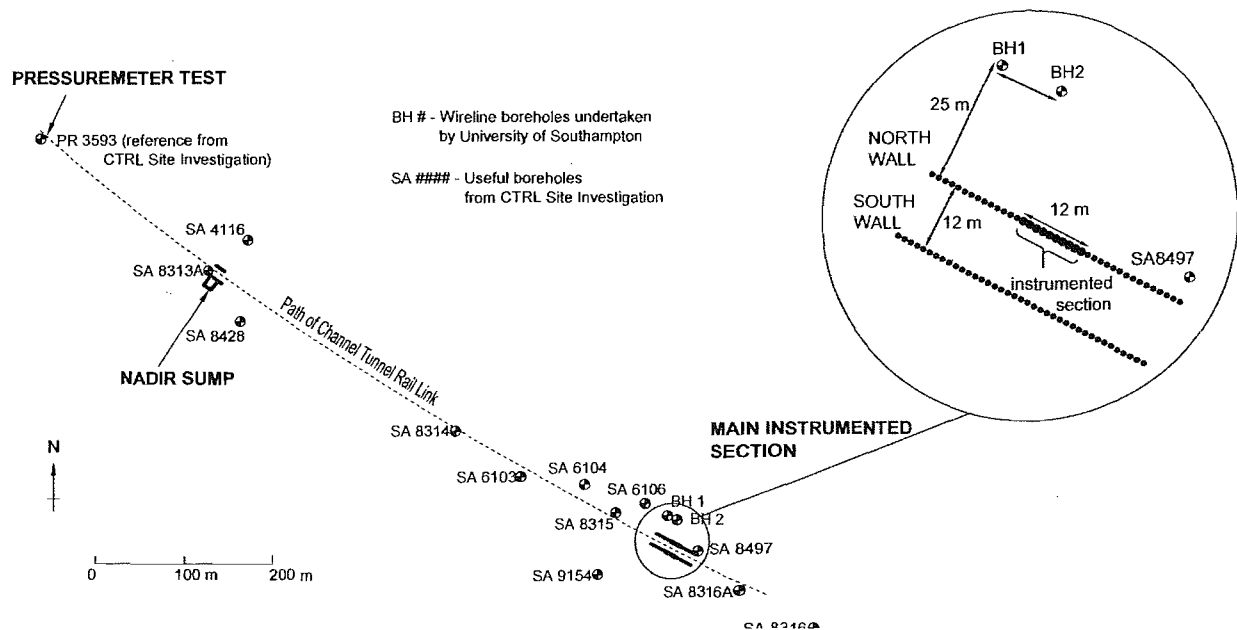


Figure 7.9: Site location and plan of instrumentation (Clark, 2006).

Made ground of 2.8m thickness overlying a 1.4m thick deposit of Hythe Beds was present at the instrumented section. High and lower plasticity Atherfield Clay of 11.9m thickness overlying Weald Clay was present at greater depths. The soil profile is shown in Figure 7.10. The soil characterisation, design and estimated in situ earth pressure parameters are listed in Table 7.9. The Atherfield Clay deposit was thicker than the rest and it is assumed in the MSD calculations that its properties govern the behaviour. Therefore, the value of parameter $A=\gamma_s/G^*$ is representative of the Atherfield Clay and is derived from results presented by Clayton *et al* (2006). Figure 7.11 shows the variation in the undrained secant Young's modulus with axial strain for an undisturbed sample of Atherfield Clay. From Figure 7.11, E_u/p'_o is equal to 800 for small strains and combining Equations (7.2) and (7.3), Equation (7.4) is derived:

$$G=Eu/[2(1+ v_u)] \quad (7.2)$$

$$p'_o=(\sigma'_{v0}+2 \sigma'_{h0}) / 3= \sigma'_{v0} (1+2 K_o)/3 \quad (7.3)$$

$$6 G (1+ v_u) / [\sigma'_{v0} (1+2 K_o)]=800 \quad (7.4)$$

From Equation (7.4), the values of the rate of increase of the undrained shear modulus with depth are calculated for $K_o=1$ and $K_o=1.5$. Assuming a value of γ_s equal to 20.6 kN/m³, parameter A is in the range of values shown in Table 7.9. The ground water table was at 1m below the ground surface. However, the data collected at the dewatered section approximately 100m away from the instrumented section indicate that the lower Atherfield and Weald clays have been subjected to a drawdown of 5m (Clark, 2006).

stratum	unit weight Mg/m ³	ϕ'	estimated OCR	estimated K_o = $(1 - \sin\phi') \times$ OCR ^{$\sin\phi'$}	hydraulic conductivity (permeability) k, m/s
Hythe Beds	1.95	27°	7.3 to 9.3	1.35 to 1.5	2×10^{-4}
Atherfield Clay	2.1	22°	3.5 to 10.3	1.0 to 1.5	2×10^{-9}
Weald Clay	2.1	21°	4.5 to 10.7	1.1 to 1.5	2×10^{-6}

Table 7.9: Soil parameters (Clark, 2006).

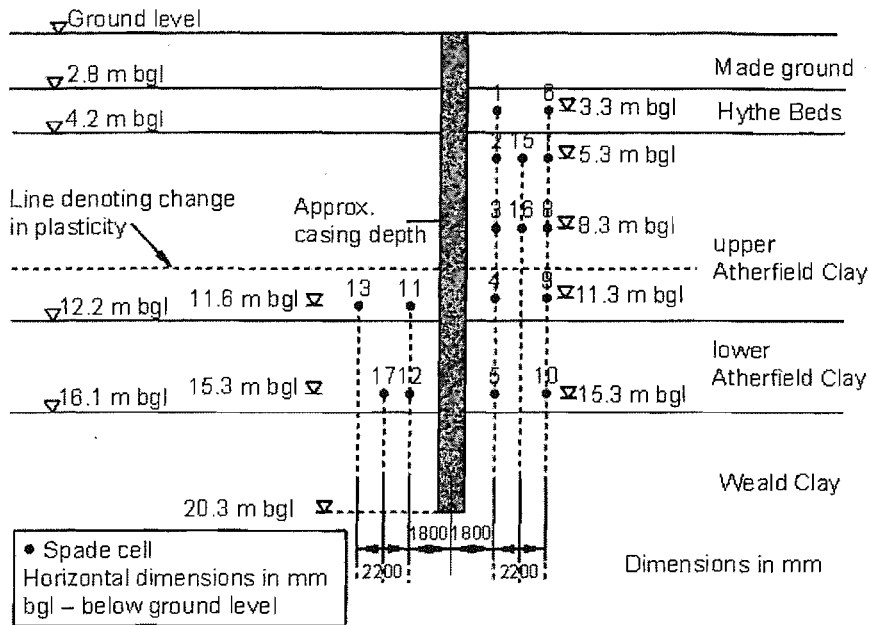


Figure 7.10: Soil profile (Clark, 2006).

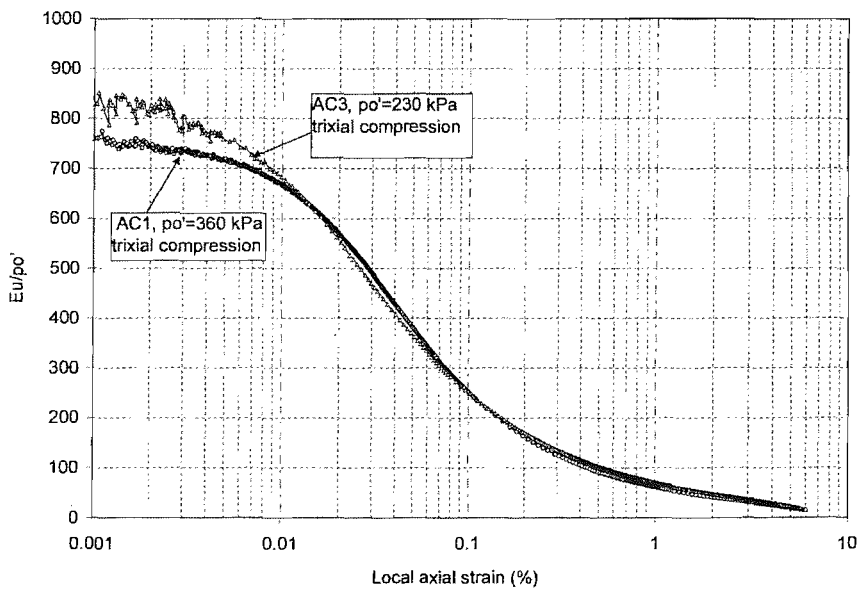


Figure 7.11: Normalised undrained Young's modulus E_u/p'_o against the logarithm of the axial strain for the Atherfield Clay (Clayton *et al*, 2006).

At the instrumented section, installation of the contiguous bored pile wall was followed by construction of reinforced concrete props at the crest and commencement of bulk excavation beneath them. Temporary props were installed at a depth of 6m, further excavation took place and a base slab was constructed at dredge level. The construction

sequence is shown in Table 7.10. For comparison with the MSD results, the data obtained before commencement of further excavation are used; at that point the wall had a retained height of 5.4m and an overall height of 20.25m.

Stage	Name	Schematic	Day	Date
1	Spade Cell Installation		1-13	8 th -20 th October 1999
2	Pile Installation		47-71	23 rd November to 17 th December 1999
3	Sand Drain Installation		349-352	20 th -23 rd September 2000
4	Capping Beam Construction		440-442	approximately 20-22 nd December 2000
5	RC (reinforced concrete) Prop Construction		465-467	Props 1 & 2: 14 th January 2001 Prop 3: 16 th January 2001
6	Excavation Phase 1		483-509	1 st -27 th February 2001 (no work 7 th -21 st Feb inclusive)
7	Temporary Prop Installation		512-522	Prop 1: 2 nd March 2001 Props 2 & 3: 12 th March 2001
8	Excavation Phase 2		530-537	20 th -27 th March 2001
9	Base Slab Construction		579	8 th May 2001
10	Temporary Prop Removal		581-595	Prop 1: 10 th May 2001 Props 2 & 3: 24 th May 2001

Table 7.10: Construction sequence (Clark, 2006).

The values of the parameters used in the MSD calculations are listed in Table 7.11. It should be noted that the upper part of the piles had a different flexural rigidity than the lower part (Clark, 2006); hence, in the MSD calculations ρ is given a range of values.

	$\rho=H^4/EI$ (m ³ /KN)	$A=\gamma_s/G^*$ (dimensionless)	ϕ'_{peak} (degrees)	γ_s (KN/m ³)	γ_w (KN/m ³)
values	$10^{-0.94} \sim 10^{-0.9}$	$10^{-2.26} \sim 10^{-2.15}$	22°	20.6	10

Table 7.11

The bending moments as measured by vibrating wire strain gauges and calculated from curve fits to the inclinometer data (Clark, 2006) are shown in Figure 7.12. In Figure 7.13 the inclinometer measurements taken following the first phase of excavation are presented.

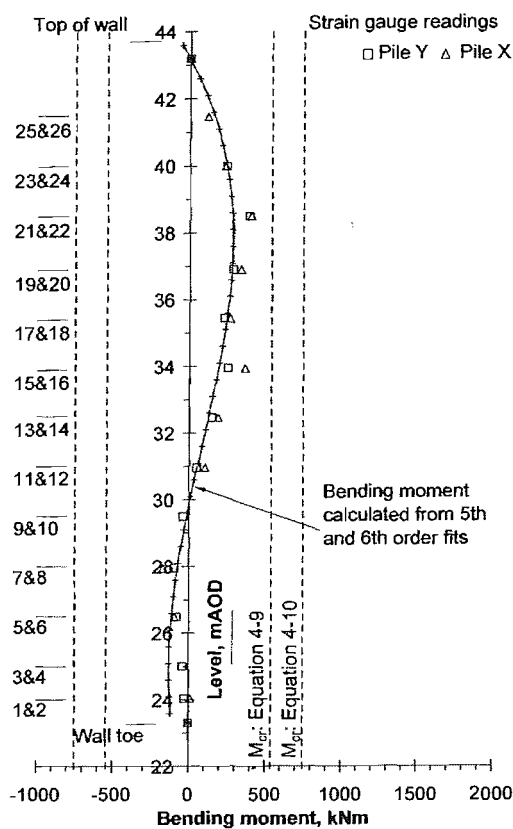


Figure 7.11: Bending moments measured by vibrating wire strain gauges after the first phase of excavation (Clark, 2006).

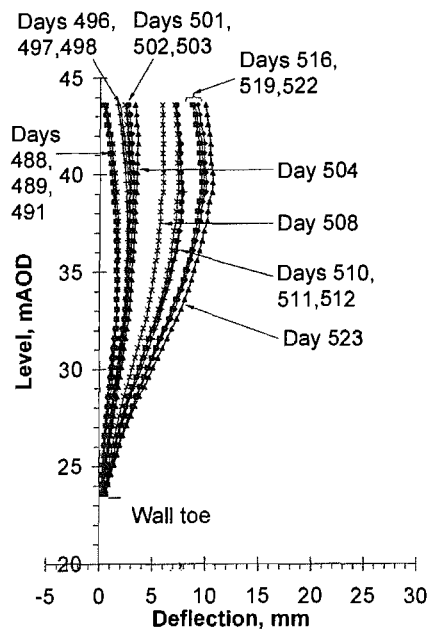


Figure 7.13: Inclinometer data after the first phase of excavation (Clark, 2006).

The MSD calculations are carried out for conditions of zero pore water pressures, since a drawdown of 5m was noticed in the clays and the retained height is taken equal to 5.4m. In Table 7.12 the maximum bending moments estimated according to the MSD method and according to Gaba *et al* (2003), as described in Section 2.3.2, together with the measured values are showed. The displacements at characteristic points along the wall (Figure 4.55) are also listed.

As indicated in Table 7.12, the MSD method calculated slightly higher values of maximum bending moments than those measured; this is expected since conservative assumptions were adopted in the MSD calculation. The maximum bending moments according to Gaba *et al* (2003) are substantially below those measured. The measured values of lateral displacements are reasonably close to those calculated by the MSD method. However, the displacement profile is different since a rigid prop was assumed in the MSD calculations.

Ground water table at $z = 6\text{m}$	M_{max} (KNm)	δ_1 (mm)	δ_2 (mm)	δ_3 (mm)	δ_4 (mm)
Estimated (MSD)	583~597	8~9.5	13.5~14.3	10.8~12.2	4~5.3
Estimated (Gaba <i>et al</i> ,2003)	188.1				
Measured by vibrating strain gauges	433				
Calculated from inclinometers	301	7.8	8.3	5	0.5

Table 7.12

7.6 CASE HISTORY 5: A secant pile embedded retaining wall at Bell Common Tunnel in Essex

A 470m long cut and cover tunnel was constructed in the early 1980's at Bell Common to take the M25 London motorway through the northern edge of Epping Forest in Essex. The tunnel is formed by a central line of piles and two embedded retaining walls propped at the crest by a simply supported roofing slab. A section of the retaining wall and the adjacent ground was extensively instrumented to monitor the behaviour of the structure (Tedd *et al*, 1984). Figure 7.14 shows a cross section of the tunnel and the instrumentation in the vicinity are showed.

The soil profile in the area comprises of a 1.5m thick deposit of Older Head, similar in nature to the Claygate Beds which lie underneath it. The Claygate Beds deposit has a thickness of 5.5m and overlies London Clay. The soil profile and the undrained strength determined from triaxial tests and Camkometer self-boring pressuremeters are shown in

Figure 7.15. The initial ground water table was at a distance of 3m below the ground surface.

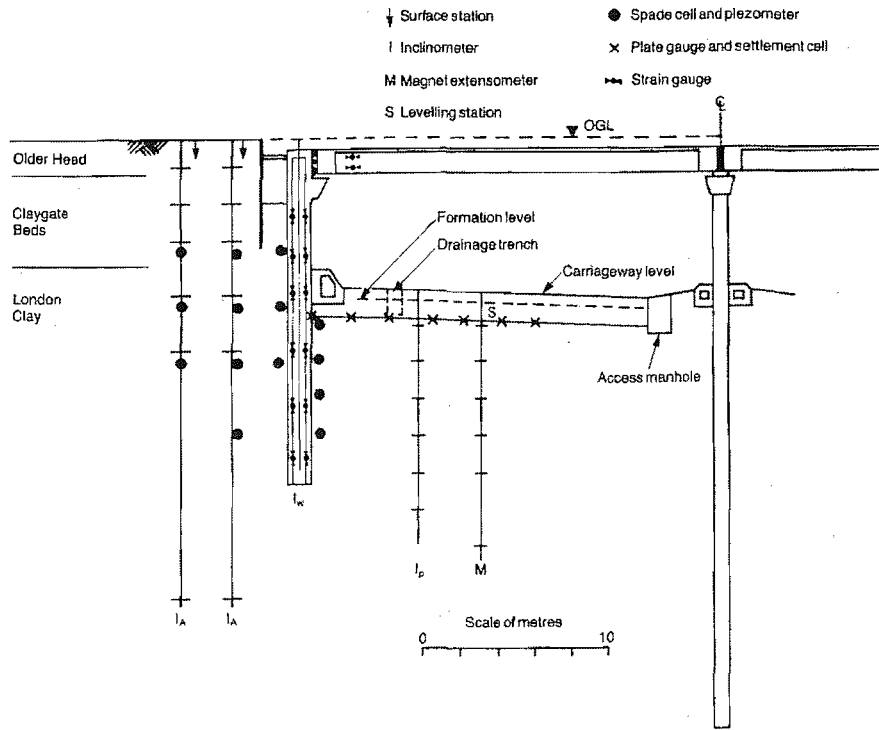


Figure 7.14: Plan of instrumentation (Tedd *et al*, 1984).

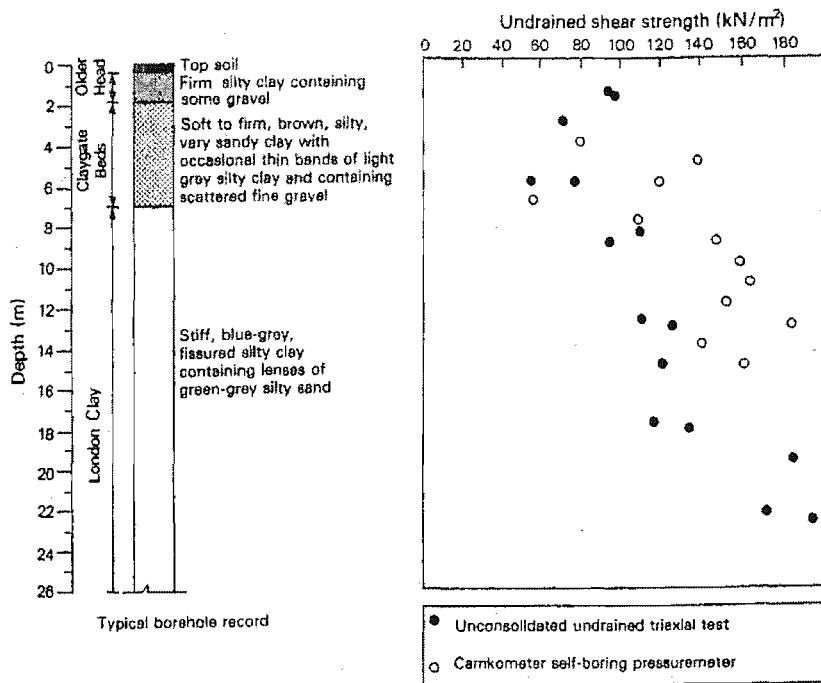


Figure 7.15: Soil properties (Tedd *et al*, 1984).

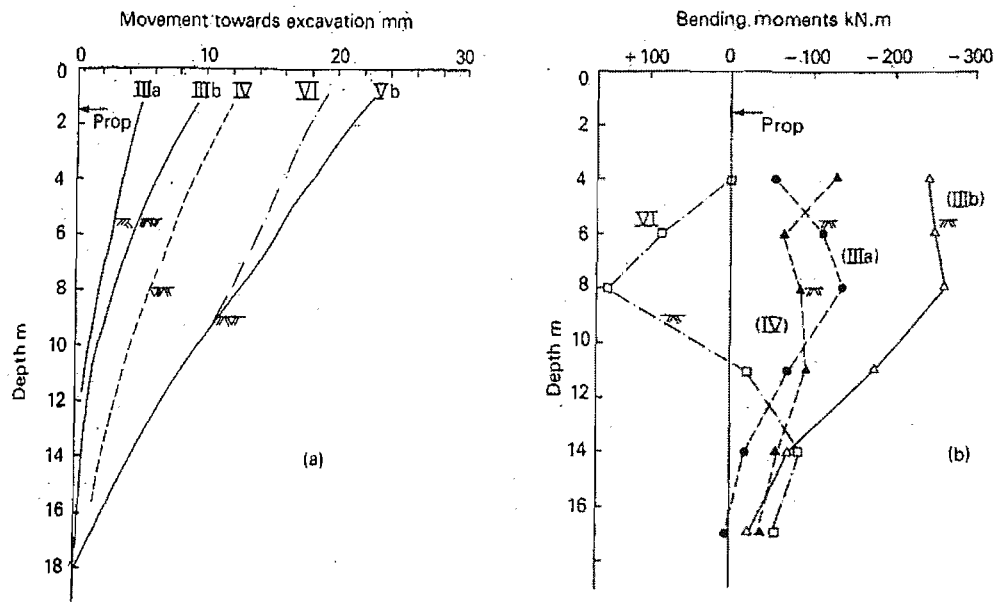
The instrumented section of the wall has been formed by 1.18m diameter bored piles spaced at 1.08m centres. Firstly, a number of primary piles were bored to a depth of 21m and secondary piles were bored in between to a depth of 19m. An initial excavation of 3.5m took place to construct the cill beam and the thrust wall and temporary shoring was placed between the secant pile wall and the closest surface instrumentation to retain the ground. Further excavation to 5m and construction of the roof beam followed. Between the roof beam and the thrust wall a compressible material 75mm thick was introduced. The final excavation to formation level was down to about 8m.

The values of the parameters used in the MSD calculations are representative of the London clay and are listed in Table 7.13.

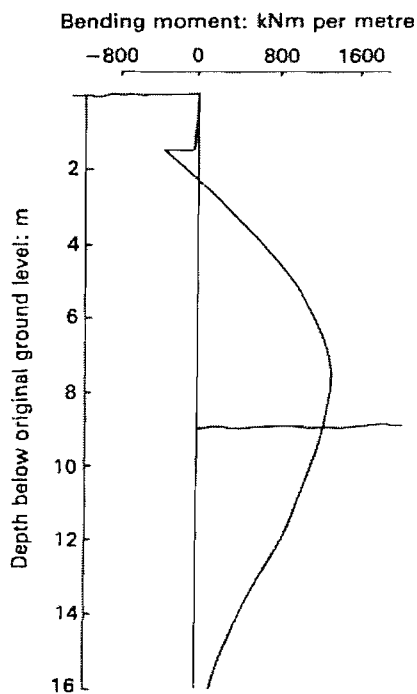
	$\rho=H^4/EI$ (m ³ /KN)	$A= \gamma_s/G^*$ (dimensionless)	ϕ'_{peak} (degrees)	γ_s (KN /m ³)	γ_w (KN/m ³)
values	$10^{-1.163}$	$10^{-2.25} \sim 10^{-2.18}$	22°	20	10

Table 7.13

The bending moments as measured by vibrating-wire strain gauges and the horizontal deformations measured by inclinometers are shown in Figures 7.16 a & b. In the bending moment diagram a negative sign represent a concave curvature towards excavation. Tedd *et al* (1984) note that both the bending moment and deformation profile depend heavily on the magnitude of the prop load which is only an approximate estimate. According to Figure 7.16a, the wall rotated about its toe and the maximum displacement at the end of the construction period occurred mainly at the crest; however, this can be explained by the compressible prop creeping at a very high rate. The bending moments appear to be very small possibly because of their sensitivity to the complex time-dependent stress-strain behaviour of the compressible material at the roof prop which caused fluctuations in the prop load. If the bending moments are estimated from the earth pressures, considerably larger magnitudes would be obtained (Tedd *et al*, 1984). Bolton and Powrie (1985) presented a bending moment diagram estimated from the earth pressure distributions as shown in Figure 7.17, where positive values represent concave curvature towards the excavation. The magnitudes in this case are far greater than those measured directly. In an elastic finite element analysis carried out by Hubbard *et al* (1984) the bending moments were also found much higher than those measured.



Figures 7.16: (a) Horizontal movements and (b) bending moment profile of the secant pile wall during various stages of excavation (Tedd *et al*, 1984).



Figures 7.17: Bending moment profile of the secant pile wall as calculated from the measured earth pressures distribution (Bolton and Powrie, 1985).

In Tables 7.14 a & b the maximum bending moments estimated according to the MSD method and according to Gaba *et al* (2003), and measured directly (Tedd *et al*, 1984) and

calculated from the earth pressure distribution (Bolton and Powrie, 1985) are shown together with displacements at characteristic points along the wall (Figure 4.55). For the values in Table 7.14 a the pore water pressures are at ground level, while in Table 7.14 b the water table is at half the retained height level.

Ground water table at $z = 0$	M_{max} (KNm)	δ_1 (mm)	δ_2 (mm)	δ_3 (mm)	δ_4 (mm)
Estimated (MSD)	1609~1620	33.2~34.5	41~43.8	44.3~45.4	39~42.1
Estimated (Gaba <i>et al</i>,2003)	1692.1				
Measured from strain gauges (Tedd <i>et al</i>, 1984)	262.5	18.4	12.9	7.8	0
Calculated from the earth pressures (Bolton and Powrie, 1985)	1378				

Table 7.14a

Ground water table at $z = 0.5 h$	M_{max} (KNm)	δ_1 (mm)	δ_2 (mm)	δ_3 (mm)	δ_4 (mm)
Estimated (MSD)	1127~1142	8~9.6	13.8~16	10.8~13.3	4.6~6.1
Estimated (Gaba <i>et al</i>,2003)	1207.76				
Measured from strain gauges (Tedd <i>et al</i>, 1984)	262.5	18.4	12.9	7.8	0
Calculated from the earth pressures (Bolton and Powrie, 1985)	1378				

Table 7.14b

The MSD method gives a reasonably close prediction of the maximum bending moments when compared to those calculated from the earth pressures for a water table at half the retained height level, while the empirical method (Gaba *et al*, 2003) might be unsafe in this case. When the water table is at ground level, the MSD results may be conservative; however, the assumption of a water table at half the retained height level is closer to the case study since the water table was at 3m from ground level. The measured values are close to those calculated by the MSD method assuming a water table at half the retained height level. A big divergence is noticed between the directly measured magnitudes and the rest of the values presented in Table 7.14 when the water table is at ground level. Moreover, the displacement profile differs from the one assumed in the MSD calculations. However, the accuracy of the directly measured values is uncertain for the reasons discussed in this Section. A finite element analysis for the Bell Common singly propped wall (Potts and Day, 1991) is presented and discussed in the next Section for further comparison.

7.6.1 CASE HISTORY 5: Finite element analysis for a propped retaining wall at Bell Common Tunnel in Essex

A finite element analysis for a propped retaining wall at Bell Common Tunnel has been performed by Potts and Day (1991). The purpose of the analysis was to assess whether flexible sheet pile walls can provide a viable alternative to concrete diaphragm or secant pile walls retaining stiff clays; hence, four different values of wall stiffness, ranging from an extreme value attributed to a very soft wall to a value equivalent to 1m thick concrete wall, as listed in Table 7.15, were used. The soil profile and properties employed in the analysis are shown in Figure 7.18. The original ground water table is at a distance of 3m from the ground surface. However, the maximum bending moments were calculated in the long term when excess pore water pressures had dissipated. During the dissipation stages of the finite element analysis the bulk modulus of the pore water was set to zero.

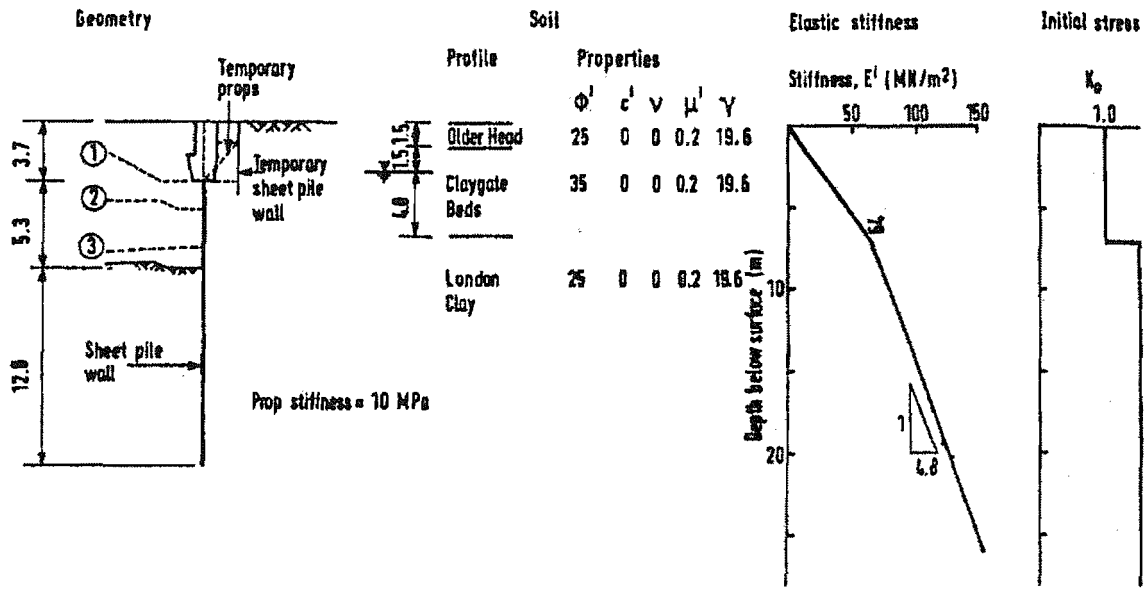


Figure 7.18: Soil properties employed in the finite element analysis (Potts and Day, 1991).

In the MSD calculations the same values of wall stiffness are used for comparison with the finite element analysis, while conservative values for the soil parameters are chosen as listed in Table 7.15. The MSD calculations are carried out assuming a water table at half the retained height level.

	$\rho = H^4/EI$ (m ³ /KN)	$A = \gamma_s/G^*$ (dimensionless)	φ'_{peak} (degrees)	γ_s (KN/m ³)	γ_w (KN/m ³)
1 st case	$10^{1.19}$	$10^{-2.3}$	25°	19.6	10
2 nd case	$10^{0.37}$	$10^{-2.3}$	25°	19.6	10
3 rd case	$10^{-0.35}$	$10^{-2.3}$	25°	19.6	10
4 th case	$10^{-1.08}$	$10^{-2.3}$	25°	19.6	10

Table 7.15

	Cases	M_{max} (kNm/m)
Estimated (MSD)	1 st case	1325
	2 nd case	1419
	3 rd case	1458
	4 th case	2054
Finite Element Analysis (Potts&Day, 1991)	1 st case	120
	2 nd case	170
	3 rd case	305
	4 th case	635
Estimated (Gaba <i>et al</i>,2003)		1080.5

Table 7.16

In Table 7.16 the results obtained from the finite element analysis are compared to those determined from the MSD method and those according to Gaba *et al* (2003). For the two stiffer walls the MSD results are reasonably close, while for the two more flexible walls the MSD method overpredicts the maximum bending moments compared to finite element analysis. It should be mentioned that the assumption of a rigid prop was followed in the MSD calculations, whereas in the finite element analysis the propping slab was modelled by a spring with a linear stiffness of 10MN/m per metre; hence the difference in the results may be explained. The values estimated according to Gaba *et al* (2003) are higher than the finite element results results. It should be noted that the first case is equivalent to a very soft wall which is not likely to be used in practice, but was included in the analysis to represent an extreme case.

7.7 SUMMARY

The comparison between the MSD results and the data obtained from five case histories show that the MSD method can provide a useful prediction of the maximum bending moments and the displacements at characteristic points along the wall for preliminary design. In all the case histories examined in this Chapter, the MSD method gives slightly

overpredicted values; however, this would be expected since conservative assumptions and lower bound parameters were employed. Moreover, in the MSD calculations the wall flexibility and soil stiffness and shear strength are taken into account, which is an improvement for preliminary design when compared to the limit equilibrium calculations or the empirical method suggested by Gaba *et al* (2003). A further more complex analysis (i.e. finite element analysis) could be carried out for a detailed design if needed.

Furthermore, it should be noted that due to the limited number of detailed case studies of embedded retaining walls propped at the crest, it was assumed that the data obtained after installation of the temporary props and before casting of the permanent base slab could resemble the behaviour of walls propped singly at the crest for some of the case histories presented herein. Even so, the accuracy of the measurements is uncertain in some cases. Some divergence between the MSD results and the measurements could be justified by these reasons.

8. CONCLUSIONS AND FURTHER WORK

8.1 CONCLUSIONS

Review of the different methods used in current engineering practice and the codes of practice for the design of retaining walls has indicated that complex and time consuming analysis is often required to model the soil behaviour. Alternatively, empirical or simple methods based on linear elasticity can be used, but their limitations are significant. The potential of the mobilised strength method to serve as a simple design framework that incorporates the real nature of soil behaviour for retaining walls propped near the crest has been investigated in this thesis.

In Chapter 3, the maximum principle stress difference failure criterion has been used to derive the total stresses behind and in front of a stiff retaining wall propped at the crest incorporating the initial earth pressure coefficient, K_o , and the rate of increase of the shear modulus with depth, G^* . The rotation of the wall at the prop and the normalized prop loads, bending moments and deformations have been calculated for different values of retained height ratios, initial earth pressure coefficients and soil stiffness. The soil/wall flexibility is characterized by a flexibility number, the critical value of which differentiates stiff from flexible walls. The critical flexibility ratio has been found to increase when the initial earth pressure coefficient and the retained height ratio decrease. The advantages of this solution are that both the wall flexibility and the soil stiffness are considered in a simple calculation and it can be applied in a reasonably general manner.

In Chapters 4 and 5, the mobilized strength method has been applied to flexible retaining walls for conditions of zero pore water pressures and linear seepage respectively. New kinematically admissible soil displacement fields have been introduced to associate the mobilized shear strain with the mobilized shear strength in each soil zone by a modified version of the hyperbolic relationship introduced by Duncan and Cheng (1970) and the wall flexibility has been idealised into a simple mechanism. Curves have been presented to illustrate the divergence in the maximum bending moments and the prop loads when the wall flexibility, soil stiffness and initial shear strength are taken into account from those calculated according to Eurocode 7 (1995). To estimate the effect of each of the wall

flexibility, soil stiffness and initial shear strength independently, a variation in one magnitude has been allowed while constant values were employed for the rest. According to the curves, a significant reduction in the maximum bending moments and prop loads is noticed when the wall flexibility or the soil stiffness increases. The reduction is more pronounced for retaining walls embedded in clays than in sands. The normalised displacements at characteristic points along the wall have been also plotted for different values of wall flexibility, soil stiffness and initial shear strength.

In Chapter 6, Rowe's (1952, 1955) experimental and theoretical curves have been redrawn on transformed axes in consistent units to show the reduction in the maximum bending moments and the prop loads when the design procedure suggested in the Eurocode 7 (EC7, 1995) is followed and moreover, to enable the comparison with the MSD curves. The reduction in Rowe's curves is greater when the design procedure suggested by Eurocode 7 (EC7, 1995) is followed than the free earth support method. However, Rowe's results were derived for sheet pile walls embedded in sands with low K_o and were based on a rather ambiguous soil parameter; hence, their general application might not be appropriate. Rowe's reduction curves and those derived from the MSD method are in good agreement when are both compared to Eurocode 7 (EC7,1995) regarding the maximum bending moments, but a difference is noticed in the prop loads. However, Rowe (1952, 1955) took also account of the surcharge, whereas in the MSD method zero surcharge was assumed. Furthermore, comparison between the MSD method, as presented in this thesis, and the geostitruktural mechanism presented by Bolton and Powrie (1988) has showed that the same results are found for low wall flexibility values; hence the MSD method is consistent.

Comparison of the MSD results with data obtained from five monitored case studies has been presented in Chapter 7. Conservative assumptions and lower bound parameters were employed to derive the MSD results and this may have led to slightly overpredicted values of maximum bending moments and prop loads compared to the measurements. Even so, the MSD method is an improvement to linear elastic soil models or empirical techniques and may be a simple and useful design tool. Its accuracy may be increased if more kinematically admissible soil displacement fields are introduced and different rates of mobilized strength with strain are allowed for behind and in front of a retaining wall to take account of the recent stress history.

8.2 FURTHER WORK

Simple soil-structure interaction analysis (i.e. using software like FREW or WALLAP) is commonly used in engineering practice for the preliminary design of retaining walls and could be compared to the results derived from the MSD method. The MSD method has been presented in this thesis in terms of an effective stress analysis; its validity could also be assessed for a total stress analysis. Moreover, the soil behind and in front of a retaining wall may be divided into a greater number of triangles with uniform but different mobilized strength within each one to approach the realistic soil/wall movements. The soil arching may be included in the stress distribution on the retained side when flexible retaining walls are analysed. The relationship for the derivation of the mobilized strength with the mobilized strain may also be improved to achieve better accuracy; however, the key point might be to retain its simplicity. Powrie, Pantelidou and Stallebrass (1998) emphasized the importance of recent stress history during wall installation on the soil behaviour during excavation; they suggested that for the soil in front of a retaining wall, the change in the stress path direction during wall installation was smaller, resulting in a significant less stiff response during excavation in comparison with the retained soil. Therefore, a more rapid rate of mobilisation of soil strength with mobilized strength may be used for the retained soil in the MSD method to incorporate the recent stress history.

REFERENCES

- Al Tabaa, A. (1987). Permeability and stress-strain response of Speswhite kaolin. PhD thesis, University of Cambridge.
- Al Tabaa, A. & Wood, D. M. (1989). An experimentally based 'bubble' model for clay. In *Numerical models in geomechanics* (eds S. Pietruszczak and G. N. Pande), *Proceedings of the 3rd International Conference on numerical methods in Geomechanics*, pp. 91-99.
- Allman, M. A. & Atkinson, J. H. (1992). Mechanical properties of reconstituted Bothkennar soil. *Geotechnique*, 42, No. 2, 289-301.
- Atkinson, J. H., Richardson, D. & Stallebrass, S. E. (1990). Effect of recent stress history on the stiffness of overconsolidated soil. *Geotechnique*, 40, No. 4, 531-540.
- Atkinson, J. H. & Salfors, G. (1991). Experimental determination of soil properties. *Proc. 10th Eur. Conf. Mech., Florence 3*, 915-956.
- Bennet, S. N., Carder, D. R. & Ryley, M. D. (1996). Behaviour during construction of a propped secant pile wall in stiff clay at Hackney to M11 link, *TRL Report 188*, Transport Research Laboratory, Department of Transport.
- Bica, A. V. D. & Clayton, C. R. I. (1998). An experimental study of the behaviour of embedded lengths of cantilever walls. *Geotechnique*, 48, No. 6, 731-745.
- Bolton, M. D. & Powrie, W. (1985). Discussion: Performance of propped and cantilevered rigid walls. Fifth Geotechnique Symposium, *Geotechnique*, 35, No. 4, 533-548.
- Bolton, M. D. & Powrie, W. (1988). Behaviour of diaphragm walls in clay prior to collapse. *Geotechnique*, 38, No. 2, 167-189.
- Bolton, M. D., Powrie, W. & Symons, I. F. (1989). The design of stiff, in situ walls retaining overconsolidated clay, Part I. *Ground Engineering* 22, No. 8, 44-48.

Bolton, M. D., Powrie, W. & Symons, I. F. (1990). The design of stiff, in situ walls retaining overconsolidated clay, Part II . *Ground Engineering* 22, No. 9, 34-40 & *Ground Engineering* 23, No. 2, 22-28.

Boussinesq, J. (1885). Applications des potentiels à l'étude d'équilibre et du mouvement des solides élastiques, Gauthier Villars, Paris.

British Standards Institution (2001) *BS8002: Code of practice for earth retaining structures*. BSI, London.

Burland, J. B., Potts, D. M. & Walsh, N. M. (1981). The overall stability of free and propped embedded cantilever retaining walls. *Ground Engineering* 14, No. 5, 28-37.

Burland, J. B. (1989). The Ninth Bjerrum Mem. Lecture: Small is beautiful – the stiffness of soils at small strains. *Can. Geot. Journal* 26, No. 4, 499-516.

Carder, D. R., Ryley, M. D. & Symons, I. F. (1991). Behaviour during construction of a propped diaphragm wall in stiff clay at the A406/A10 junction, *TRRL Research Report 331*, Transport and Road Research Laboratory, Department of Transport.

Carswell, I., Carder, D. R. & Gent, A. J. C. (1993). Behaviour during construction of a propped contiguous bored pile wall in stiff clay at Walthamstow, *TRL Project Report 10*, Transport Research Laboratory, Department of Transport.

Clark, J. (2006). Performance of a propped retaining wall at the Channel Tunnel Rail Link, Ashford. Ph.D thesis, University of Southampton.

Clayton, C. R. I., Xu, M., Bloodworth, A. G. (2006). Intrinsic soil behaviour and the development of earth pressure behind integral bridge abutments. Accepted for publication in *Geotechnique*, 2006.

Clough, G. W. & O' Rourke, T. D. (1990). Construction-induced movements of in situ walls. In *Proceedings, Design and Performance of Earth Retaining Structures*, ASCE Special Conference, Ithaca, New York, pp. 439-470.

Clough, G. W. & O' Rourke, T. D. (1990). Construction induced movements of insitu walls. *Design and performance of earth retaining structures*, Geotechnical Special Publication No 25, ASCE, New York, N. Y., 439-470.

Diakoumi, M. & Lavdas, A. (2003). Ground movements induced by deep excavations in urban areas. Dissertation thesis, Aristotle University of Thessaloniki.

Duncan, M. J. & Chang, C. Y. (1970). Nonlinear analysis of stress and strain in soils. *ASCE Journal of Soil Mechanics and Foundations Engineering Division, Proceedings of ASCE*, Vol. 96, SM 5, 1629-1653.

ECS (1997). Eurocode EC7: *Geotechnical design*, European Committee for Standardisation (ECS). Brussels, Belgium.

Fadum, R. E. (1948). Influence values for estimating stresses in elastic foundations. *In Proceedings of 2nd International conference of Soil Mechanics and Foundations Engineering*, Vol. 3, pp. 77-84.

Gaba, A., Simpson, B., Powrie, W. & Beadman, D. R. (2003). *Embedded retaining walls: guidance for more economic design*, Construction Industry Research and Information Association Report C580. CIRIA, London.

Georgiannou, V. N., Rampello, S. & Silvestri, F. (1991). Static and dynamic measurements of undrained stiffness on natural overconsolidated clays. *Proc. 10th Eur. Conf. Mech., Florence*, Vol. 1, 91-95.

Hsieh, P. G. & Ou C. Y. (1998). Shape of ground surface settlement profiles caused by excavation. *Canadian Geotechnical Journal*, 35: 1004-1017.

Hubbard, H. W., Potts, D. M., Miller, D. & Burland, J. B. (1984). Design of the retaining walls for the M25 cut and cover tunnel at Bell Common. *Geotechnique*, 34, No. 4, 495-512.

- Janbou, Nilmar (1963). Soil compressibility as determined by oedometer and triaxial tests. *Proceedings of European Conference on Soil Mechanics and Foundations Engineering, Wiesbaden, Germany*, Vol. 1, 19-25.
- Jardine, R. J., Symes, M. J. & Burland, J. B. (1984). The measurement of soil stiffness in the triaxial apparatus. *Geotechnique*, 34, No. 3, 323-340.
- Jardine, R. J., Potts, D. M., Fourie A. B. & Burland, J. B. (1986). Studies of the influence of non-linear stress-strain characteristics in soil-structure interaction. *Geotechnique*, 36, No. 3, 377-396.
- Jardine, R. J. (1992). Some observations on the kinematic nature of soil stiffness. *Soils and Foundations*, Vol. 32, No 2, 111-124, *Japanese Society of Soil Mechanics and Foundation Engineering*.
- Jovičić, V. & Coop, M. R. (1997). Stiffness of coarse-grained soils at small strains. *Geotechnique*, 47, No. 3, 545-561.
- Kondner, R. L. & Zelasco, J. S. (1963). A hyperbolic stress-strain formulation for sands. *Proceedings, 2nd Pan-American Conference on Soil Mechanics and Foundation Engineering, Brazil*, Vol. I, 289-324.
- Krey, H. (1932). *Erddruck, Erdwiderstand und Tragfähigkeit des Baugrundes*. Berlin: Ernst.
- Long, M. (2001). Database for retaining walls and ground movements due to deep excavations. ASCE, *Journal of Geotechnical and Geoenvironmental engineering*.
- Milligan, G. W. E. & Bransby, P. L. (1976). Combined active and passive rotational failure of a retaining wall in sand. *Geotechnique*, 26, No. 3, 473-494.
- Milligan, G. W. E. & Bransby, P. L. (1983). Soil deformations near anchored sheet-pile walls. *Geotechnique*, 33, No. 1, 41-55.

- Mroz, Z., Norris, V. A., Zienkiewicz, O. C. (1981). Anisotropic, critical state model for soils subject to cyclic loading. *Geotechnique* 31 (4), 451-469.
- Newmark, N. M. (1942). Influence charts for computation of stresses in elastic foundations, University of Illinois, Bulletin No. 338.
- Li, E. S. F. (1990). On the analysis of singly-propped diaphragm walls. PhD thesis, University of London.
- Osman, A. S. (2004). Predicting ground displacements in clay during construction. Ph.D. thesis, University of Cambridge.
- Ou, C. Y., Hsieh, P. G. & Chiou, D. C. (1993). Characteristics of ground surface settlement during excavation. *Canadian Geotechnical Journal*, 30(5): 758-767.
- Padfield, C. J. & Mair, R. J. (1984). *Design of retaining walls embedded in stiff clays*, CIRIA Report No. 104. London: Construction Industry Research and Information.
- Peck, R. B. (1969). Deep excavation and tunnelling in soft ground. *In Proceedings of 7th International conference of Soil Mechanics and Foundations Engineering*, Mexico City, State-of-the-art volume, pp. 225-290.
- Potts, D. M. & Fourie, A. B. (1984). The behaviour of a propped retaining wall: results of a numerical experiment. *Geotechnique* 34, No. 3, 383-404.
- Potts, D. M. & Fourie, A. B. (1985). The effect of wall stiffness on the behaviour of a propped retaining wall. *Geotechnique* 35, No. 3, 347-352.
- Potts, D. M. & Day, R. A. (1991). The effect of wall stiffness on bending moments. *Proceedings of the 4th International Conference on piling and deep foundations*, Stresa, 1991.
- Powrie, W. (1997) Soil mechanics: concepts and applications. First edition, *London. E and F N Spon.*

Powrie, W., Pantelidou, H. & Stallebrass, S. E. (1997). Soil stiffness in stress paths relevant to diaphragm wall installation.

Rankine, W. J. M. (1857). On the stability of loose earth. *Phil. Trans. Royal Society*, 147.

Richards, D. J., Roscoe, H., Powrie, W., Clark, J., Twine, D. (2006). Geotechnical design issues and observed behaviour of a contiguous bored pile multi-propped retaining wall in lower cretaceous clays. Draft paper.

Roscoe, K. H. & Schofield, A. N. (1963). Mechanical behaviour of 'wet clay'. *Proceedings of the 2nd European Conference on Soil Mechanics and Foundation Engineering, Wiesbaden*, Vol. 1, 47-54.

Roscoe, K. H. & Burland, J. B. (1968). On the generalised stress-strain behaviour of 'wet' clay. *Engineering plasticity*, J. Heyman and F. A. Leckie, eds., Cambridge University Press, Cambridge, England, 535-609.

Rowe, P. W. (1952). Anchored sheet pile walls. *Proceedings of the institution of Civil Engineers, Pt 1*, 1, 27-70.

Rowe, P. W. (1955). A theoretical and experimental analysis of sheet pile walls. *Proceedings of the institution of Civil Engineers, Pt 1*, 4, 32-69.

Rowe, P. W. (1963). Stress-dilatancy, earth pressure and slopes. *Proc. ASCE . Soil mechs and Fndns. Div.*, 89 (SM3), 37-61.

Schofield, A. N., Wroth, C. P. (1968). Critical state soil mechanics. *McGraw Hill*, London.

Simpson, B. (1992). 32nd Rankine Lecture. Retaining structures-displacement and design. *Geotechnique*, 42, No. 4, 539-576.

Smith, P. R., Jardine, R. J. & Hight, D. W. (1992). The yielding of Bothkennar clay. *Geotechnique*, 42, No. 2, 257-274.

Stallebrass, S. E. & Taylor, R. N. (1997). Development and evaluation of a constitutive model for the prediction of ground movements in overconsolidated clay. *Geotechnique*, 47, No. 2, 235-253.

Tedd, P., Chard, B. M., Charles, J. A. & Symons, I. F. (1984). Behaviour of a propped embedded retaining wall in stiff clay at Bell Common. *Geotechnique*, 34, No. 4, 513-532.

Terzaghi, K. (1943). *Theoretical soil mechanics*. John Wiley, New York.

Terzaghi, K. (1954). Anchored bulkheads. *Trans. ASCE* 119, 1243-1280.

Viggiani, G. & Atkinson, J. H. (1995). Stiffness of fine-grained soil at very small strains. *Geotechnique*, 45, No. 2, 249-265.

Williams, B. P. & Waite, D. (1993). The design and construction of sheet-piled cofferdams. Special publication 95, Construction Industry Research and Information Association, London.

Wroth, C. P. & Houlsby, G. T. (1985). Soil mechanics, Property characterization and analysis procedure. *Proc. XI ICSMFE, San Francisco*, pp.1-55.

Wroth, C. P., Randolph, M. F., Houlsby, G. T. & Fahey, M. (1979). A review of engineering properties of soils with particular reference to the shear modulus. University of Oxford. OUEL Report 1523/84.

APPENDICES

A. HYPERBOLIC STRESS-STRAIN RELATIONSHIP

Duncan and Cheng approximated the non-linear stress-strain relationship by the hyperbolic equation proposed by Kodner (1963)

$$(\sigma_1 - \sigma_3) = \varepsilon / (a + b \varepsilon) \quad (\text{A.1})$$

where σ_1 and σ_3 are the major and minor principal stresses respectively, ε is the axial strain and a and b are constants which can be derived from experimental data. Constant a is the reciprocal of the initial tangent Young's modulus E_i and constant b is the reciprocal of the asymptotic value of stress difference, $(\sigma_1 - \sigma_3)_{ult}$, which the stress-strain curve approaches at infinite strain. Equation (A.1) can be written in the form of Equation (A.2):

$$\varepsilon / (\sigma_1 - \sigma_3) = a + b \varepsilon \quad (\text{A.2})$$

The stress difference in the soil $(\sigma_1 - \sigma_3)$ at failure is usually found to be slightly less than its asymptotic value $(\sigma_1 - \sigma_3)_{ult}$ at infinite strain and a factor R_f can be used to relate them in Equation (A.3):

$$(\sigma_1 - \sigma_3)_f = R_f (\sigma_1 - \sigma_3)_{ult} \quad (\text{A.3})$$

Substituting the constants a and b and the factor R_f in Equation (A.2):

$$(\sigma_1 - \sigma_3) = \varepsilon / [1/E_i + \varepsilon R_f / (\sigma_1 - \sigma_3)_f] \quad (\text{A.4})$$

Janbu (1963) found from experimental studies that the initial tangent Young's modulus E_i is related to the confining pressure σ_3 by Equation (A.5)

$$E_i = K p_a (\sigma_3 / p_a)^n \quad (\text{A.5})$$

where p_a is the atmospheric pressure expressed in the same pressure units as E_i and σ_3 , K is a dimensionless modulus number and n is the exponent determining the rate of variation of E_i with σ_3 . In Figure A.1 the determination of the parameters K and n from drained triaxial tests is shown.

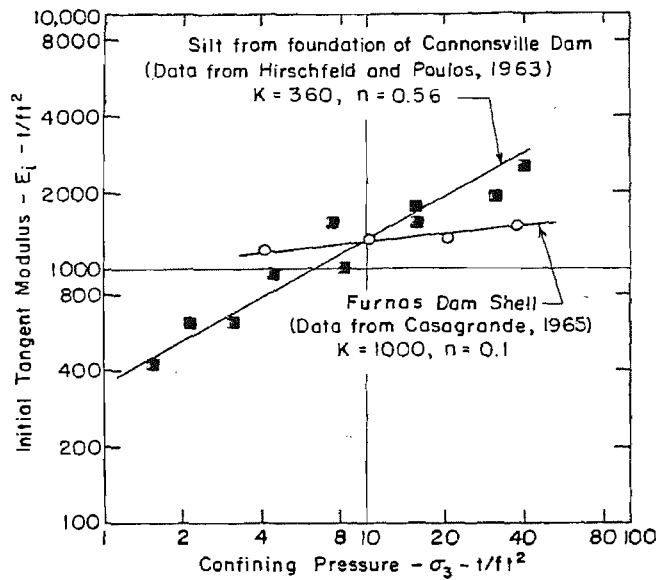


Figure A.1: Determination of parameters K and n from drained triaxial test data (Duncan and Cheng, 1970).

The stress difference at failure can be related to the confining pressure σ_3

$$(\sigma_1 - \sigma_3)_f = (2c \cos\phi + 2\sigma_3 \sin\phi) / (1 - \sin\phi) \quad (\text{A.6})$$

where c is the soil cohesion and ϕ is the friction angle.

The tangent Young's modulus may be expressed by Equation (A.7):

$$E_t = d(\sigma_1 - \sigma_3) / d\varepsilon \rightarrow E_t = (1 / E_i) / [1 / E_i + R_f \varepsilon / (\sigma_1 - \sigma_3)_f]^2 \quad (\text{A.7})$$

Duncan and Cheng (1970) rewrote Equation (A.4) in the form of Equation (A.8):

$$\varepsilon = (\sigma_1 - \sigma_3) / \{E_i [1 - R_f (\sigma_1 - \sigma_3) / (\sigma_1 - \sigma_3)_f]\} \quad (\text{A.8})$$

The expression for the tangent Young's modulus can be independent of strain by substituting Equation (A.8) in Equation (A.7)

$$E_t = (1 - R_f S)^2 E_i \quad (\text{A.9})$$

where S is the normalized stress level and is given by Equation (A.10)

$$S = (\sigma_1 - \sigma_3) / (\sigma_1 - \sigma_3)_f \quad (\text{A.10})$$

Duncan and Cheng (1970) substituted Equations (A.5), (A.6) and (A.10) in Equation (A.9)

$$E_t = [1 - R_f(1 - \sin\phi) (\sigma_1 - \sigma_3) / (2c \cos\phi + 2\sigma_3 \sin\phi)]^2 K p_a (\sigma_3 / p_a)^n \quad (\text{A.11})$$

where c is the soil cohesion, ϕ is the friction angle σ_3 is the confining pressure, p_a is the atmospheric pressure expressed in the same pressure units as E_t and σ_3 , K is a dimensionless modulus number and n is the exponent determining the rate of variation of the initial tangent Young's modulus E_i with σ_3 .

After carrying out additional tests on sands to investigate the effect of unloading and reloading on the proposed relationship, Duncan and Cheng (1970) found that the unloading-reloading Young's modulus E_{ur} may be expressed by Equation (A.12)

$$E_{ur} = K_{ur} p_a (\sigma_3 / p_a)^n \quad (\text{A.12})$$

where K_{ur} is a dimensionless modulus number for unloading and reloading and was found to be higher than for primary loading

The tangent shear modulus G may be represented by an Equation similar to the one (Equation A.11) proposed by Duncan and Cheng (1970). The radius of the Mohr circle of total stresses is:

$$t = (\sigma_1 - \sigma_3) / 2 \quad (\text{A.13})$$

Equation (A.13) can be rewritten as:

$$\sigma_1 = 2 t + \sigma_3 \quad (\text{A.14})$$

The average total stress is given by Equation (A.15):

$$s = (\sigma_1 + \sigma_3) / 2 \quad (\text{A.15})$$

Substituting Equation (A.14) into Equation (A.15):

$$s = t + \sigma_3 \quad (\text{A.16})$$

The maximum shear strain is

$$\gamma = 1/2 (3 \varepsilon_a - \varepsilon_{vol}) \quad (\text{A.17})$$

where ε_{vol} and ε_a are the volumetric and axial strain. In an undrained triaxial test $\varepsilon_{vol} = 0$, hence:

$$\gamma = 1.5 \varepsilon_a \quad (\text{A.18})$$

Considering Equations (A.13) and (A.18), Equation (A.1) can be rewritten in the form:

$$t = (\gamma / 3) / (a + b \gamma / 1.5) \quad (\text{A.19})$$

The initial shear modulus G_i is related to the initial Young's modulus by the expression

$$G_i = E_i / [2 (1 + \nu)] \quad (\text{A.20})$$

where ν is the Poisson's ratio. Therefore the parameters a and b in Equation (A.19) may be defined as:

$$a = 1 / E_i = 1 / [2 G_i (1 + \nu)] \quad (\text{A.21})$$

$$b = 1 / (\sigma_1 - \sigma_3)_{ult} = R_f / (\sigma_1 - \sigma_3)_f = R_f / (2 t_f) \quad (\text{A.22})$$

If t_f and t_{ult} are the shear stresses at failure and at infinite strain respectively, then:

$$R_f = t_f / t_{ult} \quad (A.23)$$

Substituting a and b in Equation (A.19):

$$t = \gamma / \{1.5 / [G_i(1+\nu) + \gamma R_f / t_f]\} \quad (A.24)$$

From Equations (A.5) and (A.20):

$$G_i = [K p_a (\sigma_3 / p_a)^n] / [2 (1 + \nu)] \quad (A.25)$$

Equation (A.6) can be rewritten in terms of shear stress:

$$t_f = (c \cos\phi + \sigma_3 \sin\phi) / (1 - \sin\phi) \quad (A.26)$$

The tangent shear modulus G_t can be defined by the differentiation:

$$G_t = dt / d\gamma \rightarrow G_t = 1.5 / [G_i(1 + \nu)] / \{[1.5 / [G_i(1 + \nu)] + \gamma R_f / t_f]^2\} \quad (A.27)$$

Equation (A.24) can be rewritten as:

$$\gamma = 1.5 t / [G_i(1 + \nu) (1 - R_f t / t_f)] \quad (A.28)$$

Substituting Equation (A.28) into Equation (A.27):

$$G_t = G_i(1 + \nu) (1 - S R_f)^2 / 1.5 \quad (A.29)$$

$$\text{where } S = t / t_f \quad (A.30)$$

From Equations (A.26), (A.27), (A.28), (A.29) and (A.30):

$$G_t = [1 - R_f t (1 - \sin\phi) / (c \cos\phi + \sigma_3 \sin\phi)]^2 [G_i(1 + \nu) / 1.5] \quad (A.31)$$

The advantage of Equation (A.31) is that it facilitates the determination of the tangent shear modulus G_t for any stress condition if data from triaxial tests are available.

B. MOBILISED STRENGTH

The rate of change of the mobilized friction angle φ'_{mob} with shear strain γ is a useful tool for expressing strength and stiffness at the same time, providing information on the soil state relative to its critical state. The mobilized friction angle φ'_{mob} is given by Equation (B.1).

$$\varphi'_{mob} = \sin^{-1} [t / s'] \quad (B.1)$$

Equation (A.16) can be rewritten in terms of effective stresses

$$s' = t + \sigma_3' \quad (B.2)$$

Substituting Equations (A.19) and (B.2) into Equation (B.1):

$$\begin{aligned} \varphi'_{mob} &= \sin^{-1} [(\gamma / 3) / (a + b \gamma / 1.5) / (t + \sigma_3)] \rightarrow \\ \varphi'_{mob} &= \sin^{-1} \{(\gamma / 3) / (a + b \gamma / 1.5) / [\sigma_3 + (\gamma / 3) / (a + b \gamma / 1.5)]\} \rightarrow \\ \varphi'_{mob} &= \sin^{-1} \{1 / [1 + \sigma_3 (a + b \gamma / 1.5) / (\gamma / 3)]\} \rightarrow \\ \varphi'_{mob} &= \sin^{-1} [(\gamma / 3) / (\gamma / 3 + \sigma_3 a + \sigma_3 b \gamma / 1.5)] \rightarrow \\ \varphi'_{mob} &= \sin^{-1} [\gamma / (\gamma + 3 \sigma_3 a + 2 \sigma_3 b \gamma)] \rightarrow \\ \varphi'_{mob} &= \sin^{-1} \{\gamma / [3 a \sigma_3 + (1 + 2 \sigma_3 b) \gamma]\} \rightarrow \\ \varphi'_{mob} &= \sin^{-1} \{\gamma / [A + B \gamma]\} \quad (B.3) \end{aligned}$$

In equation (B.3):

$$A = 3 a \sigma_3 \quad (B.4)$$

$$\text{where } a = 1 / E_i = 1 / [2 G_i (1 + \nu)] \quad (B.5)$$

If $\nu = 0.5$, $G_i = G^* z$ where G^* is the rate of increase of the shear modulus with depth and $\sigma_3 = \gamma_s z$ assuming that the initial earth pressure coefficient K_o is greater than unity, then from Equations (B.4) and (B.5):

$$A = 3 \gamma_s z / [2 G^* z (1 + 0.5)] \rightarrow A = \gamma_s / G^* \quad (B.6)$$

In equation (B.3):

$$B = (1 + 2 \sigma_3 b) \quad (B.7)$$

$$\text{where } b = R_f / 2 \tau_f \quad (B.8)$$

and τ_f is the shear stress at failure and is equal to $2 \sigma_3 \sin \varphi / (1 - \sin \varphi)$.

Duncan and Cheng (1970) used a value of R_f equal to 0.95, because their experiments were not continued long enough to reach failure. In this research it is assumed that the tests will be carried out long enough to reach failure and therefore a value of R_f equal to 1 is appropriate. From Equations (B.7) and (B.8):

$$B = 1 + 2 \sigma_3 (1 - \sin \varphi) / 4 \sigma_3 \sin \varphi \rightarrow$$

$$B = 1 + 0.5 (1 - \sin \varphi) / \sin \varphi \quad (B.9)$$

In Equation (B.9), φ is the angle of shearing resistance at failure.

C. TABLES: MSD RESULTS FOR CONDITIONS OF ZERO PORE WATER PRESSURES

In Tables C.1 and C.2 the value of A ($A = \gamma_s / G^*$) is kept constant and equal to 10^{-4} and 10^{-3} respectively, while ($\gamma_s \rho = \gamma_s H^4 / E I$) is in the range of 10^{-4} to 10^2 and φ' is in the range of 20° to 40° . In Tables C.3 and C.4 the value of $\gamma_s \rho$ is kept constant and equal to 10^{-1} and 10 respectively, while A is in the range of 10^{-6} to 10^{-1} and φ' is in the range of 20° to 40° . In Tables C.5 and C.6 the value of φ' is kept constant and equal to 20° and 25° respectively, while A is in the range of 10^{-6} to 10^{-1} and $\gamma_s \rho$ is in the range of 10^{-4} to 10^2 .

$$A = \gamma_s / G^* = 10^{-4}$$

φ'	$\text{Log}(\gamma_s \rho)$	M_{max} / M_{maxEC7}	F/F_{EC7}
20	-4	1.08101	1.06398
20	-3	1.07332	1.0553
20	-2	1.01526	0.995155
20	-1	0.860657	0.859888
20	0	0.785284	0.799719
20	1	0.774229	0.791035
20	2	0.773068	0.790124
30	-4	1.3101	1.15552
30	-3	1.30366	1.14748
30	-2	1.25028	1.08718
30	-1	1.03678	0.903707
30	0	0.860457	0.77512
30	1	0.82634	0.791035
30	2	0.822549	0.790124
40	-4	1.92168	1.31701
40	-3	1.91524	1.30907
40	-2	1.86179	1.24769
40	-1	1.6016	1.03982
40	0	1.17265	0.796894
40	1	1.03502	0.723693
40	2	1.01718	0.714249

Table C.1

$$A = \gamma_s / G^* = 10^{-3}$$

φ'	$\text{Log}(\gamma_s \rho)$	M_{max} / M_{maxEC7}	F / F_{EC7}
20	-4	1.08181	1.06489
20	-3	1.08101	1.06398
20	-2	1.07332	1.0553
20	-1	1.01526	0.995155
20	0	0.860657	0.859888
20	1	0.785284	0.799719
20	2	0.774229	0.791035
30	-4	1.31075	1.15636
30	-3	1.3101	1.15552
30	-2	1.30366	1.14748
30	-1	1.25028	1.08718
30	0	1.03678	0.903707
30	1	0.860457	0.77512
30	2	0.82634	0.751015
40	-4	1.92234	1.31783
40	-3	1.92168	1.31701
40	-2	1.91524	1.30907
40	-1	1.86179	1.24769
40	0	0.860657	1.03982
40	1	0.785284	0.796894
40	2	0.774229	0.723693

Table C.2

$$(\gamma_s \rho) = 10^{-1}$$

φ'	$\text{Log}(A)$	$M_{\max} / M_{\max EC7}$	F/F_{EC7}
20	-6	0.786869	0.791035
20	-5	0.805628	0.799719
20	-4	0.919407	0.859888
20	-3	1.10323	0.995155
20	-2	1.15934	1.0553
20	-1	1.16635	1.06398
30	-6	0.82634	0.723693
30	-5	0.860457	0.796894
30	-4	1.03678	1.03982
30	-3	1.25028	1.08718
30	-2	1.30366	1.14748
30	-1	1.3101	1.15552
30	-6	1.03502	1.06489
30	-5	1.17265	1.06398
30	-4	1.6016	1.0553
30	-3	1.86179	1.24769
30	-2	1.91524	1.30907
30	-1	1.92168	1.31701

Table C.3

$$(\gamma_s \rho) = 10$$

φ'	$\text{Log}(A)$	M_{max} / M_{maxEC7}	F/F_{EC7}
20	-6	0.772951	0.790032
20	-5	0.773068	0.790124
20	-4	0.774229	0.791035
20	-3	0.785284	0.799719
20	-2	0.860657	0.859888
20	-1	1.01526	0.995155
30	-6	0.822165	0.748075
30	-5	0.822549	0.748345
30	-4	0.82634	0.751015
30	-3	0.860457	0.77512
30	-2	1.03678	0.903707
30	-1	1.25028	1.08718
30	-6	1.01534	0.713272
30	-5	1.17265	0.714249
30	-4	1.03502	0.723693
30	-3	1.17265	0.796894
30	-2	1.6016	1.03982
30	-1	1.86179	1.24769

Table C.4

$\varphi'=20^\circ$

$\text{Log}(\gamma_s \rho)$	$\text{Log}(A)$	$M_{\max} / M_{\max EC7}$	F/F_{EC7}
-4	-6	1.01526	0.995155
-3	-6	0.860657	0.859888
-2	-6	0.785284	0.799719
-1	-6	0.774229	0.791035
0	-6	0.773068	0.790124
1	-6	0.772951	0.790032
-4	-4	1.08101	1.06398
-3	-4	1.07332	1.055
-2	-4	1.01526	0.995155
-1	-4	0.860657	0.859888
0	-4	0.785284	0.799719
1	-4	0.774229	0.791035
-4	-2	1.08189	1.0649
-3	-2	1.08181	1.06489
-2	-2	1.08101	1.06398
-1	-2	1.07332	1.0553
0	-2	1.01526	0.995155
1	-2	0.860657	0.859888

Table C.5

$\varphi'=25^\circ$

$\text{Log}(\gamma_s \rho)$	$\text{Log}(A)$	$M_{\text{max}}/M_{\text{max}EC7}$	F/F_{EC7}
-4	-6	1.10323	1.03402
-3	-6	0.919407	0.872667
-2	-6	0.805628	0.784117
-1	-6	0.786869	0.872667
0	-6	0.784856	0.768324
1	-6	0.784653	0.76817
-4	-4	1.16635	1.1032
-3	-4	1.15934	1.09492
-2	-4	1.10323	0.995155
-1	-4	0.919407	0.859888
0	-4	0.805628	0.784117
1	-4	0.786869	0.769851
-4	-2	1.1671	1.10425
-3	-2	1.16707	1.10416
-2	-2	1.16635	1.10329
-1	-2	1.07332	1.09492
0	-2	1.10323	1.03402
1	-2	0.919407	0.872667

Table C.6

D. TABLES: MSD RESULTS FOR CONDITIONS OF PORE WATER PRESSURES CORRESPONDING TO LINEAR SEEPAGE FROM AN ORIGINAL WATER TABLE AT GROUND LEVEL

In Tables D.1 and D.2 the value of A ($A = \gamma_s / G^*$) is kept constant and equal to 10^{-4} and 10^{-3} respectively, while ($\gamma_s \rho = \gamma_s H^d / E I$) is in the range of 10^{-4} to 10^2 and ϕ' is in the range of 20° to 40° . In Tables D.3 and D.4 the value of $\gamma_s \rho$ is kept constant and equal to 10^{-1} and 10^0 respectively, while A is in the range of 10^{-6} to 10^{-1} and ϕ' is in the range of 20° to 40° . In Tables D.5 and D.6 the value of ϕ' is kept constant and equal to 20° and 25° respectively, while A is in the range of 10^{-6} to 10^{-1} and $\gamma_s \rho$ is in the range of 10^{-4} to 10^2 .

$$A = \gamma_s / G^* = 10^{-4}$$

φ'	$\text{Log}(\gamma_s \rho)$	M_{max} / M_{maxEC7}	F/F_{EC7}
20	-4	1.01661	1.01663
20	-3	1.01253	1.01274
20	-2	0.979769	0.98315
20	-1	0.877202	0.900611
20	0	0.820557	0.857549
20	1	0.812013	0.851101
20	2	0.811113	0.850422
30	-4	1.04099	1.04098
30	-3	1.03712	1.14748
30	-2	1.00516	1.08718
30	-1	0.877202	0.903707
30	0	0.814952	0.77512
30	1	0.80206	0.791035
30	2	0.800677	0.790124
40	-4	1.08459	1.31701
40	-3	1.08127	1.03697
40	-2	1.05267	1.0056
40	-1	0.93013	0.908496
40	0	0.818948	0.848404
40	1	0.79644	0.838466
40	2	0.79393	0.837401

Table D.1

$$A = \gamma_s / G^* = 10^{-3}$$

φ'	$\text{Log}(\gamma_s \rho)$	$M_{\text{max}} / M_{\text{max}EC7}$	F/F_{EC7}
20	-4	1.01703	1.01703
20	-3	1.01253	1.01663
20	-2	1.01253	1.01274
20	-1	0.979769	0.98315
20	0	0.877202	0.900611
20	1	0.820557	0.857549
20	2	0.812013	0.851101
30	-4	1.04139	1.04139
30	-3	1.04099	1.04098
30	-2	1.03712	1.03697
30	-1	1.00516	1.0056
30	0	0.891649	0.908496
30	1	0.814952	0.848404
30	2	0.80206	0.838466
40	-4	1.08493	1.08493
40	-3	1.08459	1.08453
40	-2	1.08127	1.08071
40	-1	1.05267	1.04957
40	0	0.93013	0.937543
40	1	0.818948	0.848203
40	2	0.79644	0.83064

Table D.2

$$(\gamma_s \rho) = 10^{-l}$$

φ'	$\text{Log}(A)$	$M_{\max} / M_{\max EC7}$	F/F_{EC7}
20	-6	0.812013	0.851101
20	-5	0.820557	0.857549
20	-4	0.877202	0.900611
20	-3	0.979769	0.98315
20	-2	1.01253	1.01274
20	-1	1.01661	1.01663
30	-6	0.80206	0.838466
30	-5	0.814952	0.848404
30	-4	0.891649	0.908496
30	-3	1.00516	1.0056
30	-2	1.03712	1.03697
30	-1	1.04099	1.04098
40	-6	0.79644	0.83064
40	-5	0.818948	0.848203
40	-4	0.93013	0.937543
40	-3	1.05267	1.04957
40	-2	1.08127	1.08071
40	-1	1.08459	1.08453

Table D.3

$$(\gamma_s \rho) = 10^0$$

φ'	$\text{Log}(A)$	M_{max} / M_{maxEC7}	F/F_{EC7}
20	-6	0.811023	0.850354
20	-5	0.811113	0.850422
20	-4	0.812013	0.851101
20	-3	0.820557	0.857549
20	-2	0.877202	0.900611
20	-1	0.979769	0.98315
30	-6	0.800538	0.837293
30	-5	0.800677	0.837401
30	-4	0.80206	0.838466
30	-3	0.814952	0.848404
30	-2	0.891649	0.908496
30	-1	1.00516	1.0056
40	-6	0.793676	0.82849
40	-5	0.79393	0.828687
40	-4	0.79644	0.83064
40	-3	0.818948	0.857549
40	-2	0.93013	0.900611
40	-1	1.05267	1.04957

Table D.4

$\phi'=20^\circ$

$\text{Log}(\gamma_s \rho)$	$\text{Log}(A)$	$M_{\text{max}}/M_{\text{max}EC7}$	F/F_{EC7}
-4	-6	0.979769	0.98315
-3	-6	0.877202	0.900611
-2	-6	0.820557	0.857549
-1	-6	0.812013	0.851101
0	-6	0.811113	0.850422
1	-6	0.811023	0.850354
-4	-4	1.01661	1.01663
-3	-4	1.01253	1.01274
-2	-4	0.979769	0.98315
-1	-4	0.877202	0.900611
0	-4	0.820557	0.857549
1	-4	0.812013	0.851101
-4	-2	1.01707	1.01707
-3	-2	1.01703	1.01703
-2	-2	1.01661	1.01663
-1	-2	1.01253	1.01274
0	-2	0.979769	0.98315
1	-2	0.877202	0.90061

Table D.5

$\phi'=25^\circ$

$\text{Log}(\gamma_s \rho)$	$\text{Log}(A)$	M_{max}/M_{maxEC7}	F/F_{EC7}
-4	-6	0.990375	0.992285
-3	-6	0.882317	0.90259
-2	-6	0.816872	0.852059
-1	-6	0.806521	0.844157
0	-6	0.805422	0.843319
1	-6	0.805311	0.843235
-4	-4	1.02705	1.02705
-3	-4	1.02303	1.02305
-2	-4	0.990375	0.992285
-1	-4	0.90259	0.900611
0	-4	0.816872	0.852059
1	-4	0.80652	0.844157
-4	-2	1.0275	1.02751
-3	-2	1.02747	1.02747
-2	-2	1.02705	1.02705
-1	-2	1.02303	1.02305
0	-2	0.990375	0.992285
1	-2	0.882317	0.90259

Table D.6